Luminescent Transition Metal Complexes: Optical Characterization, Integration into Polymeric Nanoparticles and Sensing Applications

Inaugural-Dissertation

to obtain the academic degree

Doctor rerum naturalium (Dr. rer. nat.)

submitted to the Department of Biology, Chemistry, Pharmacy

of Freie Universität Berlin

by

Cui Wang

(from Shandong, China)

Berlin, 2020

This thesis was prepared in the time frame of July 2017 to December 2020 in the group of Dr. Ute Resch-Genger (Division 1.2 Biophotonics) at the Bundesanstalt für Materialforschung und -prüfung (BAM).

I hereby declare that this doctoral work was prepared autonomously and that no illegal help was used. Contributions from others, *e.g.* content, quotes, or figures are indicated by referring to the original work.

Berlin, December 2020

     (Cui Wang)

1st Reviewer: Dr. Ute Resch-Genger

2nd Reviewer: Prof. Dr. Eckart Rühl

Date of Defence: March 5th, 2021

Abstract

Photoluminescence is a fascinating phenomenon which has a huge impact on our daily life. Many important applications are based on this principle, such as imaging diagnostics, bioanalytic, photocatalysis, solar cells, or optoelectronic devices. The emerging demands for versatile photoluminescent materials have encouraged generations of scientists to develop different types of luminophores, ranging from molecular dyes to luminescent nanomaterials. Among them, luminescent transition metal complexes (TMCs), which consist of one (or more) metal center and several organic or inorganic ligands, are drawing increasing interest due to their unique photophysical and photochemical properties, such as large Stokes shift, long-lived triplet excited state, sharp emission band (f-block metal complexes), and multiple stale oxidation states (d-block metal complexes). These distinct optical properties are not only of great research interest, but also have led to commercial applications, such as imaging agents, optical sensors, light-harvesting materials, optical barcoding, and displays.

The demands and desires of optoelectronic devices and higher requirements in bioanalytic make the development of new TMCs necessary, which needs to be examined in detail not only in terms of their chemical but much more importantly their photophysical properties. In this work, a series of new types of luminescent TMCs are involved, including Cr(III)-, Pt(II)-, and Pd(II) complexes. Based on their optical studies, a series of proof-of-concept applications were designed by introducing these metal complexes to different nanomatrix, such as polymeric nanoparticles and metal-organic frameworks (MOFs), resulting various luminescent nanosensors or energy-conversion materials.

The major part of this work is based on the $[Cr(ddpd)_2]^{3+}$ complex (ddpd = N, N′-dimethyl-N, N′-dipyridine-2-ylpyridine-2,6-diamine) and his derivatives. Fundamental photophysical studies of these Cr(III) complexes showed that their photoluminescence properties can be significantly enhanced by ligand and solvent deuteration. Moreover, a choice of bulky counter anions can provide an enhancement in the photoluminescence properties as well as the oxygen sensitivity. In addition, based on the photophysical understanding of the $[Cr(ddpd)_2]^{3+}$ complex, a proof-of-concept study of photon upconversion in molecular chromium ytterbium salts was completed. Upon an excitation of the Yb^{3+} sensitizers at 976 nm, these solid-state salts produced upconverted luminescence of the Cr^{3+} activator at 780 nm at room

temperature. Another proof-of-concept study based on the $[Cr(ddpd)_2]^{3+}$ complex was investigated by designing and developing multianalyte nanosensors for simultaneously measuring temperature ("T"), oxygen ("O"), and pH ("P") in aqueous phase under one excitation wavelength.

Apart from the $[Cr(ddpd)_2]^{3+}$ complexes, four novel Pt(II)- and Pd(II)-complexes bearing tetradentate ligands were also studied regarding their photophysical properties in solutions and in polystyrene nanoparticles (PS-NPs). In PS-NPs, the aggregation-induced Metal-Metal-to-Ligand Charge-Transfer (^{3}MMLCT) state of the fluorinated Pt(II) complex is red-shifted compared to the monomeric emission and performs insensitive to oxygen, allowing the particles as self-referenced oxygen nanosensor in both the luminescence intensity and lifetime domains. Additionally, a triplet–triplet annihilation upconversion (TTA-UC) system was developed based on a crystalline MOF. A Pd(II) porphyrin complex acted as the sensitizer immobilized in the MOF walls, while a 9,10-diphenylanthracene annihilator was filled in the channels. Upon green light excitation at 532 nm, the resulting MOF crystalline showed an upconverted blue emission with delayed lifetime from 4 ns to 373 µs and a triplet–triplet energy transfer efficiency of 82%.

Zusammenfassung

Lumineszenz ist ein faszinierendes Phänomen und hat einen großen Einfluss auf unseren Alltag. Viele wichtige Anwendungen beruhen auf diesem Prinzip, wie zum Beispiel die bildgebende Diagnostik, Bioanalytik, Solarzellen, Photokatalyse, oder optoelektronische Geräte. Generationen von Wissenschaftlern haben in den letzten Jahrzehnten verschiedene Arten von lumineszenten Materialien entwickelt, die von molekularen Farbstoffen bis zu lumineszierenden Nanomaterialien reichen. Dabei sind lumineszierende Übergangsmetallkomplexe (TMCs), die aus einem (oder mehreren) Metallzentren und mehreren organischen oder anorganischen Liganden bestehen, aufgrund ihrer einzigartigen photophysikalischen und photochemischen Eigenschaften von besonderen Interesse. TMCs zeichnen sich durch eine große Stokes-Verschiebung, einem langlebigen angeregten Triplett-Zustand, scharfe Emissionsbanden (f-Block-Metallkomplexe) und mehrere stabile Oxidationsstufen (d-Block-Metallkomplexe) aus. Diese unterschiedlichen optischen Eigenschaften sind nicht nur von großem Interesse für die Forschung, sondern wurden auch in kommerziellen Anwendungen ausgenutzt, wie zum Beispiel bei Kontrastmitteln, für optische Sensoren, als Lichtsammelmaterialien, in optischen Barcodes oder auch in Displays.

Die ständige Weiterentwicklung von optoelektronischen Geräten und höhere Anforderungen in der Bioanalytik und Bildgebung macht die Entwicklung neuer TMCs nötig, welche eingehend nicht nur hinsichtlich ihrer chemischen aber viel wichtiger noch ihrer photophysikalischen Eigenschaften untersucht werden müssen. In dieser Arbeit wurden eine Reihe neuer lumineszierender TMCs untersucht, darunter Cr(III)-, Pt(II)- und Pd(II)-Komplexe. Neben ihrer detaillierten spektroskopischen Untersuchung wurden auch Konzeptstudien entwickelt, bei denen diese Metallkomplexe in verschiedene Nanomatrizen wie polymere Nanopartikel und metallorganische Gerüste (MOFs) eingebracht wurden. Dies ermöglichte die Herstellung von Nanosensoren und aufkonvertierender Nanomaterialien.

Der Hauptteil dieser Arbeit basiert auf den $[Cr(ddpd)_2]^{3+}$-Komplex (ddpd = N, N'-Dimethyl-N, N'-Dipyridin-2-ylpyridin-2,6-diamin) und seinen Derivaten. Die photophysikalischen Untersuchungen dieser Cr(III)-Komplexe zeigten, dass durch eine Deuterierung der Liganden und die Verwendung von deuterierten Lösungsmitteln die Lumineszenzeigenschaften signifikant verbessert werden können. Darüber hinaus zeigte sich eine Abhängigkeit der

Lumineszenzeigenschaften und der Sensitivität gegenüber Sauerstoff von der Art des Gegenions. Basierend auf diesen Untersuchungen wurde eine Konzeptstudie entwickelt, in der der Komplex, in einem Chrom-Ytterbium Salz eingeschlossen, hinsichtlich der Eignung für die Photon Aufkonvertierung bei Raumtemperatur evaluiert wurde. Dabei wurden die Yb^{3+}-Sensibilisatoren bei 976 nm angeregt und die aufkonvertierte Lumineszenz des Cr^{3+}-Aktivators bei 780 nm untersucht. Eine weitere Konzeptstudie basierend auf dem $[Cr(ddpd)_2]^{3+}$-Komplex war die Verwendung als Nanosensor**s** für die gleichzeitige Messungen von Temperatur („T"), Sauerstoff („O"), und pH („P") in wässrigen Phasen unter einer einzigen Anregungswellenlänge.

Weiterhin wurden in dieser Arbeit auch vier neue Pt(II)- und Pd(II)-Komplexe mit tetradentaten Liganden hinsichtlich ihrer photophysikalischen Eigenschaften in Lösungen und eingebettet in Polystyrol-Nanopartikeln (PS-NP) untersucht. In PS-NP ist der aggregationsinduzierte Metall-Metall-Ligand-Ladungsübertragungszustand (^{3}MMLCT) des fluorierten Pt(II)-Komplexes im Vergleich zur monomeren Emission rotverschoben und unempfindlich gegenüber Sauerstoff, so dass die Partikel sowohl in der Lumineszenzintensität als auch in der Lebensdauer als selbstreferenzierter Sauerstoffnanosensor fungieren können. Zusätzlich wurde ein Triplett-Triplett-Annihilations-Aufkonvertierung-System (TTA-UC) entwickelt, das auf einem kristallinen MOF basiert. Ein Pd(II)-Porphyrin Komplex fungierte als in den MOF-Wänden immobilisierter Sensibilisator, während ein 9,10-Diphenylanthracen als Akzeptor in die Kanäle gefüllt wurde. Das resultierende kristalline MOF zeigte bei Anregung mit grünem Licht (532 nm) eine aufkonvertierte blaue Emission mit einer verzögerten Lebensdauer von 4 ns auf 373 µs und einer Triplett-Triplett-Energieübertragungseffizienz von 82%.

Outline

1 Introduction

Solar energy is considered as the ultimate renewable energy source that can be harvested on Earth.[1-3] Natural photon processes are involved in the Earth activities omnipresently, *e.g.* plants can use sun light to convert CO_2 and H_2O to carbohydrates via photosynthesis;[4] vitamin D can be formed in human beings upon exposure to sunlight;[5] fireflies produce light to attract mates or prey via bioluminescence;[6] OH radicals are generated via UV photolysis of ozone for initiating the oxidation of atmospheric trace constituents,[7] colorful light emission is generated from the aurora borealis due to the ionization and excitation of atmospheric constituents.[8,9] The recognition of these naturally occurring photon phenomena has inspired and motivated generations of scientists to explore the photophysical and photochemical processes and develop technologies for light harvesting, storage and utilization. Among them, luminescence has been fascinating mankind from the ancient to modern times. The earliest written account of luminescence dates back to Song Dynasty (960–1279 A.D.) in ancient China, where a persistent phosphor material was presumably used as the ink in a painting picture.[10-12] For centuries, the exploration of luminescence and the relevant techniques never ceased. Examples of the long-lived phosphorescent material in the daily life include the glow-in-the-dark toys and paints, whose glowing time after light charging can even reach a few minutes or even up-to a few hours in dark rooms.[13,14] In 2014, the Nobel Prize in Chemistry was awarded to Eric Betzig, Stefan Hell, and William E. Moerner for their contribution in developing super-resolution fluorescence microscopy.[15,16]

Impelled by the strong interests in photoluminescence (PL), PL materials and relevant approaches have developed into a powerful technique, which is used in various fields of research and application. PL materials can serve as promising candidates for organic light-emitting diodes (OLEDs),[17] as photocatalysists[3,18,19] as well as photosensitizers for light-harvesting in solar cells.[20,21] Especially in life science, the investigation of photoluminescent probes has led to significant breakthroughs in revealing the complex biological processes and developing clinical treatments.[22-27] Currently, the spread of the COVID-19 pandemic has raised widespread concern worldwide and promoted the urgent need for medical testing and treatment tools. In this battle against the coronavirus, photoluminescence technique has been demonstrating its significance in the relevant researches, *e.g.* a magnetic chemiluminescence enzyme immunoassay (MCLIA) for coronavirus-specific antibody detection;[28] live cell imaging

of single RNA molecules through fluorogenic Mango II arrays that are highly promising for developing fluorescent testing kits for coronavirus.[29]

These broad biological application potentials of luminescent probes are promoted by their specific light-based properties. As powerful yet flexible analytical tools, photoluminescent probes perform non-destructive, rapid, sensitive, reliable, and reversible detection of the target species in biosystems, enabling the visualization with superior resolution down-to nanoscale, and the analysis of the involute bioprocesses in a contactless fashion.[24,26,30-32] More specifically, tissue, cells, and biomolecules can be stained or selectively labeled with photoluminescent probes for bioimaging or detection of molecular interactions.[23,30,33-35] In biological environments, near infrared (NIR) absorbing and luminescent probes are preferred, due to their deeper penetration depth into the biological systems compared to ultraviolet (UV) or visible light. Meanwhile, autofluorescence from biological systems can be avoided, leading to bioimaging with high spatial resolution.[36] For instance, NIR emissive dyes have been applied for *in vivo* imaging of tumor hypoxia or for tumor development.[37,38] Moreover, luminescent probes are also developed as optical chemical sensors; they can interact with the intrinsically non-fluorescent ionic or neutral analytes (*e.g.* pH, oxygen (pO_2), metal ions, hydrogen peroxide) or respond to the surroundings (*e.g.* temperature and pressure).[30,34,39-43] Among all measurable parameters, the most frequently investigated ones with optical chemical sensors are temperature, oxygen and pH due to their high relevance for biological processes (*e.g.* diseases such as cancer or inflammation) and corrosion processes in materials sciences. Furthermore, luminescent materials are of great interests for clinical treatments, *e.g.* for photodynamic therapy (PDT), where the light-absorbing and emissive photosensitizers generate reactive oxygen species (ROS), such as singlet oxygen in the presence of dioxygen. These ROS can kill the targeted cancer cells, microbial cells, bacteria, fungi, and viruses.[44,45]

To meet the various application requirements and desires, different types of luminescent materials have been developed. Generally, luminophores can be classified into molecular luminophores and nanoscale (typically 10^{-9} - 10^{-7} m) luminophores (*e.g.* luminescent nanoparticles, NPs). Molecular luminophores include organic dyes and metal complexes (coordination complexes), which are constructed by one (or more) metal center and several organic or inorganic ligands. Depending on the nature of the center metals, the group of luminescent transition metal complexes (TMCs), is assigned to the major family of the

inorganic molecular luminophores. In the last decades, luminescent TMCs have attracted increasing scientific interest due to the broad application potential based on their specific optical properties.[46-49] Among the TMCs, those featuring favorable photophysical and photochemical properties are mostly based on precious or rare metals thus far, *e.g.* the well-employed photocatalysts Ru(II) pyridine derivatives,[50,51] the oxygen sensitive Pd(II) or Pt(II) porphyrin derivatives[37,52] as well as lanthanide complexes.[53,54] In the past decade, luminescent TMCs based on earth-abundant metals (*e.g.* Cu, Zr, Fe, Cr, Mo) have drawn the attention of scientists owing to their exciting PL properties and eco-friendly application potentials.[19,55,56] In 2015, Heinze *et al.* developed a series of Cr(III) complexes coordinated with two tridentate ligands ddpd (N ,N ′-dimethyl-N ,N ′-dipyridine-2-ylpyridine-2,6-diamine). These water-soluble $[Cr(ddpd)_2]^{3+}$ complexes perform as molecular ruby analogues with exceptionally high near-infrared phosphorescence quantum yields of 11% and lifetimes of 898 μs in deaerated water at room temperature, enabling them as promising candidates for substituting the TMCs of precious and rare metals.[57] In addition to the high brightness, these Cr(III) complexes also demonstrate a luminescence response to temperature,[58] pressure,[59] and triplet oxygen[57], indicating a broad application potential for mono- or multi-analyte optical sensors.

In parallel with photoluminescence, the development of nanotechnology and nanomaterials in scientific knowledge and industrial applications has entered an exploration period.[60-62] Contemporarily, applications of nanomaterials can be found in industries of catalysis,[18] solar cells,[63] cement,[64] printed electronics,[65] food,[66] cosmetics,[67] and so on. Particularly in the fields of biology and medicine, the unique size-dependent properties of nanomaterials provided us with the idea of using these nanoprobes to explore the cellular machinery without causing too much additional interences.[68] The high functionalization flexibility of nanoparticles enables numerous configurations of the nano-bio materials, leading to a wide range of applications,[69-71] including luminescent biological labels/sensors,[24,30,35] drug and gene delivery,[72-75] photodynamic therapy,[76,77] tissue engineering.[78,79]

Together with the remarkable achievements in nanotechnology, many new types of luminescent nanomaterials have been developed. Among them are **i)** carbon-based nanomaterials, including nanodiamonds, carbon nanotubes, carbon nanodots, graphene, fullerenes, semiconducting polymers dots.[80,81] Another class of luminescent nanomaterials are **ii)** semiconductor nanocrystals (also known as quantum dots (QDs)), of which the

luminescent properties can be tuned by their size and composition. The QDs usually contain roughly 200 –10 000 atoms from various periodic groups, such as the II-VI type cadmium selenide (CdSe) and cadmium sulfide (CdS).[82-84] **iii)** Nanocrystals doped with lanthanide ions have also been intensely studied for biological applications due to their distinct photophysical properties of upconversion for converting near-infrared light into visible and ultraviolet emission.[85-87] Additionally, the group of **iv)** luminescent polymeric nanoparticles (PNPs) feature a wide diversity of PL properties, as either organic dyes, metal complexes, or inorganic nanoparticles can be introduced into the nanometer- to micrometer-sized polymer- and silica particles, yielding multi-chromophoric particulate luminescent probes.[88,89] Moreover, the molecular luminophores can also be introduced to **v)** coordination polymers, such as metal-organic frameworks (MOFs). With proper design strategies, the generated luminescent MOFs can perform enhanced luminescent properties by shielding aggregation of the luminophores in the nanomatrices.[90,91]

Depending on the optical properties of the applied luminescent material, PL response can be explicitly expressed by various parameters, including absorption wavelength, emission wavelength, intensity or quantum yield, luminescence lifetime, and emission anisotropy. A series of technologies have been developed to characterize and analyze the PL properties, such as absorption spectroscopy, fluorescence spectroscopy and fluorescence microscopy based on their emission intensity or fluorescence lifetime imaging (FLIM).

Even though the luminescent TMCs have been extensively designed and developed recently, their applications as purely molecular luminophores are still limited mainly by the application-relevant environments, which is particularly true for biological environments. Typical challenges involve luminescence quenching, such as aggregation caused quenching (ACQ), poor solubility in aqueous media, bare selectivity to biological targets, uncertain biocompatibility depending on the nature of the molecule. Exploiting the unique properties of nanomaterials, the combination of molecular luminophores and nanomatrices can address the challenges in the biological environment, as mentioned above. Moreover, the luminescent properties can be improved in the nanomatrices due to the increased molecular rigidity and thus the suppressed environmental quenching.[92-94] Furthermore, nanomatrices enable more efficient distance-dependent energy transfer processes, such as Förster resonance energy transfer (FRET),[95,96] intermolecular energy upconversion.[86,97]

Although there is a large toolbox of the luminescent TMC-based molecular and nanoscale materials, it is still highly desired to exploit more novel TMCs and their relevant nanomaterials with inspiring optical properties for eco-friendly and innovative applications. Motivated by these demands, this thesis will focus on studying the optical properties of a series of TMCs under different conditions and designing their applications (*e.g.* as optical nanosensors or for energy upconversion) by introducing them into various nanomatrices.

In this thesis, various types of luminescent TMCs are introduced, including Cr(III) complexes, Pt(II)- and Pd(II) complexes. Among them, the Cr(III) complexes bearing two tridentate ddpd ligands and their derivatives are systematically studied, involving optical characterization of the molecular complexes in various solvents and in solid-state, design of multianalyte optical nanosensors by inserting the complex and other organic dyes to PNPs, and photophysical studies of the application-relevant properties such as optical sensing behaviors and the implicated energy transfer processes. Additionally, a series of novel planar Pt(II)- and Pd(II) complexes are encapsulated into PNPs for developing optical oxygen sensors. Subsequent photophysical studies of these Pt(II)- and Pd(II) complexes doped PNPs are demonstrated, with the focus on their sensing behavior and aggregation-induced charge transfer processes. Ultimately, a study of energy upconversion is performed in a MOF system, where another Pd(II) complex is inserted in the MOF walls as a photosensitizer and acceptor which is filled in the MOF channels. For energy upconversion, the dependence of laser radiation density is studied as this involves a multiphoton process.

2 Theoretical Background

2.1 Luminophores

Jablonski Diagram

Depending on the nature of the photoactive substance and its interactions with the environment, various primary photophysical processes can occur. Upon photoexcitation, the luminophore is pumped to higher energy electronic states. The stored energy can be released radiatively in the form of luminescence or can be released non-radiatively by heat (internal conversion) or by other non-emissive pathways like collisions with other species and/or the energy or electron transfer to other species.[98] The basically involved radiative and non-radiative transitions between the electronic and vibrational states of a luminescent molecule are illustrated in the Jablonski diagram in **Figure 1**.
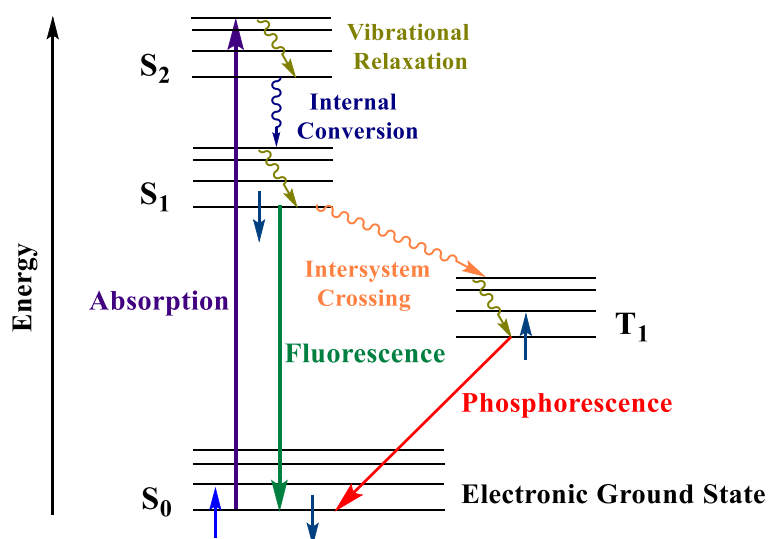
Figure 1: Simplified Jablonski diagram of a luminescent molecule for illustrating photoabsorption, non-radiative transitions (squiggly arrows) and radiative decays (straight arrows).

Upon photoabsorption, the luminophore is excited from its electronic ground state, typically a singlet state, to an excited singlet state S_n with higher energy (without changing the spin of the transferred electron). Via non-radiative transitions involving vibrational relaxation and internal conversion (time scale of ca. 10^{-12} s), the compound relaxes to a lower energy state S_1. Subsequently, the stored energy from the S_1 state can either be directly emitted in the form of fluorescence (time scale in the order of $1 - 100$ ns) or be transferred via intersystem crossing to an energetically lower lying triplet state T_1 involving the flipping of the electron´s

spin, which is allowed by the spin-orbital coupling. The radiative transition from this T_1 state to the ground state generates phosphorescence, which features a much slower decay (longer than 10^{-6} s) due to the "forbidden" nature of this transition by the spin selection rule.[31,99]

2.1.1 Organic Dyes

The common organic luminophores usually contain conjugated π-systems favoring electronic transitions upon photoexcitation. Depending on the nature of the electronic transitions, organic dyes can be classified to a locally excited dye, where delocalization of π-electrons can occur over the whole molecule, or a charge transfer dye involving an intramolecular charge transfer of a fraction of the electronic charge.[24,31]
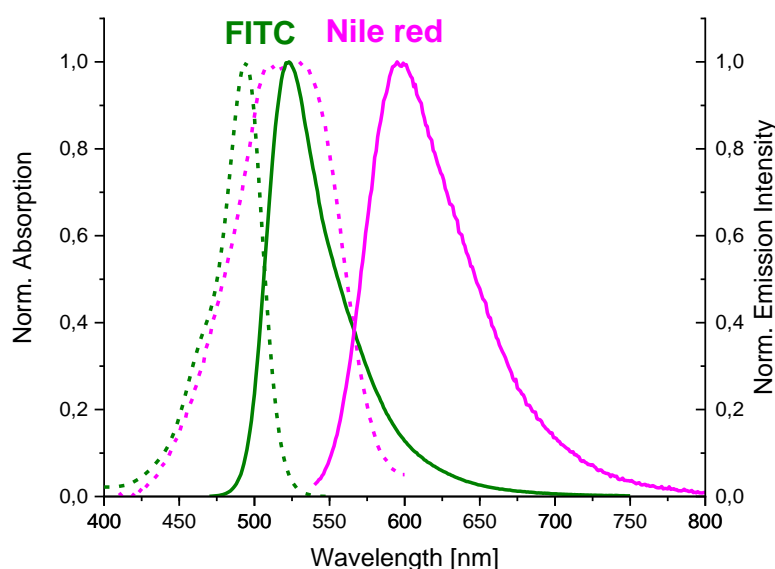
Figure 2: Absorption (dashed lines) and emission (solid lines) spectra of fluorescein isothiocyanate (FITC) (green) and Nile red (pink) in ethanol.

Typical locally excited dyes for bioanalytical applications include the well-known xanthene derivatives (*e.g.* fluorescein, rhodamine), dipyrromethene derivatives (*e.g.* BODIPY, aza-BODIPY), tetrapyrrole derivatives (*e.g.* porphyrins, phthalocyanine), and cyanine derivatives (*e.g.* cyanine). These dyes typically show relatively narrow and symmetric absorption and emission bands with small Stokes shift (< 50 nm in the UV/Vis region), which are barely sensitive to the polarity of the solvent (**Figure 2**, green spectra). These dyes usually feature high molar absorption coefficients of its long wavelength absorption maximum (ε_M of the order of 10^5 $M^{-1}cm^{-1}$) and high fluorescence quantum yield (0.80 – 1.00 in the visible region,

0.10 – 0.25 in the near-infrared (NIR) range.[24] In terms of the charge transfer dyes, such as coumarins derivatives, oxazine derivatives (*e.g.* Nile red, Nile blue) and certain naphthalene derivatives (*e.g.* dansyl fluorophores), they show a clear solvent dependence in the absorption and emission spectra (**Figure 2**, pink spectra). Commonly, most charge transfer dyes display lower molar absorption coefficients and fluorescence quantum yields compared to the locally excited dyes. Moreover, the optical properties of these dyes demonstrate stronger polarity dependence, which can influence the shape and the position of their absorption/emission bands, the Stokes shift, as well as the fluorescence quantum yield.

The optical properties of both locally excited- and charge transfer dyes can be well tuned by elaborate design and modification of their molecular structures. Many synthetic strategies have been explored and developed to improve the spectroscopic properties of organic dyes for biological and bioanalytical applications.[100-102] For instance, by inserting polymethine linkers with increasing length into the cyanine dyes containing indolenine heterocycles, a series of NIR-II emissive cyanine dyes have been developed for bioimaging with high resolution and for multiplexed biosensing.[103] Replacing the indolenines with dimethyl amino flavylium heterocycles, fluorescence emission of the formed flavylium dye can be tuned from NIR to short-wave infrared (SWIR) region with increasing length of the polymethine linkers, enabling deep bioimaging with high contrast and brightness.[104] Additionally, through precise molecular design and synthetic approaches, a plethora of purely organic luminophores with long-lived phosphorescence under ambient conditions has been realized with remarkable breakthroughs in the last decade.[105-109]

Depending on the molecular configuration, organic dyes can perform aggregation-caused quenching (ACQ) or aggregation-induced emission (AIE). ACQ is mostly observed with conventional organic dyes, such as rhodamines, cyanines, and Nile Red. When these dyes start to form aggregate due to high concentration, $\pi - \pi$ stacking interactions of their π-conjugated systems will be induced. With these interactions, the dyes tend to form H-type dimers and aggregate that are barely or non-emissive.[110] In contrast to ACQ, aggregation-induced emission (AIE), which was firstly observed by Tang *et al.* with the twisted dye 1-methyl-1,2,3,4,5-pentaphenylsilole in 2001,[111] provides a series of strategies for luminescence enhancement in dye aggregates. AIE dyes show usually a twisted skeleton conformation and propeller-like moieties.[112,113] As a monomeric AIE dye in solution, it demonstrates bare

luminescence due to the numerous non-radiative decays caused by intramolecular rotations and vibrations of the bulky substituents. In their aggregates, however, the intramolecular motions of the substituents are restricted, leading to complete or partial blocking of the non-radiative decay pathways from the excited state. Thus, the luminescence emission can be strongly enhanced.[114-117]

2.1.2   Luminescent Metal Complexes

Luminescent metal complexes are attractive inorganic luminophores with broad applications in life science, photocatalysis, solar cells, and electronic devices. The mostly investigated luminescent complexes are based on transition metals. Depending on the metals, they include the f-block lanthanide complexes (*e.g.* complexes of ytterbium, erbium, europium) and d-block transition metal complexes (TMCs) such as those containing platinum, palladium, and ruthenium. This Section will give a detailed description of these two types of luminophores.

2.1.2.1   Lanthanide Complexes (f-block)

Luminescent trivalent lanthanide complexes, namely Ln(III) complexes (such as Eu(III), Er(III), Yb(III), Tb(III)), are drawing increasing interest as light emitting materials in bioimaging and biosensing,[118] solid state display, and light conversion in solar cells.[54,119] This class of luminophores features unique optical properties, including their line-like spectra and long lifetimes (in µs to ms range).[120] The extremely sharp spectra originate from the shielded 4f transitions by the filled $5s^25p^6$ subshells, while the long lifetimes are resulting from the partially forbidden f-f transitions (symmetry and parity forbidden, Laporte forbidden transitions). These forbidden transitions lead meanwhile to low absorption coefficients of the lanthanide ions.[24,54] To enhance the absorbance and thus the emission intensity of the f-f transitions, a common strategy presents the usage of an organic aromatic ligand to sensitize the lanthanide emission. Generally, upon light absorption, the ligand is excited to its singlet excited state. Via intersystem crossing the triplet state of the ligand is populated. Subsequently, the excitation energy is transferred from the excited triplet state of the ligand to the lanthanide ions, leading to lanthanide emissions.[121] All these involved photophysical processes determine the overall luminescence properties of the lanthanide complexes.[122] Moreover, the choice of the ligand needs specific considerations, as it serves not only as an

antenna to sensitize the lanthanide ion, but also to protect the lanthanide center from potential quenchers like from water molecules in the coordination sphere.[123] Common ligands include β-diketones, pyridine carboxylic acids, quinolones, Schiff bases such as $R_2C = NR'$ (R' $\neq$ H).

In addition to the sharp and characteristic emission bands and long-lived emissive state, the luminescent lanthanide complexes can be typically excited in the short wavelength region (usually in the UV-range), while the emission signals can be observed either in the visible (*e.g.* Tb^{3+}: 490, 545 nm; Eu^{3+}: 580, 613, 690 nm; Sm^{3+}: 598, 643 nm) or in the NIR region (*e.g.* Yb^{3+}: 980 nm; Nd^{3+}: 880, 1065 nm; Er^{3+}: 1522 nm), leading to a larger Stokes shift.[124-126] Recently, Gawryszewska *et al.* demonstrated a series photostable lanthanide complexes performing extremely high overall emission quantum yields ($\Phi_{Eu}= \Phi_{Tb} = 0.98$, $\Phi_{Sm} = 0.11$, $\Phi_{Dy} = 0.17$).[127] The prominent photophysical properties of lanthanide complexes have led to commercial applications, such as time-gated arrays, optical barcoding, and displays.

2.1.2.2 Transition Metal Complexes (d-block)

Aside from the f-block lanthanide complexes, another group of the inorganic molecular luminophores are the TMCs originating from the d-block metals. This class of luminophores is usually formed through coordinative or covalent bonds between the d-block metal center and the coordinated organic/inorganic ligands. The transition metals can have an incompletely filled d sub-shell. The TMCs might exhibit two or more stable oxidation states. The applied ligands serve as Lewis bases, acting mostly as σ-donors and some as π-donors or π-acceptors, as well. Benefiting from the various transition metals and the diversity of the ligands, many assorted TMCs with distinct photophysical and photochemical properties have been developed.

In the centrosymmetric TMCs, d-d- transitions are forbidden by the Laporte selection rule,[128] resulting in weak absorption bands and mostly low intensity color in solution, *e.g.* for the octahedral titanium(III) complex. However, a change in electron distribution between the metal and a ligand will give rise to charge transfer bands, which show high molar absorption coefficients in the UV/Vis region and are selection rule allowed.[129] Decided by the nature of the TMC molecules, numerous charge transfer processes can be observed. Among them, the most common CT processes include metal-to-ligand charge transfer (MLCT) and ligand-to-

metal charge transfer (LMCT). Metal-centered (MC) charge transfer and ligand-centered (LC) charge transfer processes are usually mixed with MLCT and LMCT transitions (**Figure 3**).

In the formed molecular orbitals (MO), MLCT occurs if the electron is transferred from a MO with metal-like character to one with ligand-like character.[130,131] This process is commonly favored for TMCs featuring metal ions in a low oxidation state and ligands with energetically low-lying π^* orbitals, *e.g.* 2,2'-bipyridine (bpy), 1,10-phenanthroline (phen), CO, CN$^-$, and SCN$^-$.[132] In most cases, MLCT undergoes between the π orbitals, *e.g.* from the π_M to the π_L^* orbital (**Figure 3**), resulting in the oxidation of the metal. Typical MLCT examples include the well-known octahedral d^6 ruthenium(II) complexes bearing ligands such as bpy- or phen derivatives,[133,134] the square-planar d^8 complexes Pt(II) and Pd(II) porphyrins,[135,136] and the d^{10} copper (I) complexes such as [Cu(bfp)$_2$]$^+$ (bfp=2,9-bis(trifluoromethyl)-1,10-phenanthroline) and [Cu(N^N)(POP)]$^+$ (N^N=2,9-disubstituted 1,10-phenanthroline; POP=bis[2-(diphenylphosphino)phenyl]ether).[137-139]
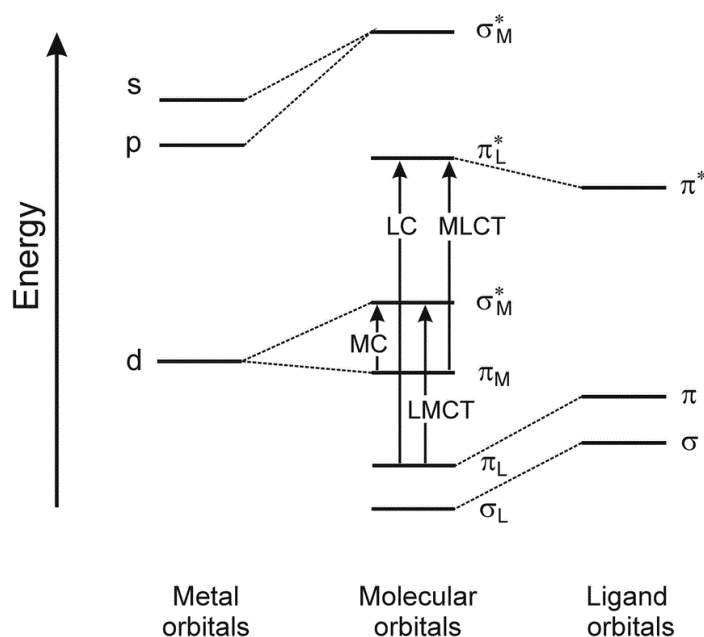
Figure 3: Simplified MO diagram for a generic transition metal complex and relative spectroscopic excitation transitions (taken with permission from Ref.[140], Copyright © The Royal Society of Chemistry 2014).

In contrast to MLCT, electron transfer transitions from the MO with ligand-like character to those with metal-like character are assigned to LMCT (**Figure 3**).[130,131] This type of charge

transfer is preferred if the ligands occupy filled orbitals with high-energy and the metal is in a high oxidation state with energetically low-lying empty or partially filled orbitals. Charge transfer from the ligand to the metal usually leads to the reduction of the metal.[141] Examples for LMCT include octahedral d^5 Ru(III) and Os(III) complexes bearing bpy derivatives as ligands.[142-144]

2.1.3 Luminescent Metal-Organic Frameworks

Metal-organic frameworks (MOFs) are a subclass of coordination polymers, which consist of metal ions or clusters (such as Zn^{2+} clusters) and organic ligands to form one-, two-, or three-dimensional structures via coordination bonds (**Figure 4**). The most famous and interesting feature of these materials is their exceptionally high porosity, leading to the large surface area typically ranging from 1000 to 10,000 m^2/g.[145] Moreover, size, functionality, and nature of the MOFs can flexibly be varied without changing their underlying topology. This class of materials performs high thermal and chemical stability, making them amenable for post-synthetic functionalization through covalent, coordinative or ionic interactions.[146] These unique capabilities enable their applications for gas storage,[147,148] heterogeneous catalysis,[90,149] biological imaging,[150,151] and biosensing.[152]
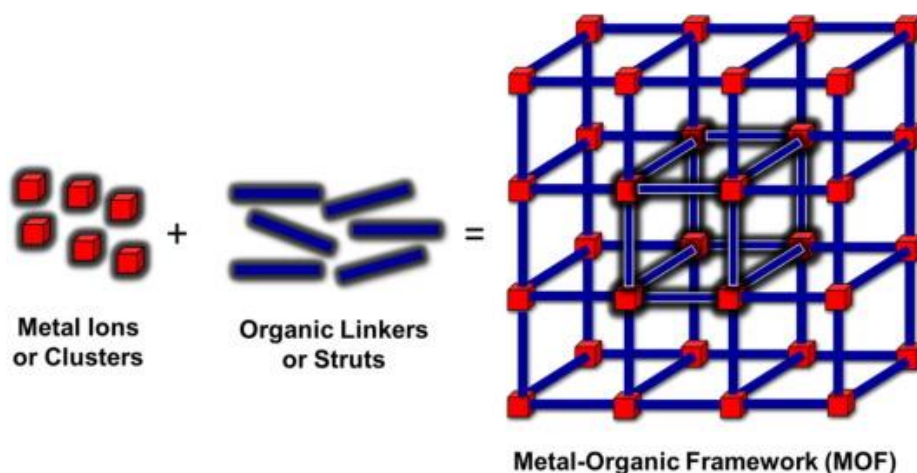
Figure 4: Generalized structural scheme for a metal-organic framework (taken with permission from Ref.[153], Copyright @ 2016 Elsevier B.V.).

Among the numerous applications, those used for bioimaging and biosensing are mostly luminescent MOFs, which can be prepared by introducing *e.g.* luminescent lanthanide ions[154] or d-block TMC molecules into the MOFs. This can be achieved via various processes. On the

one hand, TMCs can be inserted into MOFs via coordination with chelate ligands. This kind of ligand should have one coordination site for the metal center and another coordination site (*e.g.* COOH group) for combination with MOFs. Examples include inserting M-TCPP (M= Cu, Zn, TCPP = tetrakis(4carboxyphenyl)porphyrin) into MOF PCN-222 to form a Kagome-like topology,[149] introducing pincer Pt(II) complexes into MOF for oxygen sensing,[152] and preparation of luminescent lanthanide MOFs for chemical sensing.[154] On the other hand, TMCs can also be encapsulated into MOFs via electrostatic interactions, such as inserting cationic TMCs into anionic MOFs via ion-exchange process. A series of cationic TMCs were successfully inserted into various anionic MOF matrixes with this method, for instance, encapsulating a yellow-emitting Ir(III) complex ($[Ir(ppy)_2(bpy)]^+$) in the cavity of a blue-emitting anionic MOF to generate white-light emission,[155] and combining cationic Ru(II) complexes (*e.g.* $[Ru(phen)_3]^{2+}$) with the anionic MOFs for efficient singlet oxygen generation.[156] More complex luminescent MOF systems have been reported, that consist of a Pd(II) porphyrin as a photosensitizer and diphenyl anthracene (DPA) derivatives as an annihilator, which show triplet-triplet annihilation upconversion (TTA-UC) for *in vivo* imaging (**Figure 5**).[150]
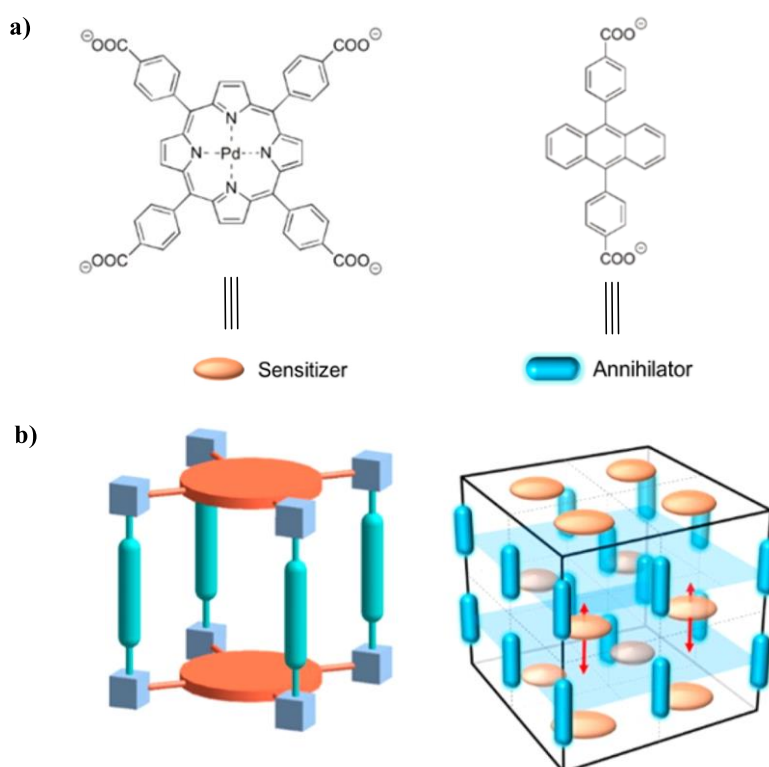
Figure 5: a) Chemical structures of annihilator and photosensitizer to be applied for TTA-UC in MOF; b) Proposed MOF structure containing the photosensitizer and annihilator (left) and the simplified topology of the MOF for TTA-UC. The cyan colored structures represent the annihilator, the orange ones represent the sensitizer as linkers, and the light blue cubes represent paddlewheel clusters, respectively (adapted with permission from Ref.[150], Copyright © 2018 American Chemical Society).

2.2 Luminescent Nanoparticles

In addition to molecular emitters, luminescent nanoparticles also play an essential role in research as well as commercial life. Among them are carbon-based nanomaterials, semiconductor nanocrystals, lanthanide nanocrystals, and luminescent polymeric nanoparticles (Chapter 1). This Section will give a brief introduction to nanoparticles and then focus on the general properties of (polymeric) nanoparticles as well as their combination with luminophores. A series of procedures will be described for preparing luminescent nanoparticles.

2.2.1 Brief Introduction to Nanoparticles

Nanoparticles (NPs) are usually defined as particles with diameters between 1 and 100 nm.[157] This term has also been adopted to signify colloidal particles with a length of 1–1000 nm in at least one dimension.[158] Naturally produced NPs can be found in interplanetary dust,[159] atmospheric dust and in biological systems, such as insects, plants, animals, and human bodies.[62] Interestingly, the application of NPs by humans dates back to more than 4500 years ago, when natural asbestos nanofibers were used in a ceramic matrix for controlled reinforcement.[160] In history, metal NPs were the extensively used in many regions as color pigments in luster and glass technology.[161-163] As one of the famous example of ancient metallic NPs usage, the Cobalt blue pigment was widely used for the blue and white porcelain in Ming dynasty (in the 15-centuray) of ancient China.[164] Until 1857, the first scientific description of the optical properties of gold (and other metals) NPs was reported by Faraday, meaning the birth of modern nanotechnology.[165,166]

Nowadays, the rapid development of nanotechnology has gained remarkable achievements, with numerous modern methodologies and techniques to synthesize, characterize, and explore the applications of nanoparticles (NPs). Based on their large surface to volume ratio, nanoparticles usually exhibit properties that differ from those of bulk materials. Applications of NPs can be found in various fields such as cosmetics,[67] foods,[66] catalysis,[18] biological applications,[70,78] electronics,[65] energy-harvesting,[63] environmental applications,[167] and mechanical industries.[168] Especially in the field of life science, NPs with various physicochemical properties and biological functions have been extensively studied and

utilized for bioimaging,[23,33] biosensing[169] and biomedicine including diagnosis, therapeutic drug delivery and treatments for many diseases and disorders.[75,170] A schematic illustration of typical multifunctional NPs for biological applications is shown in **Figure 6**. These biological applications of NPs are attributed to their nanoscale features, which demonstrate unique capabilities for enhancing cell permeability, augmenting therapeutic delivery, reducing dosage amounts and frequency, and improving the efficacy of medicines.[171] Moreover, advanced nanotechnology enables nanomaterials for multimodality, controlled release, and targeted delivery.[172]
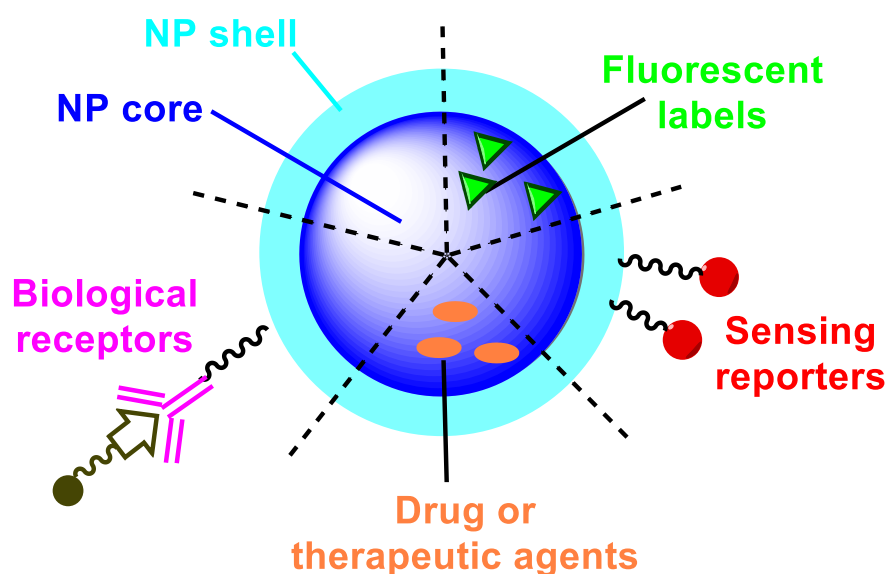
Figure 6: Scheme of multifunctional NPs for applications in life sciences.

To meet the different requirements for desired applications, many types of NPs have been developed. In general, NPs and nanomaterials (NMs) can be organized into four categories according to their composition materials:[62] **i)** carbon-based NMs, such as fullerenes, carbon nanotubes, carbon nanofibers, carbon black, graphene (Gr). These NMs are found in various morphologies including hollow tubes, ellipsoids or spheres; **ii)** inorganic-based NPs, which are mostly made from metals (*e.g.* Au or Ag NPs), metal oxides (*e.g.* TiO_2, ZnO NPs) and semiconductors, such as silicon, ceramics and quantum dots; **iii)** organic-based NPs, including dendrimers, micelles, liposomes and polymeric NPs, which are mostly formed via noncovalent (weak) interactions for self-assembly in designed structures; **iv)** composite-based NMs, which are mostly hybrid NMs consisting of various composites, such as combination of carbon-based, metal-based, or organic-based NPs. These composites are mainly combined through (at least)

one phase on the nanoscale dimension, leading to complicated structures, such as MOFs.[62] Modern nanotechnology enables the preparation of NPs in various shapes, including the most common (quasi) spherical NPs,[173] NMs in rods,[174,175] wires,[176] tubes,[177] cubes,[175,178] hexagons,[179] octahedra,[178] or rhombohedron.[175,178]

2.2.2 Polymeric Nanoparticles

Among the different types of NPs, the class of polymeric nanoparticles (PNPs), which is assigned to the majority of organic-based NPs, has gained growing interests in life sciences. PNPs consist of macromolecular materials mostly shaped in nanospheres or nanocapsules.[180] They can be applied either as nanocarriers loaded with dye molecules for high contrast imaging of cells, tissues or organs;[23,33,181] or as nanosensors bearing stimuli-responsive reporters for detecting bio-analytes or the relevant parameters;[37,182,183] or as delivery systems for controlled/sustained release of drugs or genes to the targeted tissues or organs.[184-186] The immense application potentials of PNPs are based on the polymer diversity (including various polymer composites, sizes, shapes, and structures) and the high flexibility for functionalization. Moreover, PNPs have some favorable properties over other NPs, including simple synthesis, low production cost, biocompatible, biodegradable, high resistance, bare toxicity, and high hydrophilicity.[185,187]

To meet different application requirements, many factors must be considered in the design strategies of PNPs. The most relevant characteristics of (polymeric) NPs, that can determine their properties, includes their composition, size, shape, surface chemistry, and optical properties.

Composition

PNPs can be made of either natural (*e.g.* alginate, albumin, or chitosan) or synthetic polymers, such as polyethylene glycol (PEG), polystyrene (PS), polylactic acid (PLA), poly(methyl methacrylate) (PMMA), and polylactide–polyglycolide copolymers. Depending on their composition, PNPs can be biodegradable or non-biodegradable. Natural PNPs are mostly biodegradable, leading to successful topical delivery of compounds, such as acyclovir (antiviral), retinol (vitamin A), quercetin (antioxidant), antisense oligonucleotides, and plasmid

DNA.[188-191] Synthetic PNPs can either be biodegradable or non-biodegradable, differing usually from their composition backbones: PNPs with heteroatomic (−C−X−) backbones can be easily hydrolyzed and thus degraded in biological environments, such as PLA, polylactide–polyglycolide copolymers, poly(amino acids);[192,193] while pure carbon-based backbones (−C−C−), *e.g.* PMMA, polyacrylamide, PSP, and polyacrylates, usually display high stability in the body and thus bare biodegradation.[188] Biodegradable synthetic PNPs have also been successfully used for drug delivery, *e.g.* poly(d,l-lactic-co-glycolic acid) (PLGA) have been applied for the transdermal delivery of indomethacin, Spantide II, and ketoprofen.[194,195]

Among the numerous synthetic PNPs, polystyrene nanoparticles (PSNPs), which do not degrade in the cellular environment and exhibit commonly biocompatibility without short-term cytotoxicity, are ideal candidates as model particles for studying the bio-nano interactions.[196] Polystyrene is usually obtained from polymerization of styrene monomers, acting as thermoplastic polymers featuring an atactic conformation without crystalline regions. Thus, the homopolymers show some unique properties including high transparence, durability, and can be stained easily with luminescent dyes.[197] These attractive capabilities of PSNPs enable their promising applications, *e.g.* as luminescent nanoreporters for bioimaging or biosensing.[196,198,199]

Size and size distribution

In addition to the composition of PNPs, their size and size distribution are two key parameters for determining their basic physicochemical properties (such as surface-to-volume ratio, surface area, uniformity) and thus defining their applications. Particularly for therapeutic delivery systems, size and size distribution of PNPs play a critical role for their transport properties and delivery efficiency.[200] Skin usually allows free delivery of particles <10 nm through transcellular route,[201,202] while optimal particle size for cellular uptake ranges from 30 to 50 nm, even deliveries with smaller (15 − 30 nm) or larger particle (70 − 240 nm) were also reported, yet with relatively low uptake rate.[75,180,200,203,204] In general, PNPs of sizes 50 − 200 nm are favored for *in vivo* applications, as they are large enough to be filtered by the liver, and thus following systemic circulation, meanwhile being small enough to avoid filtration in the spleen.[200,203,205]

Size and size distribution of PNPs also have an impact on the loading efficiency of luminescent dyes. For polar dyes, such as Square-730, the encapsulation degree via one step staining procedure (for the given timeframe) has shown a clear dependence on the particle size (25 – 1000 nm), where smaller particles with large surface area lead to enhanced incorporation efficiency.[206] Aggregation caused quenching (ACQ) of a dye can be efficiently hindered inside the smaller hydrophobic particles. For conjugated PNPs, highly emissive reporters are mostly reported with particle diameters ranging from 10 to 20 nm, even examples of larger conjugated PNPs with high brightness have also been reported.[33]

Shape

The spherical morphology is the most common shape of PNPs, although other shapes, such as discs, rods, fibers, and elliptical disks have also been developed for various applications.[207,208] Recent studies have revealed that shape of PNPs has significant impact on delivery process, such as extending of the *in vivo* circulation time, enhancing the tissue-binding efficiency, influencing the biodistribution of PNPs, cellular uptake and intracellular trafficking.[205,209,210] Generally, it is found that spherical PNPs penetrate cells to a greater extent than elongated cylindrical ones do, while elongation of spherical entities into cylindrical architectures is usually designed to prolong the *in vivo* circulation time.[210] For instance, it was shown that 3.5-µm long polyethylene-*b*-PEG filomicelles can circulate for up to one week in rodents after *in vivo* injection, while 200 nm-sized spherical poly(ε-caprolactone)-*b*-PEG micelles were cleared within 2 days.[211] Compared to spherical particles, the extended circulation time of filomicelles was mainly a result of their reduced binding and clearance by circulating macrophages.

Surface chemistry

Despite the key parameters mentioned above, another significant factor that defines the applications of PNPs is their surface chemistry, *i.e.* surface compositions, charge, porosity, functional groups, and surface functionalization. These surface characteristics of PNPs, which can be easily engineered due to advanced nanotechnology, determine their biologically concerned properties, such as toxicity, biocompatibility, hydrophilicity, drug or contrast agents loading capacity, penetration, target specific release, and biodistribution.[212,213]

Moreover, surface engineering of PNPs have been developed to promising techniques for understanding ophisticated biointerface processes.[214]

In terms of bioanalytical applications, the high flexibility of surface functionalization and modification of PNPs have led to a large toolbox of luminescent biomarkers and chem/biosensors. Typically, previous surface functionalization of PNPs can easily be achieved by coating a polymer or silica shell with functional groups, *e.g.* cyano, carboxyl, or amino groups.[198,215] Subsequently, luminescent dyes can be conjugated to the surface of PNPs via reacting with the functional groups. The functionalized core/shell PNPs with a variety of functional groups, high monodispersity, and narrow size distribution are nowadays also commercially available thanks to the modern nanotechnology, simplifying to a great extent the preparation procedure for the desired applications.

Optical Properties

Spherical NPs have unique size-dependent optical properties upon their interaction with electromagnetic radiation, including Rayleigh and Mie scattering.[216] Rayleigh scattering describes the light scattered by particles featuring much smaller radii than the incident light wavelength (r << λ; **Figure 7**, left), where the intensity of the scattered radiation is inversely proportional to the fourth power of the wavelength. This phenomenon is due to the electric polarizability of the particles, making them act as small radiating dipoles upon irradiation from the oscillating electric field of a light.[217] In terms of Mie scattering, it occurs mostly with particles featuring comparable or larger radii than the incident light wavelength (r ≥ λ; **Figure 7**, right), where the scattering behaves as an infinite series of spherical multipole partial waves.[218] Apart from the NP size, particle concentration as well as their refractive index can also influence the scattering profile. The NPs relevant to this work are all based on PSNPs. Their specific scattering profiles with different size ranging from 25 nm to 1 μm are illustrated in **Figure 8**.[117]
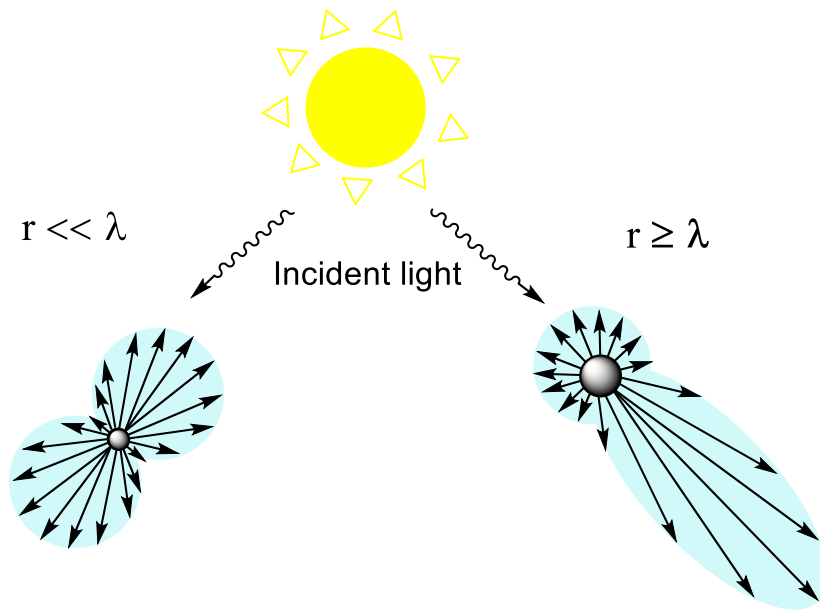
Figure 7: Schematic of Rayleigh (left) and Mie scattering (right).
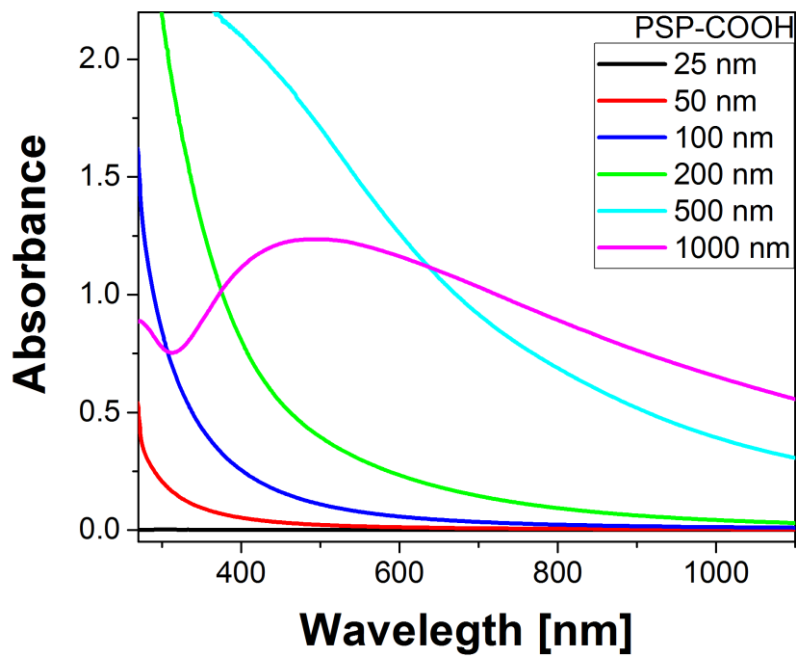
Figure 8: Absorption spectra of differently sized PSNP with their typical scattering profiles with identical 0.17 mg/mL mass concentration (taken from Fig. 2 in Ref.[117] from the Refubium of the Free University of Berlin).

2.2.3 Luminescent Polymeric Nanoparticles

2.2.3.1 A Combination of Polymeric Nanoparticles and Luminophores

One attractive property of PNPs lies on their capacity and flexibility of doping with various luminescent compounds, ranging from small organic dye molecules, transition metal complexes, to inorganic nanoscale emitters, such as quantum dots, enabling their PL properties with a wide diversity ranging from near UV to beyond 1000 nm.[23,24] In general, depending on the application requirements and the nature of the luminophores, these emitters can be either encapsulated into the nanoscale polymeric particle matrices or conjugated on the particle surface via covalent bonds (more methodological details will be discussed in Section 2.2.2.2). Moreover, with circumspect design strategies, more than one type of dye can be doped in/on the PNPs, leading to multispectral PL properties for various applications.[219] For instance, Napp *et al.* reported a PSNP-based NIR-emissive luminescent reporter, where both the oxygen-responsive emitter PdTPTBP (λ_{em} = 800 nm) and oxygen-inert reference dye DY-635 (λ_{em} = 670 nm) were encapsulated into the 100 nm-sized PSNPs. Their ratiometric luminescence readout in bioimaging revealed the *in vivo* tumor hypoxia condition induced by animal sacrifice.[37]

Through the matrix-dye combination, the non-fluorescent and photostable nature of PNPs offers the ability of exhibiting the PL properties of various luminescent emitters. In addition to this, these combinations can also address the challenges of pure molecular luminophores, such as poor water-solubility, photochemical stability, and biocompatibility, which strongly limit the application of the latter. These problems can be clarified by modifying the surface chemistry of the luminescent PNPs through grafting surfactant ligands, polymer chains or biocompatible molecules, or coating a colloidally stable polymer shell.[196] **Figure 9** shows a schematic illustration of this kind of matrix-dye combination, together with their respective and combined properties.
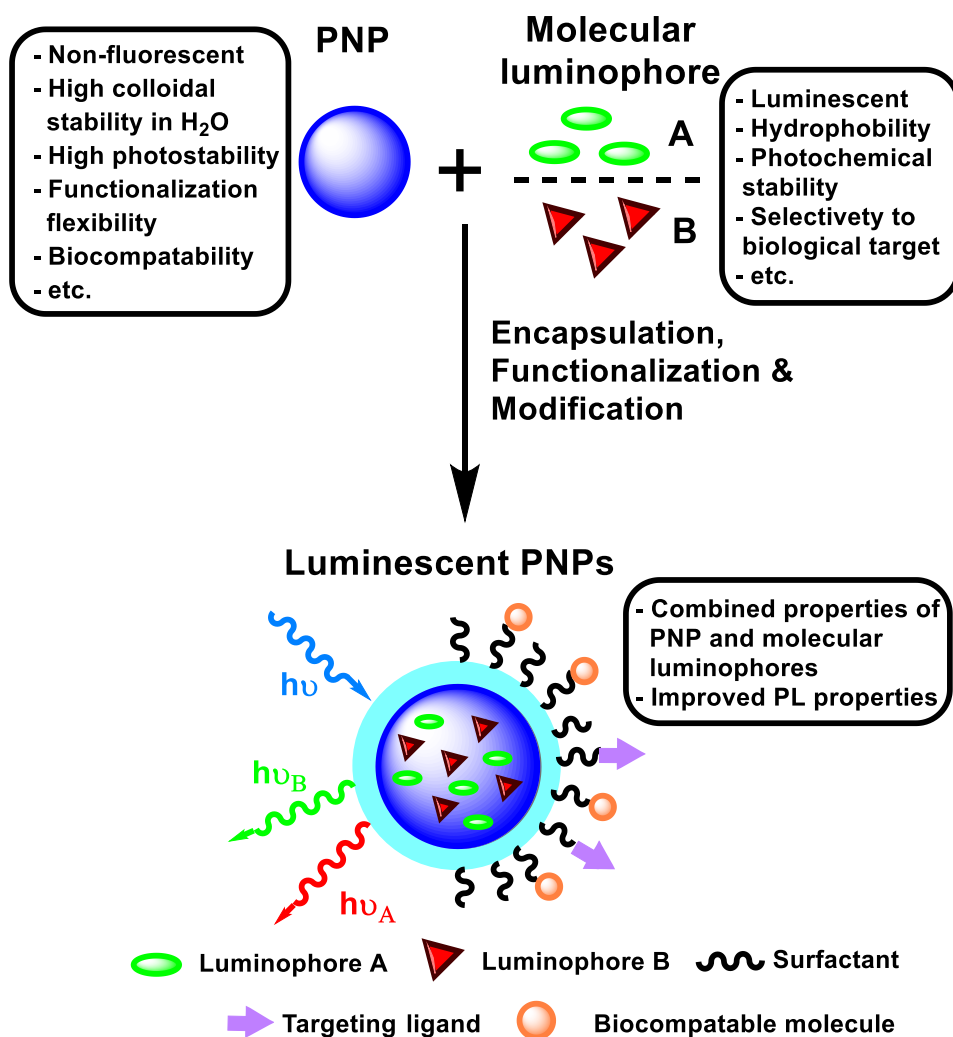
Figure 9: Schema of combining PNPs and molecular luminophores for generating luminescent PNPs, accompanied by the illustration of their respective properties.

2.2.3.2   Photoluminescent Behaviors in Nanomatrices

Luminescent PNPs can not only combine the respective properties of the molecular emitters and PNPs, but also perform enhanced PL properties, such as high brightness, increased luminescence quantum yield, extended luminescence lifetime, compared to the molecular luminophores. Typically, the excited state properties depend strongly on the environment, such as solvatochromic effect, aggregation-induced state,[220-223] encapsulated in matrixes,[94,152,224] or the presence of quenchers like triplet oxygen (in the case of triplet excited state).[39,225] In luminescent PNPs, the emitters are located in a relatively rigid environment, where vibrational relaxations are restricted and intermolecular quenching is partially eliminated due to the protection from the matrices. Thus, non-radiative decay pathways are suppressed, leading to enhanced PL properties.[94,224] Depending on the nature of the

luminophores and the choice of NPs, brightness of luminescent NPs can be enhanced by factors of 10-1000, compared to the molecular emitter.[33]

Another significant phenomenon observed in luminescent PNPs is the aggregation-induced change of the PL properties, which are usually induced by the intermolecular interactions in the aggregated emitters. Depending on the interactions, different PL behaviors can be observed, including ACQ, AIE and aggregation-induced metal-metal to ligand charge transfer state (for encapsulated d-metal complexes, will be discussed in Section 2.3.1). Behnke *et al.* reported a detailed study on the encapsulation efficiency of Nile Red and some other dyes into 100 nm-sized PSNPs and their respective PL properties.[206] ACQ resulted in a significant decrease of luminescence quantum yield from 0.76 to 0.05 with increasing dye loading from 0.05 to 0.8 wt%.[206] In contrast, a AIE dye, such as pyrrolidinylvinylquinoxaline (PVQ), can display enhanced luminescence properties in PSNPs due to the combined effect of the reduced polarity of the dye microenvironment and partial restriction of molecular motions.[226]

2.2.3.3 Procedures of Preparing Luminescent Polymer Nanoparticles

In order to obtain the desired luminescent PNPs for various applications, a series of approaches have been developed to introduce organic dyes or metal complexes to PNPs. Among them are **i)** encapsulating the luminophores into the preformed PNPs via a swelling procedure, **ii)** inserting the luminophores during the polymerization, and **iii)** post-synthetic grafting of luminophores to the PNPs´ surface. The latter requires a functionalized particle surface, which can be prepared by coating a thin silica shell with the desired functional groups.

Encapsulation of Molecular Luminophores into Preformed Polymeric Nanoparticles

Encapsulation of molecular luminophores into preformed PNPs is the simplest approach to generate luminescent PNPs. Commonly used PNPs with these swelling procedures include commercially available poly(methyl methacrylate) (PMMA) and PSNPs.[206,227] In general, the dye, which should be hydrophobic and contains no reactive groups, can be physically encapsulated into the preformed blank PNPs via simple swelling procedures.[228] Experimental details of a simple one step staining procedure will be given in Section 3.3.1. These non-covalent encapsulation procedures are mainly attributed by the hydrophobic nature of the

dye, which favors the hydrophobic polymer matrix, in comparison with the hydrophilic or less hydrophobic environment outside the particle. Therefore, the loading capacity of the dye depends strongly on the hydrophobicity. Hydrophilic or less hydrophobic dyes suffer thus from low loading efficiency and dye leaking in aqueous or biological media. Many conventional highly emissive hydrophobic dyes, *e.g.* Nile Red, Rhodamine 101, Coumarin 153 and some NIR-emissive dyes, such as cyanine, have been successfully encapsulated into PNPs via the swelling procedures, showing high brightness and colloidal stability with a potential for biological applications.[38,206] Nevertheless, most of these conventional dyes are practically limited with a satisfactory loading capacity less than 0.5 wt% due to ACQ at high dye concentration.[33] In addition to conventional organic dyes, some hydrophobic TMCs were also encapsulated into the PSNPs with these procedures, performing their luminescence response to the specific analyte (*e.g.* oxygen) in biological environment.[37]

Inserting Luminophores during the Synthesis of Polymeric Nanoparticle

Another commonly used approach for preparing luminescent PNPs is to insert the luminophores during the synthesis of the PNPs. Typically, PNPs can be prepared either through direct polymerization via different procedures (*e.g.* conventional emulsion, mini-emulsion, and micro-emulsion polymerization), or by strategies based on preformed polymers, such as emulsion solvent evaporation, nanoprecipitation, and self-assembly.[33] This offers a high flexibility of introducing the luminophores into the particles, which can be achieved via covalent binding or non-covalent interactions. With these procedures, some conventional luminophores, such as cyanine dyes, rhodamine 6G, fluorescein, and squaraine dyes are often encapsulated into various PNPs, such as PLGA NPs, PLGA-PEG block-copolymers, PMMA.[33] Similar to the swelling procedures, ACQ also strongly restricts the optimal dye loading to ca. 0.5 wt% with these processes. Additionally, as the dyes are involved in the polymerization or formation of PNPs, the physicochemical properties of the dyes must be considered, such as the compatibility between the dye and the polymer chains and their difference in solubility, which can influence the particle formation[229] and dye distribution in the PNPs.[33]

Anchoring of Surface Functionalized Nanoparticles with Reactive Dyes

In some applications, such as optical sensing of pH-value[230] or metal ions,[231] the luminophores are supposed to locate on the surface of PNPs to ensure enough exposure for the specific detection of the analyte in aqueous or biological environment. For such purpose, the dye molecules can be post-synthetically anchored to the surface of the preformed PNPs via covalent linking. This requires the dyes bearing functional groups, which can react with the surface functionalized PNPs. Compared with the swelling procedures, where the luminophores are entrapped physically inside the particles, covalent linking has the key advantage of preventing leaking of the dye. Moreover, surface labeling can also be constructed on the preformed luminescent PNPs containing another type of dye inside, yielding multi-fluorescent PNPs whit the potential for multiplexing sensing and bioimaging applications.[232]

Ammonia-catalyzed Stöber Process for Silica-coating

Surface functionalization of PNPs can be achieved with various approaches, such as introducing the ligand with desired functional groups during the polymerization, conjugating them to the polymeric chains for subsequent self-assembly,[233] or constructing a polymer or silica shell containing the functional groups around the PNP cores.[198] Among them, the core-shell strategies have been widely utilized for multi-functional PNPs due to the high functionalization flexibility and capacity for various functional groups.[234,235] One of the most frequently used approach for forming a silica shell is the ammonia-catalyzed Stöber process, which was firstly reported by Werner Stöber and his team in 1968.[236] More than 50 years later, newly acquired understanding and continuous developments based on the Stöber process enable precise control over particle size, size distribution, and fine-tunable physical properties of the silica materials applied in many fields.[237-239]

In general, the Stöber process is a one-step sol-gel method for preparing silica (SiO_2) materials. A simplified representation of ammonia-catalyzed Stöber process is illustrated in **Figure 10**. Tetraethyl orthosilicate ($Si(OEt)_4$, TEOS), acting as the silica precursor, is hydrolyzed in alcohol (*e.g.* methanol or ethanol) in the presence of ammonia as a catalyst.[236,240] The generated

ethoxysilanols (such as $Si(OEt)_3OH$, $Si(OEt)_2(OH)_2$, and even $Si(OH)_4$) can further condense with either TEOS or another silanol by losing ethanol or water, yielding crosslinked colloidal silica.[240]

The preparation of the core-shell particles containing PNP-core and silica-shell can be processed by various approaches. One is carried out during the formation of PNPs and silica, where the polymer chains containing amino groups (*e.g.* polyamines) are added together with the silica precursor TEOS in the initial steps of the Stöber process.[241] The electron pairs from the polymer nitrogen site interact with the hydrolyzed end groups of TEOS, leading to accelerated hydrolysis and silica growth around them. Consequently, the polymer composite is incorporated into the resulting silica shell, yielding the desired core-shell configuration.[241,242] Another approach can be post-synthetically proceeded with the preformed PNP core with surface functionality or stabilizer either based on nitrogen site, *e.g.* amines,[243] diazonium[244] and poly(vinylpyrrolidone) (PVP),[245] or components with silane structures, such as methyl trimethoxysilane (MTMS)[246] and 3-methactyloxyl-propyltrimethoxyl silane (KH570).[247] Hydrolysis and condensation of TEOS can then occur near or on the particle surface due to the interaction with the surface functionality and thus yielding the desired silica shell. Functionalization of the silica shell can be directly achieved by introducing silane units with the desired functional groups.[248] For instance, adding (3-aminopropyl)triethoxysilane (APTES) along with TEOS initially in Stöber process results in aminated silica surface for further conjugation with luminophores or biomolecules.[248,249]
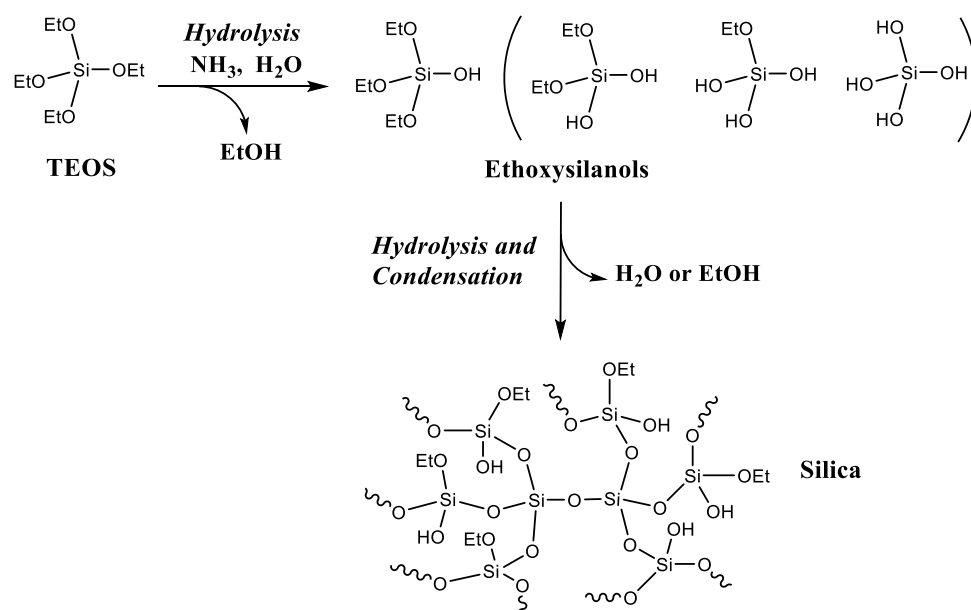

Figure 10: Simplified representation of ammonia-catalyzed Stöber process containing hydrolysis and condensation of TEOS (tetraethyl orthosilicate).

2.3 Electron and Energy Transfer Processes within and between Luminophores

Intra- and intermolecular interactions of luminophores can induce electron and energy transfer processes upon light absorption, which can change their photophysical properties. These processes are usually exploited by a rational design of the respective luminophores, enabling a fine turning of the optical properties of the luminophores. This Section will focus on several electron- and energy transfer mechanisms relevant for the represented work, as well as their influence on the PL properties, yielding *e.g.* sensor systems or light-harvesting systems.

2.3.1 Metal-Metal to Ligand Charge Transfer

In luminescent TMCs, commonly observed charge transfer processes include MLCT, LMCT, MC and LC (Section 2.1.2.2). Apart from this, metal-metal to ligand charge transfer (MMLCT) usually occurs in the self-assembled square-planar geometry of d^8 TMCs, due to the aggregation-induced metal$\cdots$metal interactions. In this geometry, the filled d_{z^2} orbitals of the metal are usually vertical to the molecule plane, which barely interact with the planar ligands' coordination sphere. Thus, the occupied d_{z^2} orbitals tend to interact with the surrounding species, such as the neighboring metal center, via intermolecular coupling of their $d_{z^2}\cdots d_{z^2}$ orbitals. Due to these interactions, a set of energetically higher ground state and lower excited state is formed in their aggregates, namely the MMLCT states (**Figure 11**).[140,250] Consequently, the newly formed MMLCT states display red-shifted absorption and emission bands, compared with that of their parent monomeric complex. Moreover, this kind of aggregation-induced MMLCT states depends strongly on the metal$\cdots$metal distance, as their intermolecular interaction starts to occur at a distance usually below 3.5 Å.[140]

Square-planar luminescent Pt(II) complexes are prone to form aggregates, regardless dissolved in solution or in their solid state, thus inducing the MMLCT states.[140,220,223,250-253] As a monomer, the luminescence properties of Pt(II) complexes are usually dominated by MLCT character. Upon dimerization, aggregation or supramolecular assembly, red-shifted ^{3}MMLCT emission arises, while depleting the monomer emission from the ^{3}MLCT state.[140,220,223,254] MMLCT states are also observed with luminescent Pd(II) complexes, yet only limited to very

few examples due to the considerably weaker Pd⋯Pd interactions and the lower energy of the 4d orbitals.[255,256] Owning to the specific ^{3}MMLCT characters, including red-shifted absorption and emission regions which are favored for biological environments, enhanced and tunable photophysical properties, this class of assembled luminescence species shows promising application potential in the fields of bioimaging[140,223] and chemical sensing.[152]
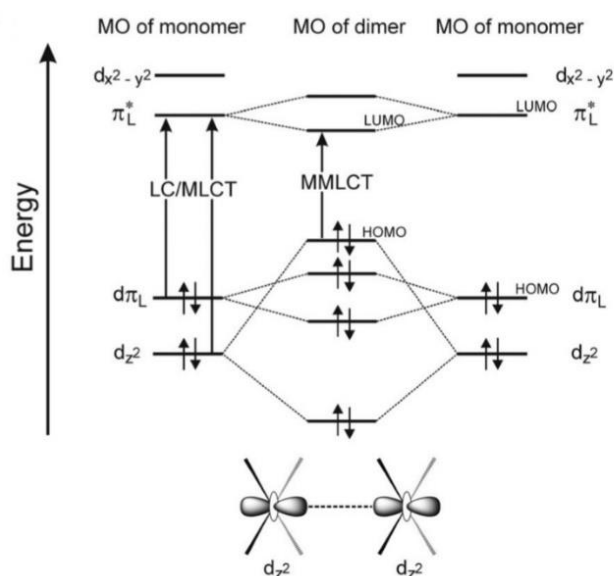
Figure 11: Simplified MO diagram of two interacting square-planar platinum(II) complexes, showing the intermolecular d_{z^2} orbital overlap in the ground-state and its influence on the energy of the MO levels (taken with permission from Ref[140], Copyright © The Royal Society of Chemistry 2014).

2.3.2 Dexter Energy Transfer

Dexter energy transfer, also called Dexter electron transfer, was firstly proposed by Dexter in 1953, describing a non-radiative process with electron exchange between the excited state of two compounds.[257] Dexter energy transfer requires the presence of two photoactive species, namely the donor (D) and the acceptor (A), which can be either two molecules (intermolecular) or two parts of one molecule (intramolecular). Depending on the chosen donor and acceptor, Dexter energy transfer can occur between their singlet states or triplet states allowed by the Wigner spin conservation rule.[258] The corresponding mechanisms are illustrated in **Figure 12**.

In a singlet-singlet energy transfer process, excitation of the donor results in a pumped electron from the highest occupied molecular orbital (HOMO) to the lowest unoccupied molecular orbital (LUMO) without spin change (**Figure 12**), yielding the singlet excited state (^{1}D*). Electron exchange occurs then between the excited donor (^{1}D*) and the ground-state

acceptor (^{1}A) due to their Coulombic interaction,[259] generating the singlet excited acceptor (^{1}A*) while releasing the donor to its ground state (^{1}D) non-radiatively. Differing from this process, the triplet-triplet energy transfer involves the non-radiative energy transfer from the initially excited triplet donor (^{3}D*) to the ground-state acceptor (^{1}A), producing the triplet populated acceptor (^{3}A*) and ground-state donor (^{1}D). A common example of this type of energy transfer is the phosphorescence quenching by (triplet) oxygen (see Section 2.4.3).
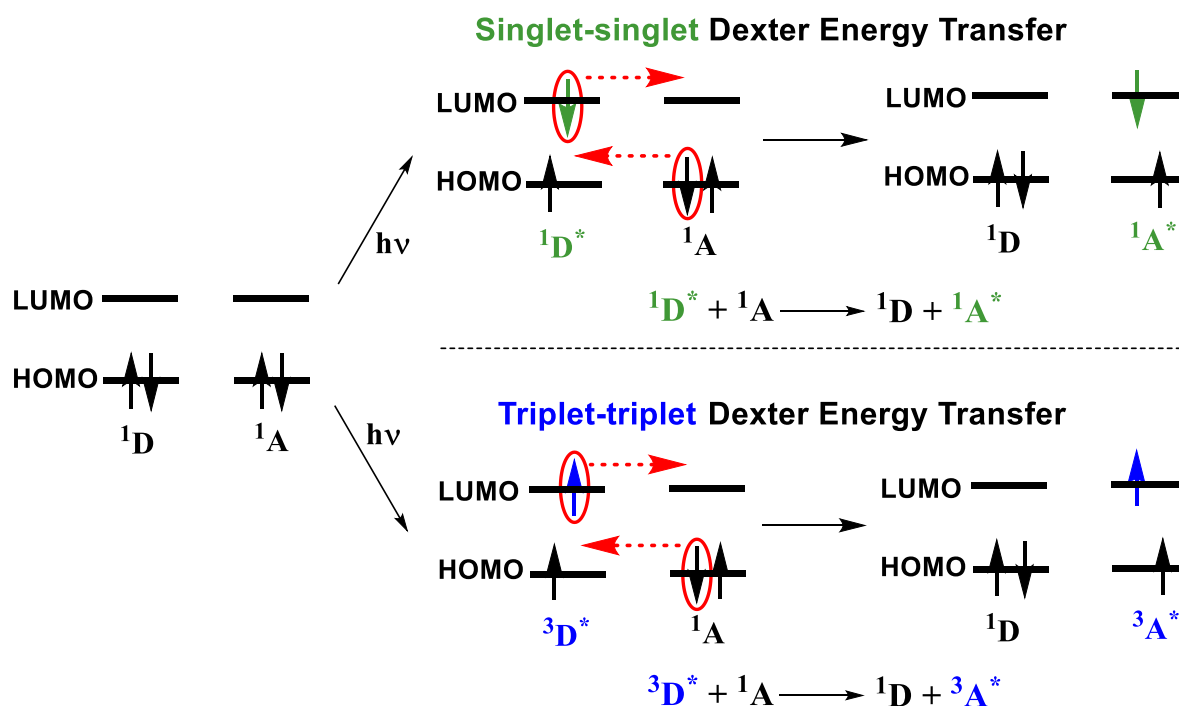
Figure 12: Schematic diagram for Dexter energy transfer.

Förster resonance energy transfer (FRET), is another process describing energy transfer from an excited donor to an acceptor non-radiatively through dipole–dipole coupling.[260] The FRET process depends strongly on the luminescent quantum yield of the donor (D), spectral overlap of the donor and acceptor, and the distance (r_{DA}) between the donor and the acceptor (inversely proportional to the sixth power of the distance). In comparison to FRET, Dexter energy transfer process has a few unique characteristics. Mechanically, Dexter energy transfer requires the overlap of wavefunctions between the donor and the acceptor, so that the electron can occupy the other´s molecular orbitals.[259] Similarly to the FRET process, the Dexter energy transfer rate constant also depends strongly on the distance r_{DA}. However, for Dexter energy transfer the efficient distance r_{DA} is generally smaller than 10 Å to ensure sufficient overlap of their molecular orbitals,[257] while the typical distance for FRET can be found in the

range of 10 – 100 Å.[261] Moreover, the Dexter energy transfer process can also be used to excite the triplet state of a molecule, which can be hardly achieved with a FRET process. Based on the Dexter energy transfer process, many novel luminescent materials have been developed for various applications, such as chemosensors[262], photosynthesis,[263] and OLEDs.[264]

2.3.3 Photon Upconversion

Photon upconversion (UC) describes a non-linear energy transfer process, where two or more low energy photons are converted to one single photon with high energy.[85,265] Differing from the typical performance of fluorescence, UC involves an anti-Stokes type emission with shorter emission wavelength upon excitation with longer wavelength. A simple comparison of typical fluorescence and photon UC is illustrated in **Figure 13** with **a)** the respective simplified Jablonski diagrams and **b)** the emission of light: upon green light excitation, fluorescence emission is generated by red photons (longer emission wavelength), while UC leads to blue-emissive photons of shorter wavelength.
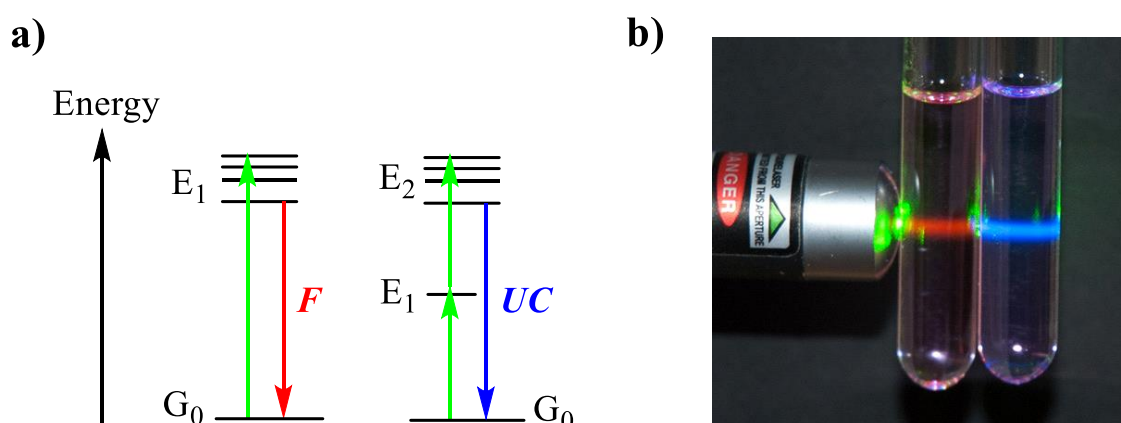
Figure 13: Illustration of a simple comparison of fluorescence and photon UC, including **a)** their simplified Jablonski diagrams and **b)** their corresponding emission light upon green light excitation (**b)** taken with license notice from Ref.[266]).

Photon UC can occur in either organic compounds (*e.g.* polycyclic aromatic hydrocarbons) or inorganic materials. The latter is more common, usually containing d-block or f-block metal ions, such as lanthanide ions Ln^{3+} (*e.g.* Yb^{3+}, Er^{3+}), Ti^{2+}, Mo^{3+}, Re^{4+} and Os^{4+}.[267] Lanthanide ions are popular species typically used for converting light from NIR to visible region. Upconversion nanoparticles (UCNPs) doped with these ions have been extensively explored for a wide range

of applications in many fields, including deep tissue imaging, drug delivery, sensing, and photocatalysis and light-harvesting in solar cells.[87,268,269] These applications are attributed by the unique properties of UCNPs, such as deep penetration depth in tissue, low toxicity, high photostability, sharp emission peaks, large anti-Stokes shift.

In general, photon UC in inorganic materials can be dominated by different mechanisms, among them the most basic ones include excited-state absorption (ESA), energy transfer upconversion (ETU), cooperative sensitization upconversion (CSU), and photon avalanche (PA) as shown in **Figure 14**.[269]

For the excited-state absorption (ESA), the photoactive specie is pumped to a long-lived excited state E_1 (**Figure 14 (a)**) upon photon excitation. Followed by subsequent absorption of a second photon, the excited compound is further populated to an energetically higher excited state E_2. Radiative relaxation from E_2 leads to emission of upconverted light. The ESA is the simplest upconversion process, favored by lanthanide ions such as Er^{3+}, Ho^{3+}, Tm^{3+}.[267]
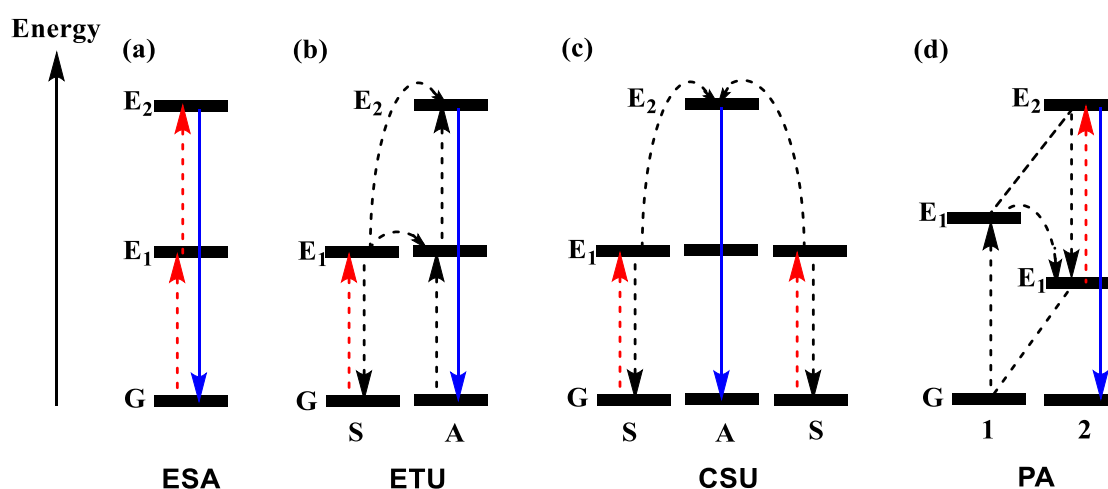
Figure 14: Basic photon UC mechanisms in inorganic materials: (a) excited-state absorption (ESA), (b) energy transfer upconversion (ETU), (c) cooperative sensitization upconversion (CSU), and (d) photon avalanche (PA). The red, black, and blue lines indicate photon excitation/absorption, energy transfer, and upconverted light emission processes, respectively (adapted with permission from Ref.[269], Copyright @ The Royal Society of Chemistry 2018).

In terms of the energy transfer upconversion (ETU), usually two neighboring ions are required, namely the sensitizer (S) and the acceptor (A) (**Figure 14 (b)**). Upon photon absorption, the sensitizer is pumped to its first excited state E_1. The stored energy is then transferred from this excited state to the acceptor ion, activating its intermediate excited state. Further energy

transfer leads to the excitation of the acceptor from its intermediate excited state to E_2. Then, photon emits from the high-energetic E_2 state as upconverted light. The ETU efficiency is depends strongly on the distance between the sensitizer and the acceptor, which can be regulated by monitoring the dopants concentration.[269]

The cooperative sensitization upconversion (CSU) process requires the presence of two sensitizer ions (typically the same) and one as acceptor (**Figure 14 (c)**). Similar to ETU, both sensitizers are firstly pumped to their first long-lived excited state E_1. Followed by simultaneous energy transfer from the E_1 states to the acceptor, the acceptor is excited to a higher energetic state E_2. Subsequent radiative relaxation from the E_2 state yields emission of upconverted light. The CSU process has generally much lower efficiency due to the involved simultaneous energy transfer from quasi-virtual pair levels.[269]

Another basic upconversion mechanisms is called photon avalanche (PA), basically a circular process involving photon absorption and cross relaxation (CR) between ion1 and ion2 (**Figure 14 (d)**). Compared with the other UC mechanisms mentioned above, the PA is an unconventional process as no resonant ground state absorption (GSA) is involved.[270] Firstly, the excited state of ion2 is populated by weak, non-resonant, ground state absorption. Followed by the resonant excited state absorption from the metastable state E_1 of ion2, the energetically higher E_2 state is excited. The CR occurs between ion1 (level G and E_1) and ion2 (level E_1 and E_2) as shown in **Figure 14 (d).** Lastly, the circle is completed when energy is transferred from the E_1 state of ion1 to ion2, yielding excited E_1 state of ion2. As a result, one single ion2 in its E_1 state produces two excited ion2 of the same state. Further circulation of this process leads to an avalanche effect of the populated E_1 state of ion2, thus generating upconverted light from its E_2 state.[268,269] An important characteristic of the PA process is the excitation power threshold value, below which bare UC luminescence is observed, while above it the UC luminescence can be improved by orders of magnitude.[268,269]

2.3.4 Triplet-Triplet Annihilation Upconversion

Mechanism of TTA-UC

Triplet-triplet annihilation upconversion (TTA-UC) was firstly discovered in 1962 by Parker and Hatchard with the observation of delayed fluorescence in anthracene derivatives.[271,272] It describes an energy transfer process between the triplet states of two kind of molecular luminophores, namely the sensitizer and the annihilator.[273] In a typical TTA-UC system (**Figure 15**), photon excitation of the sensitizer leads to the population to its singlet excited state S_1. Subsequent intersystem crossing (ISC) excites its long-lived triplet state T_1. The stored energy is then transferred from the sensitizer to the T_1 state of the annihilator via triplet-triplet energy transfer (TTET), while releasing the sensitizer to its ground state. When the excited T_1 state of the annihilator is accumulated sufficiently by repeating this process, TTA process starts to occur efficiently, yielding the populated intermediate excited state with high energy. Followed by ISC, the stored energy achieves the high-energetic singlet state S_1 of the annihilator, yielding the radiative transition by emitting upconverted light with shorter wavelength than that of the excitation.[273]
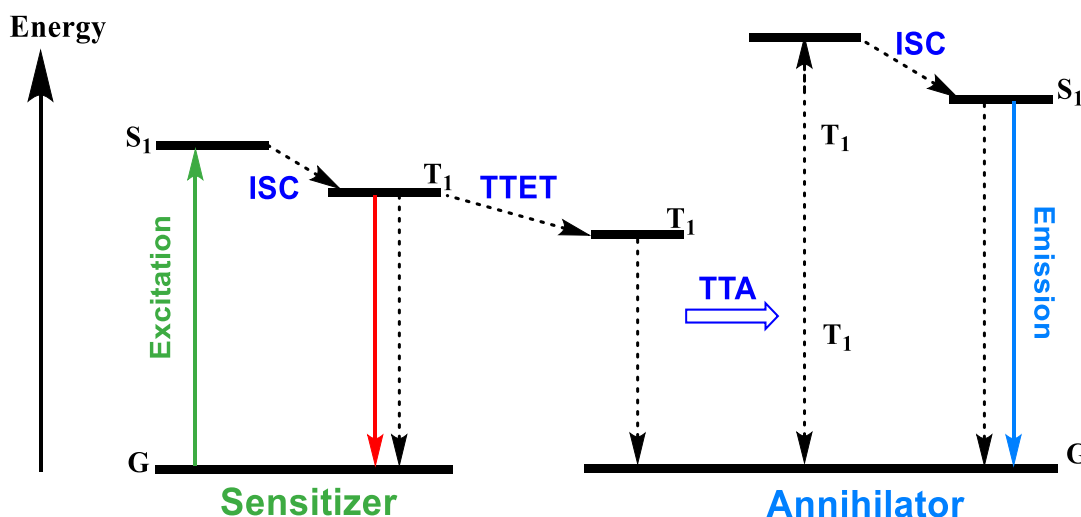
Figure 15: Energy migration diagram of the triplet–triplet annihilation upconversion (TTA-UC) process between the sensitizer and the annihilator. The green, red, and blue solid lines indicate photon excitation, sensitizer emission and annihilator emission, respectively; the black doted lines describe the energy transfer processes. ISC: intersystem crossing; TTET: triplet–triplet energy transfer.

The TTA-UC process can be evidenced with a few characteristics, including the observation of the delayed fluorescence of the annihilator, which performs an anti-Stokes shift with respect

to the excitation wavelength, and the strongly quenched luminescence emission and shortened lifetime of the sensitizer. Moreover, the generated UC luminescence shows a clear dependence on the excitation power density. Under lower excitation power density, the UC luminescence intensity depends quadratically on the power density of the incident light, as it involves a reaction of two triplet excited states of the annihilators and thus can be described as a second-order reaction. However, with high power density, the triplet excited states of the annihilators reaches a saturation and thus follows a pseudo-first order reaction with a linear dependence on the excitation power density.[274,275]

Upconversion Efficiency in TTA-UC

One of the most important parameters for evaluating the TTA-UC process is the upconversion quantum efficiency (Φ_{UC}), which is defined as the ratio of the number of emitted upconversion photons to the number of incident photons.[273] However, in the TTA-UC process, two absorbed photons can ideally generate one upconverted photon. Thus, the maximum Φ_{UC} is limited to 50%. According to the TTA-UC mechanism illustrated in **Figure 15**, the Φ_{UC} can be calculated with the following equation:[276]

$$\Phi_{UC} = \frac{1}{2} * \Phi_{ISC}\Phi_{TTET}\Phi_{TTA}\Phi_{A}$$

<div align="right">Eq. 1</div>

Φ_{ISC}: ISC efficiency of sensitizer;

Φ_{TTET}: TTET efficiency from sensitizer triplet to annihilator triplet;

Φ_{TTA}: TTA efficiency of annihilator;

Φ_{A}: Quantum yield of singlet annihilator.

Apparently, the Φ_{UC} in a TTA-UC system depends strongly on each involved energy transition step. Efficient ISC can be achieved by choosing sensitizer with a small energy gap between the singlet and triplet state. To ensure an efficient TTET process, the energy levels of both triplet states from sensitizer and annihilator must be suitably matched, *i.e.* the triplet state of annihilator should be lower than that of the sensitizer. Moreover, oxygen usually acts as a competitor by quenching the triplet excited sensitizer in a faster way. Thus, avoiding the presence of oxygen is essential to obtain a high Φ_{TTET}.[277] In terms of the TTA process, there is a theoretical Φ_{TTA} upper limit of 11.1% (with spin-statistical weight 1/9) for generating the

singlet excited state.[276] Thus, choosing an annihilator with high luminescence quantum yield Φ_A plays a significant role for an efficient TTA-UC system.

Sensitizer and Annihilator

In contrast to the lanthanide-doped UC systems with relatively fixed sensitizer (Yb^{3+}) and activator (*e.g.* Er^{3+} or Tm^{3+}), TTA-UC systems can be constructed from many different sensitizers and annihilators. To develop an efficient TTA-UC system, many factors must be considered for the suitable pairing of the sensitizer and the annihilator. Their respective requirements are listed in **Table 1**.

Sensitizer	Annihilator
High solubility in the solvent	No absorption at λ_{ex}
High absorption cross section at λ_{ex}	High fluorescence quantum yield
Efficient intersystem crossing	T_1 state with suitable energy, usually lower
Small energy gap between S_1 and T_1	than T_1 state of the sensitizer
Long phosphorescence lifetime	Long-loved T_1 state

Table 1: Requirements for the sensitizer and annihilator for an efficient TTA-UC system (summarized with permission from Ref[273], Copyright © 2015, American Chemical Society).

The requirements for triplet sensitizers can be satisfied by employing metal complexes containing heavy atoms (*e.g.* Pt(II), Pd(II), Ru(II), Re(I), and Ir(III)) and cyclometalated ligands such as porphyrin and phthalocyanine, and polyimines ligands. Besides, organic triplet sensitizers are also used, such as iodo-substituted and bromo-substituted dyes and fullerene derivatives.[273] In terms of annihilators, they are mostly based on polycyclic aromatic haydrocarbons consisting of fused benzene rings and heterocyclic compounds, such as anthracene, tetracene, pyrene, perylene, fluorene, and their derivatives.[273] Due to the diversity of the TTA-UC systems and their unique luminescence properties such as large anti-Stokes shift, tunable luminescence emission, delayed fluorescence, high upconversion efficiency (with well-designed system),[275,278] lower excitation power density (in comparison to the lanthanide-doped UC systems),[279] they are widely used for bioimaging, biosensing and light-harvesting.[150,273,280]

2.4 Optical Sensors

2.4.1 Optical Sensing – A Brief Description

In general, an optical sensor is a device that can reversibly convert light into electronic signals.[281] In an optical sensor, changes in light intensity can be detected by its interaction with a particular parameter or an analyte and the information is sent to other electric devices. They can cover a broad wavelength region, ranging from UV-Vis to NIR and IR. Parameters measured can induce optical changes in absorbance,[282] reflectance,[283] resonance,[284] polarization, or luminescence intensity and lifetime.[34,285] Optical sensors have a series of advantages over non-optical sensors, including a high sensitivity, a nondestructive detection, a rapid response, and multiplexing capabilities. Optical sensors are widely applied in the daily life, such as in smartphones for screen brightness adjusting, in healthcare devices for measuring heartbeats, in industries for quality and process control, in mining for pipeline monitoring, and for measuring specific analytes in biological environments.

Optical sensors based on luminescence are important sensing tools in different biological applications. Depending on their interaction with the target parameter, spectral and intensity changes in luminescence can be detected in various domains. These changes are usually achieved by specifically designed strategies, such as photoinduced electron transfer (PET),[286,287] photoinduced charge transfer (PCT),[288] FRET,[95,289] or Dexter type energy transfer by colloidal quenching of long-lived triplet states.[262,280] Typically, an analyte-inert reference dye, which ideally shows bare spectral crosstalk with the indicating signal, is needed in an optical sensor system. Such ratiometric sensors offer a high signal-to-noise ratio by suppressing the background interferences. Depending on the sensing analyte and the application requirements, a suitable matrix is usually desired. For instance, luminescent indicators for pH value or ions need to locate in hydrophilic environment. To date, luminescence-based optical sensors are particularly favored for selectively detecting and measuring the biologically interesting analytes or parameters, such as pH-value,[230] oxygen,[25,40] hydrogen peroxide,[290] metal ions,[231] and biomolecules.[49,102]

2.4.2 Stern-Volmer Relationship

The Stern-Volmer (SV) relationship, which was proposed by Otto Stern and Max Vomer in 1919, is a fundamental principle for describing the kinetics of luminescence deactivation (quenching) in the electronic excited state as a function of quencher concentration.[291] The SV law has led to remarkable achievements in the scientific fields of photophysics and photochemistry as well as in the development of sensing applications. Particularly for the latter, the SV approach is regarded as one of the classical methods for luminescence-based sensing.

In a classical SV model, the presence of quencher (Q) leads to deactivation of the excited state of the luminophore, yielding a quenched luminescence intensity I, a reduced quantum yield Φ and a shortened lifetime τ. The kinetics of this process follows the SV equation as **Eq. 2**:[291,292]

$$\frac{\Phi_0}{\Phi} = \frac{\tau_0}{\tau} = 1 + k_q \tau_0 [Q]$$

Eq. 2

where Φ_0 and τ_0 indicate the luminescence quantum yield and lifetime in the absence of the quencher, respectively; $[Q]$ is the concentration of the quencher and k_q denotes the quenching rate constant. In the case that the luminescence quantum yield is proportional to the emission intensity, **Eq. 2** is usually replaced by an intensity-dominated form:

$$\frac{I_0}{I} = 1 + K_{SV}[Q]$$

Eq. 3

where I_0 is the luminescence emission intensity without quencher; K_{SV} is the Stern-Volmer constant.

In a purely dynamic quenching process, K_{SV} is the product of the quenching rate constant k_q and the luminescence lifetime τ_0 in the absence of quencher (**Eq. 4**).

$$K_{SV} = k_q \tau_0$$

Eq. 4

Thus, for a dynamic quenching process, K_{SV} can be graphically determined by plotting the ratio of luminescence intensity as a function of the quencher concentration, where the slope value of the linear relationship corresponds the K_{SV} value. With a given τ_0, the quenching rate constant k_q can also be derived. For a diffusion-controlled irreversible quenching process in

homogeneous solution, the quenching rate constant k_q may be given by the classical expression:[292]

$$k_q = k_d = 4\pi DRN_A$$

where D stands for the diffusion constant of species; R is their encounter distance, usually seen as the sum of the respective molecular radii of both species; N_A is the Avogadro constant. Obviously, in homogeneous solution, the quenching rate constant depends strongly on the species´ diffusion constant, which displays a high correlation with the viscosity of the solution and the temperature.

In addition to the diffusion effect, there are many diverse factors that can influence the kinetics of the quenching process, leading to non-linear behavior which does not follow the classical SV relationship (**Eq. 3** and **Eq. 2**). Among them are self-quenching, different quenching sites, and static quenching such as chemical association prior excitation.[292-296] These observations and the derived theories offer numerous models for describing the luminescence quenching kinetics in specific cases.

2.4.3 Optical Sensing of Oxygen

Oxygen is an essential chemical species for sustaining life, which constitutes ca. 21% in the Earth´s atmosphere. Detection and measurement of oxygen are required in many fields, such as environmental monitoring, chemical or clinical analysis, and in medical field. To meet these requirements, various methods have been developed for measuring oxygen. In general, they can be classified to three types, including methods based on Winkler titration,[297] amperometry (Clark-type electrode),[298] and optical methods based on luminescence.[299,300] The titration-based methods are cumbersome and time-consuming, while the electrode-based methods usually suffer from electrical interference from the background, leading to a large error scale. In comparison to them, the luminescence-based oxygen sensing methods are regarded as superior techniques, as they are expected to be inexpensive, simple to use, easily miniaturized, free of electrical interference and oxygen consuming.[301] These oxygen sensors play an essential role in bioanalytical applications. They can be used for medical diagnostics, such as measurements of oxygen content in blood (diagnostics),[302,303] control of

wound healing processes,[304] the measurement of transcutaneous pO_2,[305] and of tumor hypoxia.[37,306] Moreover, optical oxygen sensors are attractive for continuous measurements of dissolved oxygen (DO) in bioreactors or in cell cultivating flasks,[307] imaging intra or extracellular oxygen distribution.[308,309]

Optical sensing of oxygen is usually based on the principle that oxygen can deactivate the triplet excited state of an indicator dye, resulting in quenching in luminescence intensity and/or lifetime. Commonly, phosphorescent compounds are favored as oxygen sensors due to their long-lived excited states, as they can offer sufficient time for collisional quenching by the oxygen. The corresponding quenching mechanism is illustrated in **Figure 16**.
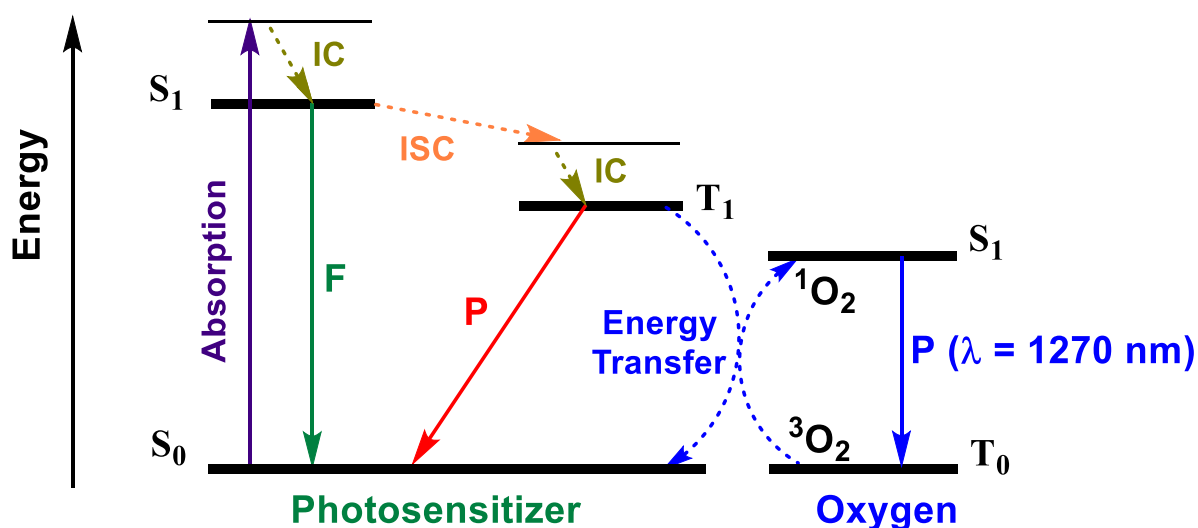
Figure 16: Simplified Jablonski diagram for illustrating photoluminescence quenching by oxygen.

Typically, the indicator luminophore (photosensitizer) can produce long-lived luminescence after absorbing a photon. Upon collision with oxygen, which is exceptionally found in the triplet ground state ($^3O_2$) due to its biradical electronic nature,[301] energy can be efficiently transferred from the triplet excited state of the luminophore to oxygen, pumping triplet oxygen to a singlet excited state and thus yielding singlet excited oxygen ($^1O_2$). Meanwhile, the photosensitizer returns to its ground state in a non-radiative way (**Figure 16**). The generated singlet excited oxygen ($^1O_2$) can then radiatively decay to its triplet ground state involving change in the electron spin, yielding phosphorescence emission which can be observed at ca. 1270 nm.[310] As singlet oxygen ($^1O_2$) is a reactive oxygen species (ROS) that can lead to deformation of many compounds, this principle is also favored for generating ROS to

destroy the unwanted biological species, such as cancer cells (photodynamic therapy).[311] The luminescence quenching kinetics by oxygen is a diffusion-controlled process and can be described with the Stern-Volmer relationship (**Eq. 2** to **Eq. 5**) discussed in Section 2.4.2.[301,312] However, in a nano- or micro heterogeneous environment, such as in polymers, the quenching mechanism is often more complicated involving more than one quenching site, where oxygen may have different accessibility to the indicator. When the luminescence response cannot be well described with the classical SV relationship (**Eq. 2** and **Eq. 3**), a modified equation (**Eq. 6**) can be applied to describe the two sites quenching kinetics:[309,312,313]

$$\frac{I}{I_0} = \frac{\tau}{\tau_0} = \frac{f}{1 + K_{SV}^1[Q]} + \frac{1 - f}{1 + K_{SV}^2[Q]} \qquad \textbf{Eq. 6}$$

where f stands for the first site fraction of the total emission; K_{SV}^1 and K_{SV}^2 are the Stern–Volmer quenching constants for the two quenching sites.

To date, a series of luminophores have been developed for oxygen sensing. Among them are organic dyes such as polycyclic aromatic hydrocarbons (pyrene and pyrene derivatives),[309] transition metal polypyridyl complexes such as $[Ru(bpy)_3]^{2+}$,[314] metalloporphyrins including platinum(II) or palladium(II) porphyrin complexes,[92,232] and fullerene derivatives.[315,316] Recently, more novel photoactive metal complexes have been reported with promising oxygen sensibility, such as the europium(III) complex $Eu(HPhN)_3(dpp)$[317] and the chromium(III) complex $[Cr(ddpd)_2]^{3+}$.[57,318] These luminescent oxygen indicators can either perform as free molecules in solution or be entrapped in a suitable matrix, depending on their application requirements. The latter is particularly favored for oxygen sensing in biological systems. For bioanalytical applications, commonly applied matrices are nanoparticles, such as silicone polymers, fluoropolymers, organic polymers (*e.g.* PS, PMMA, poly (isobutyl methacrylate)) and inorganic nanostructures such as MOF.[152,301]

An ideal oxygen sensor for bioanalytical applications should be designed under the consideration of the following criteria: avoiding excitation in the UV region, preference with large Stokes shift to avoid self-queching, high brightness, moderately long lifetime, high chemical stability and photostability, high selectivity to oxygen (low cross-sensitivity to other parameters), suitable reference dye, proper choice of the matrices with specific consideration

of high gas permeability, colloidal stability, and the indicator stability in the polymeric matrices, bare toxicity and synthetic availability.[309]

2.4.4 Multi-Analyte Sensors – The Design Principles

In general, a multi-analyte sensor consists of a series of sensors for detection of more than one analyte with a high classification accuracy.[319] In the past years, increasing attention has been attracted for developing multi-analyte sensors for simultaneous detection of multiple analytes, particularly in the field of bioanalysis.[320] In biological environment, many physiological processes are allowed to occur based on the collaborative contribution of multiple chemical events. For instance, the presence of both nitric oxide and hydrogen peroxide leads to effective pathogen killing by macrophages.[321] Abnormal pH values and oxygen content are usually associated with the growth of cancer cells.[322,323] In comparison with other sensing systems such as electrodes, optical sensing based on luminescence has the unique feature of using probes whose signals can be differentiated by spectral and/or temporal resolution, thus enabling multiple sensing.[324]

Nevertheless, the design of an ideal multi-analyte sensor for biological application is challenging. Multi-analyte sensing can be hardly achieved with molecular system. Generally, there must be a suitable matrix for carrying the different indicators. Commonly favored are nanocarriers such as PNPs, where the indicator dyes can be either encapsulated into the particles or conjugated on the particle surface. Yet depending on the target analytes, many criteria must be satisfied with respect to the matrix materials. For instance, sensing of gas such as oxygen usually requires materials featuring high gas permeability, while indicators for pH value must be exposed to the hydrophilic environment.[232] Thus, the chosen matrix should contain capacities for all these features. Moreover, the nanocarriers are supposed to feature suitable size (depending on application requirement), high colloidal stability, low toxicity, and bio-modified surface if the sensors need to be delivered to target issues. One of the most important criteria is that the analyte-responsive dyes must be chosen with absorption and emission features, which enable single wavelength excitation and spectral discrimination of the luminescence emission bands, if the respective emission intensities are used to sensing the corresponding analytes. This can be achieved by applying luminescent indicators with large Stokes shift for spectral allowance of other indicators and reference dye. Emitters are

also highly preferable if they can respond to two different analytes simultaneously with distinguishable optical outputs, such as the oxygen- and temperature-responsive platinum(II) and palladium(II) benzoporphyrins[325] and the $[Cr(ddpd)_2]^{3+}$ complexes.[57,58]

With comprehensive consideration of the factors mentioned above, many multiple-analyte sensors have been developed for detection of the species of great clinical interests (*e.g.* O_2, CO_2, pH, Na^+, K^+, Ca^{2+}, Cl^-, or glucose),[320,324] such as ultra-small dual nanosensors for intracellular detection of pH value and oxygen.[232] Yet most of them are dual sensors, while optical triple sensors are rather scarce.[324] This is more challenging than the dual sensors, as indicators are needed for detecting three analytes and they should feature overlapped excitation region but separated emission signals. Moreover, the addition of reference dye makes the design more difficult. Rare examples include a triple sensor film consisting of three different PNPs, which are doped with luminescent pH-, temperature- and oxygen-reporters respectively. Under one excitation wavelength, the emissive signals can be separated by applying optical emission filters.[326] However, this filmed-based morphology of the sensor is strongly limited for *e.g. in vivo* detection of these analytes. Thus, the development of triple-analyte sensors which are favorable for biological environment is highly desired.

2.5 Methods

In this Section, a series of methods frequently used in this thesis will be discussed, ranging from optical methods such as UV-Vis absorption spectroscopy, luminescence steady-state, quantum yield, time-resolved spectroscopies, and their relative theoretical background, to nanoparticle characterization method such as dynamic light scattering.

2.5.1 UV-Vis Absorption Spectroscopy

Absorption spectroscopy refers to a spectroscopic method that is used to determine the radiation absorbed by a material as a function of radiation frequency or wavelength. The absorption intensity performed over a range of frequency or wavelength is termed as the absorption spectrum. Absorption of radiation occurs usually at frequencies that match the energy difference between two quantum mechanical states of the material, resulting in a transition between the two states. Depending on the quantum mechanical changes induced in a material, absorption lines can be found in different spectral regions.[327] In general, change

in the rotational state of a molecule can be found in the microwave spectral region; vibrational transitions corresponds to absorption lines in infrared region; absorption lines in the UV-Vis region are typically assigned to the electronic transitions; and excitation of inner shell electrons in atoms can be represented by X-ray absorption.[327] Among them, the UV-Vis absorption spectroscopy (typically in the range of 200 – 800 nm) is regarded as a fast analytical method to identify and quantify the concentration of luminescent compounds in the liquid phase.[328]

Figure 17 illustrates the working principle of a typical UV-Vis spectrometer. In general, in a double beam instrument two light sources are applied for generating the ultraviolet light (*e.g.* using deuterium (D_2) lamp) and visible light (commonly with tungsten lamp), respectively. The electromagnetic radiation is directed to a monochromator that is used to disperse polychromatic radiation into individual wavelengths. The dispersed light is then separated into two beams with the help of a beam splitter and guided to the sample and the reference, respectively. The transmitted lights from both sample and reference channel is recorded with a photodetector and then calculated to absorbance, representing the absorption spectrum with wavelength (nm) on the x-axis and absorbance (A) on the y-axis. Typically, the transmittance and the absorbance are found in a complementary relationship.
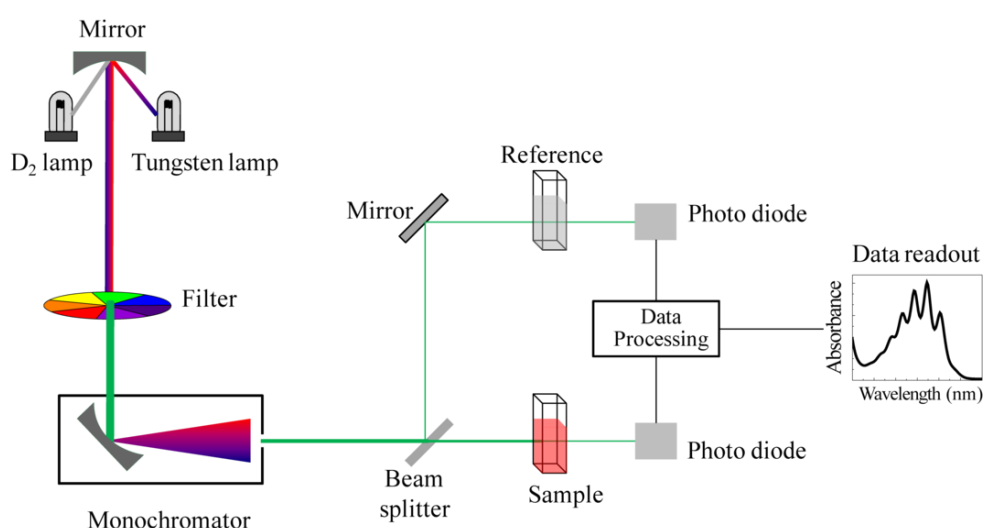

Figure 17: Schematic illustration of the UV-Vis absorption spectrometer working principle (taken from Ref[328]).

According to the Beer-Lambert law, light absorbance (A) is proportional to the sample concentration (C), light path length (l) through the sample, and the molar extinction coefficient (ε) that is an instinct property of the compound (**Eq. 7**):[329]

$$A = \ log_{10}\frac{I_0}{I} = \varepsilon \cdot l \cdot c$$

<div align="right">**Eq. 7**</div>

where I refers the measured light intensity with respect to a reference, I_0.

UV-Vis absorption spectroscopy is a powerful technique used for quantitative analysis of luminophores, which present characteristic absorption bands. In addition to the quantitative analysis, this technique is also favorably applied to derive reaction kinetics in liquid phase and to identify the mechanism at the molecular scale.[328] With a given compound, absorption changes in the breadth, wavelength as well as the intensity can be resulted by environmental influences, such as intermolecular interactions, altered physical environment like temperature and pressure, and solvent effects.[328,330,331]

2.5.2   Luminescence Steady-state and Quantum Yield Spectroscopy

Steady-state Luminescence Spectroscopy

Luminescence spectroscopy, commonly known as fluorescence spectroscopy, is one of the key analytical techniques frequently applied in life science. As a complementary method to absorption spectroscopy, this type of electromagnetic spectroscopy focuses on collecting and analyzing the luminescence generated from a sample upon photoexcitation. Light irradiation on a luminophore results in transitions between electronic states, and thus yielding radiative emission either as fluorescence or phosphorescence (Jablonski diagram, **Figure 1**). The generated photoluminescence can be recorded in different domains, either in their steady-state or in the dynamic-state (time-resolved). In a steady-state emission spectrum, with a given excitation wavelength, the luminescence emission intensity I_{em} (y-axis) is performed as a function of the wavenumber or wavelength (x-axis), while a time-resolved spectrum refers to the dynamic decay behavior of photoluminescence (y-axis) over time (x-axis). The latter will be discussed in Section 2.5.3. In addition to the steady-state emission spectrum, a fluorescence spectrometer is also often utilized to obtain the fluorescence excitation

spectrum with a given emission wavelength. The excitation spectrum usually provides the same features as recorded in the absorption spectrum.

Figure 18 represents the principle of a typical fluorescence spectrometer, which can take the luminescence excitation and emission spectra.[332] The spectrometer consists of a monochromatized-excitation light source, a sample holder, an emission monochromator and a detector. Fluorescence steady-state measurements usually require a continuous excitation source that can generate intense white light, such as continuous xenon lamps or LED light sources. The monochromators are needed in both excitation and emission channels, containing prisms or diffraction gratings and slits to obtain a chromatic light with desired wavelength and reject the rest of the excitation lamp spectrum. Double monochromators can offer better stray light suppression and therefore leading to a higher signal-to-noise ratio in the spectrum. After filtering the emitted light with the emission monochromator, the desired luminescence is collected by a photon detector, which is typically a photon-counting photomultiplier tube (PMT) that can detect single photons. The detection channel is arranged perpendicularly to the excitation to suppress the influence from the excitation light.[31,332]
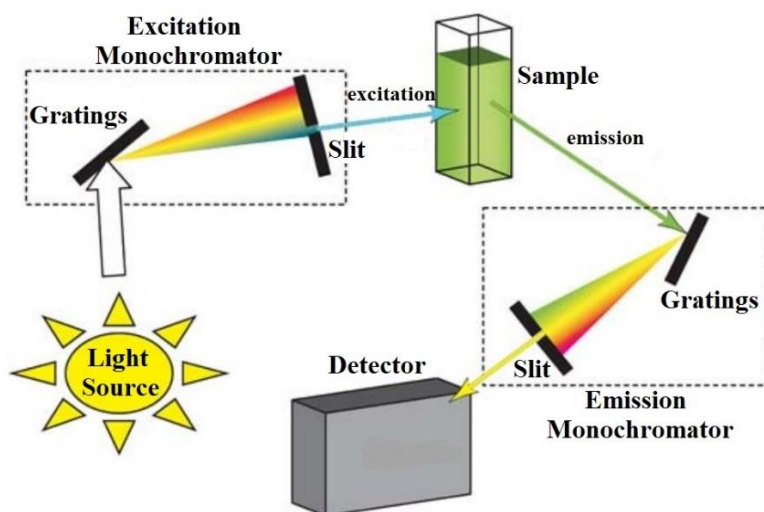
Figure 18: Simplified schematic representation of a fluorescence spectrometer (adapted with from Ref.[332] with permission from The Creative Commons Attribution 4.0 International License).

Luminescence Quantum Yield Determination

Luminescence output per luminophore ("brightness") is proportional to the product of the extinction coefficient (at the relevant excitation wavelength) and the photoluminescence quantum yield PLQY (Φ_L). As one of the key instinct parameters of a luminophore, the

quantum yield is defined as the fraction of emitted photon number N_{em} to that of the absorbed photons N_{abs} (**Eq. 8**):[31]

$$\Phi_L = \frac{N_{em}}{N_{abs}} \qquad\qquad \textbf{Eq. 8}$$

The PLQY quantifies the relation between the radiative and non-radiative decay processes of the excited state, which can be represented by the rate constants of the involved processes (**Eq. 9**):

$$\Phi_L = \frac{k_r}{k_r + k_{nr}} \qquad\qquad \textbf{Eq. 9}$$

where k_r, and k_{nr} are the rate constants of radiative decay (luminescence) and non-radiative dissipation, respectively. Meanwhile, this formulation provides the theoretical support of calculating the sample quantum yield Φ_S by comparing the emission rates constants of interest to those of the known standards Φ_{Ref}:[333,334]

$$\frac{\Phi_S}{\Phi_{Ref}} = \frac{\dfrac{N_{em,S}}{N_{abs,S}}}{\dfrac{N_{em,Ref}}{N_{abs,Ref}}} = \frac{N_{em,S}}{N_{em,Ref}} \cdot \frac{N_{abs,Ref}}{N_{abs,S}} = \frac{I_{em,S}}{I_{em,Ref}} \cdot \frac{A_{abs,Ref}}{A_{abs,S}} \qquad\qquad \textbf{Eq. 10}$$

where I_{em} and A_{abs} are the measured luminescence emission intensity and the measured absorbance, respectively. With **Eq. 10**, the PLQY of a luminophore can be relatively determined with a reference dye with known quantum yield. Yet this method is only valid, when the emission intensity and absorbance of both the sample and the reference are measured under the same conditions, including at the same excitation/detection wavelengths and in the same solvent.[334,335] Apart from these specific conditions, some other effects must be considered explicitly to obtain reliable quantum yields, including polarization effects, reabsorption/reemission effects, refractive index effects, internal reflection effects, and the sensitivity of the detector.[336,337] Particularly for the PLQY determination of TMCs, which show generally large Stokes shift and whose phosphorescence emission is usually observed at long wavelength, the relative methods often lead to low accuracy of the determined phosphorescence quantum yield. With a relative method, the commonly applied photon detectors in a spectrometer usually have relatively low sensitivity at long wavelength, such as photomultiplier tubes. Moreover, fluorescence standards are usually used to obtain the

relative PLQY value of a TMC, even the quantum yields of these standards also need to be reevaluated.[336]

To address these challenges, an absolute method has been developed to determine the PLQY of a luminophore by using an integrating sphere setup, consisting of a hollow spherical cavity internally covered with a white diffuse reflective coating, with small ports for light entrance and exit.[336,338,339] The inner coating layer enables multiple scattering reflections of the incident light in the sphere while preserving the light power. Such integrating spheres are used for a variety of measurements, such as the total power of a light source,[340] the transmittance and reflectance of a sample,[341] and the absolute PLQY.[336,338] In comparison with the relative method, the absolute method is a superior approach as it can eliminate the unwanted effects, such as reabsorption, optical anisotropy, polarization and refractive index from measurements.[336] By incorporating the integrating sphere into a fluorescence spectrometer, the coupled setup enables the straightforward measurements of upconversion quantum yield of UCNPs.[335,342] Such measurements can be hardly achieved with a pure fluorometer due to the low quantum yield of UCNPs and the relatively low sensitivity of the detector. Recently, an advanced integrating sphere setup (Quantaurus-QY Plus C13534-01) has been developed by *Hamamatsu*, providing an absolute method for determining the TTA-UC quantum yield in solution.[343]

An example from *Hamamatsu Instruments* is schematically shown in **Figure 19**, displaying the principle of measuring the absolute PLQY with such an integrating sphere.[336] Similar to fluorescence spectrometer, an integrating sphere setup also consists of light source (such as arc xenon lamp), the presence of two monochromators in both the excitation (MC1) and the emission channels (MC2), a sample holder, a multichannel photodetector, such as a back-thinned charge coupled device (BT-CCD) to converts light photons into current, and a computer for data analysis. Yet in this case the sample holder is set in a sphere, in which the internal surface is coated with a high reflectance material such as Spectralon (*Labsphere*). Additionally, the sphere is equipped with a baffle between the sample and the exit port to protect the detector from direct detection of the excitation light and/or emission from the sample. Typically, the light sources as well as the detector sensitivity need to be calibrated in accordance with the traceable measurement standards.
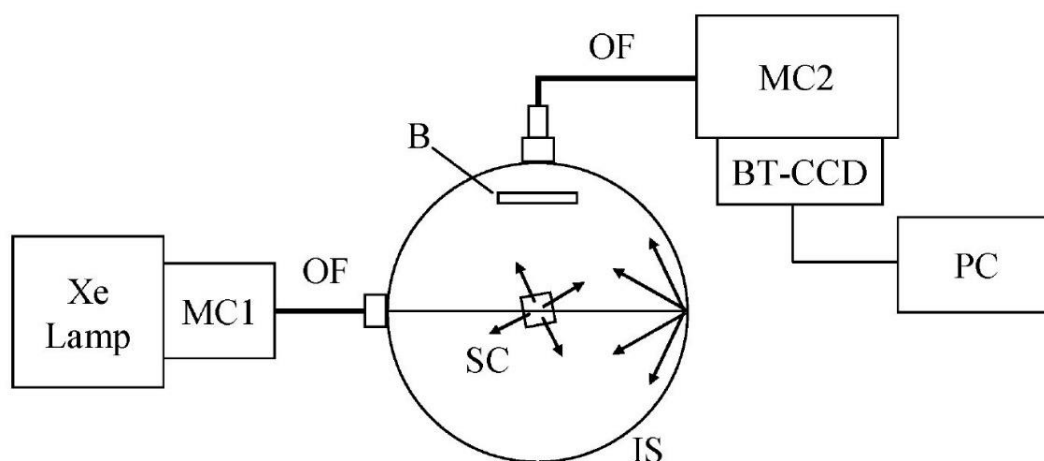
Figure 19: Schematic illustration of an integrating sphere setup (Hamamatsu, C9920-02) for measuring absolute fluorescence quantum yields. MC1, MC2: monochromators, OF: optical fiber, SC: sample cell, B: baffle, BT-CCD: back-thinned CCD, PC: personal computer (taken with permission from Ref.[336], Copyright © The Royal Society of Chemistry 2019)

With such an integrating sphere setup, the absolute PLQY of a luminescent solution can be determined by measuring the integrated light intensities of the sample (S) and the reference (Ref) (typically pure solvent). The luminescence quantum yield can be given by:

$$\Phi_L = \frac{N_{em}}{N_{abs}} = \frac{\int \frac{\lambda}{hc}\left[I_{em,S}(\lambda) - I_{em,Ref}(\lambda)\right]d\lambda}{\int \frac{\lambda}{hc}\left[I_{ex,Ref}(\lambda) - I_{ex,S}(\lambda)\right]d\lambda}$$

Eq. 11

where λ, h, and c stands for the wavelength, the Planck's constant, and the speed of light, respectively. $I_{ex}(\lambda)$ and $I_{em}(\lambda)$ represents the intensity of the excitation light and the luminescence emission at wavelength λ, respectively. According to **Eq. 11**, the absolute PLQY Φ_L can be calculated from the ratio of the difference of the integrated emission spectrum to the integrated excitation light profiles.

2.5.3 Luminescence Time-resolved Spectroscopy

Theory of Luminescence Lifetime

Luminescence lifetime τ_L is a key characteristics of a luminophore, representing the average time that a molecule spends in its excited state before spontaneous emission occurs, which can be described as a deactivation process involving radiative and non-radiative decay pathways (**Eq. 12**):[344,345]

$$\tau_L = \frac{1}{k_r + k_{nr}}$$

<div align="right">**Eq. 12**</div>

When the luminophore presents only one conformational excited state with mono-exponential lifetime, the decay process follows a first order kinetic (**Eq. 13**):[31,344,345]

$$\frac{d[N(t)^*]}{dt} = -(k_r + k_{nr}) \cdot [N(t)^*]$$

<div align="right">**Eq. 13**</div>

where $[N(t)^*]$ indicates the number of excited luminophores at time t. Since the number of excited luminophores $[N(t)^*]$ is proportional to the luminescence intensity $I(t)$, integration between $t = 0$ and t yields a mono-exponential function **Eq. 14**:[31,344]

<div align="right">**Eq. 14**</div>

$$I(t) = I_0 e^{-(k_r + k_{nr})t} = I_0 e^{-t/\tau_L}$$

where I_0 denotes the luminescence intensity at time $t = 0$. Thus, luminescence lifetime can also be understood as the time required by excited luminophores to decrease to 1/e of its initial intensity I_0 ($t = 0$) upon photoexcitation.

For a luminophore featuring multiple decay behaviors, which can originate either from the instinct nature of the compound (such as UCNPs) or due to different intermolecular interactions, the luminescence decays must be described by applying a multi-exponential model (**Eq. 15**):[31,344]

<div align="right">**Eq. 15**</div>

$$I(t) = \sum_i f_i e^{-t/\tau_i}$$

where f_i is the fractional contribution of the i-th component, featuring a characteristic luminescence lifetime τ_i. f_i is defined as each decay time to the steady-state intensity (**Eq. 16**):[31]

$$f_i = \frac{A_i \tau_i}{\sum_i (A_i \tau_i)}$$

<div align="right">**Eq. 16**</div>

where A_i denotes the amplitude of lifetime τ_i. Depending on the applications, an averaged lifetime τ_{ave} is usually required, which can be calculated either per amplitude-weighted (**Eq. 17**) or intensity-weighted (**Eq. 18**) function:[346] Typically, amplitude-weighted lifetime τ_{ave_amp} is favored for analysis of interactions between fluorophores, such as Förster resonance energy

transfer (FRET), while intensity-weighted lifetime τ_{ave_int} is usually used for dynamic quenching processes.[346,347]

$$\tau_{ave\_amp} = \frac{A_1\tau_1 + A_2\tau_2 + \cdots}{A_1 + A_2 + \cdots} = \frac{\sum_i (A_i\tau_i)}{\sum_i A_i} \qquad \text{Eq. 17}$$

$$\tau_{ave\_int} = \frac{A_1\tau_1^2 + A_2\tau_2^2 + \cdots}{A_1\tau_1 + A_2\tau_2 + \cdots} = \frac{\sum_i (A_i\tau_i^2)}{\sum_i (A_i\tau_i)} \qquad \text{Eq. 18}$$

Measurement of Luminescence Lifetime

Measurements of luminescence lifetime can be achieved by time-resolved luminescence spectroscopy. Two techniques have been developed for the lifetime measurements, namely time-gated[348] and time-correlated single photon counting (TCSPC).[349] The latter is more popular due to the high temporal resolution and high optical efficiency.[350,351] **Figure 20** shows the lifetime measurement principle using a TCSPC system with a start-stop mode.
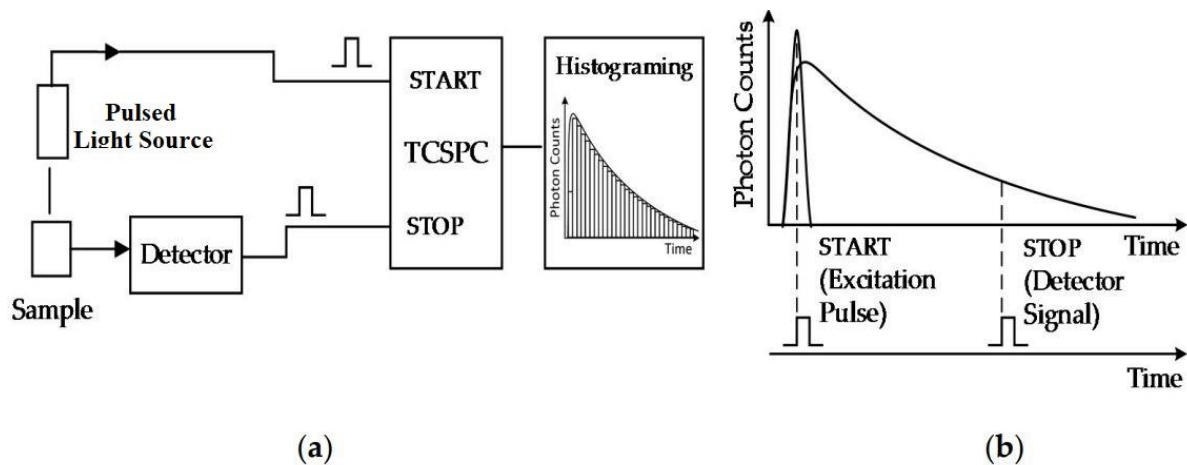
Figure 20: Schematic illustration for measuring time-resolved luminescence spectrum using time-correlated single photon counting (TCSPC) operation principle. (a) System schematic; (b) timing diagram of the "start-stop watch" mode (taken from Ref[351] with permission from The Creative Commons Attribution 4.0 International License).

In contrast to the continuous light source used in steady-state luminescence measurement, lifetime measurement requires a pulsed excitation source. Additionally, a single photon detector, a time electronics, such as a time-to-amplitude converter (TAC), and a computer are

needed (**Figure 20 (a)**). When the luminophore is excited, a synchronization pulse from the excitation is delivered to the START input of the time electronics, acting as a trigger signal for turning off the excitation. The emitted luminescence is then detected by the single photon detector and subsequently delivered in form of a pulse to the STOP input of the time electronics. The time difference between the START and the STOP corresponds to the time-of-arrival of an emitted photon. Such a timing mode is termed as "start-stop watch" mode (**Figure 20 (b)**). Accumulation of the arrived photons over time is finally performed as luminescence decay.

Luminescence lifetime is an instinct property of a luminophore and therefore is independent on the measuring methods and initial perturbation conditions, such as luminescence intensity and luminophore concentration, wavelength of excitation, duration of light exposure, one- or multiphoton excitation, method of measurement and photobleaching.[345,352] Thus, it is a promising parameter preferable for applications in intricate environment, such as biological environments. Based on the techniques for luminescence lifetime measurement, some extended methods are developed for *in vitro* and *in vivo* lifetime imaging, namely the fluorescence- or phosphorescence lifetime imaging microscopy (FLIM or PLIM).[345,353-355] These lifetime imaging methods have the flexibility of fluorescence intensity technique which is suitable for measurements in any phase (gas, liquid, solid, or their combinations). Additionally, they can be applied in various systems of interest, ranging from single molecule to cells and human bodies.[345]

2.5.4 Dynamic Light Scattering

Dynamic light scattering (DLS), also known as photon correlation spectroscopy (PCS), is a commonly used technique to for particle size analysis in suspension or in solution.[356] The working principle of DLS is based on the Brownian motion of particles in solution, which arises due to the constant collisions from solvent molecules. The collisions can thus induce particle movement, which relates to the particle size.[357] The measurement principle of DLS is illustrated in **Figure 21**.[358]
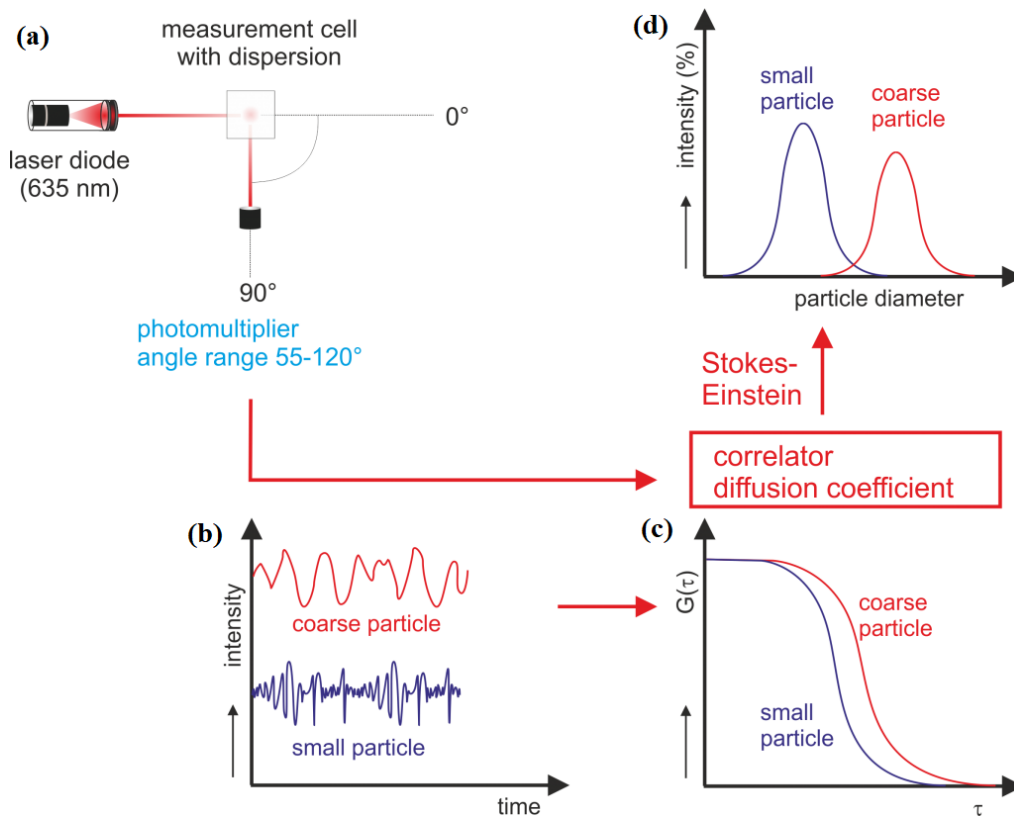
Figure 21: Measurement principle of DLS (taken from Ref.[358], Copyright @ 2020 3P Instruments)

In a DLS instrument, a laser beam encounters the liquid phase sample containing small particles (usually < 1 µm), yielding scattered incident light in all directions. Due to the Brownian motion, the particles move continuously, yielding constantly changed positions of the scattering centers and thus resulting small fluctuations in scattering intensity.[357] The light intensity fluctuations are then recorded with respect to time (ns-µs) by a detector, which is set at a certain fixed angle (usually 90°) to the incidence direction (**Figure 21 (a)**).[359] The fluctuations of the scattered light intensity relate clearly to the particle size: smaller particles move faster and thus generating faster fluctuations than larger particles, while larger particles perform higher amplitudes between the maximum and minimum scattering intensities (**Figure 21 (b)**). With help of a digital autocorrelator, the intensity fluctuations of scattered light are correlated to time, shown as a correlation function (**Figure 21 (c)**). Such a correlation function provides the general information how long a particle is located at the same spot within the sample. Linear and constant correlation indicate bare particle movement within the time window, while an exponential decay of the correlation function corresponds to the movement of the particles. Moreover, the decay contains information on the size-dependent movement:

small particles move quickly, performing a faster decay; while particles move more slowly and thus lead to a delayed correlation function. This provides the information of the viscosity (η) of the particles in the dispersion and the diffusion coefficient (D) of the particles.[357,359] With this information, the hydrodynamic diameter of the particle can be determined according to the Stokes-Einstein equation (**Eq. 19**) (**Figure 21 (d)**):[358]

$$D = \frac{k_B T}{6\pi\eta R_H}$$ **Eq. 19**
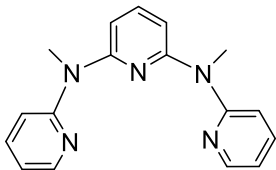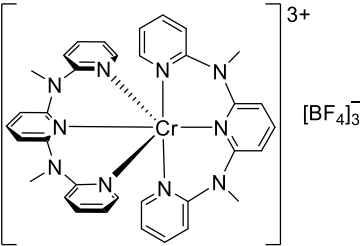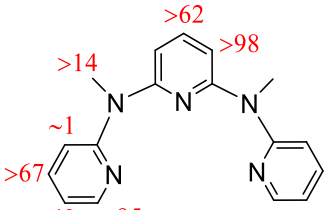
where k_B stands for the Boltzmann constant, T is the temperature, and R_H refers the hydrodynamic radius.
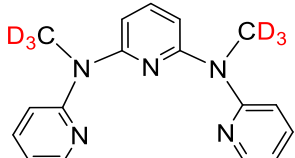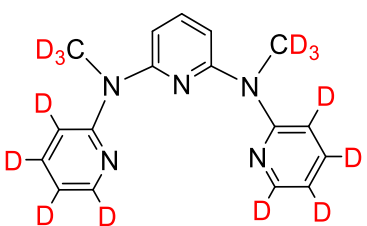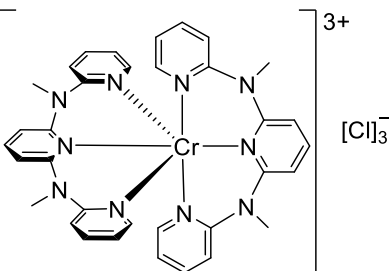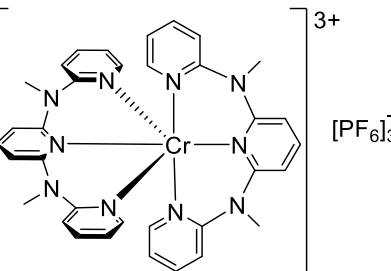
The DLS technique has high capacity for measurements with robust conditions, such as wide range of sample buffer as well as high tolerance to temperature. This technique requires also low amounts of sample and offers reliable estimates of the experimental operation rapidly.[357] As a result, DLS acts as a powerful tool to characterize size of various particles, such as proteins, polymers, micelles, vesicles,[360] carbohydrates, nanoparticles, biological cells,[361] and gels.[362]
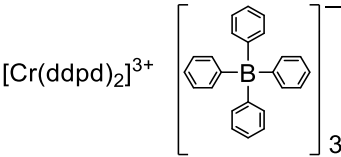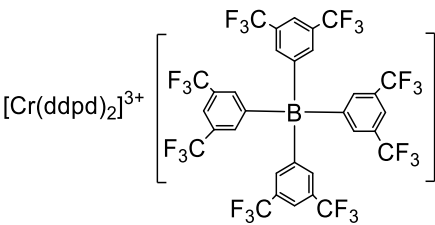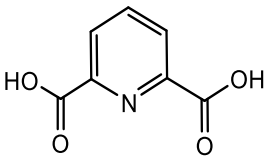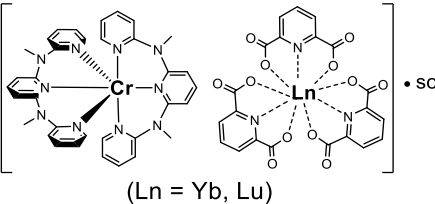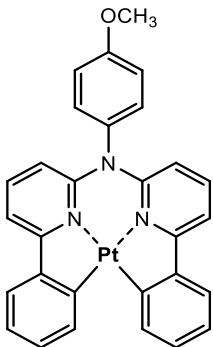
3 Experimental Section

3.1 Materials

In this thesis, different types of TMCs were studied. These TMCs were mostly synthesized by whom from the collaboration partners and the syntheses are not included in this thesis. The used TMCs as well as their respective parent ligands or anions are summarized in **Table 2**, including their chemical structures, the corresponding abbreviations, as well as the collaboration partners who made the synthesis. Commercial chemicals used in this thesis are listed in **Table 3**.

Compound	Structure	Abbr.	Synthesized by:
Cr(III)-complex series			
N,N'-dimethyl-N,N'dipyridine-2-yl-pyridine-2,6-diamine	Molecular Weight: 291.36	ddpd (parent ligand)	Group Heinze
[Cr(ddpd)$_2$][BF$_4$]$_3$	Molecular Weight: 895.12	CrBF$_4$	
[Cr([D$_9$]-ddpd)$_2$][BF$_4$]$_3$	Same structure as [Cr(ddpd)$_2$][BF$_4$]$_3$ with the following ligand. unselected [D$_9$]-ddpd (>50% D)	Cr(D$_9$)BF$_4$	

[Cr([D$_6$]-ddpd)$_2$] [BF$_4$]$_3$	Same structure as [Cr(ddpd)$_2$][BF$_4$]$_3$ with the following ligand selected [D$_6$]-ddpd (>99.5% D)	Cr(D$_6$)BF$_4$	
[Cr([D$_{14}$]-ddpd)$_2$] [BF$_4$]$_3$	Same structure as [Cr(ddpd)$_2$][BF$_4$]$_3$ with the following ligand selected [D$_{14}$]-ddpd (>99.5% D)	Cr(D$_{14}$)BF$_4$	Group Heinze
[Cr(ddpd)$_2$][Cl]$_3$	 Molecular Weight: 741.06	CrCl	
[Cr(ddpd)$_2$][PF$_6$]$_3$	 Molecular Weight: 1069.13	CrPF$_6$	

[Cr(ddpd)$_2$][BPh$_4$]$_3$	[Cr(ddpd)$_2$]$^{3+}$ Molecular Weight: 1592.4	CrBPh$_4$	Group Heinze
[Cr(ddpd)$_2$][BAr$_4$^{F24}]$_3$	[Cr(ddpd)$_2$]$^{3+}$ Molecular Weight: 3224.37	CrBArF$_{24}$	Wang
2,6-pyridine-dicarboxylate		dpa (ligand)	Group Seitz
[Cr(ddpd)$_2$][Ln(dpa)$_3$]·solv.	 (Ln = Yb, Lu)	Cr-Ln (Ln = Yb, Lu)	
Pt(II) and Pd(II) complex series			
(N,N-di(2-phenylpyrid-6-yl)-3,5-dimethoxyaniline)platinum(II)	 Molecular Weight: 622.59	PtLH	
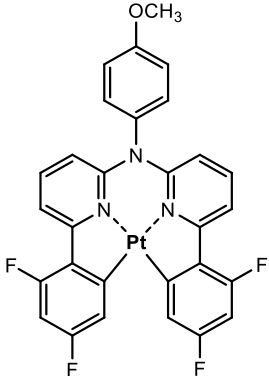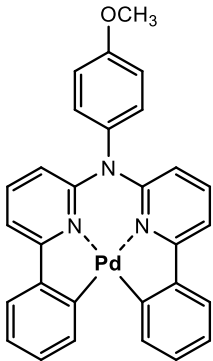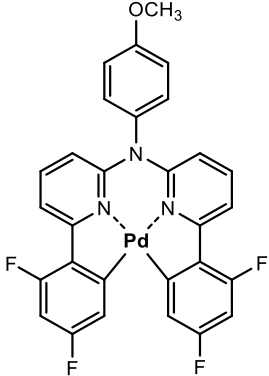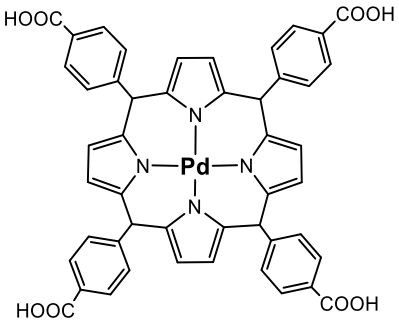
(N,N-di(2-(2,4-difluorophenyl)pyrid-6-yl)-4-methoxyaniline)platinum	 Molecular Weight: 694.55	PtLF	Group Strassert
(N,N-di(2-phenylpyrid-6-yl)-3,5-dimethoxyaniline)palladium (II)	 Molecular Weight: 533.93	PdLH	
(N,N-di(2-(2,4-difluorophenyl)pyrid-6-yl)-4-methoxyaniline)palladium(II)	 Molecular Weight: 605.89	PdLF	
(Meso-Tetrakis-(4-carboxyphenyl)-porphyrinato)palladium(II)	 Molecular Weight: 899.22	Pd(TCPP)	Group Heinze

Table 2: List of TMCs used in this work (Abbr.: abbreviation).

Chemicals	Abbr.	Purity	Producer
Ethanol	EtOH	99.9%	Merck
Deuterium oxide	D_2O	99.9%	Sigma-Aldrich
Acetonitrile	CH_3CN	99.9%	Merk
Acetonitrile-d_3	CD_3CN	99% D	abcr
Dimethylformamide	DMF	99%	Alfa Aesar
Tetrahydrofuran	THF	99.9%	Carl Roth
Oleic acid	OA	99%	Sigma-Aldrich
Caprylic acid	CA	99%	Sigma-Aldrich
Hydrochloric acid, 37 %	HCl	-	CHEMSOLUTE
Perchloric acid, 70%	$HClO_4$	-	Merck
Perchloric acid-d, 68 wt. % in D_2O	$DClO_4$	99% D	Bernd Kraft
Sodium hydroxide	NaOH	1 mol/L	Merck
Sodium phosphate	Na_3PO_4	96%	Sigma-Aldrich
Sodium hydrogen phosphate dihydrate	Na_2HPO_4	>99%	Carl Roth
Bovine serum albumin (~66,000 Da)	BSA	>98%	Sigma-Aldrich
Sodium tetraphenylborate	$NaBPh_4$	99.5%	Sigma-Aldrich
Sodium tetrakis[3,5-bis(trifluoromethyl)phenyl]borate	$NaBArF_{24}$	98%	Sigma-Aldrich
Fluorescein 5(6)-isothiocyanate	FITC	90%	Sigma-Aldrich
Phenoxazon 9 (Nile Red)	NR	98%	Fluka Chemie
5,10,15,20-tetrakis(pentafluorophenyl) porphyrin	TFPP	95%	abcr
9,10-Diphenylanthracene	DPA	99%	Thermo Fisher
Polystyrene nanoparticles (100 nm aminated)	PS-NH_2	25 mg/mL	Micromod
Polyvinyl alcohol (80% hydrolyzed)	PVOH	-	Sigma-Aldrich

N,N-dimethylacetamide	DMAc	99%	Sigma-Aldrich
Tetraethyl orthosilicate	TEOS	98%	Sigma-Aldrich
3-(aminopropyl)triethoxysilane	APTES	99%	Sigma-Aldrich
Ammonia (25% in water)	NH_3	-	Merck

Table 3: Commercial chemicals used in this work.

3.2   Ion exchange of $[Cr(ddpd)_2]^{3+}$ complex

$[Cr(ddpd)_2][BAr_4F_{24}]_3$ (CrBArF$_{24}$) complex was obtained via ion exchange. $[Cr(ddpd)_2][BF_4]_3$ (CrBF$_4$) complex (50 mg, 0.055 mmol) was dissolved in 3 mL CH$_3$CN. 4 mL CH$_3$CN solution of NaBArF$_{24}$ (155.1 mg, 0.175 mmol) was slowly added. After stirring for 30 min, deionized water was added until precipitation was completed. After 4 hours, the yellow precipitate was collected, washed three times with water (2 x 5 mL), and dried under reduced pressure. CrBArF$_{24}$ complex was obtained as a fine yellow powder (59.57 mg, 69%).

3.3   Preparation of Luminescent Polymeric Nanoparticles

In this thesis, preparation of luminescent polymeric nanoparticles involved usually three main steps: **(i)** encapsulating the hydrophobic dye of interest into the PNPs, **(ii)** silica-shell coating on the particles surface to prevent dye leaking (not necessary, depending on the dye inside); and **(iii)** conjugation of hydrophilic dye on particle surface post-synthetically (depending on the requirements). These procedures are schematically illustrated in **Figure 22**.
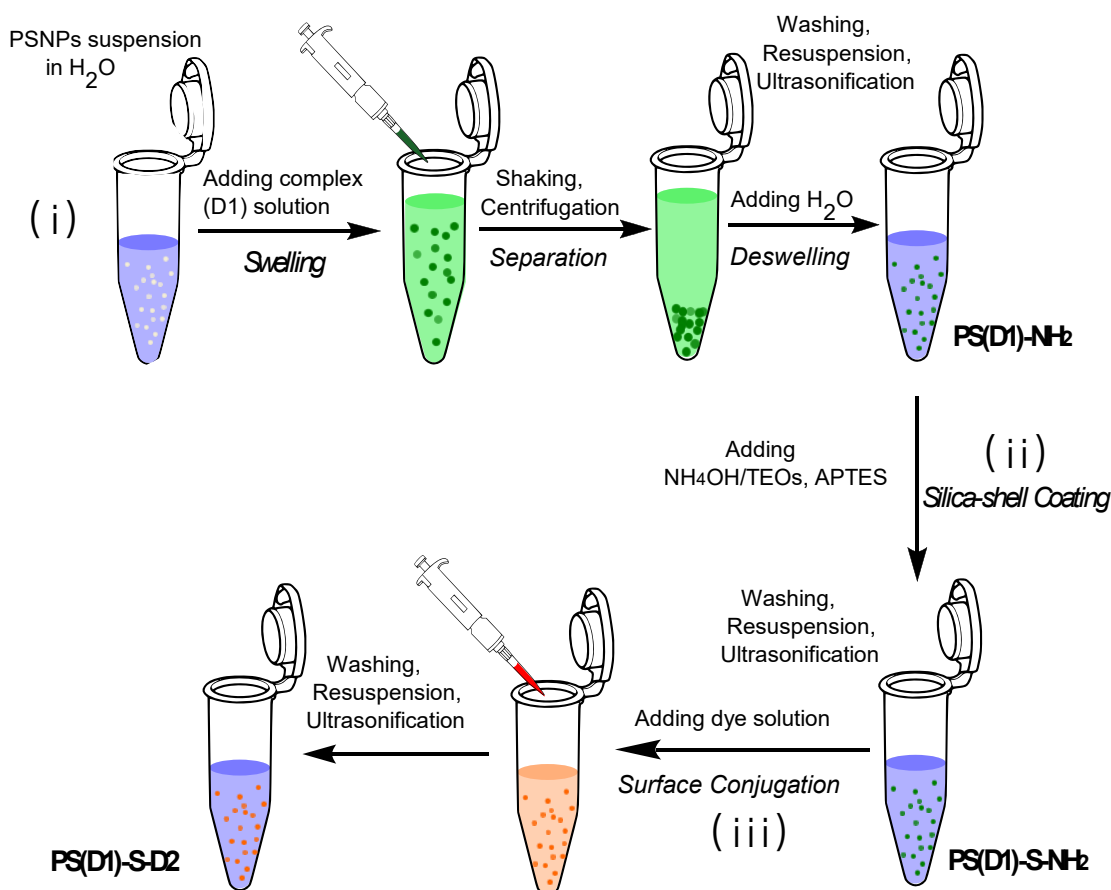
Figure 22: Schematic illustration of the complex staining procedure using 100 nm aminated PSNPs, including complex encapsulation, coating with a silica shell (employing TEOS and APTES), and surface conjugation with hydrophilic dye.

3.3.1 General encapsulating procedure

Preparation of PS(D1)-NH$_2$: The preparation of PS(D1)-NH$_2$ is illustrated in **Figure 22 (i)** according to the one-step staining procedure.[206] In general, concentrated complex- or organic dye 1 (D1) solution is prepared in a water miscible solvent, *e.g.* tetrahydrofuran (THF) or dimethylformamide (DMF) or their mixture, resulting in a D1 solution with the concentration typically ranging from 1 mM to 4 mM. 6 mg 100 nm-sized aminated PSNPs were dispersed in Milli-Q water to 2.5 mg/mL (2.4 mL) and separated in two tubes. After adding 200 μL of D1 solution to the PSNPs dispersion (1.2 mL), the samples were immediately shaken for 40 min with a lab shaker. Shrinking of the particles was induced by adding 200 μL of Milli-Q water to each tube, thereby sterically incorporating D1 molecules into the PSNPs. The particles were then centrifuged at 16000 rcf for 60 min (*Centrifuge 5415D from Eppendorf*, Germany). The precipitate was washed three times with acetonitrile/water or ethanol/water mixtures (volume ratios of 40/60, 30/70, and 20/80) and once with Milli-Q water to remove excess D1

adsorbed onto the particle surface. PSNPs stained with D1 were diluted to 600 μL with Milli-Q water, yielding a particle concentration of 10 mg/mL.

3.3.2 Silica-coating with surface functionalization

Preparation of PS(D1)-S-NH$_2$: To avoid complex leaking from the PSNPs, a thin silica shell could be constructed on the particle surface via ammonia-catalyzed Stöber process (**Figure 22 (ii)**).[236,241] 12 μL aqueous ammonia (25%) was added to 600 μL D1-stained PSNP suspension (10 mg/mL). After shaking for a few minutes, 12 μL of tetraethyl orthosilicate (TEOS) with 5.0% (w/v) (3-aminopropyl) triethoxysilane (APTES) was dissolved in 40 μL absolute ethanol and then added slowly (10 μL every 10 min) to the stirred particle dispersion. The samples were shaken for 15 h. The particles were washed with ethanol/water mixtures (volume ratios of 40/60, 30/70, and 20/80) three times and once with water. The resulting silica-coated particles PS(D1)-S-NH$_2$ were dispersed in 600 μL Milli-Q water yielding a particle concentration of 10 mg/mL.

3.3.3 Immobilization of PSNPs in a polymer film

Preparation of PS(D1)-S-PVOH films: 160 mg oxygen barrier polymer poly(vinyl alcohol) (PVOH, 80% hydrolyzed)[363] was dissolved in 4 mL N,N-dimethylacetamide (DMAc). 750 μL PVOH (40 mg/mL in DMAc) was added to 3 mg PS(D1)-S-NH$_2$ particles (10 wt% of PVOH). The PS(D1)-S particles were dispersed in PVOH and dried on a glass plate under vacuum at room temperature for overnight. The PS(D1)-S-PVOH was generated as a transparent thin film.

3.3.4 Surface conjugation with FITC

Preparation of PS(D1)-S-F: If the particles need to be further functionalized with pH-sensitive dye, such as FITC, the following post-synthetic procedure can be applied (**Figure 22 (iii)**). 0.15 mg of FITC was dissolved in 30 μL (5 mg/mL, 12.8 mM) of ethanol and added to 600 μL dispersion of the PS(D1)-S-NH$_2$ particles (10 mg/mL) at pH 8.0 (adjusted with phosphate-buffered saline (PBS)). After the reaction mixture was stirred for 3 h, the particles were washed four times with ethanol/water mixtures (volume ratios of 40/60, 30/70, and twice

20/80, respectively) and once with water. The obtained PS(D1)-S-F particles were then dispersed in 600 μL of Milli-Q water, yielding a particle concentration of 10 mg/mL.

3.4 Determination of Zeta Potential and Size Distribution

The zeta potential and size distribution of the PSNPs were subsequently determined by dynamic light scattering (DLS) with a *Zetasizer Nano ZS* from *Malvern Instrument* (**Figure 23 a**).[364] Typically, disposable cells are applied for the measurements to eliminate sample cross contamination. Particularly, measurement of zeta potential requires the capillary cell equipped with electrodes, as shown in **Figure 23 b**.
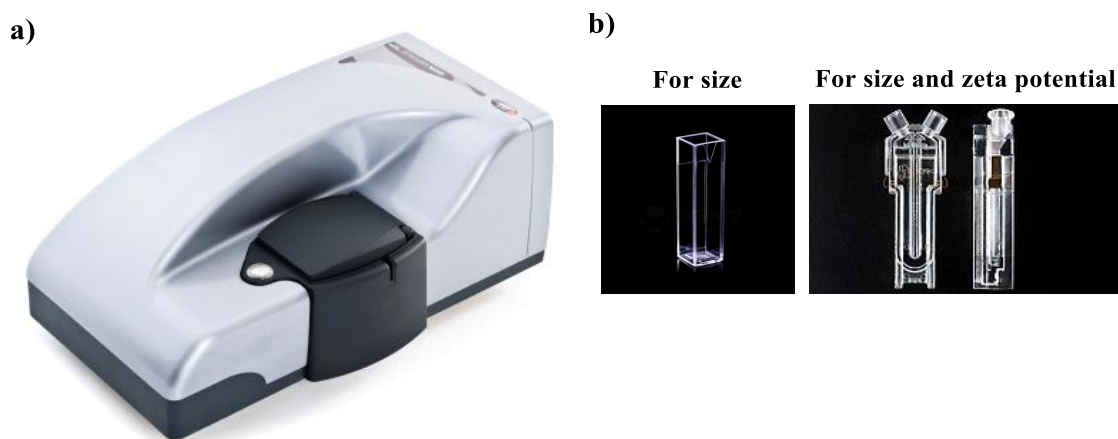
Figure 23: a) DLS instrument *Zetasizer Nano ZS (Malvern)*; b) cells for size distribution and for zeta potential measurements (taken from Ref.[364]).

To have a better insight into the changes of these parameters, particles including bare PS-NH$_2$, PS(D1)-NH$_2$, PS(D1)-S-NH$_2$, as well as PS(D1)-S-F were measured, respectively. In general, the particle samples were prepared in water with the concentration of 1 mg/mL. Each sample was handled with ultrasonication for 5 minutes before the measurements. To obtain data with low standard deviation for the zeta potential, each sample was measured 3 times with each measurement including 120 runs, while measurements of size distribution usually undergo 5 x 12 runs.

3.5 Quantitative Determination of the Dye Concentration in the PSNPs

3.5.1 TMC in the PSNPs

Determination of the amount of encapsulated TMC was carried out via absorption spectroscopy. To estimate the molecular number of the encapsulated complex in the PSNPs, the extinction coefficient of the complex must be determined firstly. This can be achieved by dissolving the PSNPs in an organic solvent DMF and the generated PSNP solution in DMF is taken as a new solvent DMF-PSNP. Usually, the PSNP concentration in DMF is quite low, typically of 0.1 mg/mL to ensure a transparent solvent. Calibration samples were prepared by dissolving the target complex in the DMF-PSNP solvent with known complex concentration. With an UV-Vis absorption spectrometer (Varian 5000), their respective absorbances were measured and the absorbance (usually of the peak at the maximum wavelength) was plotted as a function of the complex concentration. The fitted linear function acted as the calibration curve, yielding from the slope of the extinction coefficient using an optical path length of usually 10 mm through the sample.

The luminescent PSNP samples, such as PS(D1)-NH$_2$, were dissolved in pure DMF to give the final particle concentration of 0.1 mg/mL. By measuring the absorbance, the complex concentration was calculated according to the previously resulted linear calibration function. With the known mass per particle (m(PS) = 5.39307×10^{-16} g/particle, data from the manufacture) and the known particle mass concentration (recorded in the preparation protocol), the particle number can be calculated. Thus, the number of the doped complex per particle can be estimated.

3.5.2 FITC on the PSNPs

The quantification analysis of FITC on the PSNPs was achieved via absorption spectroscopy, as well. Yet in this case, it was determined indirectly by calculating the amount difference of the added FITC and the residual FITC in the washing solution. In this way, influences from the absorption bands of the other dye components can be avoided.

This indirect quantification method required to a great extent the exact control of the conjugation and the washing procedures. The conjugation was completed in a mixture of PBS (pH 8.1, 0.1 M) and ethanol, containing 25 v-% (volume-% or v-%) PBS, 20 v-% ethanol, and 55

v-% water. According to this solvent mixture, a series of absorption spectra were taken with known FITC concentration and the absorbances at 496 nm (absorption maximum) were used for generating the calibration curve. With this calibration curve, the concentration of the added FITC and the unreacted FITC in the washing solution was calculated according to their respective absorbance at 496 nm. The difference corresponded to the amount of the bound fluorescein.

3.6 Leaking Experiments of TMC-loaded Polymeric Nanoparticles

Some TMCs, especially those containing small anions, can suffer from leaking problem from the PNPs. This depends on the hydrophobicity or the hydrophilicity of the TMCs. Therefore, leaking experiments must be performed for TMC-loaded PNPs.

In this thesis, different types of TMCs were encapsulated into PSNPs. The leaking experiments were carried out and monitored by luminescence measurements. TMC-loaded PSNPs were freshly prepared and the emission spectra were recorded. After storing the particle suspension at ca. 7°C for over two days, the sample was centrifuged at 16000 rcf for 60 min. By measuring the emission spectrum of the supernatant liquid after centrifugation, the amount of leaking can be estimated by comparing the emission spectrum with the previously recorded fresh sample.

3.7 Optical Measurements

Optical characterization played a key role in this thesis, either for studying the distinct optical properties of the dye of interest or for exploiting the charge- or energy transfer processes. Typically, the photophysical information can be obtained from various optical approaches, including absorption spectra, luminescence emission spectra, luminescence kinetic decays (lifetimes), and luminescence quantum yield determination. Additionally, since all the TMCs studied in this thesis show oxygen sensitivity, their luminescence properties as well as the energy transfer efficiency from their excited states can be strongly influenced by the presence of oxygen. Therefore, this section firstly describes the strategies of preparing oxygen-sensitive samples and subsequently introduces the spectroscopic methods.

3.7.1 Strategies for Preparing O$_2$-sensitive Samples

In most cases, oxygen needed to be completely excluded from the TMC-contained samples due to its strong quenching effect. In liquid systems, this can be achieved by purging the sample solutions (V = 4 mL) with argon and sealing the cuvette airtightly. Notably, even traces of oxygen can significantly distort quantum yield and lifetime measurements of long-lived TMCs. Therefore, a long neck quartz cuvette (10 mm x 10 mm, neck of 10 cm, *Hamamatsu*) was applied to extend the argon-filled spatial isolation between the sample and the outer air (**Figure 24 a**). During purging the sample with argon through needles, the cuvette was sealed with an airtight rubber septum cap (*Sigma-Aldrich*). After purging the sample with argon for ca. 30 min, optical measurements were carried out immediately by following the measuring order of luminescence quantum yields, lifetime, emission spectra and absorption spectra. To control the air tightness of the cuvette during the measurements, the luminescent quantum yields were determined again after completing the measurement cycle. By comparing the final and the initial quantum yield values, the difference was proven to have a maximum of 2 %, indicating the high tightness of the system.
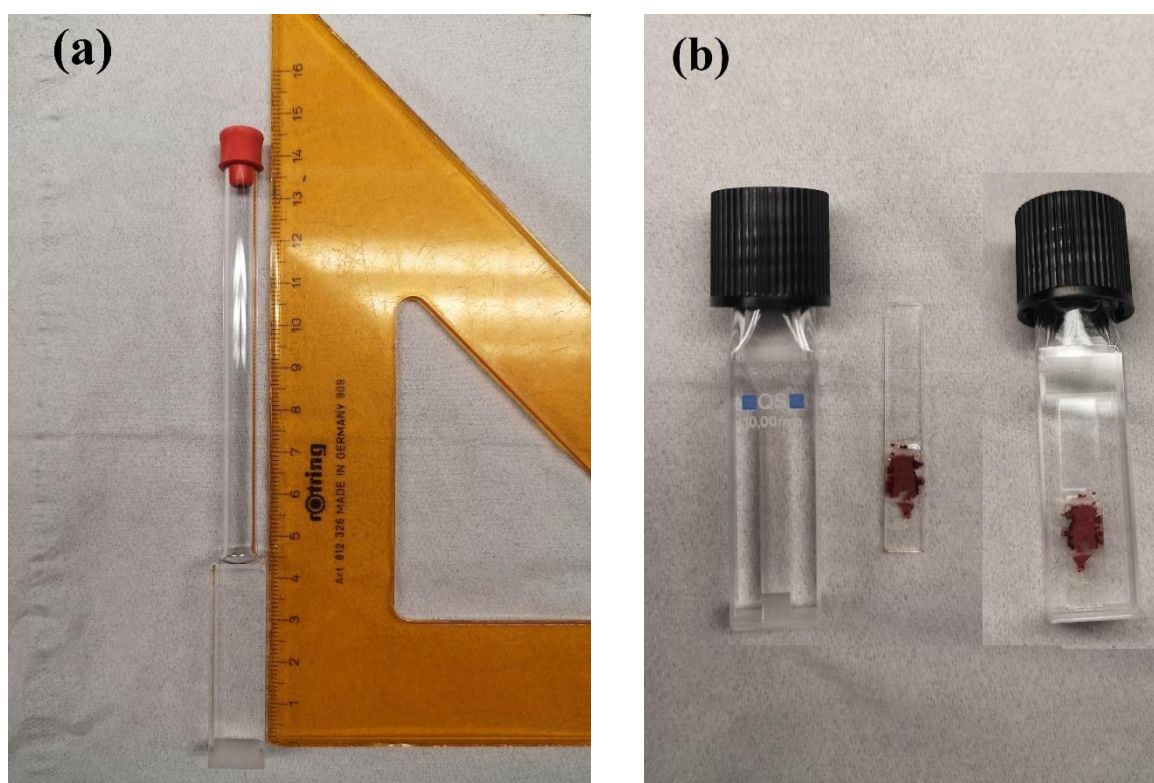
Figure 24: Optical cuvettes used for oxygen-sensitive samples in **(a)** liquid phase and **(b)** solid-state.

For optical measurements of O_2-sensitive solid-state samples, another sealing strategy was developed. The sample powder was firstly immobilized between two glass slides (7 mm x ca. 3 cm) with epoxy glue and the slide sample was sealed in a high precision screw cap cuvette (10 mm x 4 mm, *Hellma Analytics*) in a glove box (<10 ppm O_2) (**Figure 24 b**). An alternative approach was also applied by purging the sealed cuvette with argon for ca. 30 min. However, this approach is only suitable for the less oxygen-sensitive samples or processes.

3.7.2 Absorption Spectra

The UV-Vis absorption spectra of dye solutions or particles suspensions were obtained from a calibrated Varian 5000 spectrophotometer in the spectral range 200 – 2500 nm. Depending on the detection range, two detectors are available, namely a R928 PMT for the UV-Vis range and a Peltier-cooled PbS Photocell for the NIR-range.[365] The absorption measurements in this thesis were completed with the R928 PMT detector for recording the UV-Vis spectra. Prior to the measurements, the instrument needs a warmup period for ca. 2 hours. Typically, absorption scans were obtained in the range 200 – 800 nm with a scan rate of 5 nm/s.

3.7.3 Luminescence Emission Spectra and Decays

Luminescence emission spectra and decays were recorded by three calibrated spectrofluorometers, namely the FSP 920, FLS 920 and FLS 980 from *Edinburgh Instruments*. All these three spectrofluorometers offered spectrally corrected excitation and emission spectra, which are traceable to the spectral radiance or spectral photon radiance scale.[366,367] In general, luminescence emission spectra obtained excited with a continuous wave (cw) light excitation source, while lifetime measurements require a pulsed excitation light source with suitable frequency and an optimal detection mode, which depend on the luminescence delay time of the luminophores. Based on the general construction of a luminescence spectrometer (Section 2.5.2, **Figure 18**), these spectrofluorometers were equipped with different excitation light sources and detectors.

The FSP 920 fluorescence spectrometer consists of two light sources from the instrument manufacture (Xe900 continuous xenon lamp, µF920 microsecond flashlamp), double monochromators in the excitation and emission channels, respectively, for improving the

signal-to-noise ratio, sample chamber, multi-channel scaling (MCS) for recording luminescence decays in the time range between microseconds and seconds, single photon counting photomultiplier tube (PMT) as a detector, and a dedicated PC loaded with a spectrometer operating software F900.[368] The luminescence decays were analyzed by fitting the obtained decay curves mono-exponentially with the program FAST (Fluorescence Analysis Software Technology, *Edinburgh Instruments*). Depending on the spectral detection range, three detectors (*Hamamatsu Photonics*) are available, including a Vis-detector R928P (200 – 850nm), a MID-detector R2658P (200 – 1050 nm) and a NIR-detector R5509P (700 – 1700 nm), which requires a 2-h cooling period with liquid nitrogen prior to use. Upon the sample properties, polarizers can be used in the excitation and emission channels, respectively.

In comparison to the FSP 920, the FLS 920 spectrometer is favored for measurements of luminescent materials with shorter lifetimes, typically in the time range from picoseconds to nanoseconds. The FLS 920 is equipped with three types of light sources, including a continuous xenon lamp (Xe900), a SuperK FIANIUM supercontinuum laser SC400-2-PP (400 – 2500 nm, 0.5 MHz – 2.0 MHz, *NKT Photonics*), a ca. 6-W 532 nm laser diode, and EPLED lasers (*Edinburgh Instruments*) with different wavelength (250 nm, 280 nm, 330 nm, 375 nm, 485 nm, and 510 nm) and tunable repetition rate. Moreover, the FLS 920 is equipped with two detectors, namely a microchannel plate (MCP)-PMT detector R38090U-50 (200 – 850nm, *Hamamatsu Photonics*) and a MID-detector R2658P for different measurement requirements.

The calibrated photoluminescence FLS 980 spectrometer is used for upconversion luminescence measurements. This instrument is equipped with various laser diodes as light sources, such as a ca. 8-W 976-nm laser diode (*Roithner Lasertechnik GmbH*, Austria), which can be adjusted to a continuous wave (cw) or a pulsed mode. Different detectors are installed in this spectrometer, including a standard detector R928P (for Vis-range), a MID-detector R2658P in the side window and NIR-photomultiplier tubes (NIR-PMTs) up to a spectral limit of ~1700 nm.[369] Lifetime measurements in the time range of microseconds to seconds can be completed in a multi-channel scaling (MCS) mode.

According to the optical properties of the samples and the research purposes, photoluminescence measurements of emission spectra and lifetimes are classified in the following specific parts:

Samples containing [Cr(ddpd)$_2$]$^{3+}$ complexes

Luminescence emission spectra were recorded on the calibrated spectrofluorometer FSP 920 spectrofluorometer. For the measurement of the spectrally corrected emission spectra, a continuous xenon lamp and a MID-detector (R2658P PMT) were employed. Luminescence decay curves were obtained from the spectrofluorometer FSP 920 using a μs xenon flashlamp (100 Hz or 50 Hz) and multi-channel scaling mode. All luminescence measurements with FSP 920 were carried out using magic angle condition (polarization 0° in the excitation and 54.7° in the emission channel). The obtained luminescence decays were fitted exponentially with the program FAST. Luminescence emission spectra in the NIR-range (*e.g.* singlet oxygen at ca. 1270 nm) were obtained on the calibrated FSP 920 with a NIR-detector (R5509P PMT) cooled by fluid nitrogen. Measurements of luminescent PSNPs containing [Cr(ddpd)$_2$]$^{3+}$ were performed with aqueous particle dispersions with particle concentrations of 1 mg/mL in 10 mm × 10 mm quartz cuvettes (*Hellma Analytics*). All luminescence measurements were carried out at room temperature if not otherwise stated. Excitation wavelengths were typically set to 435 or 440 nm, respectively. A 455 nm long pass filter was applied between the sample and the detector to exclude second order radiation from the excitation source.

Cr-Ln Salts (solid state)

For upconversion (UC) luminescence measurements of the solid Cr-Ln salts (Ln = Yb, Lu), the calibrated spectrofluorometer FLS 980 was used. The FLS 980 spectrofluorometer is equipped with a ca. 8-W 976-nm laser diode, which can be used in a continuous wave (cw) or pulsed mode. Upconversion lifetime measurements were performed with 976-nm laser excitation in a pulsed mode (100 Hz, pulse width ca. 200 μs) using the multi-channel scaling mode. A 645 nm long pass filter was applied to exclude the second order emission from the laser at 490 nm. It needs to be mentioned that the residual irradiation stemming from the 976 nm laser was observed in the UC emission spectra. This spectral component from the laser was so strong that a short pass filter of 842 nm placed in front of the detector could not completely exclude the laser signal. Hence, decomposition of the spectra was afforded to remove the baseline from laser by using a Gaussian function.

Pt(II)- and Pd(II) complexes in solution and in PSNPs

Luminescence spectra and decay kinetics of this sample series were measured with the calibrated spectrofluorometers FSP 920 and FLS 920. For the measurement of the emission spectra, a continuous xenon lamp was applied as an excitation light source on FSP 920 and FLS 920, while the time-resolved luminescence measurements were completed with a µs xenon flashlamp on FSP 920 with detection in a multi-channel scaling mode and an EPLED laser (375 nm) on FLS 920. The luminescence decays were analyzed by fitting the obtained decay curves exponentially with the program FAST. All luminescence measurements were performed in the long neck quartz cuvettes with a precision seal rubber septa at room temperature if not otherwise stated.

MOF samples

Triplet-triplet annihilation upconversion luminescence (TTA-UCL) spectra of the MOF samples were recorded with the spectrometer FLS 920 equipped with a 532 nm cw laser (5.9 mW). A 495 nm short pass filter was placed between the laser source and the sample holder to avoid direct excitation of the annihilator. Two 532 nm notch filters were placed between the sample holder and the detector to suppress the excitation signal observed on the detector, when complete emission spectra in the range of 400– 850 nm were measured. For excitation power dependent TTA-UC measurements, the laser power was varied with a tunable OD filter.

Luminescence decay of the annihilator under direct excitation of 410 nm at 9.7 MHz was obtained from the FLS 920, in this case using a supercontinuum laser as the excitation source and a microchannel plate photomultiplier tube (MCP-PMT; R3809U50). The luminescence decay of the sensitizer in the MOF sample was determined from 524 nm excitation at 100 Hz on the spectrofluorometer FSP 920, using a µs xenon flashlamp and multi-channel scaling mode. For time-resolved measurements at excitation power densities above the saturation threshold an inverted confocal laser scanning microscope was also used. A semi-apochromat water immersion objective with a large working distance (60X, NA 1.0 by *Olympus*) focused the excitation light onto a very small spot of the sample through the glass encapsulation, while working under continuous argon flow. Measurement of the decay kinetics of the sample was done by time correlated single photon counting (TCSPC) of the emission signal employing a single photon sensitive avalanche photodiode (SPADs, from *MPD*) for detection. Decay

measurements of the annihilator were carried out under direct excitation at 405 nm using a fixed wavelength diode laser pulsed at 5 MHz and a dichroic mirror (435 nm long pass) to suppress the contribution of the excitation light. Excitation for TTA-UC decay measurements was carried out with a supercontinuum laser (*PicoQuant Solea*) set at an emission wavelength of 524 nm. Pulsed excitation was realized by mechanical modulation of the emission signal with a chopper wheel set at a frequency of 100 Hz. For TTA-UC decay measurements (440 nm) a dichroic mirror (500 nm short pass) and an additional short pass filter (500 nm) were used, while for the measurement of the MOF sensitizer decay at 690 nm (in the absence of the annihilator), a dichroic mirror (600 nm long pass) and an additional long pass filter (650 nm) have been used to minimize the background signal by suppressing contributions from the excitation light and other emission bands.

3.7.4 Luminescence Quantum Yield

Luminescence quantum yields can be determined either absolutely or relatively. In this thesis, absolute luminescence quantum yields were determined by a commercial integrating sphere setup Quantaurus-QY C11347-11 from *Hamamatsu*[370]. For luminescent samples in solution or particle suspension, measurements of quantum yields were carried out with special long neck quartz cuvettes from the instrument manufacturer (10 x 10 mm, neck length of 10 cm, **Figure 24 a**). For solid-state samples, miniaturized Petri dishes made from quartz from the instrument manufacturer were used. In some special cases, such as the determination of singlet oxygen quantum yields, a relative method was applied with a suitable reference dye with known quantum yield (Section 2.5.2).

3.8 Stern-Volmer Studies

Stern-Volmer studies were carried out by measuring the luminescence response (emission intensity and lifetime) of the liquid-phase samples to oxygen at different concentrations. The general procedure was done by following the measuring order: oxygen concentration determination of the sample – luminescence emission spectra and lifetimes measurements – control of the oxygen concentration in the sample again. The oxygen concentration was taken from the average value of the oxygen concentrations before and after the luminescence measurements cycle to minimize the effect of oxygen diffusion. The sample solutions were

sealed in an airtight long neck quartz cuvette bearing a septum cap and purged with argon for ca. 30 min to exclude dissolved oxygen. Followed by the luminescence measurements, the cap was removed for a few seconds to allow air oxygen to diffuse in the cuvette. Subsequently, the cuvette was sealed again and shaken for ca. 1 min to reach a homogeneous distribution of the dissolved oxygen. Typically, oxygen concentrations were varied in the form of partial pressure pO_2 from nearly 0 hPa to ca. 200 hPa. The determination of the oxygen partial pressure pO_2 in solution was done with a commercial fiber-optic oxygen meter Firesting O_2 from *PyroScience* and a solvent-resistant oxygen probe tip (OXSOLVPT) from the manufacturer. The luminescence responses in emission intensity and lifetime were then plotted as a function of pO_2 according to **Eq. 2** or **Eq. 3** (Section 2.4.2).

3.9 Excitation-Power Density Determination

The dependence of the luminescence on excitation power density can provide an insight into the multi-photon involved kinetic processes between/in luminophores, which are particularly favorable for photon upconversion studies. The luminescence dependence on excitation-power density was studied for two different UC systems in the solid state, namely the intramolecular UC in the Ln-Cr salts and the TTA-UC in the MOF system.

In general, these studies were carried out by measuring the UC luminescence intensity under different excitation-power density. The excitation-power density was calculated from the excitation-power divided by the laser spot size on the sample. The excitation-power of the laser, which can be varied by adjusting the current of the laser, was characterized with a power meter (*Newport* 841-PE Powermeter) at the sample position. In both studied UC systems, the solid-state samples were sealed between two glass slides and measured in a sealed cuvette (4 x 10 mm). Thus, the reflections of excitation source must be considered. The excitation- power losses caused by reflections on the glass/quartz surfaces was determined to be ca. 11 % by carrying out five separate measurements at different laser excitation-powers. Determination of the laser spot size was achieved by a digital microscope (magnification 20-200, 2 megapixels, *RS PRO*), which was previously calibrated with a standard calibration target (R1DS1N, USAF 1951 pattern, *Thorlabs*). The generated images were then processed by using the program ImageJ.

4 Results and Discussion

According to the different types of the involved transition metal complexes (TMCs), the results of this thesis will be presented and discussed in three sections. Firstly, a series of studies of the $[Cr(ddpd)_2]^{3+}$ complex and its derivatives will be given, including the fundamental photophysical studies of the effects of ligands, solvents, and counter anions on their optical properties, a proof-of-concept study of molecular upconversion system, and an application example by developing multianalyte nanosensors. Subsequently, a series of novel Pt(II)/Pd(II) complexes will be introduced, with the focus on their aggregation-controlled luminescence behaviors in polymeric nanoparticles and the promising application as self-referenced oxygen nanosensors. Finally, a photophysical study of a triplet-triplet annihilation upconversion (TTA-UC) process will be demonstrated, which involves another Pd(II) complex as the photosensitizer in a matrix of metal-organic framework (MOF).

4.1 Optical Characterization and Applications of Cr(III) complex

Introduction of the $[Cr(ddpd)_2]^{3+}$ complexes

Photoactive transition metal complexes (TMCs) are receiving increasing interest based on their promising photophysical and photochemical properties in the fields of light-harvesting in solar cells, electronic devices, photocatalysis, clinical treatments (*e.g.* photodynamic therapy) and biomedical diagnostics as well as bioimaging and biosensing.[47,48,371] However, to date the mostly used luminescent TMCs are based on precious or rare-earth metals, such as platinum, ruthenium, iridium, or lanthanides. The emerging interest in developing eco-friendly alternatives has motivated scientists to explore the TMCs made of earth-abundant metals, such as chromium, copper, and molybdenum. These TMCs show comparable or even more attractive luminescence properties in comparison with those based on expensive metals, providing enormous potential for eco-friendly applications.

Among the TMCs based on earth-abundant metals, typical examples are the previously mentioned chromium (III) complexes bearing two tridentate ligands ddpd (N, N ′-dimethyl-N, N ′-dipyridine-2-ylpyridine-2,6-diamine). In the octahedral Cr(III) complex (**Figure 25**, left), the two ddpd ligands with large N-Cr-N bite angle serve as σ-donors to the d-orbitals of the

metal. The strong σ-donating capabilities of the ligands lead to large ligand-field splitting of their molecular orbitals, pushing the deactivating and photoreactive $^4T_2$ state far above the emissive ^2E state (**Figure 25**, right). Upon photoexcitation at ca. 435 nm, mixed MC/LMCT transitions occur and lead to the population of the high energetic $^4T_2$. Via intersystem crossing and non-radiative relaxations (including internal conversion and vibrational relaxation), the emissive triplet $^2T_1/^2E$ state is populated, generating intense phosphorescence in the NIR-range (λ_{em} = 738/775 nm) featuring an exceptionally high quantum yield of 0.11 and a lifetime of 898 µs in deaerated water at room temperature due to the prevented back-intersystem crossing.[57]
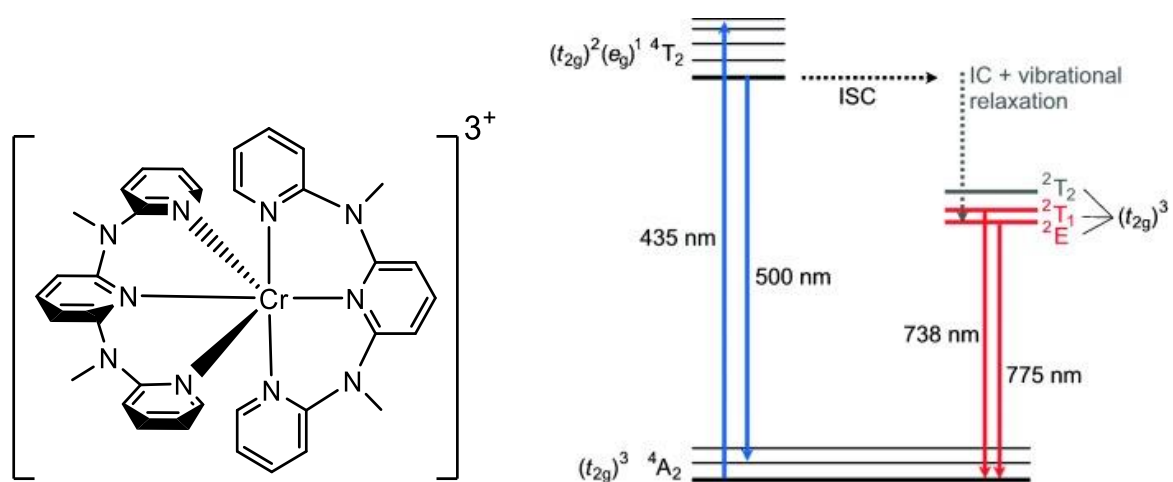
Figure 25: Molecular structure of the octahedral [Cr(ddpd)$_2$]$^{3+}$ complex (left); Jablonski diagram of [Cr(ddpd)$_2$]$^{3+}$ complex constructed from experimental solution data ($^2T_2$ state tentatively from single-crystal absorption) (right). ISC=intersystem crossing, IC=internal conversion (taken with permission from Ref.[57], Copyright © 2015 WILEY-VCH Verlag GmbH & Co. KGaA, Weinheim).

The major part of this thesis focuses on the [Cr(ddpd)$_2$]$^{3+}$ complex and its derivatives. This consists of photoluminescence studies of the complexes in terms of the effects of ligand deuteration and counter anions, photophysical studies of molecular energy upconversion and the design and applications of nanosensors based on these Cr(III) complexes.

4.1.1 Ligand deuteration effect on optical properties of [Cr(ddpd)$_2$]$^{3+}$ complex

Introduction

For the design of highly luminescent and long-lived TMCs, detrimental ligand field excited states should be either absent (d^0 and d^{10} electron configuration) or successfully shifted to high-enough energy to make sure that these states are not populated for a sufficiently long

time and thus lead to non-radiative deactivation.[372] Under this specific consideration, the [Cr(ddpd)$_2$]$^{3+}$ complex displays high photostability with a high-energetic $^4T_2$ ligand-field state (**Figure 26**, center), where substitution reactions (k_{chem}; **Figure 26**, center) are prevented as back-intersystem crossing (BISC) from the nested doublet states to the $^4T_2$ state is thermodynamically suppressed (k_{BISC}; **Figure 26**, center).[57,373] Electronic energy transfer (k_{EnT}; **Figure 26**, center) from the excited state can be excluded by the removal of phosphorescence quenchers, such as $^3O_2$.[310]

Potential energy surface crossing[374] usually leads to excited state distortion favoring non-radiative relaxation to the ground state, which is commonly observed in many copper(I)[375] complexes, some chromium(III),[376] and ruthenium(II) complexes.[377] For instance, the [Cr(sen)]$^{3+}$ (sen=4,4',4''-ethylidynetris(3 azabutan-1-amine) complex has different relaxed geometries due to the reduced quartet–doublet energy gap caused by trigonal distortion. Therefore, efficient excited state relaxation yields the doublet excited state with the quartet ground state (k_{trig}; **Figure 26**, right).[376] Thermally enabled twisting distortion also leads to a short-lived excited state, such as the cage complex [Cr(sar)]$^{3+}$ (sar = sarcophagine) featuring a lifetime <10 ns as compared to [Cr(*fac*-Me$_5$-D_{3h}tricosaneN$_6$)]$^{3+}$ with a lifetime of 235 μs in aqueous solution at room temperature.[378] However, both trigonal distortion caused by potential energy surface crossing and thermally induced twisting distortions barely contribute to the non-radiative depopulation of the [Cr(ddpd)$_2$]$^{3+}$ complex.
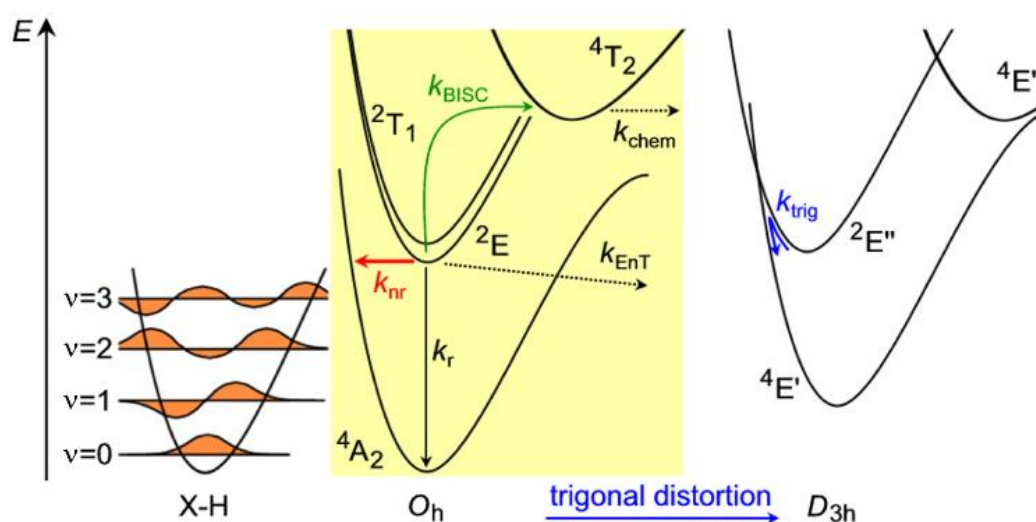
Figure 26: Center: Schematic illustration of the decay pathways of electronically excited Cr(III) complexes (radiative decay k_r; back-ISC k_{BISC}; chemical reaction k_{chem}; electronic energy transfer k_{EnT}). Left: Non-radiative decay via electronic-to-vibrational energy transfer to high-energy XH oscillators (k_{nr}). Right: Potential energy surface crossing in trigonally distorted complexes (k_{trig}) (taken with permission from Ref.[379], Copyright © 2018 Wiley‐VCH Verlag GmbH & Co. KGaA, Weinheim).

Consequently, the k_{BISC} and the k_{chem} are impeded by the high-energetic $^4T_2$ ligand-field state, while electronic energy transfer k_{EnT} can be excluded in the absence of oxygen. Without the influence of the trigonal distortion (k_{trig}) followed by potential energy surface crossing, k_{nr} is considered as the sole substantive contributor to the non-radiative depopulation of the $[Cr(ddpd)_2]^{3+}$ complex. In terms of non-radiative decay k_{nr}, an important contribution is assigned to the vibrational coupling with the environment, which usually leads to the electronic-to-vibrational energy transfer to overtones of high-energetic oscillators, such as OH, NH, or CH (**Figure 26**, left).[128,380] This phenomenon is also typically observed for luminescent materials containing lanthanides.[381] For instance, ligand deuteration of Yb(III) complexes was reported to significantly improve the luminescence quantum yield.[382] Also for Yb/Er upconversion nanoparticles, the decrease of k_{nr} can also be achieved by removing high-energy XH oscillators by applying deuterated solvents.[383]

Sample Preparation and Measurements Results

To have a deeper insight into the deuteration effect on the luminescence properties of the $[Cr(ddpd)_2]^{3+}$ complex, a series of ligand-deuterated derivatives was prepared and optically characterized in different solvents and their deuterated analogues. For this purpose, the ligand of the Cr(III) complex was deuterated statistically ([D_9]-ddpd with approximately 53 % average deuterium incorporation at different positions) and selectively ([D_6]-ddpd on the methyl groups and [D_{14}]-ddpd on the methyl groups and the terminal pyridines). These complexes were prepared as tetrafluoroborate salts according to established procedures,[57] yielding $[Cr([D_9]\text{-}ddpd)_2][BF_4]_3$ (**Cr(D$_9$)BF$_4$**), $[Cr([D_6]\text{-}ddpd)_2][BF_4]_3$ (**Cr(D$_6$)BF$_4$**) and $[Cr([D_{14}]\text{-}ddpd)_2][BF_4]_3$ (**Cr(D$_{14}$)BF$_4$**). The molecular structures of the selectively and unselectively deuterated ddpd ligand are given in **Figure 27**. Their vibrational signatures were derived from IR spectra measured in KBr disks at different temperatures, indicating the expected C-(H/D) stretching modes of each complex. ESI mass spectrometry and ^1H NMR spectra supported the structural analysis of the prepared complexes.[379]
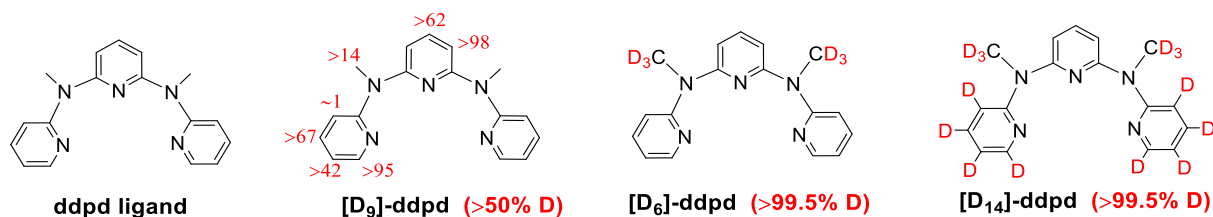
Figure 27: Molecular structures of the deuterated ddpd ligands (adapted with permission from Ref.[379], Copyright © 2018 Wiley‑VCH Verlag GmbH & Co. KGaA, Weinheim).

The deuteration effect was determined by measuring the luminescence emission spectra, quantum yields Φ, and lifetimes τ (mono-exponentially fitted) of the Cr(III) complexes in deuterated and non-deuterated solvents with air-saturation and under oxygen exclusion. The measured Φ and τ values as well as the Ar:air ratios and D:H factors with respect to ligand and solvent, respectively, are summarized in **Table 4**. It needs to be mentioned that complex **Cr(D$_{14}$)BF$_4$** contained traces of residual chloride ions which could not be removed due to the limited amount of the material. These chloride ions have in water no effect on the photophysical properties of the complex, while in CH_3CN they allow strong ion pairing which results in self-quenching.[384] Such effects were also reported for $[Cr(bpy^R)_3]^{3+}$ and $[Cr(phen^R)_3]^{3+}$ complexes with reduced ^2E lifetime.[384] Thus, the quantum yield and lifetime data obtained for **Cr(D$_{14}$)BF$_4$** in CH_3CN and CD_3CN will not be discussed here.

Solvent	CrBF$_4$ (prototype)		Cr(D$_9$)BF$_4$* (unselective)		Cr(D$_6$)BF$_4$* (selective)		Cr(D$_{14}$)BF$_4$* (selective)	
	Φ [%]	τ [µs]	Φ [%]	τ [µs]	Φ [%]	τ [µs]	Φ [%]	τ [µs]
H$_2$O (air)	2.1	177	3.1 (1.5)	190 (1.1)	2.0 (1.0)	180 (1.0)	2.4 (1.1)	190 (1.1)
H$_2$O (Ar)	11.0	898	12.4 (1.1)	1300 (1.4)	9.0 (0.8)	870 (1.0)	11.5 (1.0)	1200 (1.3)
Ratio (Ar:air)	5.2	5.1	4	6.8	4.5	4.8	4.8	6.3
D$_2$O (air)	2.0	150	2.5 (1.3)	190 (1.3)	2.2 (1.1)	160 (1.1)	2.1 (1.0)	170 (1.1)
D$_2$O (Ar)	14.2	1164	22.4 (1.6)	1700 (1.5)	14.1 (1.0)	1200 (1.0)	21.6 (1.5)	2100 (1.8)
Ratio (Ar:air)	7.1	7.8	9.0	8.9	6.4	7.5	10.3	12.4
D$_2$O/H$_2$O (Ar)	1.3	1.3	1.8	1.3	1.6	1.4	1.9	1.7
CH$_3$CN (air)	0.6	44	0.7 (1.2)	28 (0.6)	0.6 (1.0)	28 (0.7)	-	-
CH$_3$CN (Ar)	12.1	899	22.0 (1.8)	1800 (2.0)	12.4 (1.0)	910 (1.0)	-	-
Ratio (Ar:air)	20.2	20.4	31.4	64.3	20.7	32.5	-	-
CD$_3$CN (air)	0.6	24	0.6 (1.0)	48 (2.0)	0.6 (1.0)	34 (1.4)	-	-
CD$_3$CN (Ar)	11.7	810	30.1 (2.6)	2300 (2.8)	14.4 (1.2)	1000 (1.2)	-	-
Ratio (Ar:air)	19.5	33.8	50.2	47.9	24.0	29.4	-	-
CD$_3$CN/ CH$_3$CN (Ar)	1.0	0.9	1.4	1.3	1.2	1.1	-	-

Table 4: Summary of the luminescence quantum yield Φ and lifetime τ of the deuterated Cr(III) complexes in different solvents at 295 K ($\lambda_{exc.}$ = 435 nm, $\lambda_{em.}$ = 778/780 nm). *: The ratio of luminescence quantum yield and lifetime with respect to **CrBF$_4$** is given in parenthesis (D:H factor). Uncertainty of the measured Φ, and τ is estimated to be 5 % and 10%, respectively (adapted with permission from Ref.[379], Copyright © 2018 Wiley‒VCH Verlag GmbH & Co. KGaA, Weinheim).

Optical Response to Oxygen in Different Solvent

Apparently, oxygen strongly quenches the phosphorescence of the Cr(III) complexes, which is attributed to a triplet-triplet energy transfer process as described in Section 2.4.3. Since the photoluminescence quenching by oxygen is a diffusion-controlled process following the classical Stern-Volmer relationship, the quenching efficiency varies in different solvents due to the solvent-relevant diffusion constant (**Eq. 5**, Section 2.4.2). Additionally, at room temperature oxygen has a much lower solubility in water (1.0 mM)[385] than in organic solvents,

such as CH_3CN (8.1 mM).[386] Thus, the luminescence emission intensity I, quantum yield Φ, and lifetime τ differ strongly in terms of their Ar:air ratio in different solvents such as H_2O and CH_3CN (**Table 4**, yellow marked values). An example is illustrated in **Figure 28**, providing an overview of the Ar:air ratio in the emission intensity I and lifetime τ of complex **Cr(D$_9$)BF$_4$** in H_2O and CH_3CN. Notably, in CH_3CN the Ar:air ratio reaches up to ca. 65 in both intensity and lifetime domains, which is about 10 times higher than the values (ca. 6) in H_2O. Such an optical sensitivity to oxygen exceeds far the classic $[Cr(bpy)_3]^{3+}$ complex with the Ar:air ratio of 1.8 and 1.5 in CH_3CN and H_2O, respectively.[387]
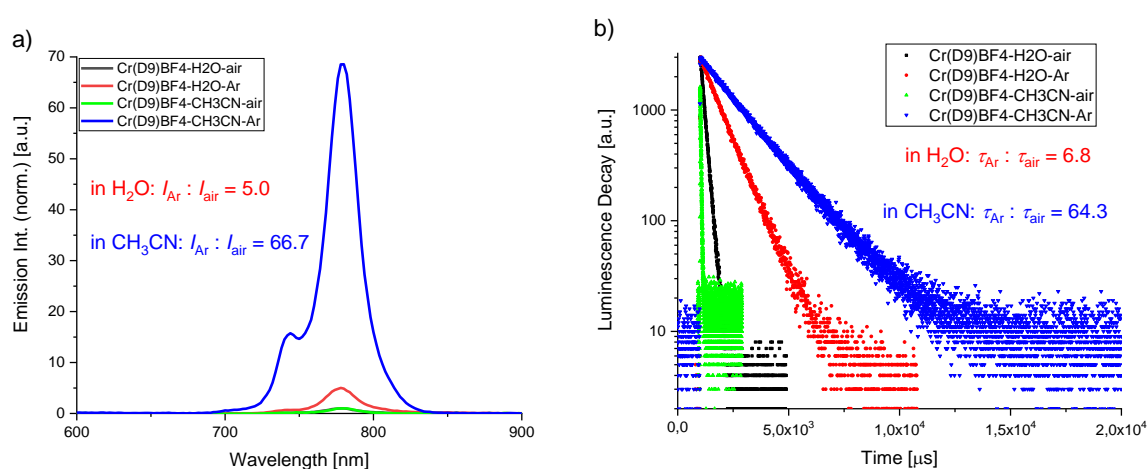
Figure 28: Luminescence emission spectra (a) and decays (b) of complex **Cr(D$_9$)BF$_4$** dissolved in H_2O and CH_3CN under air and Ar saturation ($\lambda_{exc.}$ = 435 nm, $\lambda_{em.}$ = 778/780 nm). Emission spectra under air saturation are normalized in both solvents for comparison.

Ligand Deuteration Effect on Luminescence Properties

In the presence of oxygen, solvent or ligand deuteration have only weak effect on the luminescence quantum yields (ca. 1 – 3 %) and lifetimes (**Table 4**). This is because the energy transfer from the excited Cr(III) complexes to oxygen (k_{EnT}) dominates over the electronic-to-vibrational energy transfer (k_{nr}) under air saturation. However, in the absence of oxygen, non-radiative energy transfer to the C–H vibrations of the ligand plays a major role on the Φ and τ values. Yet the C–H oscillators provide different contribution to the k_{nr}, depending on their position on the ligand. The complex **Cr(D$_6$)BF$_4$,** which features selective deuteration on the methyl groups in the outer coordination sphere, exhibits similar Φ and τ values as the

prototype complex **CrBF$_4$**. This negligible contribution results from the rather longer Cr⋯H distance of 4.8 – 5.3 Å according to the DFT calculation (**Figure 29**).[57]
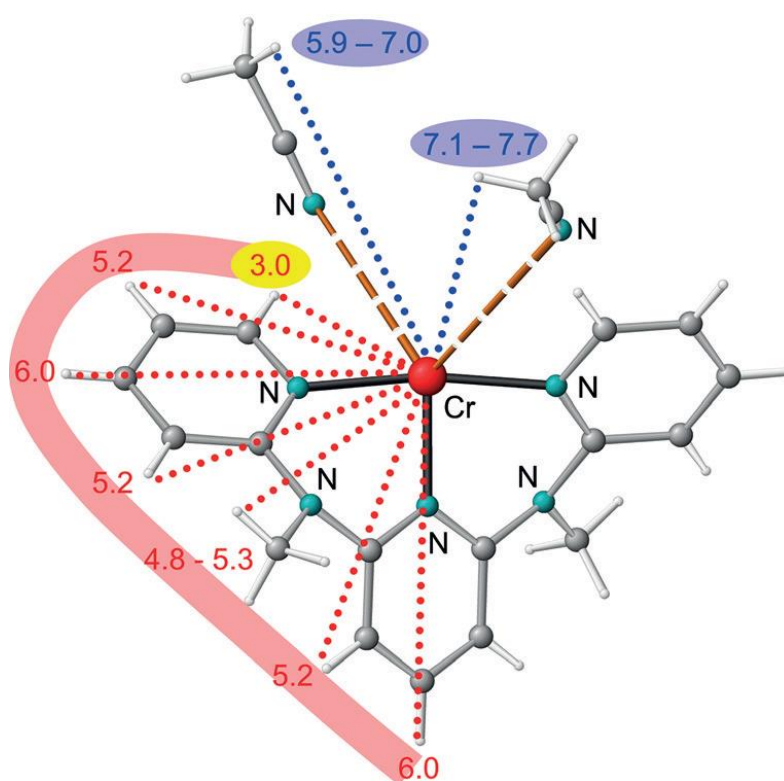
Figure 29: Cr⋯H distances to the ddpd ligand of **CrBF$_4$** as determined by a DFT calculation and to CH$_3$CN as estimated by single-crystal X-ray diffraction,[57] illustrating the first coordination sphere in red and the second coordination sphere in blue (one ddpd ligand omitted for clarity). Distances given in Å (taken with permission from Ref.[379], Copyright © 2018 Wiley-VCH Verlag GmbH & Co. KGaA, Weinheim)

In comparison with **CrBF$_4$** and **Cr(D$_6$)BF$_4$**, complexes **Cr(D$_9$)BF$_4$** and **Cr(D$_{14}$)BF$_4$** display significantly improved luminescence properties by ligand deuteration. Particularly, the complex **Cr(D$_9$)BF$_4$** shows the highest D:H enhancement factors in deaerated H$_2$O (1.4), D$_2$O (1.5), CH$_3$CN (2.0), and CD$_3$CN (2.8) with respect to lifetime (**Table 4**, values in parenthesis). Obviously, the aromatic C–H bonds of the pyridines contribute to a large extent to the deactivation of the excited state. This is mainly attributed by the shorter Cr⋯H distance of 3.0 Å according to the DFT models (**Figure 29**),[57] which fits well to the expected distance dependence ($k_{nr} \propto r_{CrH}^{-6}$)[388] of the non-radiative quenching efficiency. Therefore, deuteration of these C–H oscillators can suppress the non-radiative deactivation pathways of the excited state. This yields unprecedentedly high quantum yields and lifetimes for **Cr(D$_9$)BF$_4$** with Φ = 30.1 % and τ = 2.3 ms in CD$_3$CN under Ar, and for **Cr(D$_{14}$)BF$_4$** with Φ = 21.6 % and τ = 2.1 ms in O$_2$-free D$_2$O (**Table 4**). These luminescence enhancements by ligand deuteration are highly

promising in comparison with other examples in the literature, yielding more than one order of magnitude improvements of τ and Φ in some cases.[382,383,389,390] Hence, ligand deuteration at these privileged positions might serve as a promising strategy to enhance the luminescence properties of such spin-flip complexes under the condition that all other deactivation pathways (k_{EnT}, k_{BISC}, etc.) are already prohibited.

Solvent Deuteration Effect on Luminescence Properties

In addition to ligand deuteration, another deactivation pathway is the energy transfer to XH vibrations (X = C or O) of the solvent. The OH stretching vibrations result in D_2O:H_2O factors ranging from 1.3 to 1.9, while the CH oscillators of the solvent acetonitrile yield D:H factor of 0.9 – 1.4 (**Table 4**, values in green). Particularly, the complex **Cr(D$_{14}$)BF$_4$** exhibits the most pronounced luminescence enhancement upon deuteration of solvent OH oscillators by factors of 1.9 and 1.7 in terms of Φ and τ, respectively (**Table 4** and **Figure 30**). By comparing the D:H factors of OH- and CH-oscillators, it is noticeable that OH-oscillators are slightly favored as energy acceptors than CH-oscillators. This refers to a combined effect of the higher vibrational energy ($\tilde{v}_{OH}$ = $\approx$3400 cm^{-1} vs. $\tilde{v}_{CH}$ = $\approx$2900 cm^{-1}) and the crucially higher anharmonicity (x_{OH} = $\approx$90 cm^{-1} vs. x_{CH} = 60 cm^{-1})[391,392] of the OH-oscillators.

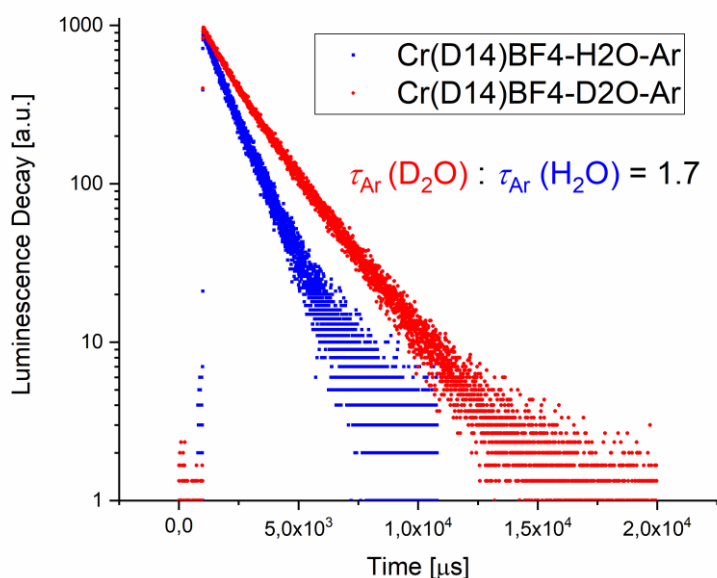**Figure 30**: Luminescence decays of complex Cr(D$_{14}$)BF$_4$ in D_2O and in H_2O under Ar saturation ($\lambda_{exc.}$ = 435 nm, $\lambda_{em.}$ = 778 nm).

Conclusion

In summary, the photoluminescence properties of a series of Cr(III) complexes are significantly enhanced by ligand and solvent deuteration. Especially, the complex **Cr(D$_9$)BF$_4$** shows a record luminescence quantum yield of 30 % and a luminescence lifetime of 2.3 ms for a 3d^n metal complexes (n < 10) in CD$_3$CN solution under Ar saturation at room temperature. Moreover, solvent deuteration shows that OH-oscillators contribute more strongly to the deactivation of the excited state than the CH-oscillators. Additionally, photophysical studies reveal much higher O$_2$-sensitivities of these complexes than the previously used Cr(III) complexes, which is promising for their application as optical oxygen sensors. These fundamental photophysical and deuteration studies provide on the one hand a closer insight into the deactivation pathways of spin-flip emitters. On the other hand, deuteration of such strong-field multidentate ligands at decisive positions can serve as a promising approach to design highly luminescent metal complexes based on earth-abundant metals, which will certainly lead to a plethora of eco-friendly applications in the future.

4.1.2 Counter anions effect on optical properties and oxygen sensitivity of [Cr(ddpd)$_2$]$^{3+}$ complexes

Introduction

In our previous studies, a series of NIR-emissive ruby-analogue [Cr(ddpd)$_2$]$^{3+}$ (ddpd = N,N'-dimethyl-N,N'-dipyridine-2ylpyridine-2,6-diamine) complexes were reported with record luminescence quantum yield (30%) and extremely long luminescence lifetimes (ms-range) in deuterated solution at room temperature.[57,318,379,393] In these studies, improvements of the photoluminescent properties of these Cr(III) complexes were mainly achieved by rational design of the ligand, *e.g.* introducing tridentate ddpd ligand with strong σ-donating capabilities to realize a large ligand-field splitting,[57,393] or deuterium incorporation at specific positions on the ligand to reduce deactivation pathways caused by the XH oscillators (X = C, O).[379] The emitted doublet phosphorescence (λ_{em} at 738 and 775 nm) of the [Cr(ddpd)$_2$]$^{3+}$ complex can be quenched by molecular oxygen via triplet-triplet energy transfer while yielding singlet oxygen, enabling the complex as photosensitizer for photodynamic therapy.[394]

Meanwhile, the ultra-high sensitivity to oxygen promises their application as optical O_2-indicators.[57,310,379]

It was found that bulky counter anions can affect the properties of TMCs in many aspects, especially the photophysical properties.[395-398] For instance, the luminescence quantum yield of the cationic iridium(III) complexes can be significantly improved by introducing bulky boracic anions, so that molecular aggregation and the thus resulting quenching pathways can be suppressed.[399] Yet most of these studies focus mainly on crystalline complexes, because the counter anions can have a stronger impact on the way of molecular packing in crystalline solids than in solution.

With this inspiration, a comparative study of the $[Cr(ddpd)_2]^{3+}$ complexes with various counter anions was carried out by exploring their photophysical properties in solution, in polymer matrix and as crystalline solids. Photophysical studies were completed by absorption spectroscopy, luminescence steady state and time-resolved spectroscopy, and quantum yield determination. In addition to the four Cr(III) complexes involved in the previous work, namely $[Cr(ddpd)_2]^{3+}$ with the anions Cl⁻ (**CrCl**), BF_4^- (**CrBF₄**), PF_6^- (**CrPF₆**), and tetrakis(phenyl)borate ($[BPh_4]^-$, complex **CrBPh₄**), which were prepared according to the literature,[57,379,400,401] one more bulky counter anion tetrakis[3,5-bis(trifluoromethyl)phenyl]borate ($[BArF_{24}]^-$, complex **CrBArF₂₄**) (**Figure 31**) was prepared via ion exchange (Section 3.2).[400]
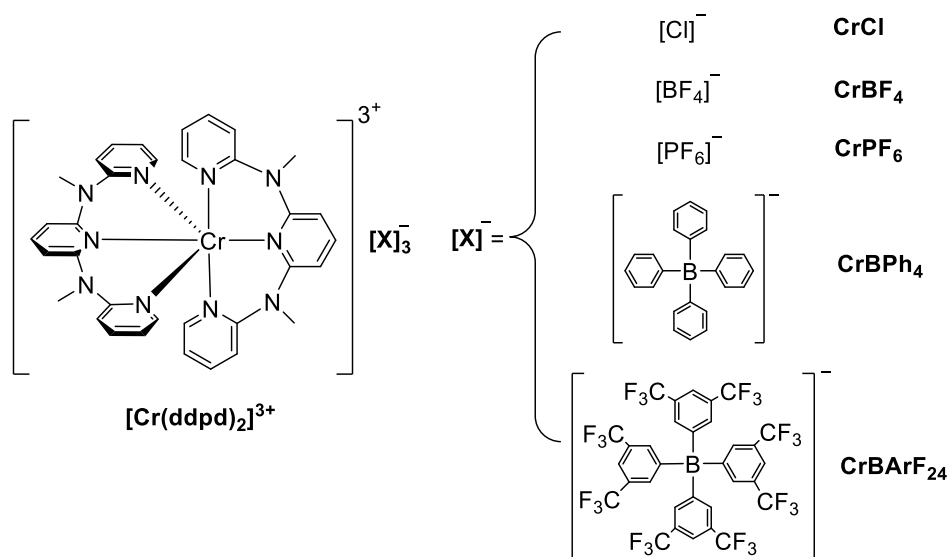
Figure 31: Molecular structures of $[Cr(ddpd)_2]^{3+}$ complexes with different counter anions.

These Cr(III) complexes were encapsulated into the 100 nm-sized aminated polystyrene nanoparticles (PSNPs) via one-step staining procedure[37,38,206] (Section 3.3 (i)) with the exception of complex **CrCl** due to its poor hydrophobicity. The resulting luminescent particles were subsequently coated with a thin silica-shell using the ammonia-catalyzed Stöber process (Section 3.3 (ii)) for preventing the complexes from leaking.[236,238,400] Moreover, the generated particles with silica-shell were immobilized in an oxygen-barrier film from polyvinyl alcohol (PVOH) (Section 3.3 (iii)). Furthermore, Stern-Volmer studies were carried out for all the complexes in CH_3CN solution. Additionally, the singlet oxygen quantum yields ($\Phi[^1O_2]$) of complexes **CrPF$_6$**, **CrBPh$_4$** and **CrBArF$_{24}$** in DMF solution were determined relatively with **CrBF$_4$** as the reference compound ($\Phi[^1O_2]$ = 0.61)[310] (Section 2.5.2 and 3.7.4).

Counter Anions Effect on Luminescence Properties

In CH_3CN solution, different counter anions have barely an influence on the absorption and luminescence emission spectra of these complexes (**Figure 32, a)**). The luminescence quantum yield Φ_{Ar}, however, is enhanced from Φ = 7.5% (**CrCl**) to 13.6% (**CrBArF$_{24}$**) with increasing size of the counter anions (**Figure 32 b), Table 5**). Meanwhile, the luminescence lifetime is also extended by a factor of ca. 2 by comparing **CrCl** (τ_{Ar} = 580 μs) and **CrBArF$_{24}$** (τ_{Ar} = 1100 μs). These improvements in Φ and τ are attributed to the steric effect of bulky counter anions, which can effectively inhibit the molecular aggregation and quenching caused by high concentration.[399]

Figure 32: Luminescence measurements of the Cr(III) complexes with different counter anions in CH_3CN: **a)** Absorption and emission spectra; **b)** Quantum yield (left y-axis, black squares) and fitted lifetime (right y-axis, red circles) obtained under air-saturation (full symbols) and argon-saturation (open symbols) (298 K, λ_{exc} = 435 nm).

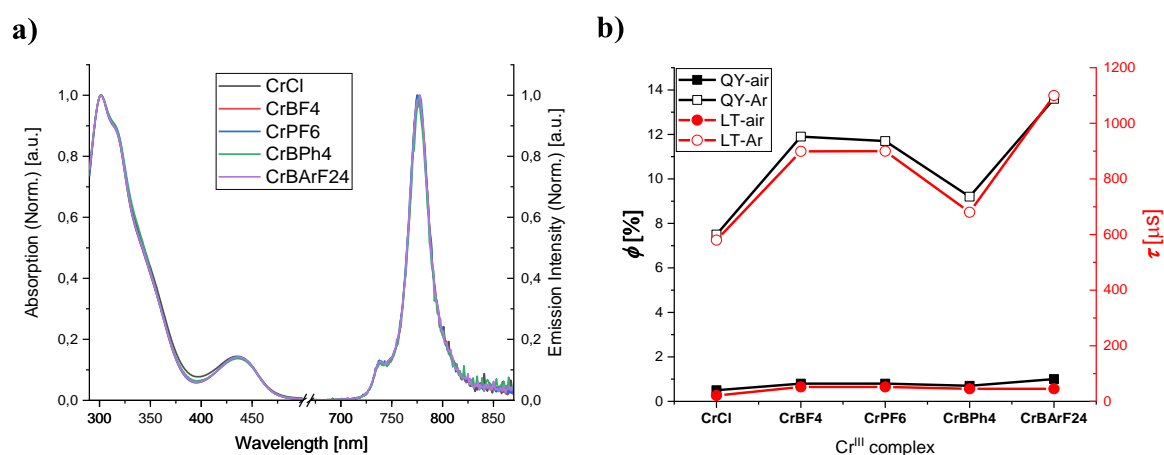The relative bulky salt **CrBPh₄** has a lower Φ and a shorter τ than the simplest boracic salt **CrBF₄** (**Figure 32 b)**), regardless with or without oxygen quenching. This is tentatively ascribed to the phenyl-rings on the [BPh₄]⁻ anion, which tend to form $\pi - \pi$ stacking interactions with rings on the complex ligands. Moreover, it is hypothesized that the CH groups of the [BPh₄]⁻ anions can approach the excited Cr(III) center much easier due to stacking effects, and thus induce additional multi-phonon relaxation pathways. This can explain the extremely low Φ_{air} of crystalline **CrBF₄** with only 0.7%, while crystalline **CrBF₄** shows a Φ_{air} of 10.9% (**Table 5**). By exchanging the [BPh₄]⁻ counter anions with a bulky fluoro-derivative [BArF₂₄]⁻, the resulting complex **CrBArF₂₄** displays significantly enhanced Φ and τ in CH₃CN solution (**Figure 32 b)**) and in the solid state (**Table 5**) due to the decreased molecular aggregation and relaxation pathways caused by anions.

	CrCl	**CrBF₄**	**CrPF₆**	**CrBPh₄**	**CrBArF₂₄**
In CH₃CN solution					
Φ_{air} [%]	0.5	0.8	0.8	0.7	1.0
Φ_{Ar} [%]	7.5	11.9	11.7	9.2	13.6
τ_{air} [µs]	21	52	52	45	45
τ_{Ar} [µs]	580	899	900	680	1100
Crystalline State					
Φ_{air} [%]	-	7.5	10.9	0.70	1.34
τ_{air} [µs]*	-	τ_{ave}: 336	τ_{ave}: 547	τ_{ave}: 281	τ_{ave}: 225
τ_{Ar} [µs]*	-	-	τ_{ave}: 823	τ_{ave}: 223	τ_{ave}: 920
In PSNPs					
Φ_{air} [%]	-	3.6	2.9	2.7	1.7
Φ_{Ar} [%]	-	10.0	10.3	6.4	14.4
τ_{air} [µs]*	-	277	241	254	τ_{ave}: 196
τ_{Ar} [µs]*	-	885	928	686	τ_{ave}: 1270
In PS-PVOH Film					
Φ_{air} [%]	-	11.7	15.2	11.3	13.4
τ_{air} [us]*	-	τ_{ave}: 893	τ_{ave}: 929	τ_{ave}: 929	τ_{ave}: 901

Table 5: Luminescence quantum yield and lifetime data summary of the Cr(III) complexes in CH₃CN, as crystalline, and in PSNPs under 435 nm excitation. *Lifetimes were fitted multi-exponentially; the averaged lifetimes τ_{ave} were calculated intensity weighted according to **Eq. 18**. Uncertainty of the measured Φ and τ is estimated to be 5 % and 10%, respectively.

To explore the effect of counter anions on the luminescence properties of the complexes in application-relevant polymer matrix, these Cr(III) complexes were encapsulated into PSNPs to

produce oxygen nanosensors except for complex **CrCl**. Similar to the CH_3CN solutions, the effect of bulky counter anions has a negligible effect on the shapes of the luminescence excitation and emission spectra (**Figure 33 a)**). Analogue changes in $\varPhi$ and τ were observed in PSNPs suspension with increasing effect of bulky counter anions as in the CH_3CN solutions (**Table 5**). As expected, these complexes present in the PSNPs higher $\varPhi$ and longer τ under air-saturation than in aqueous solution.[57,379] This is ascribed to the protection effect of the PSNPs, where molecular oxygen needs firstly to diffuse into the PSNPs and then quenches the emissive complexes. In the PSNPs, the complex **CrBArF24** shows a $\varPhi_{Ar}$ of 14.4 % and $\tau_{Ar,ave}$ of 1270 µs with an enhancement factor of 1.4 in comparison with the simplest boracic salt **CrBF4**. Interestingly, by sealing the complex-stained PSNPs in an oxygen-barrier PVOH film, the complexes **CrBF4, CrPF6, CrBPh4** and **CrBArF24** reach $\varPhi$ values of 11.7%, 15.2%, 11.3%, and 13.4%, respectively, even in air (**Table 5**), while basically leaving the luminescence excitation and emission spectra unchanged (**Figure 33 b)**). This strategy yields O_2-inert NIR-emitting films with a high photoluminescence quantum yield under illumination with blue (435 nm) light.

a)   **b)**
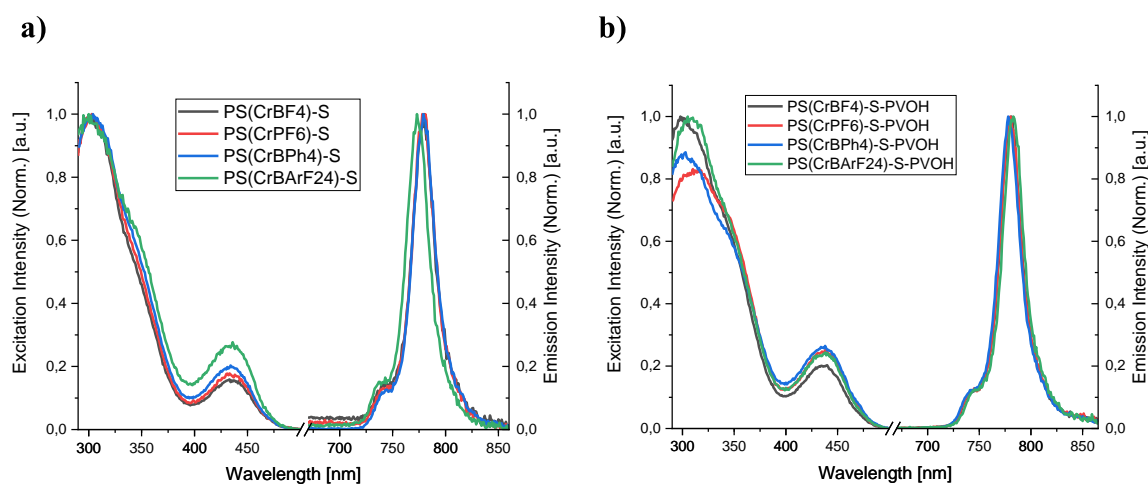
Figure 33: Luminescence excitation and emission spectra of PS(Cr)-S suspension (0.25 mg/mL) in water (a) and in PVOH film acting as an oxygen-barrier(air) (b) under 435 nm excitation.

Counter Anion Effect on Oxygen Sensitivity

To have a better insight into the counter anion influence on the dynamic phosphorescence quenching by molecular oxygen, Stern-Volmer studies were completed for all the $[Cr(ddpd)_2]^{3+}$ complexes in CH_3CN solution, based on the luminescence response in intensity and lifetime domains under different oxygen partial pressure (pO_2) (Section 3.8). An example of complex

CrBArF₂₄ is illustrated in **Figure 34**, showing the optical response in luminescence intensity and decay kinetics to oxygen partial pressure ranging from 0.3 hPa to 164.5 hPa.
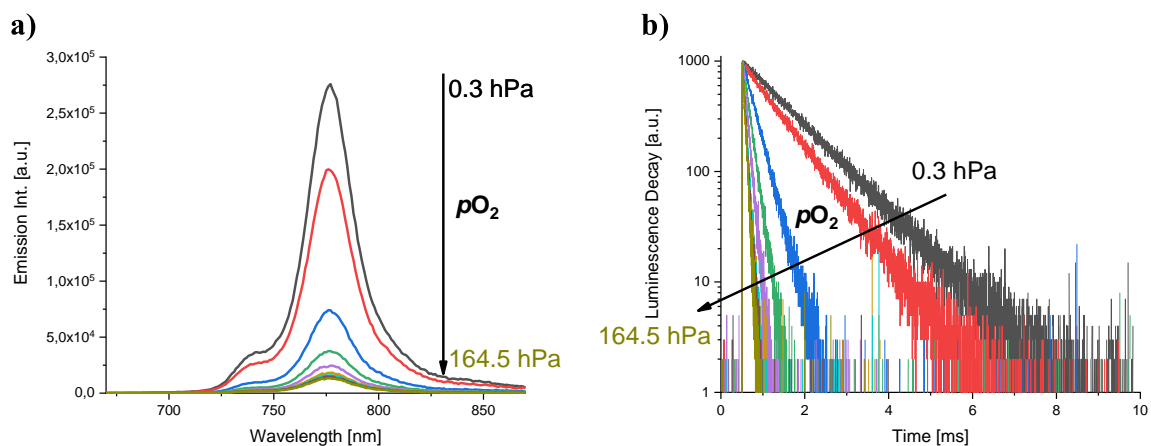
Figure 34: Luminescence response of complex **CrBArF₂₄** (CH₃CN solution) to oxygen in the intensity (a) and lifetime (b) domains ($\lambda_{exc.}$ = 435 nm, $\lambda_{em.}$ = 778 nm).

The optical response of all the Cr(III) complexes to oxygen follows a linear Stern-Volmer relationship according to **Eq. 2** and **Eq. 3**. The derived slope values, namely the Stern-Volmer constants K_{SV}, agree well from measurements in intensity and lifetime domains (**Table 6**), suggesting a typical dynamic quenching process. The linear Stern-Volmer plots based on luminescence emission intensity and lifetime are shown in **Figure 35**. As expected, the K_{SV} values show a clear tendency to increase for bulky anions due to the enhanced luminescence lifetimes in the absence of a quencher, with the exception of the complex **CrBPh₄**, which has a similar K_{SV} as the complex **CrBF₄**.
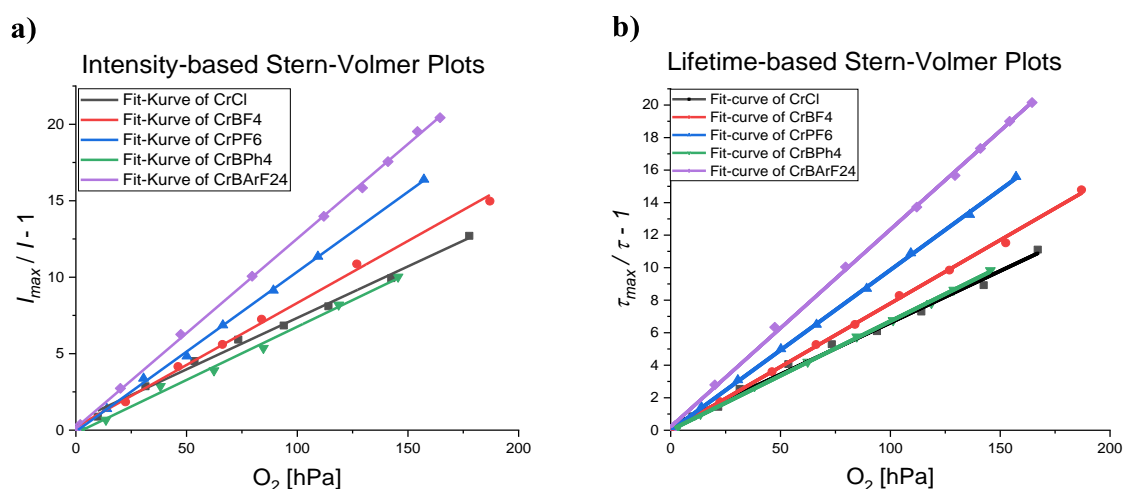
Figure 35: Luminescence emission intensity- and lifetime-based plots of the Cr(III) complexes in CH₃CN. Uncertainties are estimated to be 5%.

	CrCl	CrBF$_4$	CrPF$_6$	CrBPh$_4$	CrBArF$_{24}$
Intensity-based K_{SV} [hPa^{-1}]	0.06730	0.08107	0.10445	0.06959	0.12367
Lifetime-based K_{SV} [hPa^{-1}]	0.06361	0.07796	0.09863	0.06699	0.12134
Intensity-based K_q [hPa^{-1}s^{-1}]	172.56	117.49	116.05	133.83	112.43
Lifetime-based K_q [hPa^{-1}s^{-1}]	163.10	112.99	109.59	128.83	110.31

Table 6: Luminescence emission intensity- and lifetime-based K_{SV} and K_q values of the Cr(III) complexes in CH$_3$CN. Uncertainties are estimated to be 5%.

In contrast to the K_{SV} values, the corresponding quenching rate coefficients K_q ($K_q = K_{SV}/\tau_{max}$, **Eq. 4**) decrease from ca. 170 hPa^{-1}s^{-1} of **CrCl** to 110 hPa^{-1}s^{-1} of **CrBArF$_{24}$** with increasing bulkiness of the anions. In homogeneous solution, K_q is proportional to the mutual diffusion constant D of the luminophore and the quencher (**Eq. 5**).[292] In solution, the diffusion constant D of a molecule is inversely proportional to its hydrodynamic radius according to the Stokes–Einstein equation.[402] Hence, the complexes with increasingly bulky anions show a decreased K_q. The relatively determined $\Phi[^1O_2]$ decreases from 61% for **CrCl** to 51% for **CrBArF$_{24}$**, indicating the weakened oxygen quenching process by using bulky anions (**Figure 36**). Affected by possible π-π stacking between anions and ligands, the anion [BPh$_4$]$^-$ can lose its shielding effect from oxygen quenching and thus displays a relatively higher K_q of ca. 130 hPa^{-1}s^{-1}.

Figure 36: Absorption spectra (left) and singlet oxygen emission spectra (right) (λ_{exc} = 433 nm) of complexes **CrBF$_4$**, **CrPF$_6$**, **CrBPh$_4$** and **CrBArF$_{24}$** in DMF with the concentration of 0.05 mM (298 K, air).

Conclusion

In summary, the photoluminescence properties of the molecular ruby $[Cr(ddpd)_2]^{3+}$ can be improved by the choice of bulky counter anions. In CH_3CN solution, complex **CrBArF$_{24}$** reaches $\Ph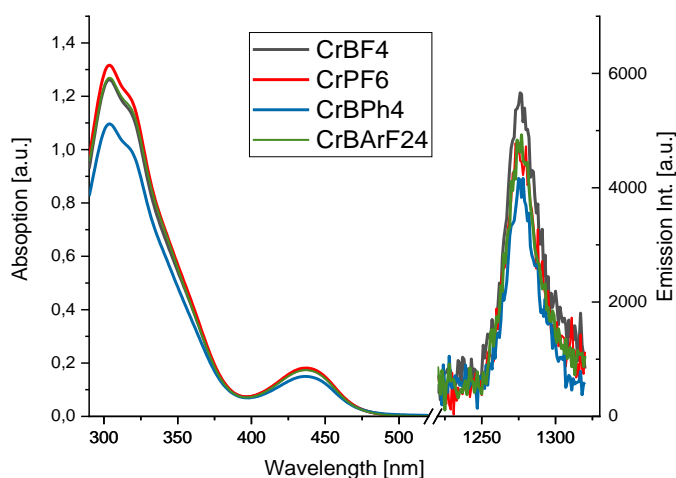i$ and τ of 13.6% and 1.1 ms, respectively, at room temperature, leading to an enhancement factor of ca. 1.8 in comparison with complex **CrCl**. Similar optical enhancements are also observed in polymer matrix PSNPs. This is contributed by the bulky anion effects, where molecular aggregation and non-radiative relaxation pathways are significantly reduced. Moreover, comparative Stern-Volmer studies show on the one hand that bulky anions can provide a shielding effect from oxygen quenching, yielding a reduced oxygen quenching rate coefficient. On the other hand, the Stern-Volmer constant exhibits a clear increase for bulky anions, suggesting an improved sensitivity which can be interesting for oxygen sensor applications. This fundamental photophysical study provides another design approach to improve the luminescence properties of cationic metal complexes with earth-abundant metals.

4.1.3 Study of excitation-power density dependent NIR to NIR upconversion luminescence in molecular chromium ytterbium salts

Introduction

Photon upconversion (UC) is an attractive energy transfer process for fundamental studies as well as for luminescence applications.[273] Such UC processes are mostly based on solid inorganic host matrices doped with metals, *e.g.* transition metal or lanthanoid cations.[267,403] Yet such UC systems were commonly found in bulk materials[267,404] or nanocrystalline systems.[267,405,406] Recent scientific advances have realized UC in molecular complex species.[407,408] Among them are metal chelate-organic chromophore combinations,[409] mononuclear metal complexes,[410] and heterooligometallic sensitizer–activator architectures.[411,412] Particularly, the latter performed high potential for efficient UC, either for energy transfer upconversion (ETU) or for cooperatively sensitized upconversion (CSU) (description of ETU and CSU can be found in Section 2.3.3). Both UC mechanisms require that the sensitizer (S) metal has appropriate energy levels and a sufficiently long luminescence lifetime, so that the activator (A) can be excited to an excited state with approximately twice the energy of the excited sensitizer state.

The most popular sensitizing metal centers include Yb^{3+} ($^2F_{5/2}$ at ≈ 10250 cm^{-1}, ≈ 976 nm) and Cr^{3+} (octahedral geometry: $^2E/^2T_1$ at $\approx 15000\text{-}12400$ cm^{-1}, $\approx 665\text{-}805$ nm depending on the ligand field). Both metal centers are promising sensitizers for molecular UC systems, typically in combination with lanthanoid activators, such as Er^{3+} and Tb^{3+}.[412-414] Two decades ago, Güdel *et al.* reported on UC luminescence in solid-state matrices, such as $Y_3Ga_5O_{12}$ co-doped with Yb^{3+} as a sensitizer and Cr^{3+} as an activator.[415,416] The corresponding UC scheme involves a CSU process (**Figure 37**). Photon excitation of the Yb^{3+} (980 nm) populates the $^2F_{5/2}$ state. Subsequently, cooperative energy transfer occurs from two excited Yb^{3+} to an excited quartet state of Cr^{3+} ($^4T_2/^4T_1$). Followed by intersystem crossing (ISC), the ^2E state of Cr^{3+} is populated, yielding an UC emission at 775 nm.
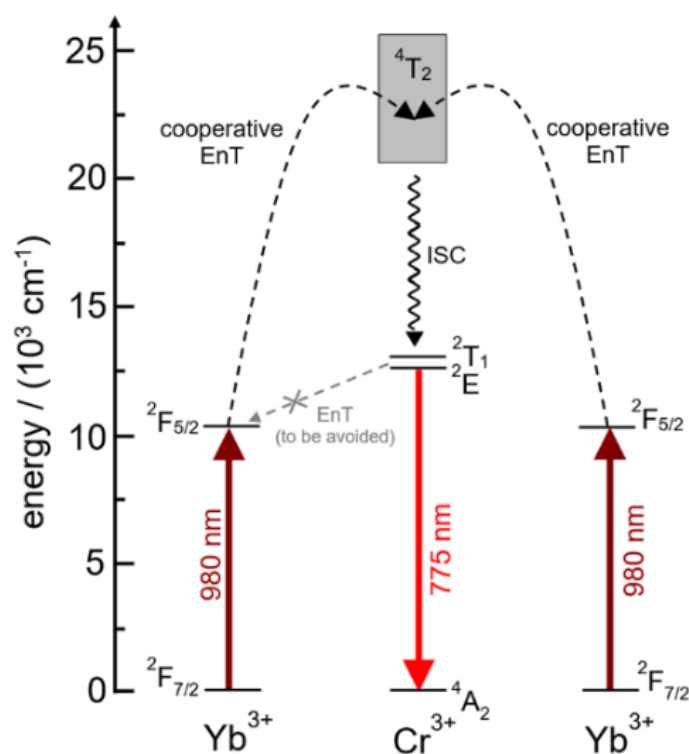
Figure 37: Schematic partial energy level diagram of the energy levels of Yb^{3+} and Cr^{3+} (energies given for *mer*-[Cr(ddpd)$_2$]$^{3+}$) relevant for cooperatively sensitized UC involving two Yb^{3+} centers absorbing 980 nm light sensitizing the emission of the Cr^{3+} activator (taken with permission from Ref.[417], Copyright © 2020 The Authors. Published by Wiley-VCH GmbH).

Such UC system is very attractive, as both excitation and emission are in the NIR region, which are particularly favored for bioimaging applications. However, this has been rarely realized in molecular systems. The few reported Cr^{3+}/Yb^{3+} UC molecular systems were investigated at low temperature (usually below 100 K) in extended solid inorganic matrices.[415,416] The main challenge is due to the unfavorably efficient downshifting energy transfer $^2E(Cr^{3+})\rightarrow{}^2F_{5/2}(Yb^{3+})$

that leads to deactivation of the UC-emissive ^2E state. Such downshifting energy transfer includes highly efficient Dexter energy transfer and less efficient Förster energy transfer.[418] Hence, the main idea of this work is to develop an efficient molecular $Yb^{3+} \rightarrow Cr^{3+}$ UC system which can be easily realized at room temperature with relatively low excitation power densities.

To avoid Dexter energy transfer, the Cr^{3+} and the Yb^{3+} metal centers were spatially separated in a discrete coordination system, so that only less efficient Förster energy transfer is allowed. Cationic complex $[Cr(ddpd)_2]^{3+}$ and anionic complex $[Yb(dpa)_3]^{3-}$ were chosen as the ionic counter pair, which was able to form the crystallization of the desired **Cr-Yb** salt (structure shown in Section 3.1). Elemental analysis revealed that both solid salts contain large amounts of lattice water and methanol in the material. As C-H and O-H oscillators lead to non-radiative deactivation of the excited states of both the Cr^{3+} and Yb^{3+} via multiphonon relaxation,[379] the salt **Cr-Yb** was also prepared in a deuterated solvent, yielding **Cr-Yb(D)** for a comparison. Meanwhile, a reference compound **Cr-Lu(D)** was prepared as a structural analogue of the **Cr-Yb** and **Cr-Yb(D)** salts, thereby using the photoinactive nature of Lu^{3+} with its $4f^{14}$ electronic configuration. Single crystal XRD studies confirmed that these salts are isostructural, racemic mixtures of the complex ions. In the crystal, each Cr^{3+} center is surrounded by five Yb^{3+} sensitizers as nearest neighbors with a distance distribution of 8.75 Å < r_{Cr-Yb} < 9.07 Å.

Downshifting energy transfer $Cr^{3+} \rightarrow Yb^{3+}$

With such a sensitizer-activator distance, downshifting energy transfer $Cr^{3+} \rightarrow Yb^{3+}$ was observed in the **Cr-Yb** salt. Upon selective excitation of **Cr-Yb** at 435 nm, phosphorescence emission of $[Cr(ddpd)_2]^{3+}$ ($^2E/^2T_1$) was produced at around 780 nm. Meanwhile, luminescence emission of $[Yb(dpa)_3]^{3-}$ ($^2F_{5/2} \rightarrow {}^2F_{7/2}$) was observed at around 1000 nm. As the pure Yb^{3+} complex is not emissive under 435 nm excitation, the luminescence observation of Yb^{3+} confirmed the downshifting energy transfer. Additionally, time-resolved luminescence measurements as well as quantum yield determination of **Cr-Yb**, **Cr-Yb(D)** and the reference compound **Cr-Lu(D)** provided further evidences for this **Cr^{3+}$\rightarrow$Yb^{3+}** downshifting process (**Table 7**). Details of the luminescence lifetime and quantum yield measurements can be found in Sections 3.7.3 and 3.7.4, respectively.

Samples	τ_{783} (air) [μs][1]	τ_{783} (Ar) [μs][1]	τ_{980} (air) [μs][1]	$\Phi_{Cr(III)}$ (air) [%][2]
Cr-Yb	τ = 390 (100%)	τ = 380 (100%)	τ_1 = 9 (rise, -2%) τ_2 = 369 (decay, 102%)	5.9
Cr-Yb (D)	τ_1 = 160 (15%) τ_2 = 390 (85%)	τ_1 = 180 (12%) τ_2 = 370 (88%)	τ_1 = 12 (rise, -3%) τ_2 = 373 (decay, 103%)	5.8
Cr-Lu (D)	τ_1 = 280 (11%) τ_2 = 660 (89%)	τ_1 = 320 (12%) τ_2 = 720 (88%)	-	6.8

Table 7: Luminescence lifetimes τ and quantum yields Φ of compounds Cr-Ln (Ln = Yb, Lu) in the solid state at 298 K for excitation at 435 nm. [1] Lifetimes are fitted mono- or biexponentially, percentages in parentheses give relative amplitudes of the components, estimated τ uncertainty of ± 5%. [2] Luminescence quantum yields are estimated with an uncertainty of ± 5% (adapted with permission from Ref.[417], Copyright © 2020 The Authors. Published by Wiley-VCH GmbH).

Upon 435 nm excitation, the **Cr-Yb** salt showed the chromium emission at 783 nm with a mono-exponential decay kinetics, yielding a lifetime of 390 μs. Meanwhile, at 980 nm the Yb^{3+} displayed a biexponential decay with a long-lived luminescence of 369 μs. Such a long luminescence lifetime exceeds far the characteristic lifetime of molecular Yb^{3+} species in the low μs-range, which, however, matches closely the Cr^{3+} lifetime of 390 μs. Notably, a rise time component of 9 μs was observed, which is typically assigned to the energy transfer process from the long-lived ^2E state of Cr^{3+} to Yb^{3+}.[419-421] To quantify this undesired downshifting energy transfer efficiency, chromium phosphorescence quantum yields of the Cr-Ln salts were determined with an absolute method at 435 nm excitation (**Table 7**). By a comparison of the $\Phi_{Cr(III)}$ values in **Cr-Yb, Cr-Yb(D)** and **Cr-Lu(D)**, the presence of a Yb^{3+} acceptor led to a decrease of the Cr^{3+} quantum yield by ca. 15%. This is favorably lower than the reported analogues showing downshifting Förster energy transfer efficiency ranging from 20% to 50%.[419-421] Additionally, time-resolved measurements indicated that the **Cr-Lu(D)** salt had considerably longer ^2E lifetimes than the salts without Yb^{3+} acceptor (**Table 7**).

Surprisingly, the solid-state crystalline salts showed barely a luminescence response to oxygen. This is probably attributed to the combined effect of limited oxygen access in the crystals and the protection effect of the surrounded Yb^{3+} or Lu^{3+} counter complexes. Moreover, crystallization of **Cr-Yb** from deuterated solvents had no significant effects on the luminescence decay kinetics of emissive state of Cr^{3+}.

NIR to NIR upconversion Yb^{3+}→ Cr^{3+}

Subsequently, UC measurements of **Cr-Yb**, **Cr-Yb(D)** and **Cr-Lu(D)** were performed with the FLS 980 spectrometer using an ca. 8-W 976 nm laser diode at room temperature (see Section 3.7.3). As expected, no UC emission was observed for the reference compound **Cr-Lu(D)** by 976 nm excitation. By comparison, **Cr-Yb** and **Cr-Yb(D)** produced clearly a ^{2}E/^{2}T$_1$ UC emission of the Cr^{3+} activator with a maximum around λ_{em} = 780 nm upon 976 nm excitation of the Yb^{3+} sensitizers (**Figure 38 (a)**). Time-resolved UC luminescence studies confirmed successful UC in both **Cr-Yb** and **Cr-Yb(D)**, while no luminescence signal was observed for **Cr-Lu(D)** (**Figure 38 (b)**).

(a)   **(b)**
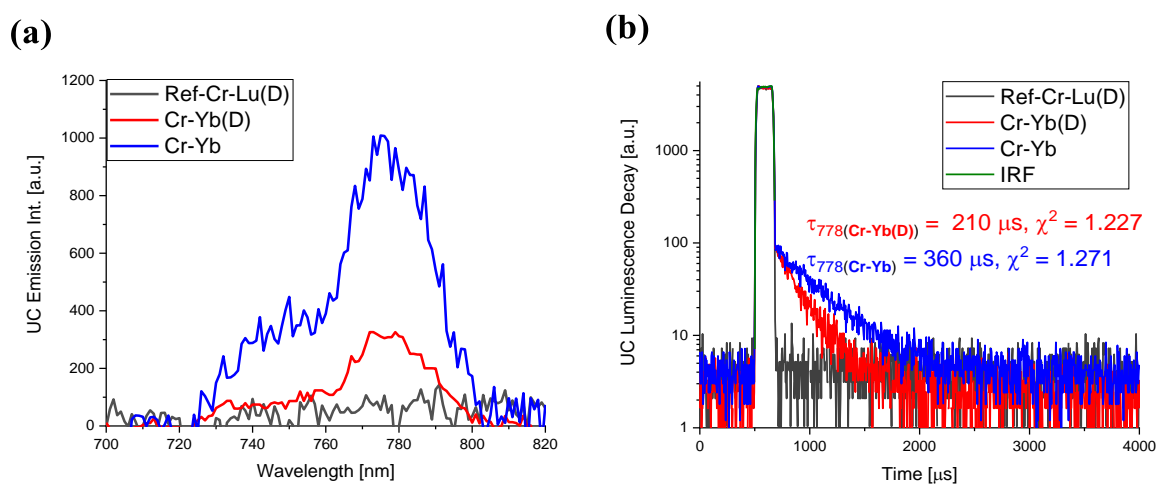
Figure 38: UC luminescence **(a)** emission spectra and **(b)** decays of Cr-Ln salts under 976 nm laser excitation at 298 K in an ambient atmosphere. UC luminescence decays obtained from 778 nm emission are fitted monoexponentially (Figure **(b)** is adapted with permission from Ref.[417], Copyright © 2020 The Authors. Published by Wiley-VCH GmbH).

As shown above in **Figure 37**, the Yb^{3+}→ Cr^{3+} UC follows a cooperatively sensitized upconversion (CSU) process (Section 2.3.3), which requires simultaneous energy transfer from two excited Yb^{3+} sensitizers to one Cr^{3+} activator. Therefore, the UC emission intensity depends strongly on the number or concentration of the excited sensitizers, and thus on the excitation power density P.[275,383,410,422] The P-dependent UC emission spectra of **Cr-Yb(D)** and **Cr-Yb** are illustrated in **Figure 39 (a)** and **(c)**, respectively, accompanied by the corresponding log-log plots of integrated UC emission intensity versus the excitation-power density P (**Figure 39 (b)** and **(d)**).
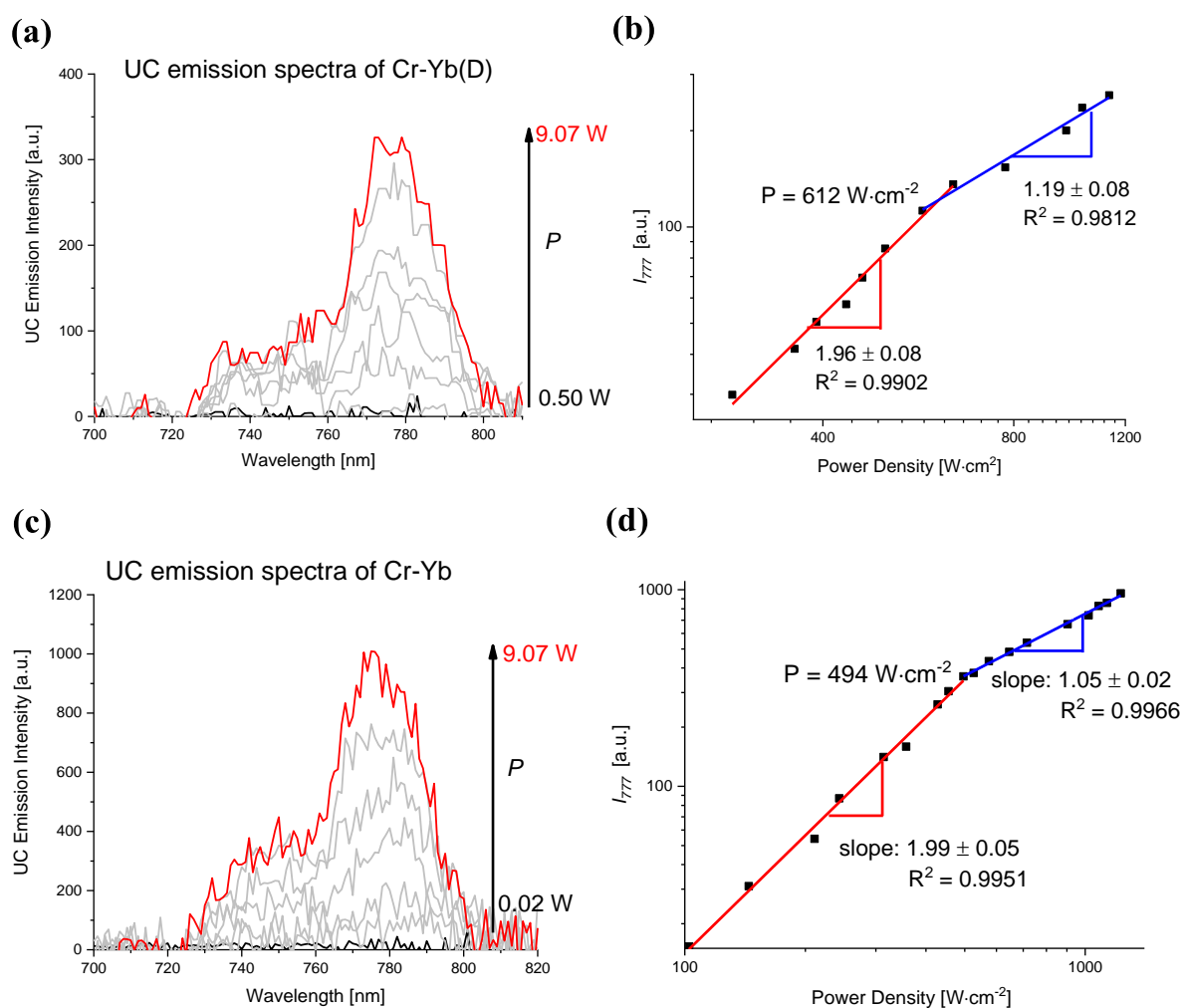
Figure 39: Excitation power-density (P) dependence of the UC luminescence of **(a) Cr-Yb(D)** and **(c) Cr-Yb** (298 K, solid, air) for Yb^{3+} excitation at λ_{ex} = 976 nm. Log–log plot of the upconversion ^2E luminescence (λ_{em} = 777 nm) versus the incident power density in **(b) Cr-Yb(D)** and **(d) Cr-Yb** — slopes obtained from linear fitting for the low (red) and high (blue) power density regimes (**(c)** and **(d)** adapted with permission from Ref.[417], Copyright © 2020 The Authors. Published by Wiley-VCH GmbH).

For both **Cr-Yb(D)** and **Cr-Yb** salts, UC emission intensity at ca. 780 nm increased significantly by varying *P* from nearly 0 W up to 9.07 W (**Figure 39 (a)** and **(c)**). The *P* dependence of the UC emission intensity can be linearly fitted in two distinct regions (**Figure 39 (b)** and **(d)**). With low excitation power density, the number of excited Yb^{3+} is low and UC depends quadratically on *P*, confirmed by a slope value of 1.99 ± 0.05 for the **Cr-Yb** salt and 1.96 ± 0.08 for the **Cr-Yb(D)** salt. This reveals a two-photon process, which follows a second order photonic reaction. At higher *P*, the number of excited sensitizers reaches a saturation and the UC process follows a pseudo-first order photonic reaction (slope value of 1.05 ± 0.02 for the **Cr-Yb** salt and 1.19 ± 0.08 for the **Cr-Yb(D)** salt), indicating a typical one-photon process.[275,383,410,422] Interestingly,

the non-deuterated **Cr-Yb** salt performs a lower threshold value between these two regions with $P_{th} \approx 494$ W·cm^{-2}, in comparison with **Cr-Yb(D)** ($P_{th} \approx 612$ W·cm^{-2}). Moreover, a minimal excitation power density for the observation of UC in **Cr-Yb** was needed with $P \approx 67$ W·cm^{-2}, which is reasonably low for a normally not very efficient CSU process.[407,408,420,423]

Conclusion

In summary, NIR to NIR upconversion (UC) was realized in molecular chromium ytterbium salts in the solid state by carefully redesigning the earlier downshifting Cr^{3+}/Yb^{3+} systems. Via a cooperative sensitized upconversion (CSU) mechanism, excitation of the Yb^{3+} sensitizers at 976 nm produced UC luminescence of the Cr^{3+} activator at ca. 780 nm, which was confirmed by the UC emission spectra and the UC luminescence decays. At low excitation power density (P), the UC emission intensity displayed a quadratic dependence on P due to the two-photon process, while with higher P the UC followed a typical one-photon process. Surprisingly, this UC system performs quite robust and can be reached with non-deuterated/non-halogenated building blocks at room temperature in the presence of oxygen and water molecules. Such molecular UC systems are rare, particularly with both excitation and UC emission in the NIR region which is of importance for bioanalytical studies. This proof-of-concept study will offer a new class of molecular UC materials and may lead to a series of UC applications in the future.

4.1.4 Design and development of multianalyte optical nanosensors for measuring temperature, oxygen and pH values

Introduction

In the past years, optical sensing based on photoluminescence has been favored for nondestructive detection of biologically and bioanalytically relevant analytes or parameters.[42,309,424] This technique provides a series of attractive properties over other sensing tools, such as high optical sensitivity, rapid response, high reversibility, high spatial resolution on the nanoscale, multiparametric readout and remote sensing. Upon the luminescent indicator-analyte interactions, optical changes can be observed in different domains, such as absorbance, luminescence emission intensity, lifetime and quantum yield (see Section 2.4.1).[42,289,424,425]

Among the most interesting parameters or analytes in biological systems are the temperature T, oxygen partial pressure pO$_2$, and pH ("TOP") due to their relevance for biological processes, and diseases like cancer or inflammations. For optical measurements of pH value, typical luminescent indicators include HPTS (8-hydroxypyrene-1,3,6-trisulfonate),[326] fluorescein and rhodamine derivatives,[426,427] and boron dipyrromethene (BODIPY) dyes. Common emitters for optical sensing of oxygen are transition metal porphyrins (*e.g.* PtTFPP,[428]) or polypyridyl complexes (*e.g.* [Ru(bpy)$_3$]$^{2+}$), and polycyclic aromatic hydrocarbons like pyrene.[309] Additionally, the recently reported chromium(III) complex [Cr(ddpd)$_2$]$^{3+}$ displays also high a NIR-phosphorescence response to oxygen in both the emission intensity and lifetime domains (**Figure 40 (a)**).[57,379] Typical T-sensitive molecular emitters are rhodamine B[429] and certain iridium(III) complexes.[430] Surprisingly, the complex [Cr(ddpd)$_2$]$^{3+}$ can also act as a molecular thermometer with its ratiometric readout of the dual emission (**Figure 40 (b)**).[58]
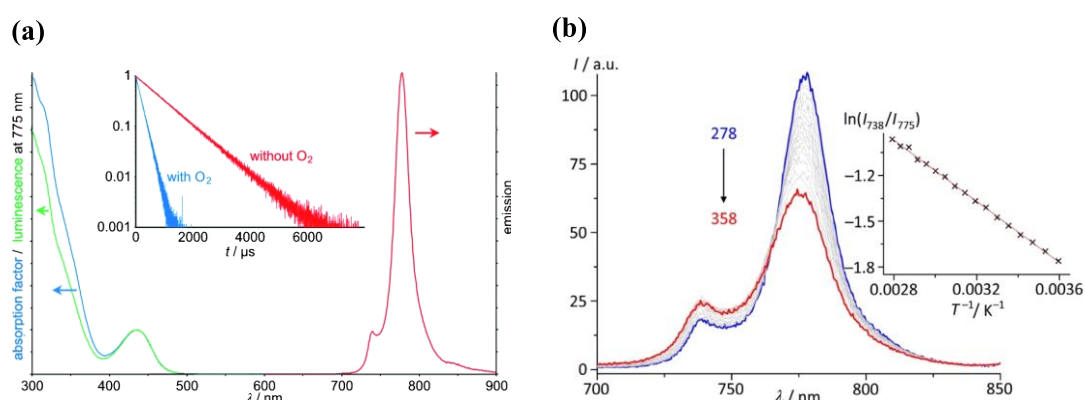
Figure 40: (a) Absorption (blue), excitation (λ_{obs} = 775 nm, green) and emission spectrum (λ_{exc} = 435 nm, red) of [Cr(ddpd)$_2$][BF$_4$]$_3$ in deaerated H$_2$O at room temperature; the inset shows the emission decay curves of the complex in H$_2$O with and without O$_2$ (taken with permission from Ref.[57], Copyright © 2015 WILEY‑VCH Verlag GmbH & Co. KGaA, Weinheim); **(b)** Variable-temperature emission spectra of [Cr(ddpd)$_2$][BF$_4$]$_3$ in H$_2$O from 278 to 358 K (air saturated), the inset shows the respective Boltzmann plots ln(I_{738}/I_{775}) vs. T^{-1}. The T-induced changes in emission are fully reversible (taken with permission from Ref.[58], Copyright © 2017 Wiley‑VCH Verlag GmbH & Co. KGaA, Weinheim).

Even though there is a large toolbox of luminescent indicators for optical sensing of T, pO$_2$, and pH ("TOP"), the desire of multianalyte sensors for the simultaneous measurement of these parameters at a same position is still considerably high, particularly for monitoring biological or biotechnological processes (see Section 2.4.4).[306,322,323,431] Commonly, multianalyte sensors are prepared by doping polymer films or particles with different indicator dyes, where each dye is optically sensitive to a single analyte.[285,319,324] However, the design of such triple

parametric "TOP" sensors is rather challenging, as the emission features of the indicator dyes and the reference dye are supposed to be spectrally distinguishable and these dyes can be excited with one single excitation wavelength (see Section 2.4.4). This can be achieved the luminophores featuring a large Stokes shift, which enables the use of other dyes. Favorable are sensing molecules showing an optical response either to two analytes or parameters simultaneously with spectrally distinguishable outputs. Yet such examples are extremely rare, such as the oxygen- and temperature-sensitive platinum(II) and palladium(II) benzoporphyrins reported by the Klimant group[325] and the $[Cr(ddpd)_2]^{3+}$ complex developed by us (**Figure 40**).[57,58,318,379] Although some dual sensors have been made for simultaneous measurements of pO_2 and T,[318,325,428,430] or pO_2 and pH,[317,432,433] only very few examples have been presented for sensing the TOP parameters simultaneously,[326] and most of them are based on planar thin films or layers, which are strongly limited for *e.g.* intracellular biological studies. To the best of our knowledge, a single wavelength excitable luminescent TOP nanosensor has not yet been reported. Hence, this study was carried out aiming to develop the desired multianalyte TOP nanosensors, followed by the design strategy, preparation methods, characterization of the nanosensors, and their luminescent sensitivity studies in different aqueous media.

Design and preparation of multianalyte optical nanosensors

In this study, two novel luminescent multianalyte nanosensors were developed, namely a dual sensor for O_2 and pH, and a TOP sensor. The previously studied NIR-emissive chromium(III) complex $[Cr(ddpd)_2]^{3+}$ with tetraphenylborate $[BPh_4]^−$ counter anions (**CrBPh₄ in Figure 41 a)**) was chosen as the hydrophobic T- and O_2-responsive sensor dye. Fluorescein-5-isothiocyanate (**FITC**) (see **Figure 41 a)**) with a pK_a in the bioanalytically relevant pH window, was selected as the pH-sensitive indicator, which can react with amino functionalities. Two analyte-inert reference dyes were chosen due to their spectral matching, namely 5,10,15,20-tetrakis-(pentafluorophenyl) porphyrin (**TFPP**; **Figure 41 a)**) and Nile Red (**NR**; **Figure 41 a)**), and thus enabling two multianalyte sensor systems. Since **TFPP** shows an optical inertness against pO_2 and pH but a slight T-dependence, the sensor system containing **TFPP** is only suitable for the construction of a dual nanosensor (for O_2 and pH). By comparison, **NR** shows no optical response to these three parameters and thus can only be used as reference for a TOP sensor.

As shown in **Figure 41 b-1) and b-2),** the chosen sensor constituents **CrBPh₄**, **FITC**, **TFPP**, and **NR** can be excited in the spectral window of 430 – 450 nm and reveal clearly distinguishable emission bands centered at 740/778, 520, 663, and 596 nm, respectively. The keystone for designing these multianalyte nanosensors is the extraordinarily large energy difference of the O_2-indicator $[Cr(ddpd)_2]^{3+}$ [57,379] between its absorption maximum at 435 nm and the dual emission at 740/778 nm (spectral window of 9475 cm^{-1}, equaling here 305 nm). This is considerably larger in comparison with the commonly employed O_2-sensitive dyes, such as the red emissive benzoporphyrins with a substantially narrower spectral window of about 3000 cm^{-1} (equaling 150 nm) in average.[325] Hence, the $[Cr(ddpd)_2]$ emitter[57,379] is ideal for combining with some other dyes, such as the pH-sensitive dye and an additional reference dye with minimum spectral crosstalk. Importantly, the optical responses of the Cr(III) complex to *T* and to *pO₂* are spectrally distinguishable. Its NIR emission is quenched by molecular oxygen via Dexter energy transfer[57,310,379,394], while its dual emission (I_{740}/I_{778}) corresponds ratiometrically to the temperature in the range of –50 °C to 100°C.[58]

After choosing the dye combinations, a suitable matrix is need. 100 nm – sized aminated polystyrene (**PS-NH₂**) nanoparticles were chosen as carriers. The prefabricated **PS-NH₂** nanoparticles are commercially available and show a high gas permeability, ensuring access of oxygen to the indicator dye inside the particles. The O_2- and *T*-responsive **CrBPh₄** and the reference dyes **TFPP** or **NR** were mechanically encapsulated into the **PS-NH₂** particles via a simple one-step staining procedure (**Figure 41 c**), **step 1**),[37,38,206] yielding **PS(CrBPh₄-Ref)** (**Ref = NR** or **TFPP**). Experimental details can be found in Section 3.3.1. One major issue of such loading approach is the leaking of the sensor components, which can be due to slight water solubility of the dye, presence of, *e.g.* traces of organic solvents, surfactants or proteins or for neutral indicators by protonation or coordination to a charged analyte. Particularly for the prior $[Cr(ddpd)_2]^{3+}$ complex with the $[BF_4]^-$ counter anion (**CrBF₄**), water solubility is an issue, as severe leaking of **CrBF₄** from the PS-NH₂ nanoparticles was observed over time (experimental details in Section 3.6). As discussed in Section 4.1.2, the hydrophobicity of $[Cr(ddpd)_2]^{3+}$ can be well tuned by the choice of the bulky counter anion, while remaining its favorable optical properties. Thus, the less hydrophilic $[PF_6]^-$ salt **CrPF₆** ($(Cr(ddpd)_2][PF_6]_3$[57]) and the more hydrophobic $[BPh_4]^-$ salt **CrBPh₄** ($[Cr(ddpd)_2][BPh_4]_3$) were prepared and subsequently characterized.
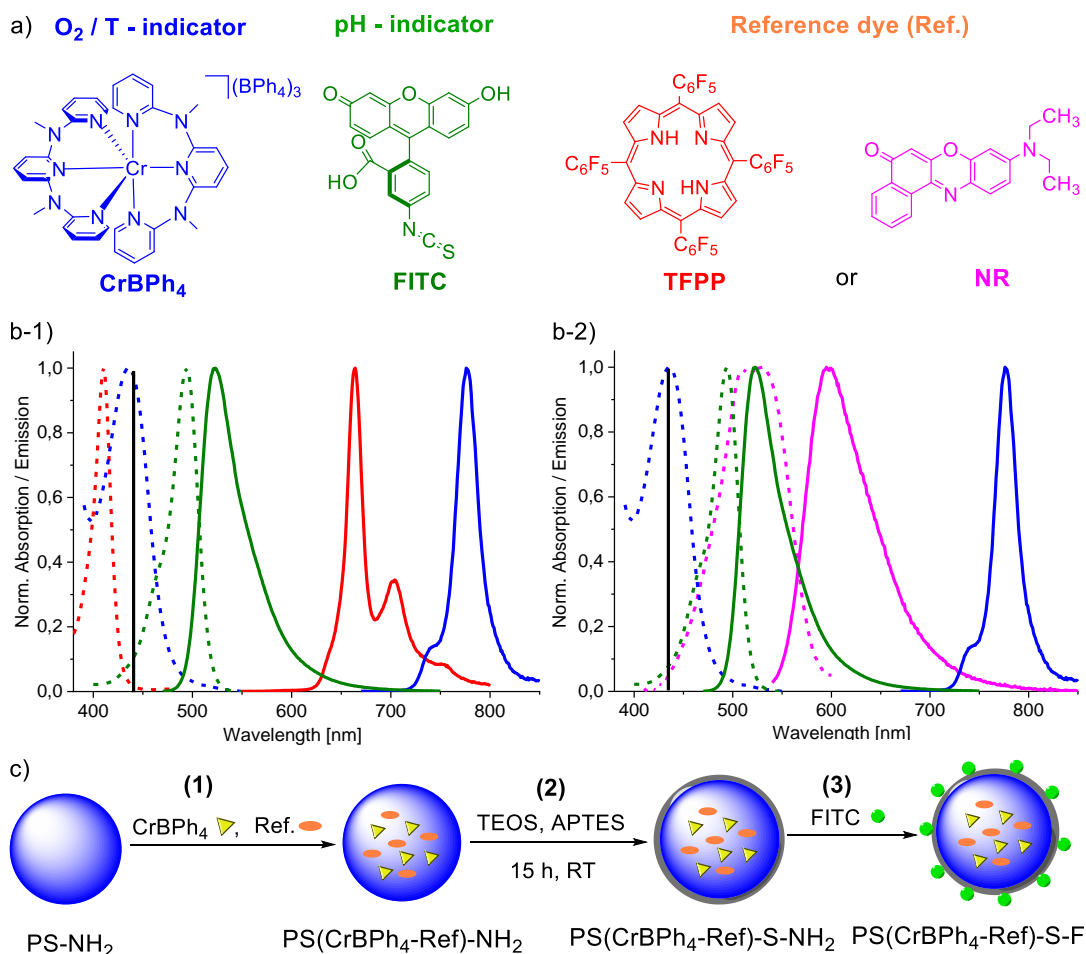
Figure 41: a): Chemical structures of the luminescent constituents of the dual and TOP nanosensors; **b-1)** and **b-2)**: Absorption (dashed lines) and emission (solid lines) spectra of the dyes used for sensor fabrication. **CrBPh$_4$** (λ_{em} = 740/778 nm, blue) and **FITC** (λ_{em} = 520 nm, green) were applied as O$_2$- and pH-responsive indicators and the ratiometric dual emission of **CrBPh$_4$** I_{740}/I_{778} provides *T*-sensitivity. As reference dyes, **TFPP** (λ_{em} = 663 nm, red) was chosen in **b-1)** and **NR** (λ_{em} = 596 nm, pink) in **b-2)**. All dyes can be excited at 440 or 435 nm (as indicated by the black lines) and reveal spectrally distinguishable emission bands. **c)**: Schematic illustration of the nanosensor fabrication using 100 nm aminated polystyrene (**PS-NH₂**) nanoparticles, that involves dye encapsulation, silanization (employing TEOS = tetraethyl orthosilicate and APTES = (3-aminopropyl)triethoxysilane), and surface functionalization with **FITC** (adapted with permission from Ref.[400], Copyright © 2019, American Chemical Society).

Leaking studies (Section 3.6) revealed that the complex **CrPF₆** leaked heavily from the particles (up to ca. 70% referred to the fresh sample) over 2 days in phosphate-buffered saline (PBS, 0.1 M, pH 8.0) at room temperature (**Figure 42 (a)**), while the complex **CrBPh₄** demonstrated improved immobility in the particles under the same storage conditions, some leaking was still observed of the order of 40 % (**Figure 42 (b)**).
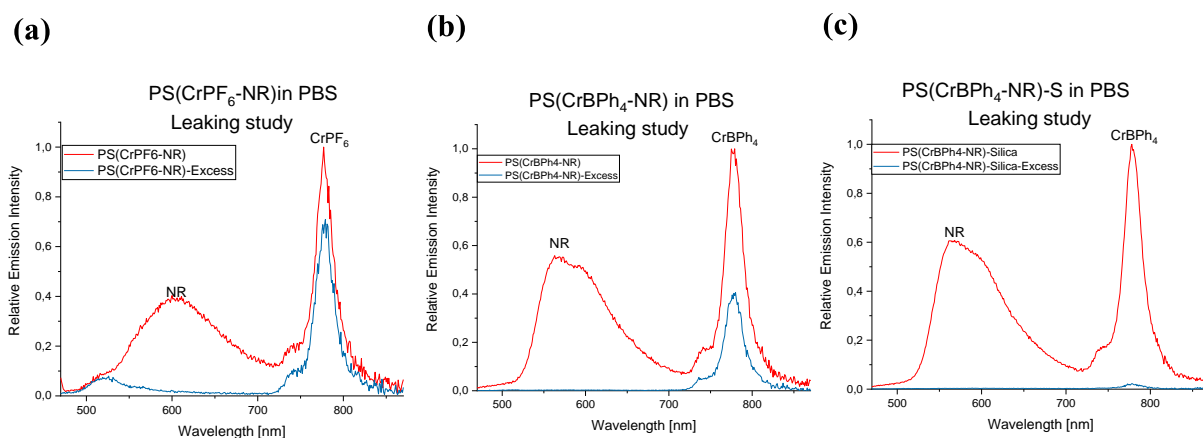
Figure 42: Fluorometrically monitored leaking studies of the nanosensors **(a)** PS(CrPF$_6$-NR), **(b)** PS(CrBPh$_4$-NR), and **(c)** PS(CrBPh$_4$-NR)-S in PBS buffer (0.1 M, pH 8.0) under 435 nm excitation. For each nanosensor the emission spectra of the freshly prepared particles (red) and the supernatants after particle removal were compared after two days of storage at room temperature (dark blue) (taken with permission from Ref.[400], Copyright © 2019, American Chemical Society).

To prevent dye leaking from the particles, the nanosensors were "sealed" by a thin silica shell using an ammonia-catalyzed Stöber-like procedure,[236,238,240] resulting **PS(CrBPh$_4$-Ref)-S-NH$_2$** (**Ref = NR** or **TFPP**) as shown in **Figure 41 c)**, **step 2**. The aminated silica source APTES ((3-aminopropyl) triethoxysilane) was applied to ensure amino groups on the particle surface for further conjugation with amine-reactive dyes like **FITC**. Experimental details are described in Section 3.3.2. The successful formation of the silica-shell was confirmed by the increased size and decreased zeta potential of the nanoparticles using DLS measurements (Section 3.4). By comparison with bare PS-NH$_2$ and silica-shelled PS-NH$_2$, an increase of the particle radius by ca. 8 nm and a decrease of zeta potential by ca. 24 eV evidenced the formation of a negatively charged silica-shell (**Table 8**). With this approach, the silica-coated particles doped with **CrBPh$_4$** and **NR** demonstrated in PBS high colloidal and chemical stability of these nanoparticles over a period of two months with negligible leaking (**Figure 42 (c)**). Finally, the pH-sensitive indicator with the thiocyanate derivative **FITC** was covalently bound to the surface of the sensor particles via a reaction with the surface amino functionalities (**Figure 41 c)**, **step 3**),[235,434] yielding the multianalyte nanosensors **PS(CrBPh$_4$-NR)-S-F** and **PS(CrBPh$_4$-TFPP)-S-F.** Experimental details can be found in Section 3.3.4.

	PS-bare in H₂O	PS-Silica in H₂O	Difference
	Averaged hydrodynamic diameter [nm]		Radius difference [nm]
Record 1	107.0 ± 25.2	123.8 ± 29.0	-
Record 2	105.4 ± 25.1	122.5 ± 29.6	-
Record 3	108.3 ± 24.3	124.1 ± 29.2	-
Average	**106.9 ± 24.9**	**123.5 ± 29.3**	**8.3**
	Zeta Potential [mV]		Zeta potential difference [mV]
Record 1	-34.9 ± 8.6	-59.6 ± 13.6	-
Record 2	-34.5 ± 8.6	-58.3 ± 11.7	-
Record 3	-34.3 ± 9.9	-59.0 ± 12.5	-
Average	**-34.6 ± 9.0**	**-59.0 ± 12.6**	**-24.4**

Table 8: Averaged hydrodynamic diameter with standard derivation and zeta potential of the bare PSNPs and PSNPs with a silica-shell in H_2O (1 mg/mL) (adapted with permission from Ref.[400], Copyright © 2019, American Chemical Society).

Characterization of nanosensors

The both prepared multianalyte nanosensors **PS(CrBPh₄-Ref)-S-F** (**Ref** = **NR** or **TFPP**) were then characterized systematically, including determination of the their final size and size distribution via DLS, quantitative analysis of the amount of indicator dyes in the nanosensors (**CrBPh₄**) or bound to the surface (**FITC**), and the stability studies of the nanosensor dispersions.

Size distribution

DLS measurements (details in Section 3.4) revealed a hydrodynamic diameter of the generated nanosensors of about 130 nm (**Figure 43**), which indicated an increase of radius of 12 – 14 nm in comparison with the bare blank particle **PS-NH₂** (ca. 107 nm, **Table 8**). The corresponding DLS data (size distribution by number) of both nanosensors are summarized in **Table 9**.
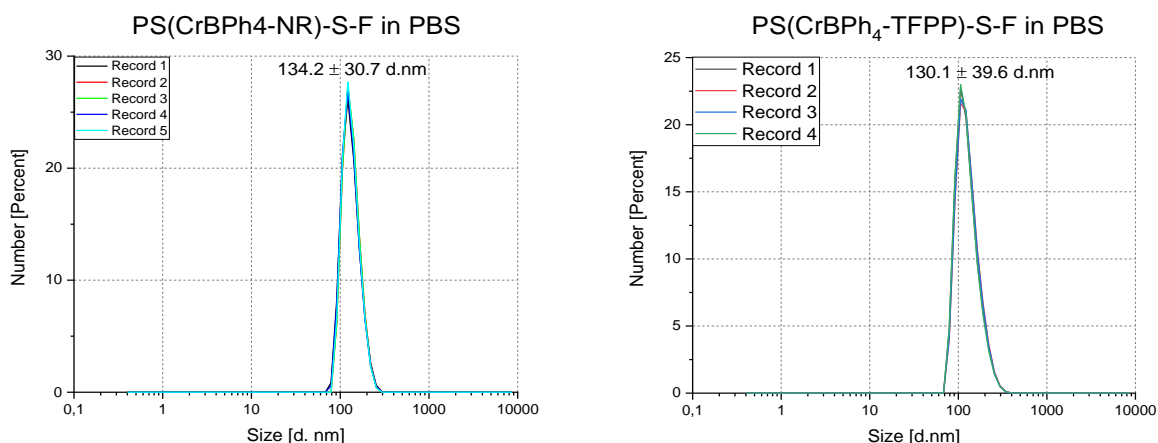
Figure 43: Size distribution by number of measurements of the multianalyte nanosensors **PS(CrBPh₄-NR)-S-F** (left) and **PS(CrBPh₄-TFPP)-S-F** (right) in PBS (0.1 M, pH8) with the particle concentration of 1 mg/mL (taken with permission from Ref.[400], Copyright © 2019, American Chemical Society).

	PS(CrBPh₄-NR)-S-F in PBS	PS(CrBPh₄-TFPP)-S-F in PBS
	Averaged hydrodynamic diameter [nm]	
Record 1	133.4 ± 31.9	129.4 ± 40.1
Record 2	135.3 ± 30.4	131.7 ± 39.8
Record 3	135.0 ± 30.1	130.9 ± 39.3
Record 4	133.1 ± 30.9	128.4± 39.1
Record 5	134.0 ± 30.0	-
Average	**134.2 ± 30.7**	**128.0 ± 39.7**

Table 9: Size distribution by number of both multianalyte nanosensors in PBS (0.1 M, pH8) with the particle concentration of 1 mg/mL (adapted with permission from Ref.[400], Copyright © 2019, American Chemical Society).

Quantitative analysis of loaded indicator dyes

Quantitative analysis of the encapsulated **CrBPh₄** in PSNPs and the conjugated **FITC** on the particle surface was completed by absorption spectroscopy. General procedures are described in Section 3.5.1.

For the quantitative determination of entrapped **CrBPh₄**, 0.14 mg bare PSNPs were dissolved in 1 mL DMF, serving as the solvent (DMF-PSNP) for **CrBPh₄**. By dissolving **CrBPh₄** in this solvent and measuring the absorption spectra, its molar absorption coefficient (λ_{abs} = 435 nm) was determined from a calibration with previously known concentrations of **CrBPh₄**. **Figure 44** shows **(a)** the obtained absorption spectra and **(b)** the resulting calibration curve of **CrBPh₄** in

DMF-PSNP. The resulting slope value of the linear calibration (**Figure 44 (b)**) relates to the product of the molar absorption coefficient and the optical pathlength (here 10 mm-quartz cells). The **CrBPh₄**-loaded PSNPs were then dissolved in DMF to obtain a particle concentration of 0.14 mg/mL. Measurement of the absorption spectrum gave an absorbance of 0.0223 at 435 nm, which corresponds to a **CrBPh₄** concentration of 2.84 µM according to the calibration curve (**Figure 44 (b)**). Consequently, the concentration of the encapsulated **CrBPh₄** was determined to be 20.7 µM in the PS(CrBPh₄)-S-NH₂ (1 mg/mL) suspension. With the known particle density (Section 3.5.1), the molecule number of **CrBPh₄** per PSNP particle was estimated to be around 6700 ± 500.
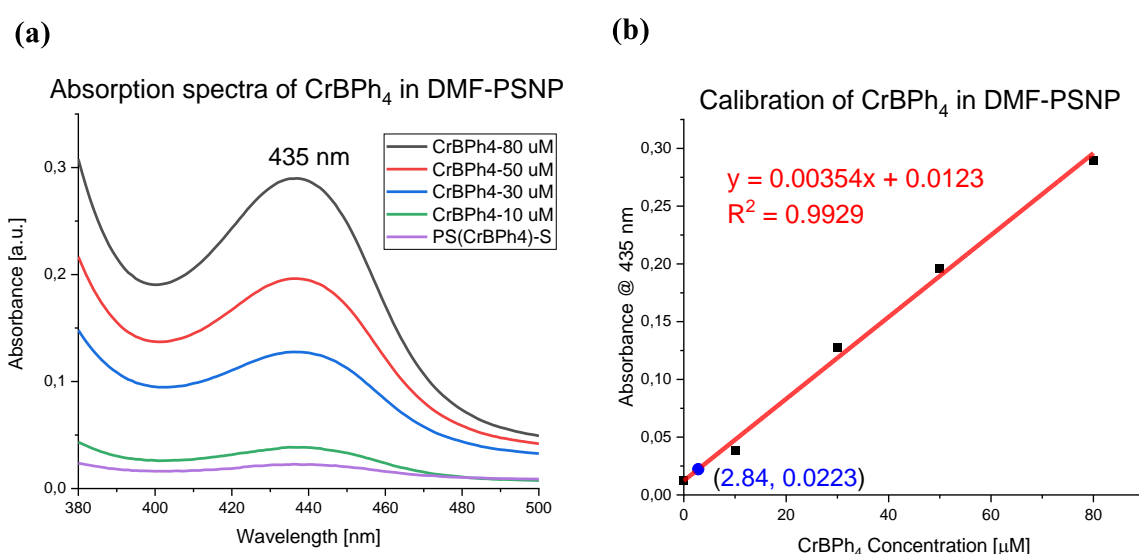
Figure 44: (a) Absorption spectra of **CrBPh₄** in DMF-PSNP (PSNP concentration of 0.14 mg/mL) with known concentration and **(b)** their respective calibration plot with absorbance vs. concentration (adapted with permission from Ref.[400], Copyright © 2019, American Chemical Society).

In terms of the quantitative determination of the bound **FITC** on the particle surface, an indirect method via absorption spectroscopy was applied by calculating the difference between the used **FITC** and the residual **FITC** in the washing solution. Experimental details are given in Section 3.5.2. As shown in **Figure 45 (a)** and **(b)**, by measuring the absorption spectra of FITC in a solvent mixture (PBS-EtOH-H₂O) with various given concentrations, a linear calibration function was obtained. According to this straight calibration line, the concentrations of the added FITC and the unreacted FITC in the washing solution were calculated. As a result, the concentration of conjugated fluorescein was calculated to be 6.3 ±

0.4 µM in PS(CrBPh$_4$-NR)-S-F dispersion (1 mg/mL), corresponding to 2000 ± 110 fluorescein molecules per nanoparticle.

(a)

(b)
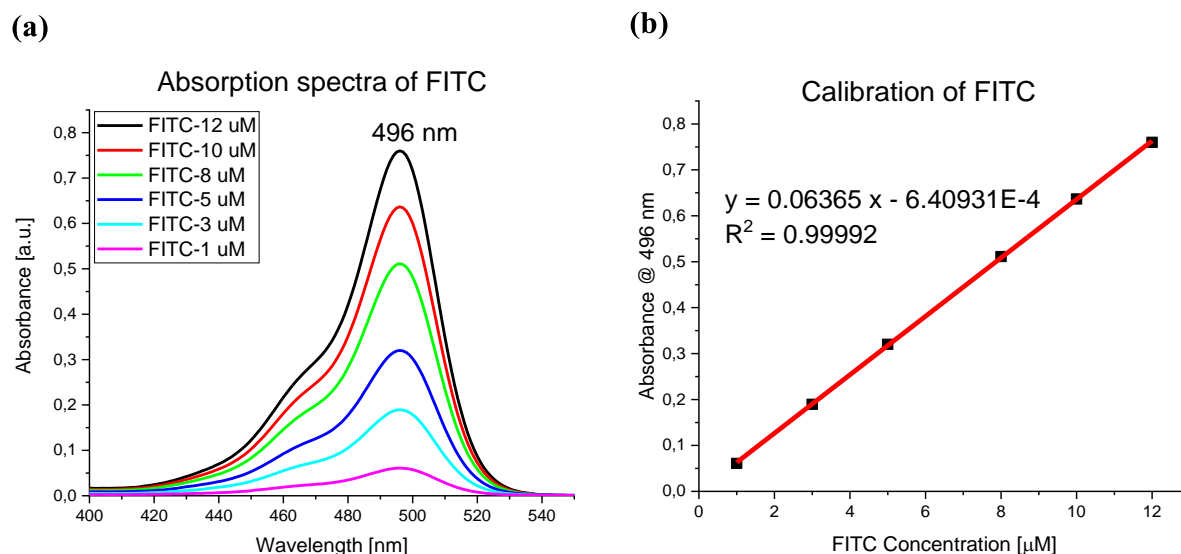
Figure 45: **(a)** Absorption spectra of FITC in a PBS-EtOH-H$_2$O mixture containing known dye concentrations and **(b)** the resulting calibration curve by plotting *absorbance* vs. *concentration* (adapted with permission from Ref.[400], Copyright © 2019, American Chemical Society).

Photo- and thermal stability studies of the nanosensor dispersions

In addition to the high colloidal and chemical stability as described in **Figure 42 (c)**, the generated nanosensors showed high photostability and thermal reversibility. In cell culture media (PBS with 0.5% mass to volume percent (w/v) BSA), illumination at 435 nm (using the xenon lamp of the spectrofluorometer) of both multianalyte nanosensors **PS(CrBPh$_4$-Ref)-S-F** (**Ref** = **NR, TFPP**) for 2 hours revealed no spectral changes (**Figure 46**), confirming the high photostability of the nanosensors.

The thermal stability of the nanosensors was studied by monitoring their temperature response between 283 K and 343 K for three heating-cooling cycles (**Figure 47**). The logarithm of the ratio of the emission intensities *I*$_{740}$/*I*$_{778}$ of the multianalyte nanosensor **PS(CrBPh$_4$-NR)-S-F** always tuned to the same value at the chosen temperature (here 10 °C, 40 °C, and 70 °C), and thus revealing the high thermal stability and stable *T*-sensing reversibility of the system in the studied temperature range.
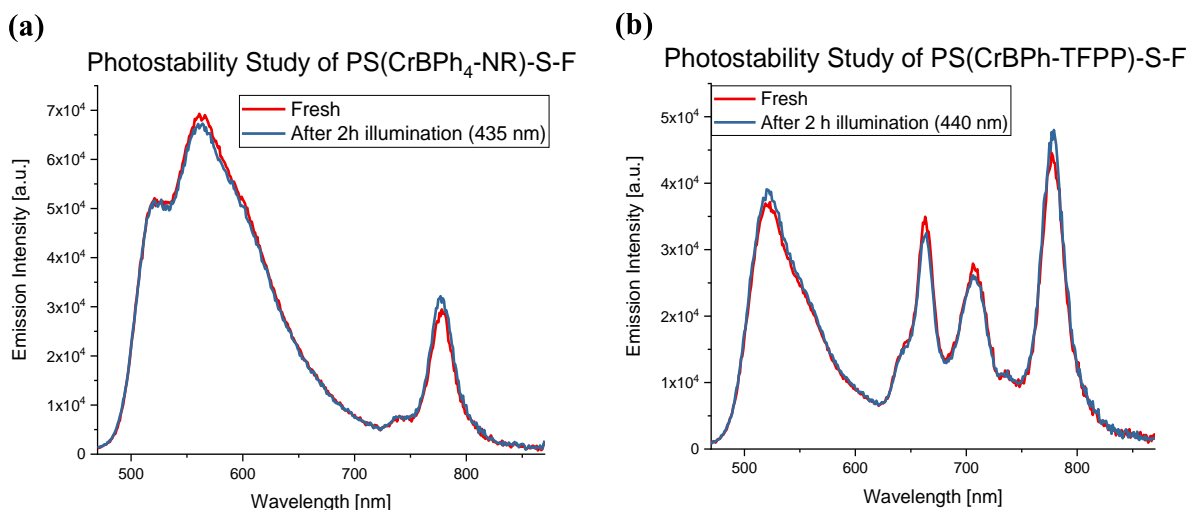
Figure 46: Optical stability test of both multianalyte nanosensors **(a) PS(CrBPh₄-NR)-S-F** and **(b) PS(CrBPh₄-TFPP)-S-F** in cell culture PBS/BSA (0.5% (w/v)) medium. Both nanosensors were illuminated with a xenon lamp excitation wavelength of 435 nm or 440 nm for about 2 h and the emission spectra were obtained upon the same excitation wavelength (adapted with permission from Ref.[400], Copyright © 2019, American Chemical Society).
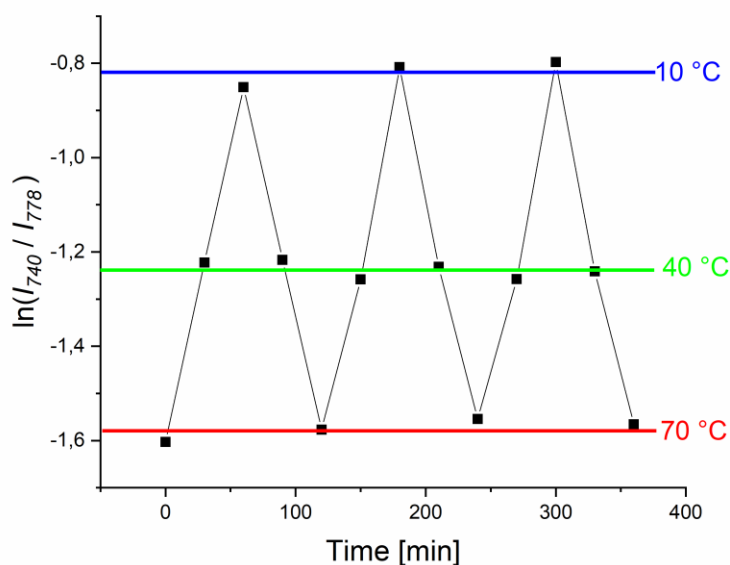
Figure 47: Thermal stability test of the multianalyte nanosensor **PS(CrBPh₄-NR)-S-F** in PBS buffer by plotting the logarithm of the ratio of the emission intensities $\ln(I_{740}/I_{778})$ in the temperature range of 10 °C (283 K) to 70 °C (343 K) for three cycles (adapted permission from Ref.[400], Copyright © 2019, American Chemical Society).

Sensing studies

To ensure that different components in the multianalyte nanosensors do not interfere with each other, sensing studies of the molecular indicators, the mono- and the multianalyte nanosensors were carried out in different media, respectively.

Sensing behavior of molecular indicators in solution

The sensing studies of the molecular indicator dyes **CrBPh₄** and **FITC** were carried out in solutions via measurements of luminescence emission spectra and lifetime. Due to the extremely low water-solubility, the *O₂*- and *T*-sensing behaviors of dye **CrBPh₄** were studied in acetonitrile instead of water, while the pH-sensing study of **FITC** was done in PBS (0.1 M). Their respective sensing behaviors are shown in **Figure 48**.
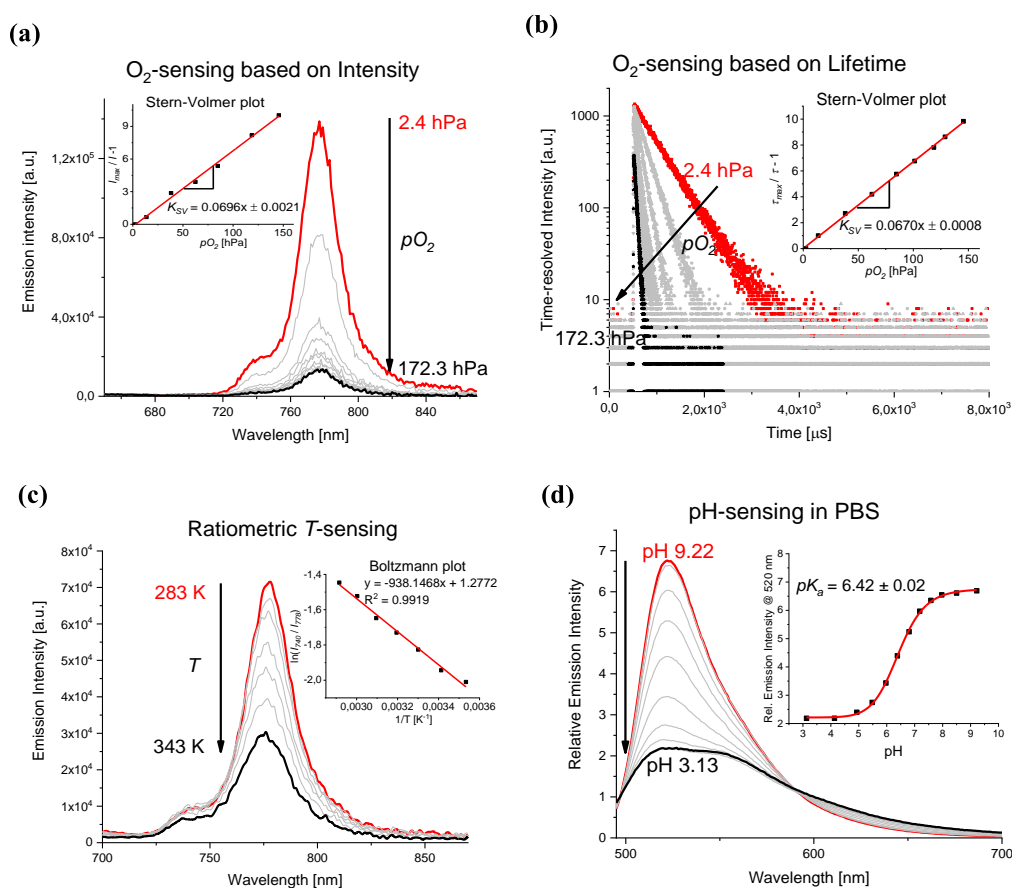
Figure 48: pO_2- and *T*-sensitivity of **CrBPh₄** in acetonitrile and pH-sensitivity of **FITC** in PBS. **(a)**: O₂-sensitivity based on luminescence intensity (I_{778}) measurements and the respective Stern-Volmer plots I_{max}/I-1 vs. pO_2; **(b)**: O₂-sensitivity based on luminescence lifetime (λ_{778}) and the respective Stern-Volmer plots τ_{max}/τ-1 vs. pO_2; **(c)**: *T*-sensitivity based on the ratiometric dual emission I_{740}/I_{778} and the respective Boltzmann plots $\ln(I_{740}/I_{778})$ vs. T^{-1}. The **CrBPh₄** is excited by a 435 nm light source; **(d)**: Luminescence emission intensity-based pH-sensitivity of free **FITC** in PBS (0.1 M) and the respective calibration plots I_{520} vs. pH value. FITC is excited by a xenon lamp at 440 nm (adapted with permission from Ref.[400], Copyright © 2019, American Chemical Society).

By monitoring the oxygen partial pressure (pO_2) from 2.4 hPa to air saturation, **CrBPh$_4$** showed a clear response with quenched emission intensity and slower decays (**Figure 48 (a)** and **(b)**). Stern-Volmer studies taken at both intensity and lifetime domains revealed basically the same Stern-Volmer constant K_{SV} of 0.068 ± 0.02 hPa^{-1} (slope value of the linear fits) in acetonitrile at room temperature (insets in **Figure 48 (a)** and **(b)**). In terms of the T-sensing, the ratiometric readout of the dual emission I_{740}/I_{778} increased with decreasing temperature in the range from 283 K to 343 K, following a linear Boltzmann plot, as shown in **Figure 48 (c)**. Both the oxygen- and T-sensing behaviors performed fully reversible. For the pH-sensing study, the indicator dye **FITC** revealed an increase in its emission intensity at ca. 520 nm in PBS buffer, yielding a pK_a value of 6.42 ± 0.02 (**Figure 48 (d)**). By adding sodium hydroxide solution (0.1 M) to the acidic FITC solution, the emission spectra can be fully restored, indicating the reversibility of the pH-sensitivity.

Sensing behavior of the monoanalyte nanosensors

Sensing behaviors of monoanalyte nanosensors loaded with one indicator dye were studied in PBS buffer, exemplarily using NR as reference dye. Two single indicator nanosensors were prepared, namely the oxygen- and T- sensitive **PS(CrBPh$_4$-NR)-S-NH$_2$** (Section 3.3.1 and 3.3.2) and the pH nanosensor **PS-F** (Section 3.3.4). The corresponding luminescence-based sensing studies are exhibited in **Figure 49**.

For the nanosensor stained with one single indicator dye **CrBPh$_4$** and a reference dye **NR**, oxygen sensing studies were performed in the NIR emission intensity and luminescence lifetime domains. By monitoring pO_2 from 0.3 hPa (Ar-saturated) to 214.5 hPa (air-saturated), a decrease in the emission intensity I_{778} as well as the lifetime τ_{778} was observed, as shown in **Figure 49 (a)** and **(b)**. The respective Stern-Volmer studies displayed in both domains the same K_{SV} of 0.011 hPa^{-1} (insets in **Figure 49 (a)** and **(b)**), which is smaller than K_{SV} (slope value of 0.068) of **CrBPh$_4$** in acetonitrile. This is mainly attributed to the different chemical environment of the oxygen-sensitive **CrBPh$_4$**, including the solvent-dependent diffusion constants, intramolecular interactions of the indicator with the surrounding molecules, and the protection effect from the silica-coated particle matrix. The O$_2$ response of nanosensor

PS(CrBPh₄-NR)-S-NH₂ was proven fully reversible by alternating the luminescence measurements cycles with *pO₂* between air- and argon-saturation.
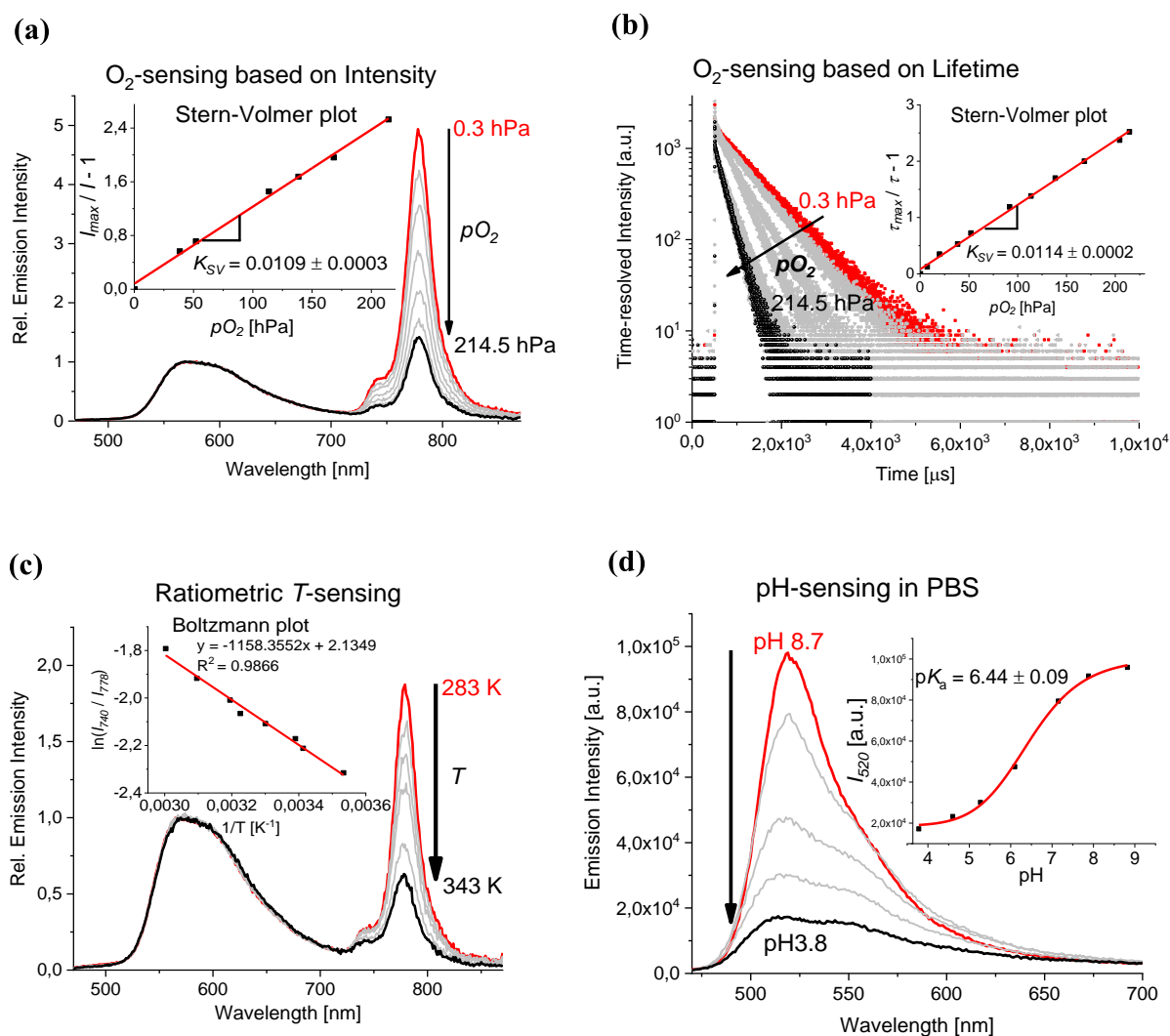
Figure 49: Sensing studies of the monoanalyte nanosensors **PS(CrBPh₄-NR)-S-NH₂** and **PS-S-F** via luminescence emission intensity and lifetime measurements. **(a)**: O₂-sensitivity of **PS(CrBPh₄-NR)-S-NH₂** derived from luminescence intensity (λ_{em} = 778 nm) measurements and the respective Stern-Volmer plot I_{max}/I-1 vs. *pO₂*; **(b)**: O₂-sensitivity of **PS(CrBPh₄-NR)-S-NH₂** obtained from luminescence lifetime studies (λ_{exc} = 435 nm; λ_{em} = 778 nm) and the respective Stern-Volmer plot τ_{max}/τ-1 vs. **pO₂**; **(c)**: T-sensitivity of **PS(CrBPh₄-NR)-S-NH₂** determined at air saturation from the ratiometric dual emission I_{740}/I_{778} and the respective Boltzmann plot $\ln(I_{740}/I_{778})$ vs. T^{-1}. Nanosensor **PS(CrBPh₄-NR)-S-NH₂** was excited at 435 nm and the lifetimes were measured at 778 nm. **(d)**: Luminescence emission intensity-based pH-sensitivity of the single analyte nanosensor **PS-S-F** in PBS (0.1 M) and the respective calibration plots I_{520} vs. pH values. The pK_a value was obtained from a fit of the sigmoidal titration curve (pK_a = 6.44 ± 0.09; R^2 = 0.9981). Nanosensor **PS-S-F** was excited at 440 nm (adapted with permission from Ref.[400], Copyright © 2019, American Chemical Society).

In terms of the *T*-sensing of **PS(CrBPh₄-NR)-S-NH₂**, a self-referenced ratiometric readout I_{740}/I_{778} yielded an increase with rising temperature from 283 K to 343 K (**Figure 49 (c)**), while the τ_{778} remained constant. The *T*-sensing studies of indicator **CrBPh₄** revealed linear Boltzmann plots, regardless in acetonitrile (inset in **Figure 48 (c)**) or in nanosensor **PS(CrBPh₄-NR)-S-NH₂** (inset in **Figure 49 (c)**), indicating a similar thermochromic behavior of both systems. For the *T*-dependent luminescence measurements, the signal change caused by O₂-solubility was considered in the corresponding calibration parameter derived from the Boltzmann plot. By cooling the nanosensor to room temperature, the emission spectra as well as the intensity ratio I_{740}/I_{778} were fully restored, which indicates the *T*-sensing reversibility.

For the pH-sensing study of **PS-S-F** in PBS buffer, a decrease in its emission intensity at 520 nm was observed by changing the pH from 8.7 to 3.8 (**Figure 49 (d)**). This yields a sigmoidal plot with a pK_a value of 6.44 ± 0.09, which is in agreement with the previously determined pH response of the molecular FITC in PBS (pK_a = 6.42 ± 0.02). This indicates that the protonation/deprotonation of the on particle conjugated FITC molecules is facile as that of the dissolved dye, confirming the suitability of the chosen nanostructure of the nanosensor and the conjugation chemistry for pH sensing. A rise in pH value was accompanied by the restored emission intensity at 520 nm, revealing the full reversibility of the pH nanosensor **PS-S-F**.

Sensing behavior of the multianalyte nanosensors

The sensing studies of the multianalyte TOP nanosensors **PS(CrBPh₄-NR)-S-F** (for *T*, pO_2 and pH) and dual nanosensor **PS(CrBPh₄-TFPP)-S-F** (for pO_2 and pH) were carried out by detecting their response in luminescence intensity and/or lifetime to changes in *T*, pO_2, and pH. The results of the TOP- and the dual nanosensors are illustrated in **Figure 50** and **Figure 51**.

Upon photoexcitation at 435 nm or 440 nm, both nanosensors **PS(CrBPh₄-NR)-S-F** and **PS(CrBPh₄-TFPP)-S-F** generated spectrally distinguishable emission bands. By monitoring pO_2 from nearly 0 hPa to ca. 200 hPa (air saturated), oxygen indicator **CrBPh₄** displayed a clear drop in its emission intensity I_{778} (**Figure 50 (a)** and **Figure 51 (a)**) and in the corresponding lifetime τ_{778} (**Figure 50 (b)** and **Figure 51 (b)**). Stern-Volmer studies of both nanosensors in their luminescence intensity and lifetime reveal basically the same K_{SV} value of around 0.014 hPa^{-1} (insets in **Figure 50 (a), (b)** and in **Figure 51 (a), (b)**), indicating that neither the

simultaneously encapsulated reference dyes nor the pH-responsive fluorescein have an effect on the O_2-sensitivity of the system. As expected, the emission bands of the reference dye and the pH-indicator remained constant during changing pO_2. Moreover, these luminescence responses to oxygen are fully reversible. Consequently, O_2 sensing approaches based on luminescence intensity and lifetime of **CrBPh$_4$** are feasible in both multianalyte nanosensors. Nevertheless, lifetime-based sensing is generally preferred, as time-resolved measurements eliminate many possible signal distortions from the background and perform independently from artefacts such as dye concentration and excitation light power.[326] More importantly, the NIR phosphorescence of **CrBPh$_4$** has a large lifetime scale ranging from 170 µs to 680 µs, which ensures a high accuracy for O_2-sensing.

Figure 50: Luminescence emission intensity and lifetime of the TOP nanosensor **PS(CrBPh$_4$-NR)-S-F** in PBS with changes in pO_2, T, and pH (λ_{exc} = 435 nm): **(a):** O_2-sensitivity derived from I_{778} and the respective Stern-Volmer plot I_{max}/I-1 vs. pO_2; **(b):** O_2-sensitivity obtained from τ_{778} and the respective Stern-Volmer plot τ_{max}/τ-1 vs. pO_2; **(c):** T-sensitivity and the respective Boltzmann plot $ln(I_{740}/I_{778})$ vs. T^{-1}; and **(d):** pH-sensitivity and the respective calibration plots I_{520}/I_{570}-1 vs. pH values (adapted with permission from Ref.[400], Copyright © 2019, American Chemical Society).

For the TOP nanosensor **PS(CrBPh₄-NR)-S-F**, a rise of *T* from 283 K to 343 K led to an increased ratio of *I₇₄₀/I₇₇₈* (**Figure 50 (c)**), while the emission bands of the pH-indicator *I₅₂₀* and reference NR *I₅₆₀* were constant. This *T*-dependence follows a linear Boltzmann-type plot (inset in **Figure 50 (c)**), which is highly coincident with the thermal behavior of the molecular chromium(III) system in solution (**Figure 48 (c)**) and that of the single analyte nanosensor PS(CrBPh₄-NR)-S-NH₂ (**Figure 49 (c)**). Repeats of the thermal response in the *T*-range from 283 K to 343 K evidenced its reversible performance in *T*-sensing (**Figure 47**).
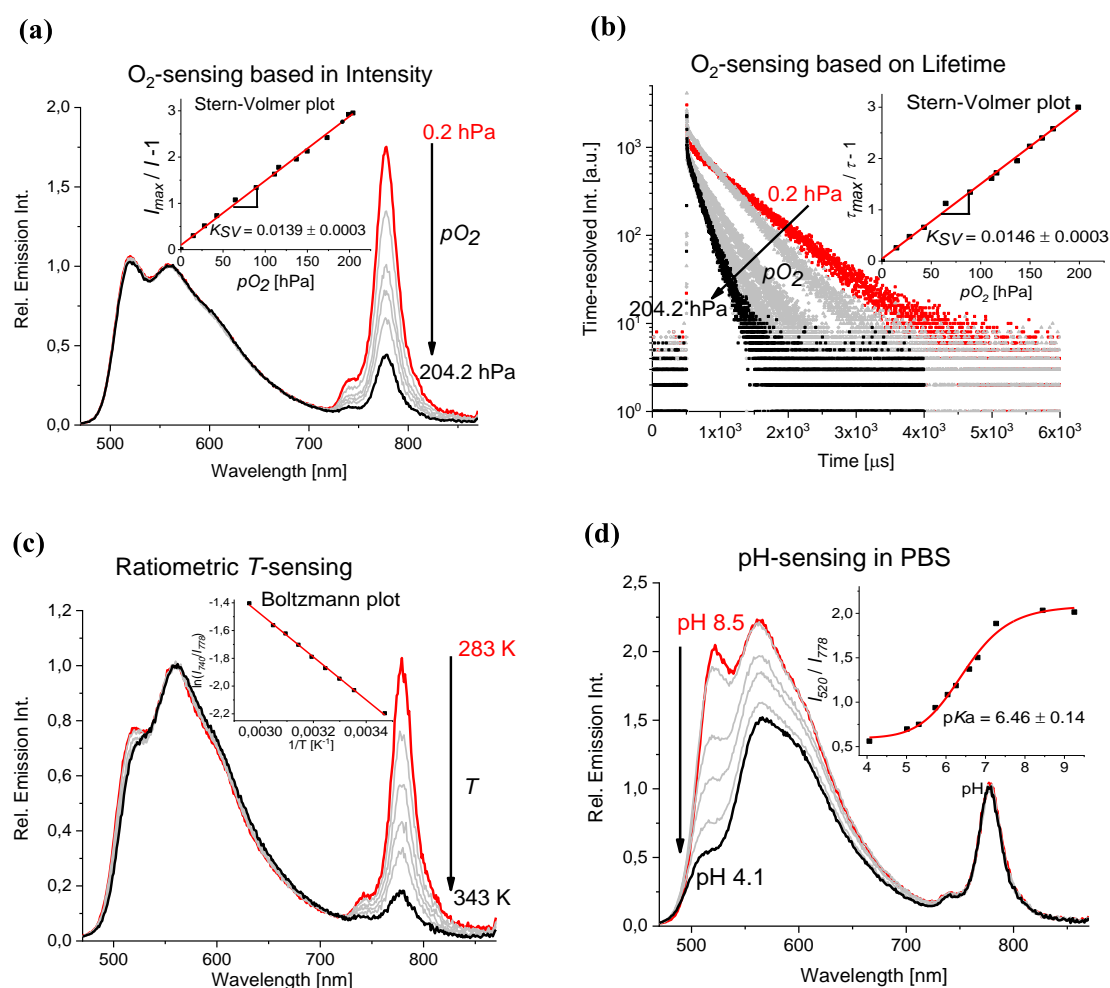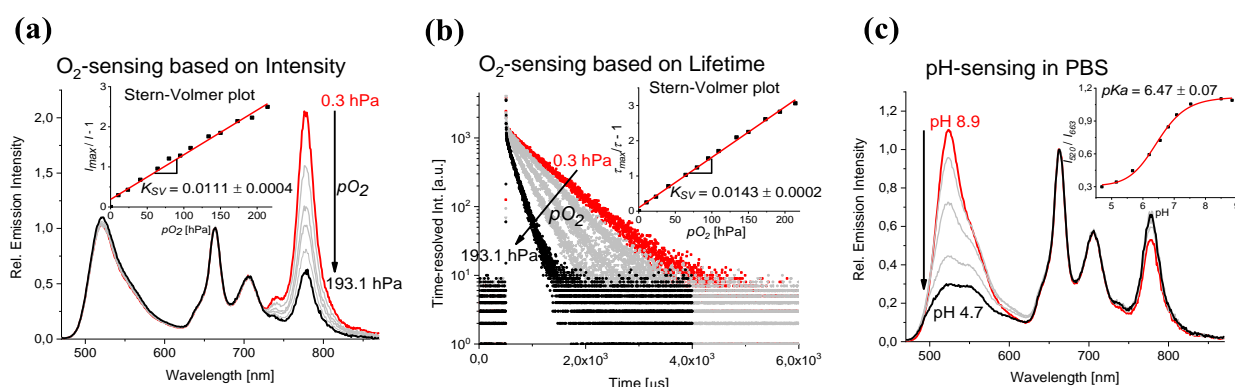

Figure 51: Luminescence emission intensity and lifetime of the dual nanosensor **PS(CrBPh₄-TFPP)-S-F** in PBS with changes in *pO₂* and pH (λ_{exc} = 435 nm): **(a)**: O₂-sensitivity derived from *I₇₇₈* and the respective Stern-Volmer plot *I_max/I-1* vs. *pO₂*; **(b)**: O₂-sensitivity based on τ_{778} and the respective Stern-Volmer plot τ_{max}/τ-1 vs. *pO₂*; **(c)**: pH-sensitivity and the respective calibration plot *I₅₂₀/I₅₇₀*-1 vs. pH values (adapted with permission from Ref.[400], Copyright © 2019, American Chemical Society).

For both nanosensors **PS(CrBPh₄-NR)-S-F** and **PS(CrBPh₄-TFPP)-S-F**, a decrease of pH from ca. 9 to 4 led to strongly weakened emission intensity *I₅₂₀* of the fluorescein (**Figure 50 (d)** and **Figure 51 (c)**). Notably, nanosensor **PS(CrBPh₄-NR)-S-F** displays partial spectral overlap in the emission bands of **FITC** and **NR**, resulting signal distortions for the luminescence readout of the reference dye. This issue can be addressed by applying the pH-inert emission intensity *I₇₇₈* of **CrBPh₄** as the reference signal. Hence, pH-sensing can be achieved with the intensity ratio *I₅₂₀/I₇₇₈*. By comparison, nanosensor **PS(CrBPh₄-TFPP)-S-F** showed bare spectral overlap between the emission band of different components. Thus, a ratiometric readout of the pH-indicator **FITC** and reference **TFPP** (*I₅₂₀/I₆₆₃*) is used for pH-sensing. The ratiometric pH-calibration plots of both nanosensors give the same p*Kₐ* value of around 6.4 (insets in **Figure 50 (d)** and **Figure 51 (c)**), which shows agreement with the p*Kₐ* value of **FITC** as molecular system in solution (**Figure 48 (d)**) and in monoanalyte nanosensor **PS-S-F** (**Figure 49 (d)**).

By comparing the sensing behaviors of the molecular indicators (**CrBPh₄** and **FITC**), the monoanalyte nanosensors (**PS(CrBPh₄-NR)-S-NH₂** and **PS-S-F**), and the multianalyte nanosensors (**PS(CrBPh₄-NR)-S-F** and **PS(CrBPh₄-TFPP)-S-F**), the conclusion can be drawn that the different components in the nanosensors do not interfere with each other and provide independent sensing behaviors.

These multianalyte nanosensors are designed for bioanalytical applications and their sensing behaviors to pO_2, pH, and T are supposed to be expressed in cell culture medium. Thus, sensing studies of the both TOP- and dual nanosensors were carried out in a model body liquid containing bovine serum albumin (BSA). The derived calibration parameters are listed in **Table 10** and compared with the results obtained in PBS. Each parameter was generated from measurements of three independent nanosensor samples and every sample was independently calibrated twice, yielding the respective standard derivations.

Nanosensors	Intensity-based K_{SV} [hPa^{-1}]	Lifetime-based K_{SV} [hPa^{-1}]	pK_a	Boltzmann slope [K]
PS(CrBPh₄-NR)-S-F in PBS	0.0139 ± 0.0024	0.0146 ± 0.0031	6.46 ± 0.14	-1546 ± 129
PS(CrBPh₄-NR)-S-F in cell culture	0.0106 ± 0.0012	0.0118 ± 0.0014	6.57 ± 0.17	-1551 ± 141
PS(CrBPh₄-TFPP)-S-F in PBS	0.0121 ± 0.0010	0.0143 ± 0.0012	6.47 ± 0.07	-
PS(CrBPh₄-TFPP)-S-F in cell culture	0.0103 ± 0.0019	0.0131 ± 0.0013	6.53 ± 0.13	-

Table 10: Sensing calibration parameters: Stern-Volmer slope for oxygen, pK_a value for pH sensing, and Boltzmann slope for temperature sensing with both multianalyte nanosensors **PS(CrBPh₄-NR)-S-F** and **PS(CrBPh₄-TFPP)-S-F** in PBS buffer and in cell culture medium (taken with permission from Ref.[400], Copyright © 2019, American Chemical Society).

Expectedly, both multianalyte nanosensors show the desired sensing behavior in cell culture medium as observed in PBS buffer (**Table 10**). Notably, in the culture medium the K_{SV} values derived from emission intensity and lifetime of both nanosensors are slightly lower than those in PBS buffer, pointing to a slightly reduced oxygen sensitivity. This may be attributed to the interaction of the nanoparticles with BSA molecules, which act as a model for the most abundant serum protein. The BSA proteins can be partially adsorbed to the particle surface, and thus forming a protein corona which limits the access of oxygen to the indicator inside

the particle. Formation of such a protein corona on nanoparticles is often undesired for biological applications. Yet this can be prevented *e.g.*, by modifying the nanosensors surface with a polyethylene glycol (PEG) shell.[435] In cell culture medium, the acidofluorometric behavior of the both nanosensors reveals pK_a values of 6.5, which match excellently with the derived results in PBS (**Table 10**). *T*-sensing studies of the TOP nanosensor **PS(CrBPh₄-NR)-S-NH₂** prove its linear Boltzmann-type thermal response with the same slope value in both cell culture medium and PBS (**Table 10**). In both media, the multianalyte nanosensors **PS(CrBPh₄-NR)-S-NH₂** and **PS(CrBPh₄-TFPP)-S-NH₂** yield a reversible response to temperature *T*, pO_2, and pH.

Conclusion

In summary, two multianalyte nanosensors are designed and developed for simultaneously measuring the biologically interesting parameters temperature *T*, oxygen partial pressure pO_2, and pH (TOP). This was achieved by combining the O_2- and *T*-sensitive $[Cr(ddpd)_2][BPh_4]_3$ complex (**CrBPh₄**) featuring extremely large Stokes shift with a pH-responsive fluorescein derivative (**FITC**) and an inert reference dye like Nile Red (**NR**) or 5,10,15,20-tetrakis-(pentafluorophenyl) porphyrin (**TFPP**) using a matrix of polystyrene nanoparticle (**PSNP**). The resulting nanosensors show high colloidal-, photo- and thermal stabilities in aqueous media. Upon one single wavelength excitation, these novel nanosensors perform independent and reversible luminescence response to the certain parameters (temperature, oxygen, pH) in PBS buffer and in a cell culture medium containing bovine serum albumin (BSA). Moreover, these nanosensors have wide dynamic ranges for these TOP parameters, covering biologically and physiologically relevant concentration scales. Furthermore, systematic sensing studies of molecular indicator systems, monoanalyte nanosensors and multianalyte nanosensors revealed that different sensor components do not interfere with each other and perform independently. This study will expand the concepts and approaches for developing multianalyte nanosensors for biological and bioanalytical applications. Further research will be extended to the bioanalytical sensing studies with these nanosensors, including surface modification with targeted bioligands, cellular uptake studies, and eventually sensing studies *in vivo*.

4.2 Optical Characterization and Sensor Applications of Pt(II)- and Pd(II) complexes

4.2.1 Introduction

Monomeric Pt(II)- and Pd(II) complexes yield generally phosphorescence emission (oxygen-sensitive) arising from a metal to ligand charge transfer (MLCT) process (Section 2.1.2). When these d^8 metal complexes feature a specific coordination geometry, such as square-planar, they tend to form aggregates due to the intermolecular coupling of the $d_z^2 \cdots d_z^2$ orbitals of the metals. As described above in Section 2.3.1, these interactions lead to the generation of the an energetically higher ground state and a lower excited state, namely the metal-metal to ligand charge transfer (MMLCT) states.[140,250] Typically, the newly formed ^{3}MMLCT emissive state of Pt(II) complexes is red-shifted and behaves insensitive to oxygen quenching.[436-438] In comparison with numerous luminescence Pt(II) complexes, examples of luminescent Pd(II) complexes are rather rare. This is mainly attributed to the significantly lower ligand-field splitting, yielding thermally accessible antibonding orbitals which favor nonradiative deactivations by excited-state distortions.[439,440] Examples of Pd(II)-based MMLCT process are even fewer due to the considerably weaker Pd$\cdots$Pd interactions and the lower energy of the 4d orbitals (Section 2.3.1).[255,256]

Although these d^8 metal complexes display promising photophysical and photochemical properties, their application potential is still limited by *e.g.* poor water-solubility and ACQ. These issues can be addressed by incorporating these complex molecules into a nanomatrix, such as metal-organic-frameworks, polymeric particles or films (see Section 2.2.3.1). Moreover, their luminescence properties can be improved due to the suppressed non-radiative deactivation pathways and intermolecular quenching (see Section 2.2.3.2). Furthermore, the matrix can enable the tuning of the optical properties by concentration control of the metal$\cdots$metal distances, leading to the formation of aggregation-induced MMLCT states by metal$\cdots$metal interactions (Section 2.3.1).

This study is focused on a series of ligand-controlled novel pincer Pt(II) – and Pd(II)-complexes. According to their molecular features, they are abbreviated as **PtLH**, **PtLF**, **PdLH** and **PdLF** (see **Table 2** in Section 3.1). These complexes were synthesized (by the Strassert´s group) and fully characterized regarding their structures and photophysical properties. Moreover, by encapsulating these complexes into polystyrene nanoparticles (PSNPs), their photophysical

properties were significantly enhanced. Meanwhile, the ^{3}MMLCT states of the Pt(II)– and Pd(II)-complexes were induced via aggregation inside the PSNPs, respectively. Benefiting from the newly formed oxygen-inert ^{3}MMLCT state, a colloidally stable, self-referenced oxygen nanosensor was developed by simply monitoring the complex loading concentration in the PSNPs, whose dynamic quenching by triplet oxygen was calibrated via Stern-Volmer studies based on luminescence emission intensity and kinetic decays.

4.2.2 Preparation and characterization of Pt(II)- and Pd(II) complexes loaded PSNPs

The highly hydrophobic complexes **PtLH**, **PtLF**, **PdLH** and **PdLF** were encapsulated into 100 nm-sized aminated PSNPs, respectively, via a simple one-step staining procedure (Section 3.3.1), yielding luminescent particles **PS(PtLH-series)**, **PS(PtLF-series)**, **PS(PdLH-series)** and **PS(PdLF-series)** (series indicates the complex loading concentration C_L). Increasing C_L from 0.1 mM to 2.0 mM and 4.0 mM leads to an increase in the hydrodynamic diameter of the stained particles from ca. 130 nm to ca. 150 nm, as determined by DLS measurements (Section 3.4). DLS results of the **PtLF**-loaded PSNPs are shown in **Table 11** as example. The generated luminescent PSNPs are highly homogeneous as confirmed by High Resolution Transmission Electron Microscopy (HRTEM), High-Angle Annular Dark-Field Microscocpy (HAADF) and Energy-dispersive X-ray spectroscopy (EDX). The HRTEM images are shown in **Figure 52** and the HAADF and EDX images are illustrated representatively for **PS(PdLF-0.5 mM)** in **Figure 53**.

Samples	Averaged hydrodynamic diameter [nm]	PDI (Polydispersity Index)
Blank PSNPs	131.1 ± 0.8	0.007 ± 0.005
PS(PtLF-0.1 mM)	132.3 ± 0.5	0.003 ± 0.001
PS(PtLF-0.5 mM)	136.6 ± 0.1	0.020 ± 0.014
PS(PtLF-1.0 mM)	140.8 ± 0.4	0.049 ± 0.007
PS(PtLF-2.0 mM)	146.0 ± 1.5	0.063 ± 0.027
PS(PtLF-3.0 mM)	142.6 ± 1.4	0.062 ± 0.006
PS(PtLF-4.0 mM)	153.4 ± 0.5	0.095 ± 0.015

Table 11: Size distribution of the **PS(PtLF-series)**, dispersed in H_2O with particle concentration of 1 mg/mL (submitted to Chemical Science).

PS(PtLH)   **PS(PtLF)**

PS(PdLH)   **PS(PdLF)**
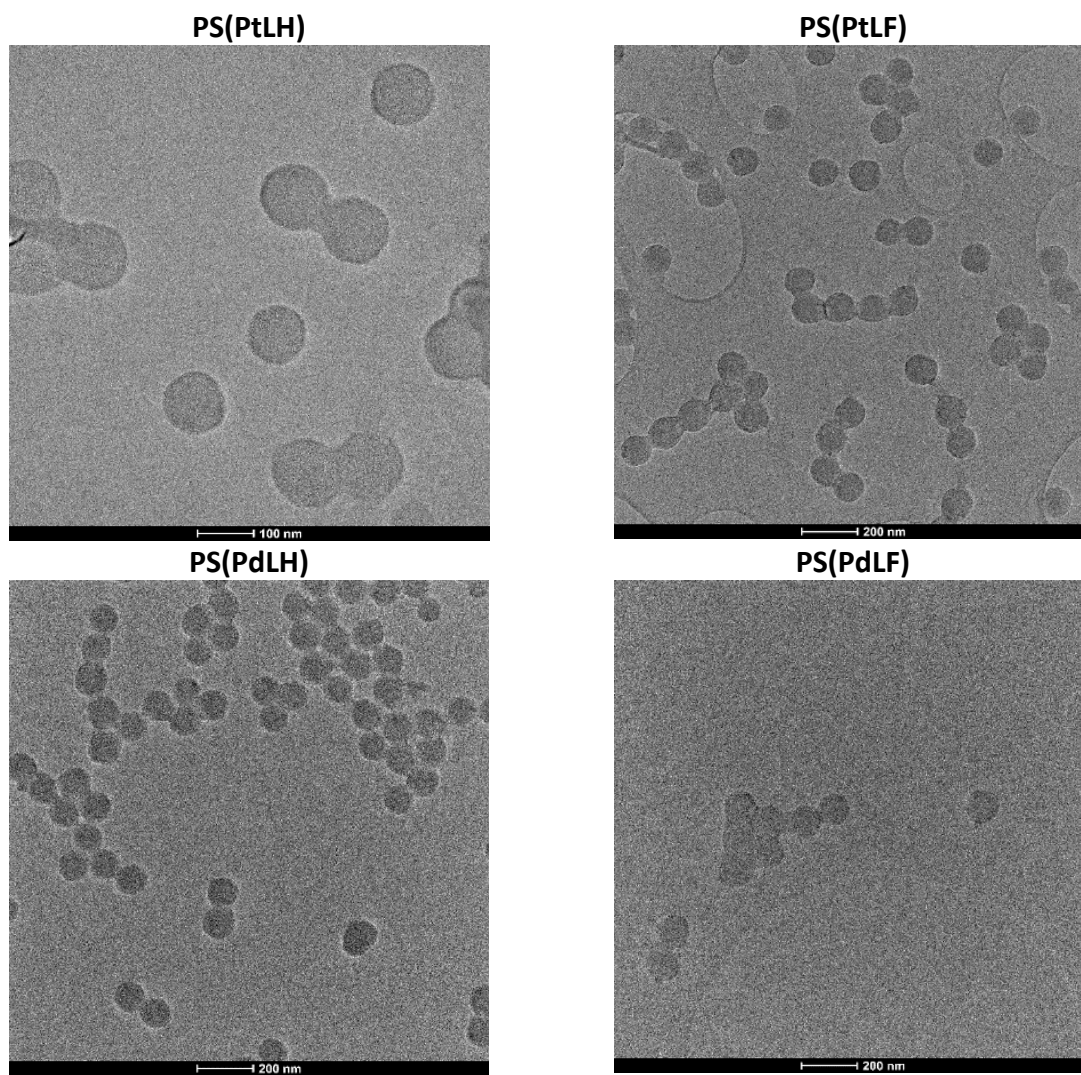
Figure 52: HRTEM images of monodispersed PSNPs loaded with **PtLH**, **PtLF**, **PdLH** and **PdLF** complexes, respectively (C_L = 0.5 mM). Images were taken by Dr. Ivan Maisuls (submitted to Chemical Science).
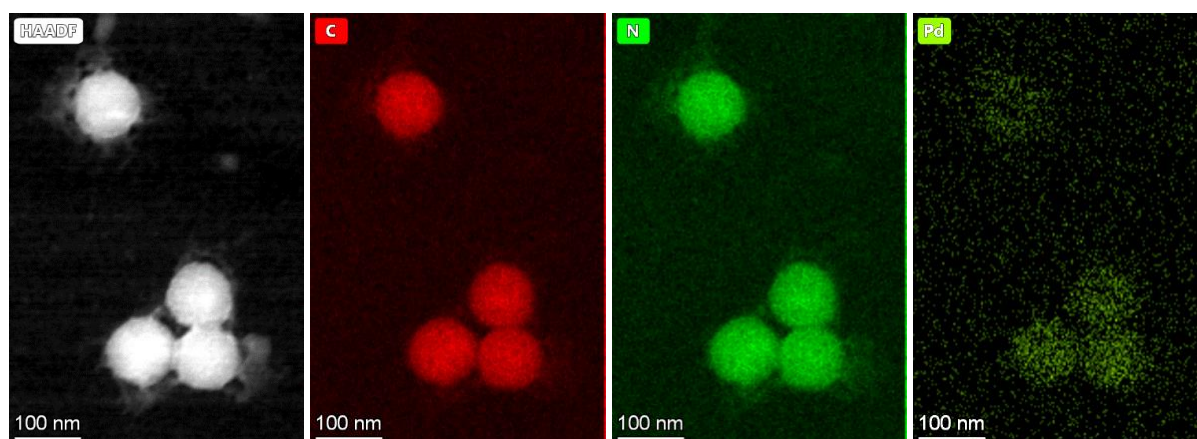
Figure 53: HAADF image and the corresponding EDX maps of monodisperse PSNPs loaded with **PdLF** complex (PS(PdLF-0.5 mM)). Images were taken by Dr. Ivan Maisuls (submitted to Chemical Science).

Additionally, leaking studies (Section 3.6) reveal the high stability of the entrapped complexes. Examples are shown in **Figure 54** with the spectral control of the **PS(PtLF)** suspension with low and high loading concentration of **PtLF**. After two days storage at room temperature, the negligible emission signal of **PtLF** in excess indicates the stability of the complex inside the particles, which is independent from C_L.

(a) **(b)**
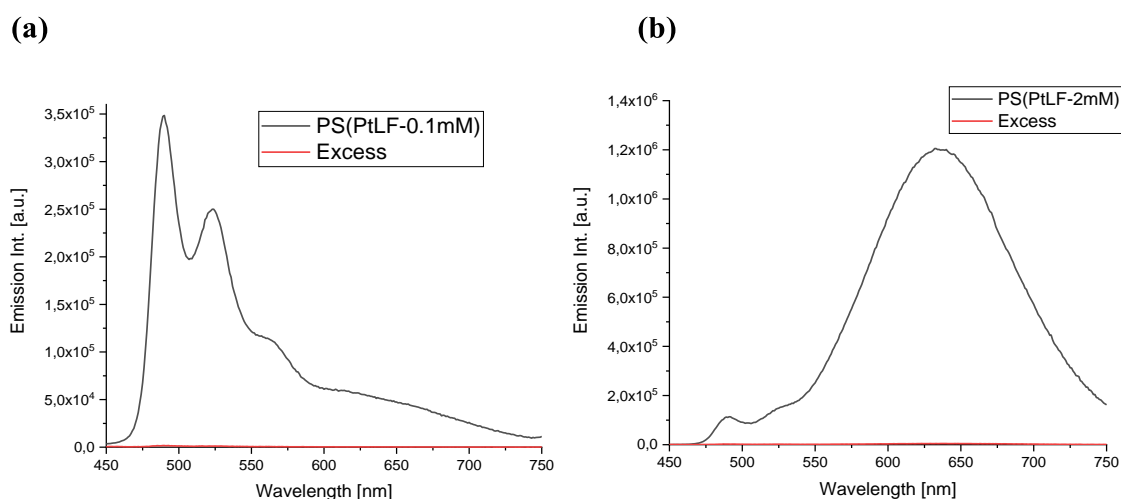
Figure 54: Emission spectra of freshly prepared **PtLF** loaded particles and of the corresponding excess after 2 days storage. (a) **PS(PtLF-0.1 mM)** in H_2O (black) and its excess (red); (b): fresh **PS(PtLF-2.0 mM)** in H_2O (black) and its excess (red) (submitted to Chemical Science).

Moreover, the spectroscopic quantification of the average complex loading number per particle was determined via absorption spectroscopy (see Section 3.5.1). Taking complex **PtLF** as an example, calibration samples were prepared in the DMF-PSNP (mass concentration of PSNP 0.1 mg/ml) with known **PtLF** concentration. Their respective absorbances (λ_{abs} = 325 nm) were measured and plotted as a function of the **PtLF** concentration (**Figure 55**). According to the obtained linear calibration curve, the **PtLF** concentrations were calculated by measuring the absorbance at 325 nm of the dissolved PS(PtLF-series) samples in DMF. The estimated number of **PtLF** molecules stained in each particle of PS(PtLF-series) are listed in **Table 12**.
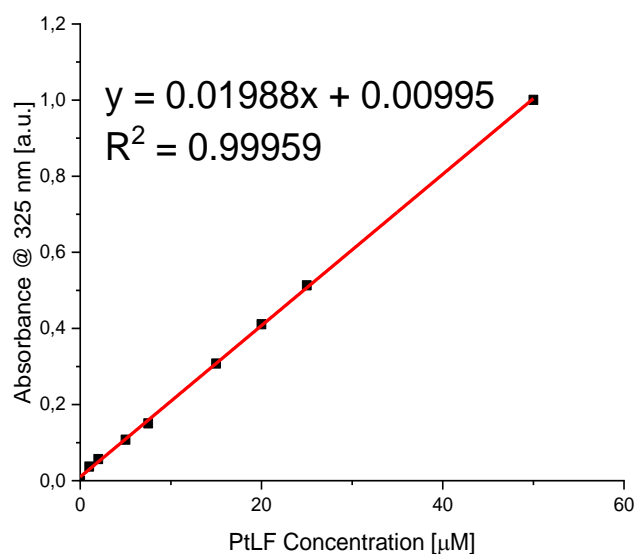
Figure 55: Calibration curve of **PtLF** in DMF-PSNP (0.1 mg/mL) with absorbance at 325 nm *versus* **PtLF** concentration (submitted to Chemical Science).

PS(PtLF-series)	y (Absorbance)	x (PtLF concentration in 0.1 mg/mL PS, μM)	N (Number of PtLF molecules per PSNP)
C_L-0.1 mM	0.02508	0.76 ± 0.01	2472 ± 33
C_L-0.2 mM	0.04670	1.85 ± 0.01	6004 ± 32
C_L-0.5 mM	0.09594	4.33 ± 0.03	14048 ± 97
C_L-1.0 mM	0.13119	6.10 ± 0.05	19806 ± 162
C_L-2.0 mM	0.26685	12.92 ± 0. 10	41969 ± 325

Table 12: Molecule number of **PtLF** stained in each PSNP particle of PS(PtLF-series) and the corresponding parameters (submitted to Chemical Science).

4.2.3 Photophysical studies of the PSNPs stained with Pt(II)- and Pd(II) complexes

Luminescence enhancement in PSNPs

Photophysical studies of the resulting luminescent PSNPs were carried out at room temperature via absorption spectroscopy (Section 3.7.2), luminescence steady-state and time-resolved spectroscopy (Section 3.7.3), and determination of absolute luminescence quantum yield (Section 3.7.4). By encapsulating the Pt(II)- and Pd(II)-complexes with various loading concentration C_L into the PSNPs, photophysical properties of these metal complexes

are improved with significantly increased luminescence quantum yields Φ_L and extended lifetimes τ, as summarized in **Table 13** and **Table 14**. Comparing the Pt(II)-complex stained PSNPs with the complex solution in THF, *e.g.* **PS(PtLF-0.1 mM)** with the lowest **PtLF** loading concentration C_L of 0.1 mM, the Φ_L is significantly enhanced by a factor of 26 under air saturation, while a removal of oxygen leads to a Φ_L approaching 80% (**Table 13**). The luminescence lifetimes of both Pt(II)-complexes are extended from a few hundred ns-range in THF solution to ca. 10 µs in the PSNPs under air saturation (**Table 13**).

Medium	PtLH ($\lambda_{exc.}$ = 405 nm)				PtLF ($\lambda_{exc.}$ = 388 nm)					
	$\Phi_L{}^{[3]}$ [%]		$\tau_{510}{}^{[2]}$ [µs]		$\Phi_L{}^{[3]}$ [%]		$\tau_{490}{}^{[2]}$ [µs]		$\tau_{635}{}^{[2]}$ [µs]	
	Air	Ar	Air	Ar	Air	Ar	Air	Ar	Air	Ar
in THF	1.4	51.4	0.11	4.00	1.8	46.9	0.25	8.06	-	-
$C_L{}^{[1]}$: 0.1 mM	36.0	55.1	8.97	12.56	47.3	79.3	10.28	15.10	7.52	9.94
C_L: 0.5 mM	23.4	32.7	8.99	12.80	61.5	72.1	10.77	15.34	6.71	6.57
C_L: 1.0 mM	14.5	19.8	9.67	12.81	59.1	66.2	9.79	14.57	6.70	6.84
C_L: 2.0 mM	7.9	10.9	8.90	12.09	64.6	70.3	10.05	14.30	7.66	7.96

Table 13: Luminescence quantum yields Φ_L and lifetimes τ data of the Pt(II)-complexes stained PSNPs dispersed in MilliQ water with a particle concentration of 0.25 mg/mL. **[1]**: The initial loading concentration C_L of metal complex for encapsulation into the PSNPs. **[2]**: Lifetimes τ_{510} and τ_{490} were fitted mono-exponentially, while lifetime τ_{635} were fitted bi-exponentially. The averaged lifetimes were calculated intensity-weighted, estimated τ uncertainty of ± 5%. **[3]**: Luminescence quantum yields Φ_L are estimated with an uncertainty of ± 5% (submitted to Chemical Science).

In terms of the Pd(II) complexes, both **PdLH** and **PdLF** demonstrate bare luminescence in THF solution with the Φ_L below 0.5%, yet these complexes can be lightened up by encapsulating them into the PSNPs, and thus achieve a quantum yield of 11.5% and 6.4% in the cases of degassed **PS(PdLH-0.1 mM)** and **PS(PdLF-3.0 mM)**, respectively (**Table 14**). Moreover, lifetimes τ_{488} and τ_{520} of the **PS(PdLH-series)** reach values above 100 µs in the absence of oxygen, which are extended around 300-folds compared with the free **PdLH** molecules in THF. Similarly, lifetimes τ_{480} and τ_{530} of **PS(PdLF-series)** are also increased to dozens µs from a few ns in THF solution. These improved optical properties of the complexes in PSNPs are probably attributed by the fact that in polymer matrix the molecular rigidification of the complexes is strengthened and the molecular vibrations, such as C-H oscillators on the ligands, are partially

prohibited due to steric limitation. It is hypothesized that non-radiative decays or quenching pathways are probably suppressed, accompanied by the enhanced luminescent properties.

Medium	PdLH ($\lambda_{exc.}$ = 335 nm)							
	Φ_L[3] [%]		τ_{488}[2] [µs]		τ_{520}[2] [µs]		τ_{561}[2] [µs]	
	Air	Ar	Air	Ar	Air	Ar	Air	Ar
in THF	0.2	0.4	0.11	0.37	_[4]	_[4]	_[4]	_[4]
C_L[1]: 0.1 mM	2.3	11.5	19.46	113.39	21.02	111.70	20.34	108.39
C_L: 0.5 mM	3.0	8.8	32.66	113.15	32.34	116.00	32.34	117.86
C_L: 1.0 mM	1.1	2.5	44.65	119.24	44.57	112.98	41.22	114.22
C_L: 2.0 mM	0.7	2.4	21.31	119.08	23.73	116.14	21.29	108.22
C_L: 3.0 mM	0.7	2.2	25.97	120.63	23.57	114.12	21.37	109.00
C_L: 4.0 mM	0.5	1.6	22.70	108.09	22.06	106.72	20.03	111.54
Medium (RT)	PdLF ($\lambda_{exc.}$ = 368 nm)							
	Φ_L[3] [%]		τ_{480}[2] [µs]		τ_{530}[2] [µs]		τ_{565}[2] [µs]	
	Air	Ar	Air	Ar	Air	Ar	Air	Ar
in THF	0.1	0.5	7.7E-3	13.1E-3	9.1E-3	17.7E-3	10.2E-3	16.6E-3
C_L: 0.1 mM	1.5	4.6	10.61	78.12	11.78	90.35	18.08	106.38
C_L: 0.5 mM	2.2	5.6	14.18	70.55	15.33	86.65	20.25	79.00
C_L: 1.0 mM	2.7	5.5	13.38	61.40	16.17	76.69	17.43	73.23
C_L: 2.0 mM	3.2	6.0	14.75	48.05	16.56	67.38	16.08	71.19
C_L: 3.0 mM	3.7	6.4	16.41	44.78	19.52	62.93	22.6	67.67
C_L: 4.0 mM	4.0	5.7	16.46	39.98	22.91	50.69	24.4	54.07

Table 14: Luminescence quantum yields Φ_L and lifetimes τ data of the Pd(II)-complexes stained PSNPs dispersed in MilliQ water with a particle concentration of 0.25 mg/mL. **[1]**: The initial loading concentration C_L of metal complex for encapsulation into the PSNPs. **[2]**: Lifetimes of PdLH and PdLF were fitted tri-exponentially and calculated intensity-weighted, estimated τ uncertainty of ± 5%. **[3]**: Luminescence quantum yields Φ_L are estimated with an uncertainty of ± 5%.[4]: Decay signals were too weak to be measured (submitted to Chemical Science).

Luminescence changes caused by aggregation

Increasing the complex loading concentration C_L 0.1 mM to 2.0 mM and eventually to 4.0 mM, complex aggregation is induced in different manners, depending on their molecular structures. Changes in Φ_L of the luminescent particles stained with the Pt(II)- and Pd(II)-complexes are illustrated in **Figure 56**. A rise of C_L leads to a clear drop of Φ_L of the **PS(PtLH-series)** and the

PS(PdLH-series), while the Φ_L of the **PS(PtLF-series)** and the **PS(PdLF-series)** tends to increase slightly under air saturation (**Figure 56**).
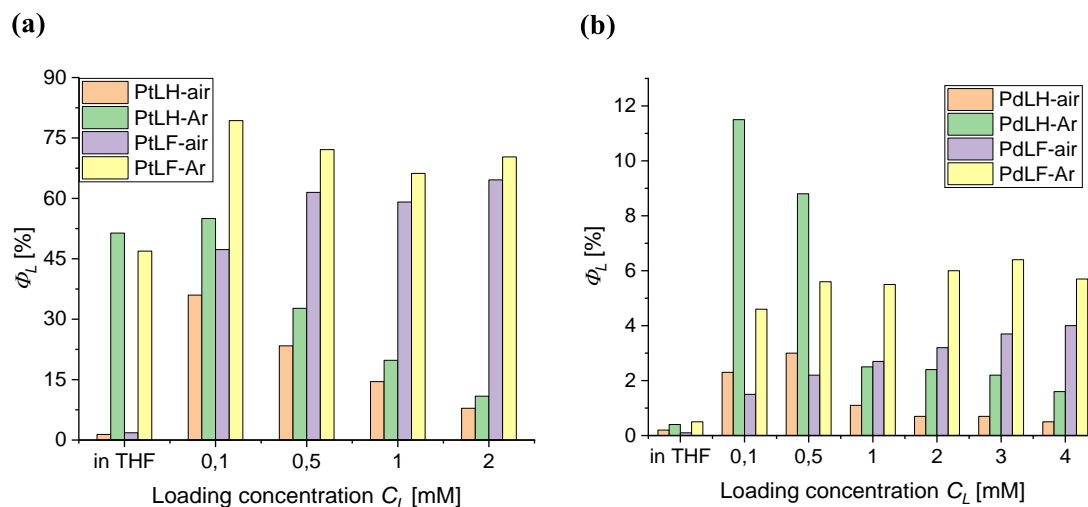
Figure 56: Φ_L *vs.* loading concentration C_L of the complexes **PtLH/PtLF (a)** and **PdLH/PdLF (b)** in PSNPs (submitted to Chemical Science).

To have more insights into the changes in luminescence caused by complex aggregation, luminescence emission spectra of the four complexes in PSNP with different loading concentrations are shown in **Figure 57**. With increasing C_L of **PtLH** and **PdLH** (**Figure 57 a)** and **c)**), the emission intensity of both the **PS(PtLH-series)** and **PS(PdLH-series)** increases (C_L from 0.1 to 0.5 mM) and then subsequently decreases (C_L above 0.5 mM). This phenomenon is usually caused by Aggregation-Caused-Quenching (ACQ) due to intermolecular π-π stacking interactions of the planar aromatic rings on the ligand.[221,222,441] The lifetimes of both **PtLH**- and **PdLH**-stained PSNPs series were independent to the C_L (**Table 13** and **Table 14**), while their $\Phi_{L(Ar)}$ were reduced significantly from 55.1% and 11.5% to 10.9% and 1.6% for the **PS(PtLH-series)** and the **PS(PdLH-series)**, respectively (**Figure 56**, **Table 13** and **Table 14**), revealing static quenching. The normalized emission spectra of **PS(PdLH-series)** were basically unchanged, indicating independence on C_L. (**Figure 57 c)**, upper panel).
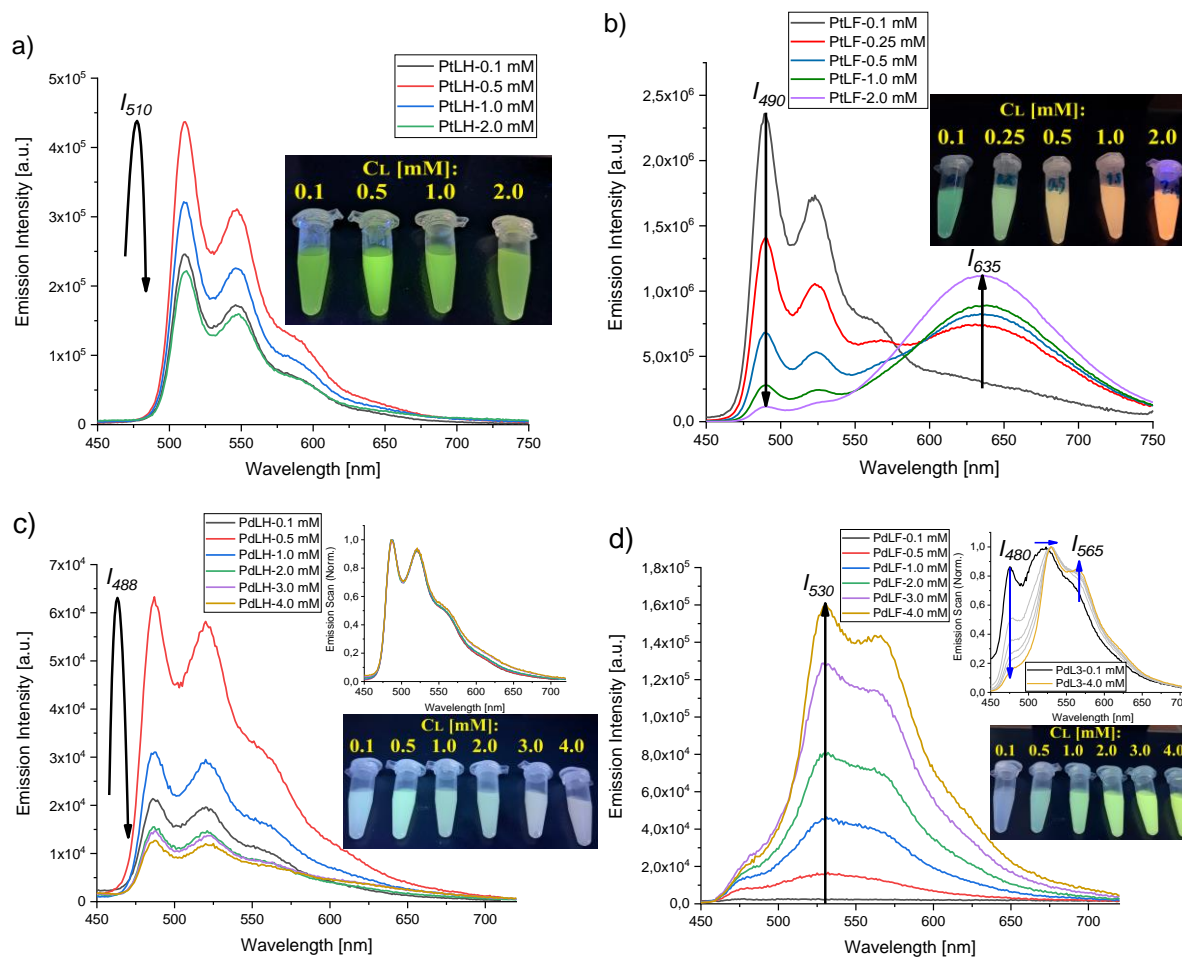
Figure 57: Luminescence emission spectra of the complex-stained PSNPs (1 mg/mL dispersed in MilliQ water) with different loading concentration. **a)** Luminescence emission spectra of PS(**PtLH**-series) under 405 nm excitation. Insets: PS(**PtLH**-series) dispersed in MilliQ water with C_L ranging from 0.1 mM to 2.0 mM; **b)** Luminescence emission spectra of PS(**PtLF**-series) under 388 nm excitation. Insets: PS(**PtLF**-series) dispersed in MilliQ water with C_L ranging from 0.1 mM to 2.0 mM; **c)** Luminescence emission spectra of PS(**PdLH**-series) under 335 nm excitation. Insets: (upper) normalized emission spectra of PS(PdLH-series) and (down) PS(PdLH-series) dispersed in MilliQ water with C_L ranging from 0.1 mM to 4.0 mM; **d)** Luminescence emission spectra of PS(**PdLF**-series) under 368 nm excitation. Insets: (upper) normalized emission spectra of PS(PdLF-series) and (down) PS(PdLF-series) dispersed in MilliQ water with C_L ranging from 0.1 mM to 4.0 mM. The insets pictures were taken under 365 nm UV lamp illumination under air saturation (submitted to Chemical Science).

By comparison, PSNPs stained with the fluorinated complex **PtLF** and **PdLF** indicate different aggregation-induced optical responses. Increasing the C_L of **PtLF** in the PSNPs (**Figure 57 b)**), the formed complex aggregate displays a rise of a red MMLCT emissive state at ca. 635 nm, while the green emission of the monomeric **PtLF** at 490 nm is depleted, and thus resulting in the colorimetric change of the **PS(PtLF-series)** samples (**Figure 57 b)** inset). Moreover, the quantum yield measurements of both the monomeric emission bands and the aggregate emission band also recorded the decrease of the monomer and the increase of the aggregate component (**Figure 58**). It has been reported that the formation of MMLCT strongly depends

on the Pt···Pt distance, which is typically under 3.5 Å[140,442]. In this system, the four F-atoms on the **PtLF** ligand enable the hydrogen bond interactions between the planar ligands and thus shortening the Pt···Pt distance in the aggregate to a desired value of 3.55 Å, as proven by the DFT calculation done by the cooperation partner. Consequently, the MMLCT states are formed in the PSNPs. Additionally, the bathochromical shift and existence of the long-wavelength absorption tail are usually assigned to the lowest excited state from MMLCT,[250,251,443] which were confirmed in this work with the absorption spectra of the **PtLF**-loaded PSNPs (**Figure 59 (a)**). Notably, the newly formed MMLCT emissive state of **PtLF** features shorter lifetime with bare oxygen sensitivity, in comparison with its monomer. More details will be discussed in the following oxygen sensitivity section.
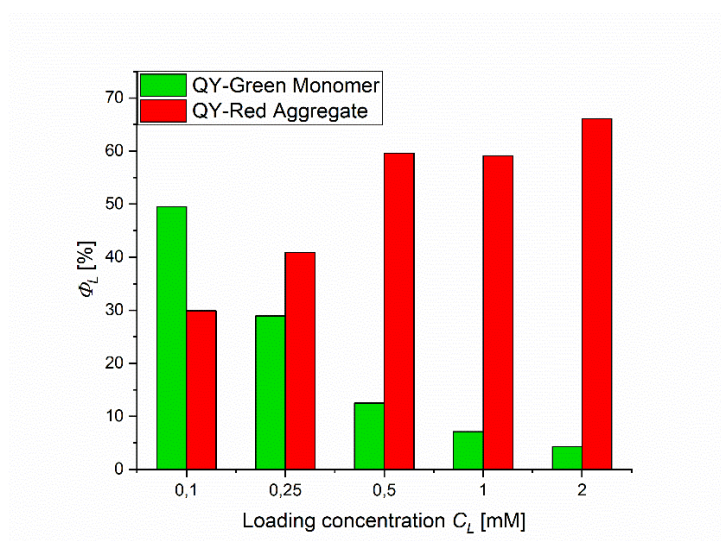

Figure 58: Quantum yields of monomer and aggregate emission of the **PS(PtLF-series)** under Ar-saturation (submitted to Chemical Science).
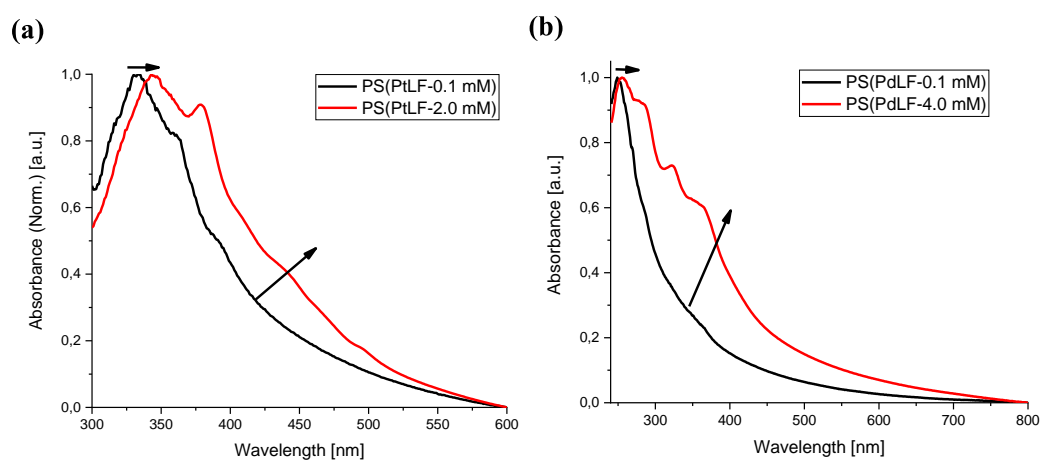

Figure 59: Absorption spectra of **(a) PS(PtLF-series)** and **(b) PS(PdLF-series)** with low (black) and high (red) loading concentration of 0.1 mM and 2.0 or 4.0 mM, respectively (submitted to Chemical Science).

In term of the **PS(PdLF-series)**, a rise of C_L from 0.1 to 4.0 mM led to an enhanced Φ_L of **PdLF** from 1.5% to 4.0% and 4.6% to 6.4% under air and Ar saturation (**Figure 56 (b)** and **Table 14**), respectively, accompanied by clearly enhanced emission intensity (**Figure 57 (d)**) and slightly extended lifetimes (τ_{480}, τ_{530} and τ_{565}) in the presence of oxygen (**Table 14**). However, the intensity-weighted average lifetimes of the degassed samples showed a clear tendency to decrease along the increasing C_L. This is assigned to the increased proportion of the emissive **PdLF** aggregate, which have a shorter lifetime compared to the monomer in PSNPs (**Table 14**). Notably, the normalized emission spectra of PS(**PdLF**-series) presented a clear change with decreased I_{480}, arise of I_{565} and the bathochromically shifted band around 530 nm (**Figure 57 (d),** upper inset), while the non-fluorinated **PdLH**-stained PSNPs displayed no spectral change in the normalized spectra (**Figure 57 (c),** upper inset). Similar to the **PtLF** aggregates discussed previously, we suggest that a new MMLCT excited state is also induced in the fluorinated **PdLF** aggregate formed in PSNPs. Yet the weak Pd···Pd interactions result in the formation of an energetically slightly lower MMLCT emissive state,[255] which is spectroscopically blended with the monomer emission bands. Thus, an increase in C_L yields an enhanced aggregate/monomer ratio and consequently changed spectra as shown in the upper inset of **Figure 57 (d)**. Absorption spectra revealed an increase in absorbance at ca. 400 nm (**Figure 59 (b)**), which confirms the newly formed MMLCT ground state of the **PdLF** aggregate.

Exponential decomposition based on lifetime measurements

In order to have a closer insight into the monomer/aggregate distribution of complex **PtLF** and **PdLF** in PSNPs, exponential decomposition studies were carried out based on the measurements of lifetime amplitudes of various components. Under air-saturation, time-resolved luminescence decays of **PS(PtLF-0.5 mM)** ($\lambda_{exc.}$ = 388 nm) and **PS(PdLF-0.5 mM)** ($\lambda_{exc.}$ = 368 nm) were obtained along their respective emission range of both monomer and aggregates. By fitting the luminescence decays multi-exponentially, the generated amplitudes for various lifetime components were plotted as a function of emission wavelength, accompanied by their respective normalized emission spectrum (**Figure 60**).

(a)

PS(PtLF-0.5 mM)

(b)
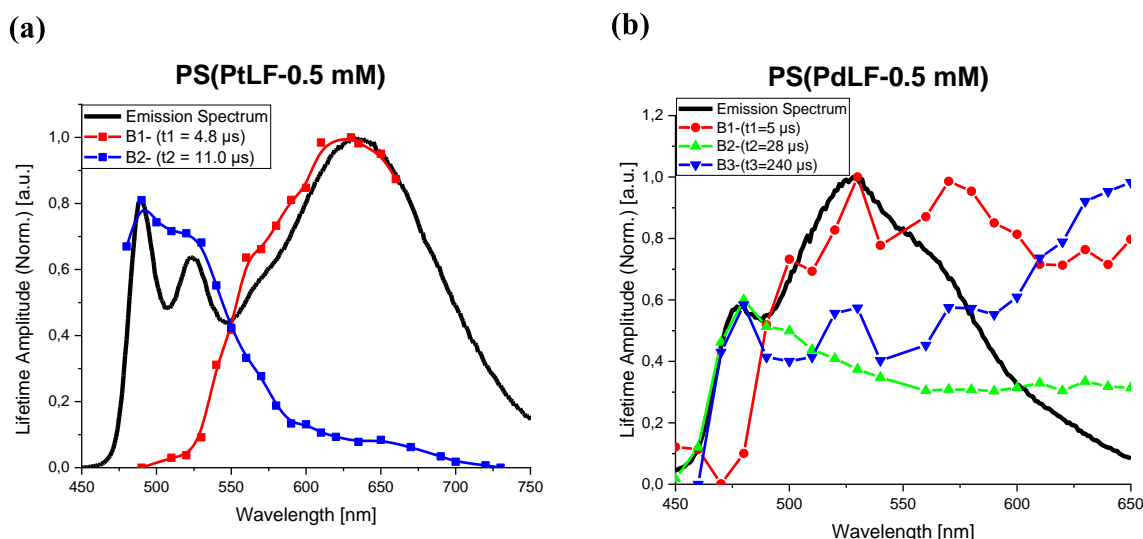
PS(PdLF-0.5 mM)

Figure 60: Lifetime amplitudes of **(a) PS(PtLF-0.5 mM)** and **(b) PS(PdLF-0.5 mM)** plotted as a function of the emission wavelength, together with the emission scan (solid line). **(a)** Amplitude B1 (red dotted line) corresponds to the fixed aggregate lifetime of τ_1 = 4.8 µs and amplitude B2 (blue dotted line) describes the monomer component with the fixed lifetime of τ_2 = 11.0 µs; **(b)** Amplitude B1 (red dotted line) corresponds to the fixed lifetime of τ_1 = 5.0 µs, B2 (green dotted line) describes the fixed lifetime component of τ_2 = 28.0 µs, while B3 (blue dotted line) is assigned to the component with the fixed lifetime τ_2 = 240.0 µs (submitted to Chemical Science).

For **PS(PtLF-0.5 mM)**, a bi-exponential decomposition of the luminescence decays led to a clear separation of the aggregate (τ_1 = 4.8 µs) and the monomer (τ_2 = 11.0 µs), as shown in **Figure 60 (a)**. Distributions of the corresponding lifetime amplitude B1 and B2 are highly consistent with their respective emission band, revealing the contribution of monomer and aggregate at each emission wavelength. Luminescence decay of **PS(PdLF-0.5 mM)** was decomposed by a tri-exponential lifetime fitting. The amplitude B1 (τ_1 = 5.0 µs) showed response at ca. 530 nm and 565 nm, yet with bare contribution at ca. 480 nm, demonstrating a similarity with the normalized emission spectra of **PS(PdLF-series)** (**Figure 57 (d),** upper inset). This confirms the lifetime component of τ_1 = 5.0 µs is originating from aggregates. Meanwhile, amplitude B2 (τ_2 = 28.0 µs) and B3 (τ_3 = 240.0 µs) display a peak at the monomeric emission band around 480 nm, supporting their generation from **PdLF** monomers. In comparison with the emission spectra, these lifetime-based exponential decomposition studies can provide a deeper understanding of the respective contribution of monomer and aggregate as a function of the emission wavelength.

4.2.4 Oxygen sensitivity studies of the PSNPs stained with Pt(II)- and Pd(II) complexes

The phosphorescence emission of the monomeric Pt(II)- and Pd(II) complexes can be quenched by triplet oxygen via Dexter-type energy transfer. To have a better insight into the dynamic quenching by oxygen, Stern-Volmer studies were systematically carried out with the Pt(II)- and Pd(II)-stained PSNPs with various loading concentration.

Stern-Volmer studies of PSNPs stained with Pt(II) complexes

By varying the oxygen partial pressure pO_2 from nearly 0 to ca. 200 hPa (air-saturated), luminescence response of **PS(PtLH-series)** and **PS(PtLF-series)** was measured in both steady-state and time-resolved spectra (details in Section [3.8](#)). For **PS(PtLH-series)**, dynamic quenching by oxygen resulted in a weakened emission intensity I_{510} and shortened lifetime τ_{510} of **PtLH**, as shown representatively for **PS(PtLH-0.5 mM)** in **Figure 61 (a)** and **(c)**. Their corresponding Stern-Volmer plots based on I_{510} and τ_{510} revealed a similar K_{SV} of 0.0029 ± 0.0001 and 0.0022 ± 0.0001 hPa^{-1}, respectively (**Figure 61 (b)** and **(d)**).
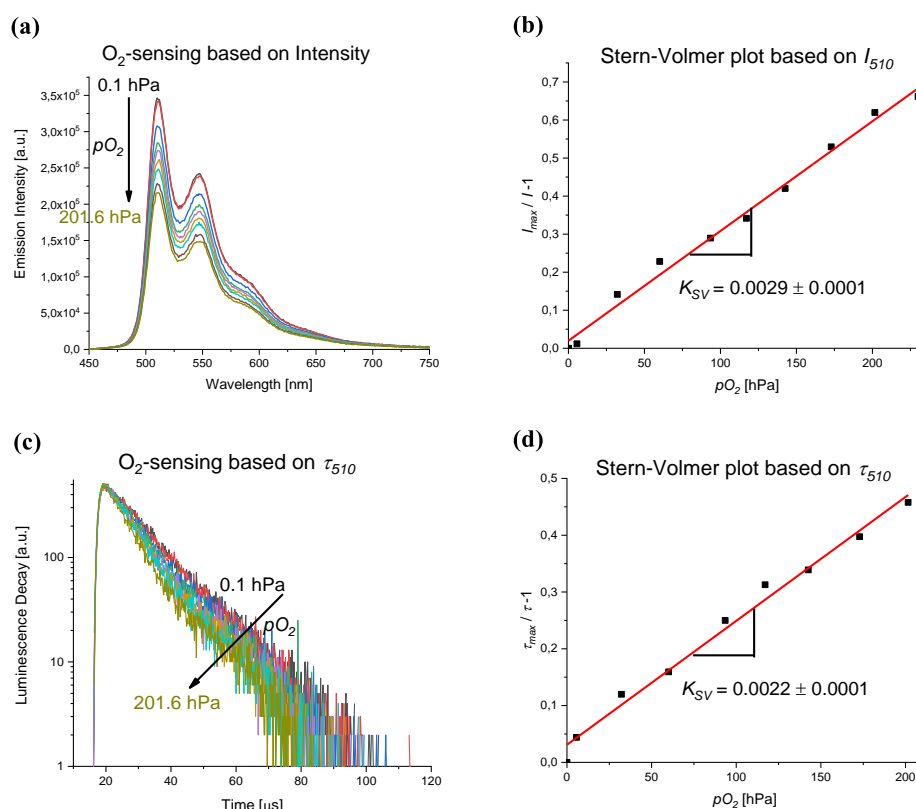

Figure 61: Stern Volmer studies of **PS(PtLH-0.5 mM)** based on emission intensity and lifetime ($\lambda_{exc.}$ = 405 nm): **(a)** Emission intensity response to pO_2 and **(b)** the corresponding I_{510}-based Stern-Volmer plot; **(c)** Luminescence decay (510 nm) response to pO_2 and **(d)** the τ_{510}-based Stern-Volmer plot (submitted to Chemical Science).

Interestingly, even though a rise of C_L in the PSNPs leads to ACQ of the **PtLH** luminescence, the oxygen sensitivity remains constant, as proven by the basically unchanged K_{SV} and K_q (quenching rate constant) values, as summarized in **Table 15**.

Samples	Stern-Volmer constant K_{sv} [hPa^{-1}]		Quenching rate constant K_q *[hPa^{-1} s^{-1}]	
	Intensity-based	Lifetime-based	Intensity-based	Lifetime-based
C_L-0.1 mM	0.0028 ± 0.0004	0.0021 ± 0.0003	223 ± 32	167 ± 24
C_L-0.5 mM	0.0029 ± 0.0001	0.0022 ± 0.0001	227 ± 31	164 ± 23
C_L-1.0 mM	0.0029 ± 0.0004	0.0023 ± 0.0003	226 ± 31	180 ± 23
C_L-2.0 mM	0.0026 ± 0.0004	0.0021 ± 0.0003	215 ± 33	174 ± 25

Table 15: Stern-Volmer constant K_{SV} and quenching rate constant K_q derived from the oxygen response (I_{510} and τ_{510}) of **PS(PtLH-series)**. *: $K_q = K_{SV}/ \tau_{max}$ (submitted to Chemical Science).

By comparison, **PS(PtLF-series)** displayed multiplexing emission bands including the oxygen-sensitive monomeric pattern with a maximum at 490 nm and the aggregate-induced MMLCT excited state at 635 nm with bare oxygen-sensitivity owning to the short lifetime. Such a combination realizes a self-referenced ratiometric oxygen sensor by utilizing the emissive state at 635 nm as the oxygen-inert reference signal. Taking **PS(PtLF-0.5 mM)** for instance, an increase in pO_2 resulted in decreasing I_{490} and τ_{490} of **PS(PtLF-0.5 mM)** (**Figure 62 (a)** and **(c)**), following linear Stern-Volmer plots with the similar K_{SV} values of 0.0032 ± 0.0001 and 0.0026 ± 0.0001, respectively (**Figure 62 (b)** and **(d)**). Meanwhile, the MMLCT emissive state performed its O$_2$-inertness in both intensity and lifetime domains (**Figure 62 (a), (e)** and **(f)**). Such a self-referenced ratiometric nanosensor is highly desired, as no additional reference dye is needed and only one excitation wavelength is required for the sensor system. Additionally, by monitoring the C_L of **PtLF** in PSNPs, the indicator/reference ratio (I_{490}/I_{635}) can be easily tuned for application relevant requirements. Importantly, the oxygen-sensitivity of **PtLF** performs independently from the C_L in PSNPs, as proven by the respective Stern-Volmer calibrations shown in **Table 16**. This confirms that oxygen quenching of the monomeric **PtLF** is not influenced by the formation of the aggregate and the MMLCT state, which is consistent with the stable oxygen-sensing behavior of **PS(PtLH-series)** described above (**Table 15**). Nevertheless, the $\tau_{490, max}$ decreased slightly with increasing C_L and thus resulted in an increase

of the quenching rate constant K_q. This might be due to a decreased monomer proportion, as aggregate with shorter lifetime tends to dominate the emission bands.
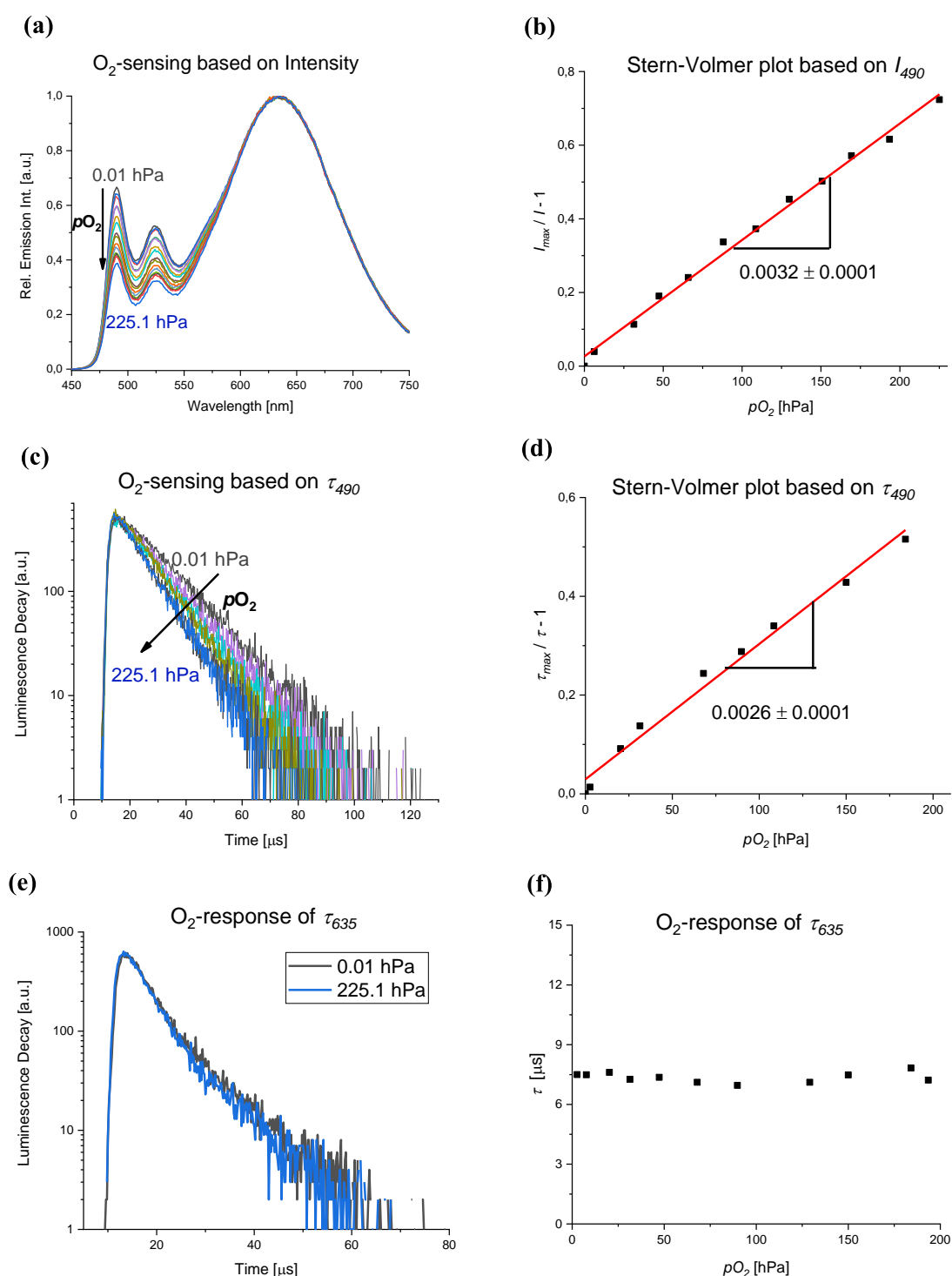
Figure 62: Stern-Volmer studies of **PS(PtLF-0.5 mM)** based on emission intensity and lifetime. **(a)** Emission intensity response to pO_2 and **(b)** the corresponding I_{490}-based Stern-Volmer plot; **(c)** Luminescence decay (490 nm) response to pO_2 and **(d)** the τ_{490}-based Stern-Volmer plot; (e) Luminescence decay (635 nm) with and without O_2 and (f) τ_{635} inertness to pO_2 (submitted to Chemical Science).

Samples	Stern-Volmer constant K_{sv} [hPa^{-1}]		Quenching rate constant K_q *[hPa^{-1} s^{-1}]	
	Intensity-based	Lifetime-based	Intensity-based	Lifetime-based
C_L-0.1 mM	0.0039 ± 0.0004	0.0026 ± 0.0003	249 ± 26	166 ± 19
C_L-0.5 mM	0.0032 ± 0.0004	0.0026 ± 0.0003	209 ± 26	170 ± 20
C_L-1.0 mM	0.0030 ± 0.0004	0.0026 ± 0.0003	206 ± 27	178 ± 21
C_L-2.0 mM	0.0030 ± 0.0004	0.0026 ± 0.0003	210 ± 28	182 ± 21

Table 16: Stern-Volmer constant K_{SV} and quenching rate constant K_q derived from the oxygen response (I_{490} and τ_{490}) of **PS(PtLF-series)** (submitted to Chemical Science).

Stern-Volmer studies of PSNPs stained with Pd(II) complexes

Similarly, optical response of both **PS(PdLH-series)** and **PS(PdLF-series)** to oxygen were studied based on luminescence measurements of emission spectra and kinetic decays (Section 3.8). Differing from the Pt(II) complexes, both monomeric Pd(II) complexes consist of multiple components. Different lifetime components might demonstrate various oxygen response, thus the overall Stern-Volmer plots do not follow a linear fit.[292]

For **PS(PdL1-series)**, oxygen quenching of the emission intensity I_{488} followed a linear Stern-Volmer mode, while the intensity-weighted average lifetime τ_{488} yielded a non-linear response to oxygen, as shown for **PS(PdLH-0.5 mM)** in **Figure 63**. Yet this non-linear plot can be separated in two sections, yielding two linear fits.
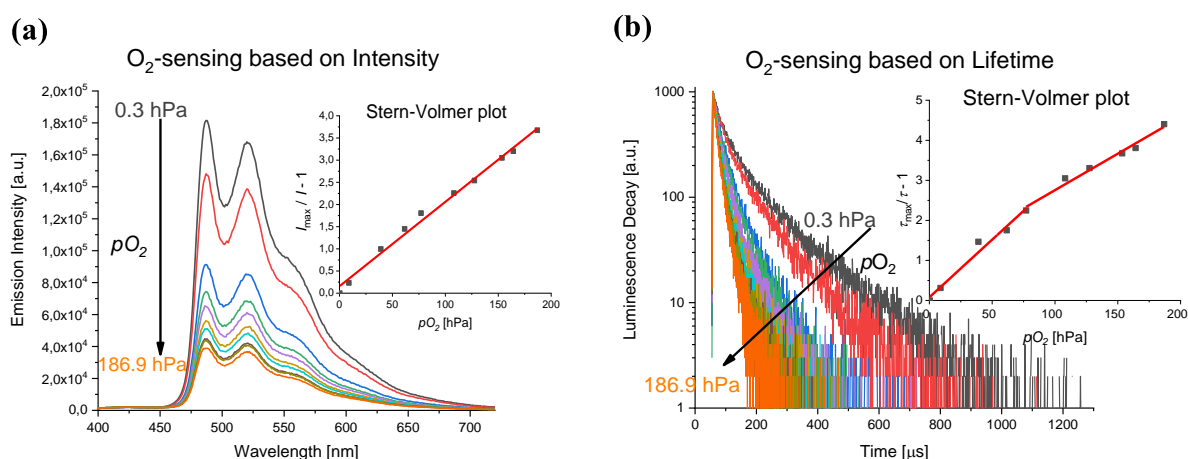

Figure 63: Stern-Volmer studies of **PS(PdLH-0.5 mM)** based on emission intensity and lifetime ($\lambda_{exc.}$ = 335 nm). **(a)** Emission intensity response to pO_2 and the corresponding Stern-Volmer plots based on I_{488} (inset); **(b)** Luminescence decay (488 nm) response to pO_2 and the τ_{488}-based Stern-Volmer plot (inset).

To explore the oxygen-sensing behavior of the multiple components in **PdLH** complex, Stern-Volmer studies of **PS(PdLH-series)** were systematically carried out at different emissive states, namely at 488 nm and at 520 nm. The resulting calibration parameters are summarized in **Table 17**. The K_{SV} derived from I_{488} and I_{520} are identical with the value around 0.018 hPa^{-1}, while the I_{488}- and I_{520}-based K_{SV} display value of ca. 0.030 and 0.017 in the first and second fitting section, respectively. Obviously, changes in C_L demonstrate bare influence on the K_{SV} and K_q of **PdLH**, which is coincident with the phenomena observed in **PS(PtLH-series)** and **PS(PtLF-series)**.

C_L [mM]	λ_{em} [nm]	Intensity-based K_{sv} [hPa^{-1}]	Lifetime-based K_{sv} [hPa^{-1}]		Quenching rate constant K_q [hPa^{-1}s^{-1}]	
			Section 1	Section 2	Section 1	Section 2
0.1	488	0.0166 ± 0.0009	0.0306 ± 0.0025	0.0173 ± 0.0006	270 ± 22	153 ± 5
0.5	488	0.0190 ± 0.0006	0.0288 ± 0.0026	0.0182 ± 0.0013	254 ± 23	161 ± 11
	520	0.0186 ± 0.0006	0.0299 ± 0.0015	0.0142 ± 0.0022	258 ± 13	122 ± 19
1.0	488	0.0176 ± 0.0004	0.0301 ± 0.0018	0.0168 ± 0.0008	253 ± 15	141 ± 7
	520	0.0174 ± 0.0003	0.0303 ± 0.0020	0.0166 ± 0.0005	268 ± 18	147 ± 4
2.0	488	0.0183 ± 0.0004	0.0299 ± 0.0026	0.0171 ± 0.0006	251 ± 22	144 ± 5
	520	0.0182 ± 0.0004	0.0279 ± 0.0019	0.0175 ± 0.0003	240 ± 16	151 ± 3
3.0	488	0.0168 ± 0.0011	0.0320 ± 0.0023	0.0169 ± 0.0012	265 ± 19	140 ± 10
	520	0.0164 ± 0.0010	0.0299 ± 0.0015	0.0153 ± 0.0004	262 ± 13	134 ± 4
4.0	488	0.0135 ± 0.0006	0.0315 ± 0.0021	0.0175 ± 0.0004	291 ± 19	162 ± 4
	520	0.0132 ± 0.0006	0.0267 ± 0.0015	0.0148 ± 0.0006	250 ± 14	139 ± 6

Table 17: Stern-Volmer constant K_{SV} and quenching rate constant K_q derived from the oxygen response of $I_{488/520}$ and $\tau_{480/520}$ of **PS(PdLH-series)** (submitted to Chemical Science).

On the contrary, Stern-Volmer plots of **PS(PdLF-series)** revealed clear differences with increasing C_L. With lower C_L, *e.g.* PS(PdLF-0.5 mM), oxygen-sensitivity based on I_{475} (and τ_{475}) and I_{530} (and τ_{530}) revealed basically the same slope value, namely the same K_{SV} (**Figure 64 a), b)** and **c)**). However, with a high C_L of 4 mM the oxygen response of I_{480} (and τ_{480}) differed clearly from that of I_{530} (and τ_{530}), yielding various K_{SV} (slope) values, regardless in the emission intensity or lifetime domains (**Figure 64 d), e)** and **f)**). The calibration parameters are summarized in **Table 18**. Interestingly, the K_{SV} and the K_q values derived from I_{530} (or τ_{530}) show high tendency to decrease with rising C_L. This is assigned to the increasing contribution of the

aggregation-induced MMLCT state of **PdLF**, which shows also a slight oxygen sensitivity. This observation offers another piece of evidence that the emission band at ca. 530 nm is supported by both the monomer- and aggregate emissive states. Moreover, the K_{SV} and the K_q of the second section derived from $I_{475/480}$ (or $\tau_{475/480}$) becomes gentler along the increasing C_L. Possibly, the oxygen-sensitive components of **PdLF** monomer can be influenced by the formation of aggregate.
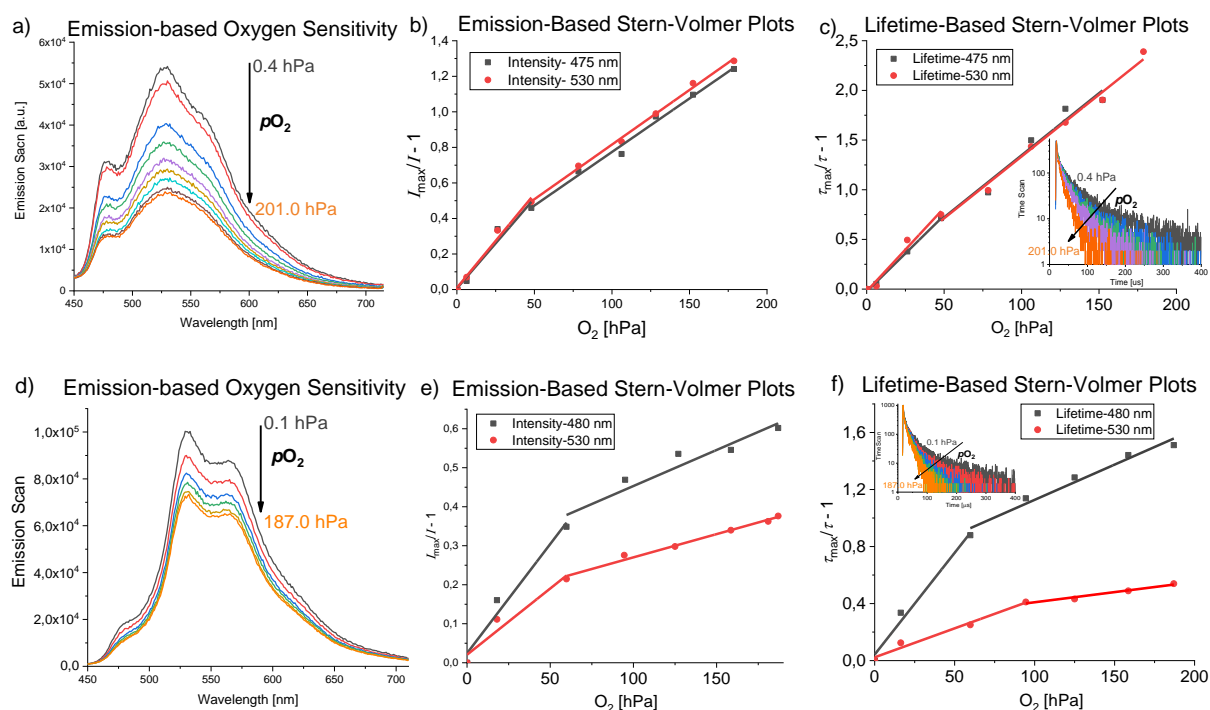
Figure 64: Stern-Volmer studies of **PS(PdLF-0.5 mM)** and **PS(PdLF-4.0 mM)**. a) Emission spectra of PS(PdLF-0.5 mM) at various pO_2; b) Emission intensity I_{475}- and I_{530}-based Stern-Volmer plots; c) Lifetime (τ_{475} and τ_{530})-based Stern-Volmer plots; inset: Lifetime τ_{475} response to pO_2; d) Emission spectra of **PS(PdLF-4.0 mM)** at various pO_2; e) Emission intensity I_{480}- and I_{530}-based Stern-Volmer plots; f) Lifetime (τ_{480} and τ_{530})-based Stern-Volmer plots; inset: Lifetime τ_{480} response to pO_2 (submitted to Chemical Science).

C_L [mM]	λ_{em} [nm]	Intensity-based K_{sv} [hPa^{-1}]		Lifetime-based K_{sv} [hPa^{-1}]		Quenching rate constant K_q [hPa^{-1}s^{-1}]	
		Section 1	Section 2	Section 1	Section 2	Section 1	Section 2
0.1	475	0.0068 ± 0.0003	0.0022 ± 0.0002	0.0191 ± 0.0007	0.0121 ± 0.0011	224 ± 8	142 ± 13
	510	0.0120 ± 0.0003	0.0044 ± 0.0004	0.0240 ± 0.0008	0.0131 ± 0.0004	266 ± 9	145 ± 4
0.5	475	0.0101 ± 0.0015	0.0060 ± 0.0003	0.0153 ± 0.0005	0.0125 ± 0.0014	196 ± 6	160 ± 18
	530	0.0106 ± 0.0010	0.0062 ± 0.0002	0.0168 ± 0.0019	0.0124 ± 0.0007	194 ± 22	143 ± 8
1.0	480	0.0114± 0.0021	0.0044 ± 0.0003	0.0220 ± 0.0023	0.0127 ± 0.0005	312 ± 33	180 ± 7
	530	0.0094 ± 0.0021	0.0036 ± 0.0002	0.0211 ± 0.0014	0.0061± 0.0007	276 ± 18	80 ± 9
2.0	480	0.0105 ± 0.0005	0.0049 ± 0.0003	0.0171 ± 0.0003	0.0083 ± 0.0007	279 ± 5	135 ± 11
	530	0.0094 ± 0.0007	0.0029 ± 0.0001	0.0090 ± 0.0011	0.0029 ± 0.0001	134 ± 16	43 ± 2
3.0	475	0.0083 ± 0.0005	0.0015 ± 0.0003	0.0174 ± 0.0016	0.0046 ± 0.0003	362 ± 33	96 ± 6
	530	0.0065 ± 0.0009	0.0008 ± 0.0003	0.0076 ± 0.0003	0.0006 ± 0.0004	121 ± 5	9 ± 6
4.0	480	0.0056 ± 0.0010	0.0019 ± 0.0003	0.0143 ± 0.0017	0.0049 ± 0.0005	319 ± 38	109 ± 11
	530	0.0034 ± 0.0009	0.0012 ± 0.0007	0.0041 ± 0.0004	0.0014 ± 0.0002	81 ± 8	28 ± 4

Table 18: Stern-Volmer constant K_{SV} and quenching rate constant K_q derived from the oxygen response of $I_{480/530}$ and $\tau_{480/530}$ of **PS(PdLH-series)** (submitted to Chemical Science).

4.2.5 Conclusion

In summary, by encapsulating the novel Pt(II)- and Pd(II) complexes into PSNPs, their luminescence properties have been significantly enhanced, reaching a quantum yield of ca. 80% for the fluorinated Pt(II) complex and extended lifetime over 100 μs for the Pd(II) complex. Particularly, the barely luminescent Pd(II) complexes were successfully lightened up in PSNPs due to the rigidization-induced suppression of the non-radiative decays of the emissive states. In PSNPs, increasing loading concentration of the complex led to formation of the aggregate, which induced the MMLCT states of the fluorinated Pt(II)- and Pd(II)- complexes. This is contributed by the four-fluoride atoms on the complex ligand, which can form hydrogen-interactions with another complex ligand and thus yielding complex aggregation and metal···metal interactions. Interestingly, the newly formed MMLCT emissive state (I_{635}, τ_{635}) of the fluorinated Pt(II) complex displayed bare response to oxygen, while the O_2-senstivity of the monomeric emissive state (I_{490}, τ_{490}) performed independence on the formation of aggregation. This realized a self-referenced ratiometric nanosensor with tunable indicator/reference ratio. O_2-sensing studies of the PSNPs stained with Pd(II) complexes

revealed non-linear Stern-Volmer behaviors due to the instinct multiple components of the complexes and the formation of the aggregation-induced MMLCT state. This photophysical study will provide strategies for improving and changing the luminescent properties of transition metal complexes. Moreover, it will expand the few examples of self-referenced ratiometric nanosensors, particularly by utilizing the MMLCT state. The combination of these complexes with polymeric nanoparticles will serve as an application platform for providing luminescent nanoparticles for bioimaging and biosensing.

4.3 Energy Upconversion Study in Metal-Organic Framework doped with Pd(II) complex

4.3.1 Introduction

Triplet–triplet annihilation upconversion (TTA-UC) is drawing increasing interests for applications range from bioimaging and sensing to solar energy conversion.[150,273,280] Typically, this two-photon process requires a strongly absorbing and long-lived sensitizer such as heavy metal compounds (*e.g.* Pt(II)- and Pd(II) porphyrins), and annihilator molecules with a high luminescence quantum yield like 9,10-diphenylanthracene (DPA, Φ_{DPA} = 95%) (Section 2.3.4). Such combinations have yielded high upconversion efficiency Φ_{UC} in solution.[274,275,444]

Nevertheless, TTA-UC systems in solid state are also considerably desired for energy upconversion devices as well as sensors. This can be achieved by introducing the chromophores in soft materials, such as organic or coordination polymers, nanocapsules, or micelles.[445-448] However, in less ordered systems, control over the relative orientation of the chromophores and their intermolecular interactions is rather challenging. In comparison, highly ordered systems, such as metal-organic frameworks (MOFs), allow the optimization of the diffusion length of the triplet excitons.[449] Promising examples of MOF-based TTA-UC system are realized by *e.g.* using anthracene-based linkers and palladium sensitizers on surfaces (I_{thresh} = 104 mW·cm^{-2}; Φ_{UC} = 0.46%),[450] two surface-anchored MOFs containing the palladium- and anthracene-based linkers, respectively (I_{thresh} = 25-117 mW·cm^{-2}; Φ_{UC} = 0.1%),[451] and MOFs encompassing mixed sensitizer/annihilator linkers (I_{thresh} = 2.5 mW·cm^{-2}; Φ_{UC} = 1.28%).[150] Such geometries can sufficiently reduce dimerization/aggregation of the porphyrin sensitizers and thus aggregation-caused quenching.

In this study, a novel MOF-based TTA-UC system was developed. Pd(II) porphyrin derivative **Pd(TCPP)** and **DPA** were chosen as the sensitizer and the annihilator, respectively. This combination is energetically favored for a TTA-UC process, as illustrated in **Figure 65 (a)**. Details of the mechanism can be found in Section 2.3.4. A crystalline mesoporous MOF structure PCN–222 was used as the matrix with $Zr_6(\mu_3\text{-OH})_8(OH)_8$ as the secondary building units (SBUs) and metalloporphyrin as a linker. The PCN-222(M) series (M = Mn, FeCl, Co, Ni, Cu and Zn) is well-known for high thermal and chemical stability.[149] As shown in **Figure 65 (b)**, the **Pd(TCPP)** sensitizer was coordinatively immobilized in the MOF hexagonal channel walls as the linkers, while the DPA annihilator was filled in the channels of the MOF via adsorption. To improve the mobility of DPA and thus enabling efficient TTET and TTA processes, hydrophobic caprylic acid (CA; octanoic acid) was coordinated to the SBUs of the MOF for offering a "solvent"-like microenvironment. The MOF samples in this study were synthesized by the Heinze´s group.[452]
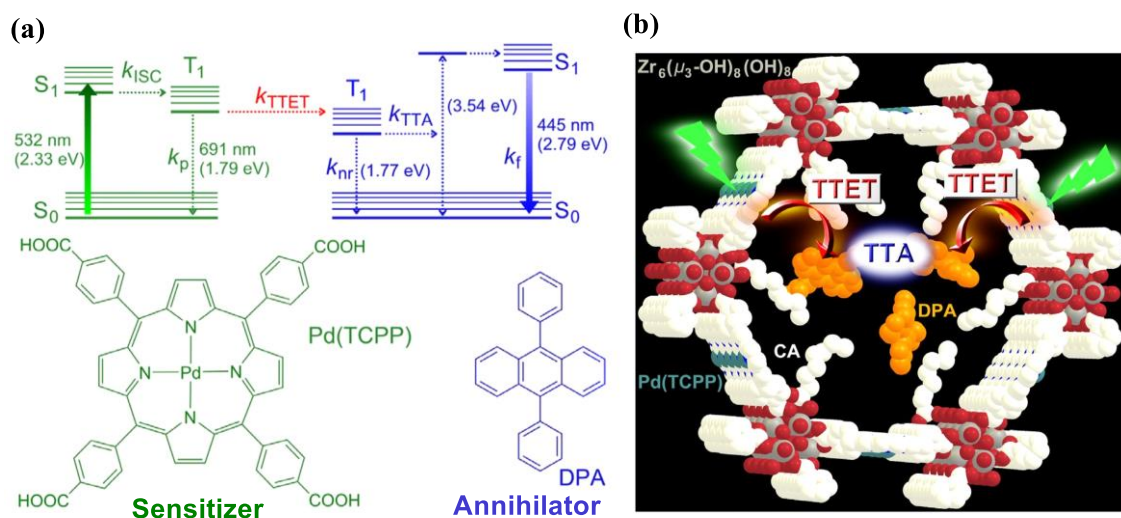
Figure 65: (a) Jablonski diagram of TTA-UC with **Pd(TCPP)** as a sensitizer and **DPA** as an annihilator and **(b)** design concept for the **CA/DPA@PCN-222(Pd)** TTA-UC MOF; **Pd(TCPP)** as a linker and triplet donor; $Zr_6(\mu_3\text{-OH})_8(OH)_8$ as SBUs; **DPA** as a triplet acceptor; CA as "solvent" in the hexagonal channels coordinated to the SBUs; grey (Zr), red (O), blue (N), white (C), light blue (Pd), H atoms omitted (adapted with permission from Ref.[452], Copyright © 2019 The Authors. Published by Wiley-VCH Verlag GmbH & Co. KGaA.).

Single-crystal XRD studies of the generated TTA-UC MOFs **CA/DPA@PCN-222(Pd)** revealed a hexagonal unit cell (a = b = 42.455(7) Å; c = 17.1037(2) Å) of the resulting needle-shaped crystals, which matches that of the reported analogue PCN-222(FeCl).[149] The Pd···Pd distances across the small trigonal pore, the large hexagonal pore and along the channels were

determined to be ca. 9.9, 16.9 and 19.8 Å, respectively. Such distances can efficiently prevent porphyrin aggregation, thus supporting efficient energy transfer. Successful insertion of DPA in the MOF channels was confirmed via NMR spectroscopy with a ^{19}F-labelled 1,2,3,4,5,6,7,8-octafluoro-9,10-bis(4-trifluoromethyl-phenyl) anthracene (DPA-F$_{14}$) and UV/Vis absorption spectra measurements. IR spectrum of the CA-coated MOF **CA@PCN-222(Pd)** demonstrated different binding modes to the SBU, including the dominating coordination bonds and a few hydrogen-bond. The uptake amount of **DPA** in **CA/DPA@PCN-222(Pd)** was determined photometrically to 0.29 – 0.66 mg **DPA**/ mg **PCN-222(Pd)**. Leaking studies in toluene and in water at 70°C proved that DPA molecules are favorably localized in the hydrophobic host in water. Experimental details for the photophysical studies can be found in Section 3.7.3.

4.3.2 Challenges caused by oxygen

The major challenge for detection of TTA-UC process is oxygen. In a TTA-UC process, oxygen quenching of the triplet sensitizer (such as **Pd(TCPP)**) yields the formation of singlet oxygen $^1O_2$. This Dexter-type energy transfer (to oxygen) acts as a undesired deactivation pathway of the triplet excited sensitizer, which occurs much faster than the TTET process between sensitizer and annihilator.[453] Thus, a TTET-TTA-UC process hardly occurs in the presence of residual oxygen. Moreover, the resulting reactive $^1O_2$ can lead to photobleaching of the MOF system. Due to the extremely porous MOF structure, complete removal of oxygen is hardly achieved by purging with argon. Notably, after consuming the traces of O_2 in the MOF channels, sensitizer **PCN-222(Pd)** became photostable, as shown in **Figure 66 (a)**. To exclude oxygen in the MOF system, various approaches have been tested, including using Na$_2$SO$_3$ as an O_2 scavenger, or sealing the MOF with an O_2-barrier polymer, such as polyvinyl alcohol (PVOH) (Section 3.3.3). The latter presented a better exclusion of oxygen according to the irradiation study (**Figure 66 (b)**). However, even minimal oxygen quenching can suppress the TTET efficiency and thus reduces the overall TTA-UC efficiency.
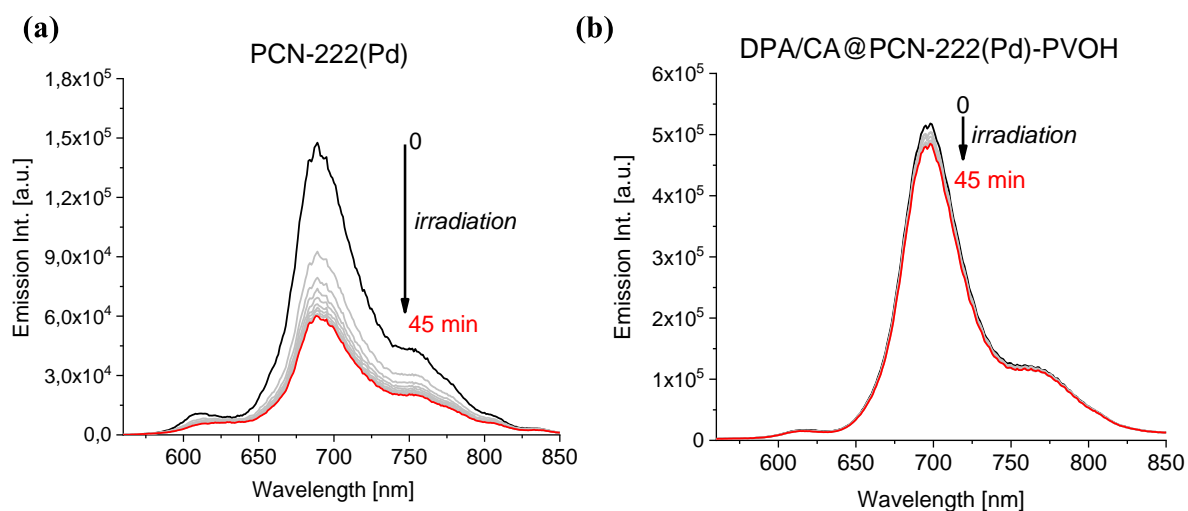
Figure 66: Photostability study of **(a) PCN-222(Pd)** and **(b) DPA/CA@PCN-222(Pd)-PVOH** under laser irradiation (λ_{exc} = 532 nm, 5.25 mW, 45 min) in the presence of O_2 traces (**(a)** adapted with permission from Ref.[452], Copyright © 2019 The Authors. Published by Wiley-VCH Verlag GmbH & Co. KGaA.).

In order to ensure a complete absence of oxygen in the MOF channels, all synthetic post-modification procedures and optical studies were carried out under rigorous exclusion of O_2. As a result, **PCN-222(Pd)** demonstrated high photostability (**Figure 67**) without photobleaching or quenching.
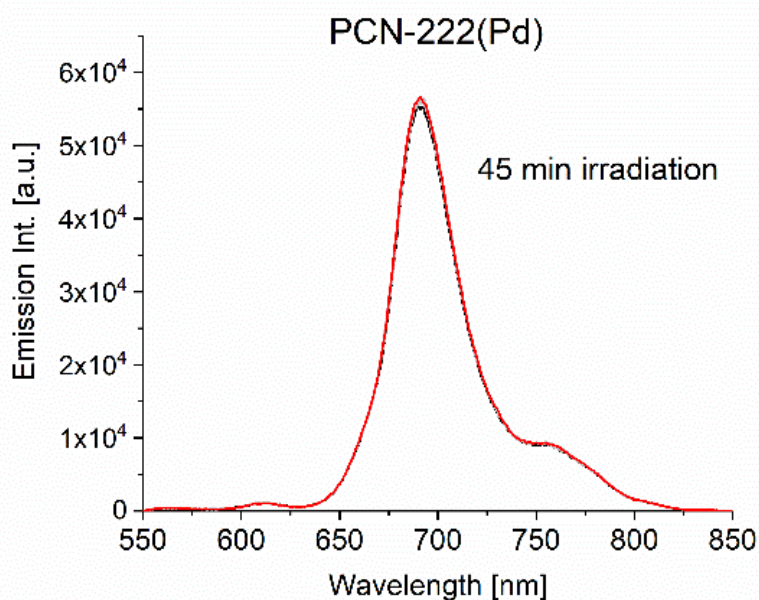
Figure 67: Photostability study of **PCN-222(Pd)** under laser irradiation (λ_{exc} = 532 nm, 5.25 mW, 45 min) in the absence of O_2.

4.3.3 Triplet-Triplet Annihilation Upconversion Luminescence

The TTA-UC studies was carried out by measuring the luminescence emission spectra and lifetimes of the MOF-based TTA-UC sample **CA/DPA@PCN-222(Pd)** (Section [3.7.3](#)). Upon photo excitation ($\lambda_{exc.}$ = 532 nm), UC luminescence spectra were obtained, covering the emission range of the sensitizer and the annihilator (**Figure 68 (a)**). A blue emission of DPA is observed near 440 nm, proving the successful TTA-UC process.[451] Moreover, both the **Pd(TCPP)** phosphorescence and the TTA-UC emission from **DPA** present high photostability under laser irradiation. By introducing oxygen to the system on purpose, the DPA emission disappeared immediately (**Figure 68 (b)**). As oxygen has no effect on DPA fluorescence, this O_2-response clearly confirms that the DPA emission originates from TTA-UC.
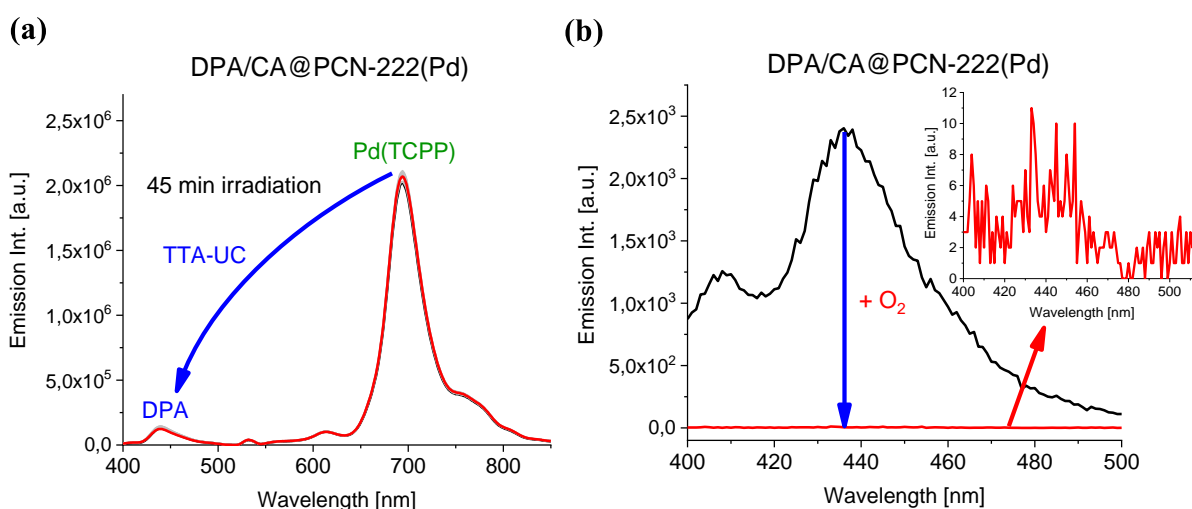
Figure 68: UC luminescence spectra of **CA/DPA@PCN-222(Pd)**: **(a)** photostability study under laser irradiation (λ_{exc} = 532 nm, 5.25 mW, 45 min) in the absence of O_2 and **(b)** deactivation of UC luminescence by oxygen (adapted with permission from Ref.[452], Copyright © 2019 The Authors. Published by Wiley-VCH Verlag GmbH & Co. KGaA.).

Furthermore, TTA-UC process was also confirmed by measuring the delayed fluorescence of **DPA** in **CA/DPA@PCN-222(Pd)**. For this purpose, lifetime of pristine DPA in solid state was firstly determined. As different fluorescence spectrometers were used in this study, luminescence decay of DPA crystal was measured on the FLS 920 spectrometer and a fluorescence microscope (Section [3.7.3](#)), respectively (**Figure 69**). By comparison, both decays obtained from different instruments reveal the same DPA fluorescence lifetime of 4.1 ± 0.2 ns. Expectedly, the luminescence decay of DPA in the MOF is significantly delayed due to the TTA-UC process, achieving a far longer lifetime of 373 ± 5 µs (**Figure 70**). Additionally, the rise

behavior before decay demonstrates the TTA-UC energy migration. These lifetime measurements confirmed the TTA-UC process, as well.

(a) DPA Decay obtained on FLS 920

(b) DPA Decay obtained on Microscope

τ_{av} = 3.9 ns
R_2 = 1.318

τ_{av} = 4.3 ns
R_2 = 1.078
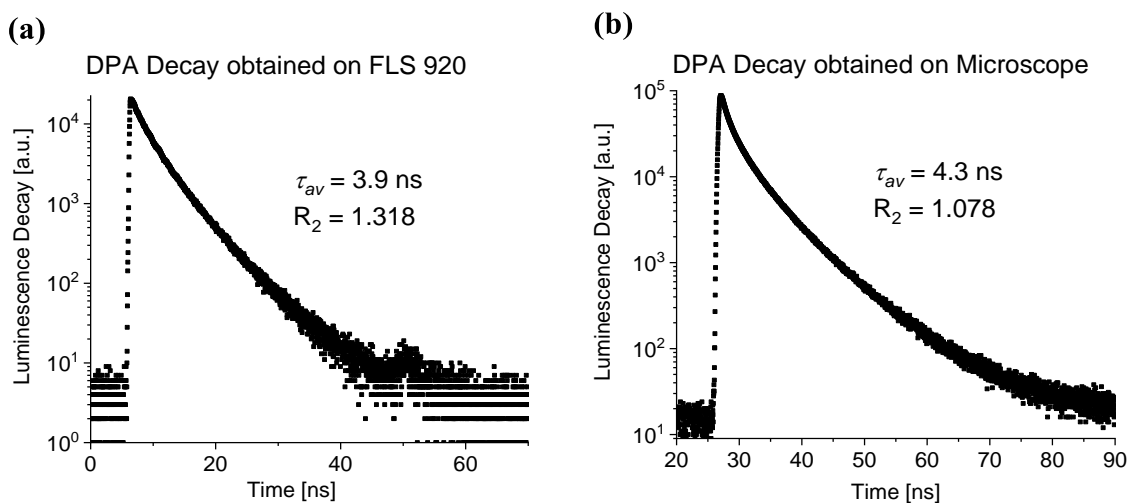
Figure 69: Luminescence decays of DPA ($\lambda_{em.}$ = 440 nm) in solid state under direct excitation: **(a)** DPA decay obtained from the FLS 920 spectrometer under 405 nm excitation (9.7 MHz), and **(b)** DPA decay obtained from a fluorescence microscope under 410 nm excitation (5.0 MHz) (adapted with permission from Ref.[452], Copyright © 2019 The Authors. Published by Wiley-VCH Verlag GmbH & Co. KGaA.).

TTA-UC Luminescence Decay

- TTA-UCL Decay of DPA
- Fit-curve
- IRF

τ_{av} = 373 ± 5 µs
R_2 = 1.264
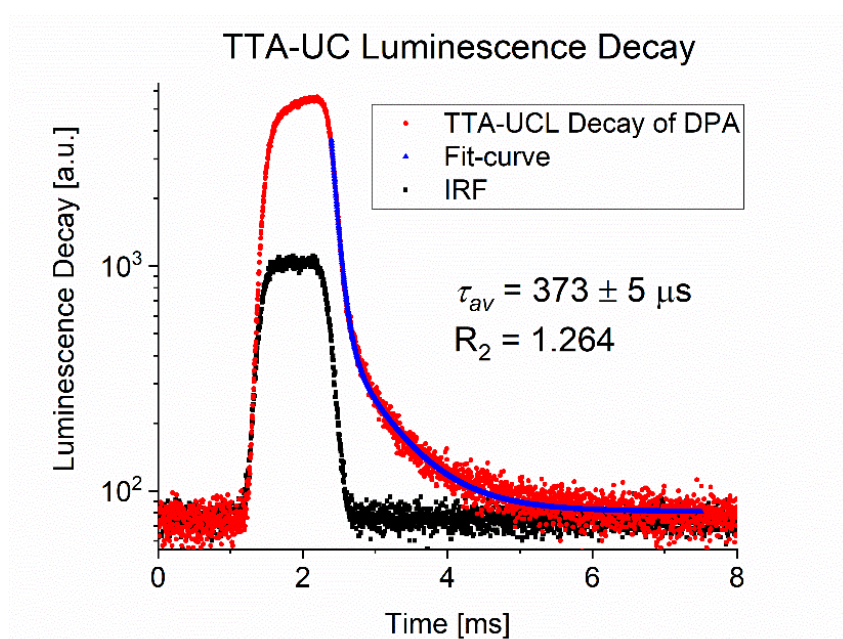
Figure 70: TTA-UC luminescence decay of **DPA** in **CA/DPA@PCN-222(Pd)** ($\lambda_{exc.}$ = 524 nm, $\lambda_{em.}$ = 440 nm, determined by the fluorescence microscope) (adapted with permission from Ref.[452], Copyright © 2019 The Authors. Published by Wiley-VCH Verlag GmbH & Co. KGaA.).

4.3.4 UC efficiency determination

Another figure of merit of the TTA-UC is the UC efficiency. In this study, the UC efficiency was determined relatively according to **Eq. 1** (Section 2.3.4). Firstly, the TTET efficiency Φ_{TTET} needs to be determined. For this purpose, steady state emission spectra and kinetic decays of the **Pd(TCPP)** sensitizer in **PCN-222(Pd)** and in **CA/DPA@PCN-222(Pd)** were measured. As shown in **Figure 71**, the sensitizer displays in **PCN-222(Pd)** a lifetime of $\tau_{S,0}$ = 702 ± 1 µs, while the presence of the annihilator **DPA** leads to a strong lifetime decrease to τ_{S-A} = 129 ± 1 µs due to the TTET process. Thus, the Φ_{TTET} derived from lifetime is determined to be 82% (Φ_{TTET} = 1 - τ_{S-A} / $\tau_{S,0}$). Similarly, the Φ_{TTET} can also be estimated according to the emission intensities of the sensitizer Pd(TCPP) in the absence and presence of the annihilator DPA (**Figure 72**). Luminescence emission spectra of the solid CA/DPA@PCN-222(Pd) were obtained from several different points of the sample. This yields the intensity-based Φ_{TTET} in the range of 77 – 85%, supporting the lifetime-based data. According to **Eq. 1** (Section 2.3.4), the maximal UC efficiency $\Phi_{UC,max}$ of CA/DPA@PCN-222(Pd) is estimated to be 4.3%, with the assumption that Φ_{ISC} = 100%, Φ_{TTA} = 11.1% and Φ_{DPA} = 95%.
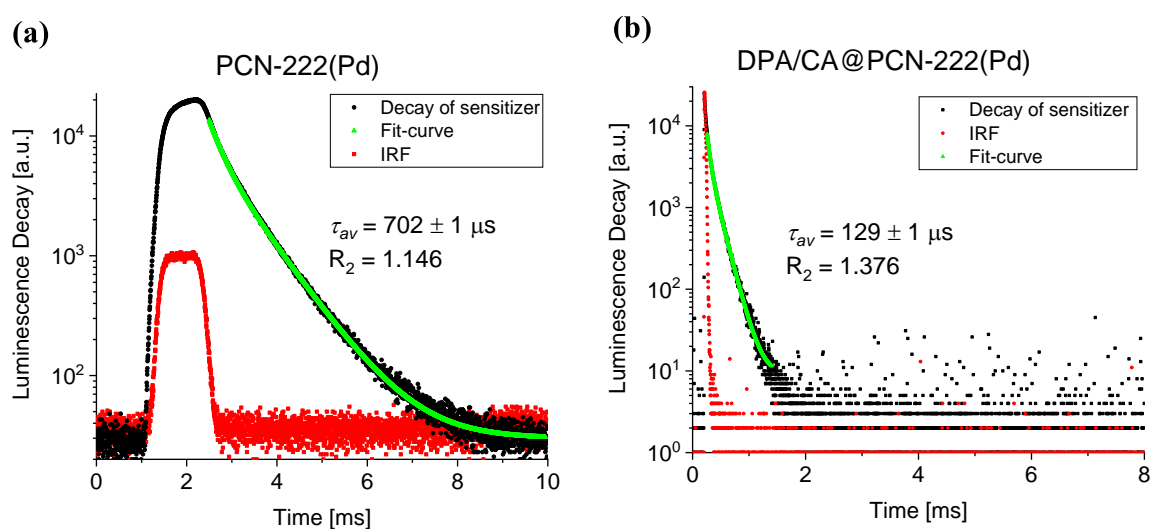
Figure 71: Luminescence decay of the sensitizer **Pd(TCPP)** in **(a) PCN-222(Pd)** (λ_{exc} = 524 nm, λ_{em} = 707 nm) and in **(b) DPA/CA@PCN-222(Pd)** (λ_{exc} = 524 nm, λ_{em} = 690 nm) (adapted with permission from Ref.[452], Copyright © 2019 The Authors. Published by Wiley-VCH Verlag GmbH & Co. KGaA.).
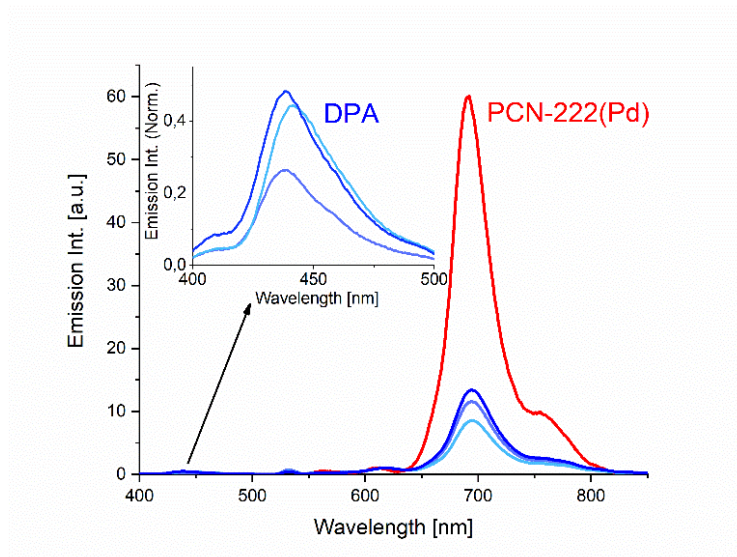
Figure 72: Luminescence emission spectra of **PCN-222(Pd)** (red) and UCL emission of **CA/DPA@PCN-222(Pd)** at three different points of the same sample (blue) (λ_{exc} = 532 nm) (adapted with permission from Ref.[452], Copyright © 2019 The Authors. Published by Wiley-VCH Verlag GmbH & Co. KGaA.).

### 4.3.5 Excitation-power density dependence of TTA-UC

In order to obtain a closer insight into the triplet migration process in **DPA/CA@PCN-222(Pd)**, excitation-power dependent UCL measurements were implemented (**Figure 73 (a)**). An increase of the excitation-power density leads to enhanced upconverted emission intensity. With low excitation-power density, the concentration of the triplet excited annihilator is low. The TTA-UC process follows a second order reaction, which can be assigned to the quadratic excitation-power dependence with the slope of 1.84 ± 0.05 (**Figure 73 (b)**). At a threshold of 329 mW/cm^2, the excitation-power dependence of UCL switches from being quadratic to linear. Above this threshold, the triplet excited annihilators concentration is high enough to allow the TTA-UC undergoing a pseudo-first order reaction,[275,278] where a linear excitation-power dependence (slope of 1.01 ± 0.05) can be observed. In the latter case, the TTA-UC reaches a saturation with the UC efficiency remaining constant. In the **DPA/CA@PCN-222(Pd)** system, the threshold of 329 mW/cm^2 is higher compared to the best systems reported (a few mW/cm^2).[150,275,278,451,454] However, this is much lower than that of typical two-component porphyrin-DPAs systems (several kW/cm^2).[150,278,449-451,455]

(a)

Excitation-Power dependet UCL

(b)

Excitation-Power Dependence of UCL
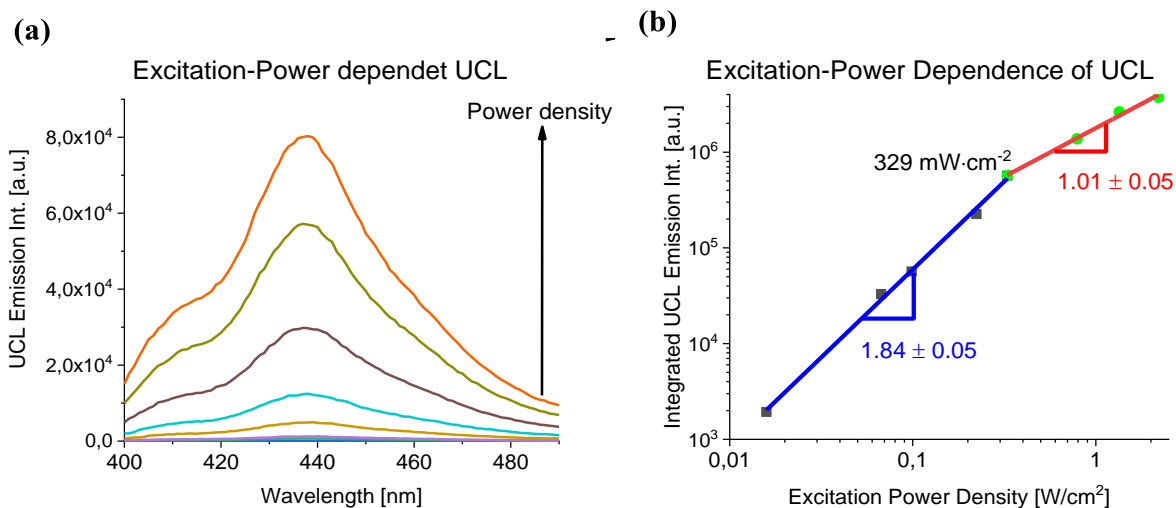
Figure 73: **(a)** TTA-UC luminescence (UCL) intensity of solid **CA/DPA@PCN222(Pd)** with increasing excitation-power density (λ_{exc}=532 nm), and **(b)** integrated UCL intensity of **CA/DPA@PCN-222(Pd)** as a function of the excitation-power density (adapted with permission from Ref.[452], Copyright © 2019 The Authors. Published by Wiley-VCH Verlag GmbH & Co. KGaA.).

4.3.6 Conclusion

In summary, a novel TTA-UC system was developed based on the thermally stable **PCN-222(Pd)** MOF crystalline. Pd(II) porphyrin is inserted as a sensitizer in the MOF walls, while DPA serves as a annihilator which is filled the CA-coated MOF channels. Upon photoexcitation at 532 nm, this solid system produces blue upconverted emission from DPA at 440 nm with a delayed luminescence lifetime of 373 ± 5 µs. The triplet–triplet energy transfer efficiency reaches 82%, which allows theoretically a maximal UC efficiency of 4.3%. The UC luminescence of the TTA-UC system shows a clear excitation-power density dependence from quadratic to linear, revealing a threshold value of 329 mW/cm^2. This study serves as a promising example for developing thermally and chemically stable TTA-UC system in solid state. Further studies will focus on suppressing the oxygen influence and increasing the retention of the trapped annihilators. Additionally, efforts will be made to improve the UC efficiency by optimizing the sensitizer/annihilator interface.

5 Conclusions and Outlook

This work aims to explore the photophysical properties of different luminescent transition metal complexes (TMCs) based on Cr(III), Pt(II), and Pd(II) and their corresponding applications. Depending on the nature of the TMCs, various strategies are developed to improve and tune the photoluminescence properties of these complexes, such as modifying the ligand, changing the counter anions, and inducing the emissive states from complex aggregates. Based on their application-relevant properties, such as their optical sensing behavior and the implicated energy conversion processes, a series of proof-of-concept applications are designed by inserting these TMCs into nanostructures, *e.g.* polystyrene nanoparticles (PSNPs) and metal-organic frameworks (MOFs). Consequently, various types of TMC-based mono-and multi-analyte nanosensors and energy upconversion systems are developed.

Photophysical studies of Cr(III) complexes

Among the luminescent TMCs, the ones based on earth-abundant metal chromium show excellent photophysical properties, which are comparable to those based on precious or rare-Earth metals, indicating their substantial application potentials. As a brief introduction, the cationic Cr(III) center is coordinated octahedrally with two tridentate ddpd ligands showing strong σ-donating capabilities. This unique coordination combination yields large ligand-field splitting of the complex molecular orbitals, resulting in intense near-infrared (NIR) phosphorescence featuring exceptionally high quantum yield of 11.1 % and lifetime of 898 ± 45 µs in deaerated water at room temperature.[57] In order to reach a deeper understanding of the deactivation pathways of the Cr(III) excited state and thus to improve the luminescence properties, photophysical studies on the $[Cr(ddpd)_2]^{3+}$ complexes were carried out to modify the ligand and counter anions, respectively.

As detailed in Section 4.1.1, ligand deuteration of the Cr(III) complexes leads to a significant enhancement of their photoluminescence properties by suppressing the non-radiative deactivation pathways caused by vibrational coupling with the high-energetic X-H oscillators (X = C, O, N). Particularly, the non-selectively deuterated complex **Cr(D₉)BF₄** reaches a record luminescence quantum yield of 30% with an exceptionally long luminescence lifetime of 2.3 ±0.1 ms for a $3d^n$ metal complexes (n < 10) in deuterated acetonitrile at room temperature.

Moreover, by comparing the complex solutions in deuterated/non-deuterated H_2O and CH_3CN, it is shown that O-H oscillators result in a stronger deactivation of the excited state than the C-H oscillators. Furthermore, ligand deuteration yields higher oxygen-sensitivity with a three-folds enhancement for **Cr(D$_9$)BF$_4$** in CH_3CN (τ_{Ar}/τ_{air} = 64.3) in comparison with the prototype Cr(III) complexes (τ_{Ar}/τ_{air} = 20.3). These fundamental photophysical studies reveal the non-radiative deactivation pathways of the Cr(III) excited state due to the O-H or C-H vibrations. Ligand and solvent deuteration serves as a promising strategy to eliminate the unwanted deactivation pathways, and thus improving the luminescent properties of TMCs based on earth-abundant metals.

In addition to ligand deuteration, photoluminescence properties of the molecular ruby $[Cr(ddpd)_2]^{3+}$ can also be improved by choosing bulky counter anions, as described in Section . A comparative study of the Cr(III) complexes with various counter anions ranging from simple Cl^- to bulky tetrakis(phenyl)borate $[BPh_4]^-$ demonstrate a clear enhancement of the photophysical properties with increasing steric effects. Especially, complex **CrBArF$_{24}$** shows an enhanced luminescence quantum yield of 13.6% and extended lifetimes of 1.1 ± 0.1 ms in acetonitrile at room temperature, presenting an improvement factor of 1.8 by comparison with the complex **CrCl**. These enhancements are attributed by the suppressed non-radiative relaxation pathways and molecular aggregation. By encapsulating these complexes into polystyrene nanoparticles (PSNPs), similar luminescence improvements confirm the bulky anion effects. Additionally, the bulky counter anions also present a shielding effect from oxygen quenching according to Stern-Volmer studies, leading to reduced oxygen quenching rate constants K_q. In contrast, the obtained Stern-Volmer constants K_{SV} show a clear increase with increasing bulkiness of the counter anions, suggesting the improved oxygen sensitivity for sensor applications. This comparative photophysical study offers another approach to improve the luminescent properties of cationic TMCs by the choice of counter anions.

Energy upconversion in molecular chromium ytterbium salts

Based on the photophysical understanding of the $[Cr(ddpd)_2]^{3+}$ complex, an intramolecular energy upconversion (UC) system is developed in solid-state chromium ytterbium salts (Section). By carefully redesigning the earlier $Cr^{3+} \rightarrow Yb^{3+}$ downshifting system, a cooperative sensitized upconversion (CSU) mechanism is introduced into the **Cr-Yb** salts.

Photoexcitation of the Yb^{3+} sensitizers at 976 nm yields UC luminescence of the Cr^{3+} activator at around 780 nm, as observed in the UC luminescence emission spectra and time-resolved decays. Moreover, this molecular UC system shows a clear excitation-power density (P) dependence, which changes from a quadratic dependence at low P to linear relationship at high P. This P – dependence offers a threshold value of 494 ± 25 W/cm^2, above which the UC process reaches a saturation. Interestingly, neither deuteration nor the presence of oxygen or water molecules can affect the UC luminescence, indicating the robustness of the UC system. Such molecular NIR to NIR UC systems are rare and particularly favored for bioimaging. Further studies will focus on improving the UC efficiency to obtain a lower threshold value by, *e.g.* anchoring both sensitizer and activator closer to each other.

Multianalyte optical nanosensors

Phosphorescence quenching of the $[Cr(ddpd)_2]^{3+}$ complex by triplet oxygen allow for its application as an oxygen sensor.[57] Additionally, the ratiometric readout of the dual emission (I_{738} / I_{775}) shows a T-sensitivity due to the thermal equilibrium between both emissive states $^2T_1/^2E$.[58] The dual sensing function of this single Cr(III) complex molecule makes it as a promising candidate for multianalyte sensing. Moreover, the Cr(III) complex has an extremely large energy gap between the excitation and emission maxima ($\lambda_{exc.}$ = 435 nm, $\lambda_{em.}$ = 778 nm), suggesting its spectral compatibility for combining with other dyes in the sensing system, such as a pH-responsive indicator and a reference dye. Hence, two multianalyte nanosensors were designed and developed for simultaneously sensing temperature T, oxygen partial pressure pO_2, and pH (TOP), as shown in Section 4.1.4. Sensing of pH is achieved by using the pH-responsive fluorescein derivative (**FITC**), while the inert reference signal generates from Nile Red (**NR**) or 5,10,15,20-tetrakis-(pentafluorophenyl) porphyrin (**TFPP**). A matrix of polystyrene nanoparticle (**PSNP**) is applied with the hydrophobic Cr(III) complex and a reference dye entrapped inside the particle and the fluorescein is conjugated on the particle surface. In order to prevent dye leaking, an aminated silica shell is coated on the particle before surface conjugation with **FITC**. Both multianalyte nanosensors have a high colloidal-, photo- and thermal stabilities in aqueous media. Upon photoexcitation at 435 nm or 440 nm, both nanosensors generate spectrally distinguishable emission bands, which show reversible luminescence responses to changes of the respective analyte or parameter in various aqueous media, such as water, PBS buffer or a cell culture. Particularly, the luminescence response to

oxygen is supported by both the emission intensity (I_{778}) and lifetime (τ_{778}), as confirmed by the respective Stern-Volmer studies yielding the same Stern-Volmer constants. The dynamic sensing ranges for these TOP analytes cover the physiologically relevant range, suggesting their application potential for biosensing. Moreover, the sensing abilities of the different indicators show in polymeric particles no interference with each other, revealing the same calibration parameters regardless as single molecule, in monoanalyte or multianalyte nanosensors. Biosensing applications with these nanosensors *in vitro* and *in vivo* will be a future research interest.

Photophysical studies of Pt(II)- and Pd(II) complexes and their sensor applications

In addition to the Cr(III) complexes, a series of novel pincer-like Pt(II)- and Pd(II) complexes are presented in Section 4.2. These complexes feature a square planar geometry, which is favored for self-assembly or aggregation. By encapsulating these complexes into PSNPs, their photoluminescence properties are significantly enhanced due to the rigidization-induced suppression of the non-radiative decay pathways of their emissive states. Particularly, the fluorinated Pt(II) complex reaches a luminescence quantum yield Φ_L of ca. 80%, while the barely luminescent Pd(II) complexes can be lightened up with extended lifetime from a few ns in solution to over 100 μs in PSNPs. Moreover, a rise of the complex loading concentration C_L in PSNPs leads to formation of complex aggregates, thus inducing the metal···metal interactions and the corresponding MMLCT states. Surprisingly, in contrast to the oxygen-sensitive monomer emission (I_{490}, τ_{490}) of the fluorinated Pt(II) complex, the newly formed MMLCT emissive state (I_{635}, τ_{635}) shows no luminescence response to changes in oxygen partial pressure, suggesting its potential as an internal reference signal for oxygen sensing. This led to a self-referenced ratiometric oxygen nanosensor, which provides luminescence readouts in the emission intensity and lifetime domains. Moreover, the oxygen sensitivities of the Pt(II) complexes are not influenced by the formation of aggregation. However, the Pd(II) complexes display non-linear Stern-Volmer behaviors, which are resulted by a combined effect of the instinct multiexponential decay kinetics, formation of the aggregation-induced MMLCT state and the various quenching sites by oxygen.[292] This study paves the way to develop self-referenced ratiometric oxygen nanosensors with the MMLCT state as the internal reference. Moreover, it offers a platform of nanoreporters, which present tunable luminescence

emission by monitoring the complex loading concentration. Such nanoreporters are promising candidates for bioimaging and biosensing applications.

MOF-based energy upconversion with Pd(II) as the photosensitizer

In Section 4.3, a MOF-based TTA-UC system is developed by applying Pd(II) porphyrin as the photosensitizer and DPA as the annihilator. In this study, the thermally and chemically stable MOF crystalline **PCN-222(Pd)** acts as a Kagome matrix, where the sensitizer is immobilized in the MOF walls and the annihilator is filled in the MOF channels. Caprylic acid (CA), which is anchored to the MOF channels, serves as a solvent for providing hydrophobic environment for DPA. Photoexcitation of the TTA-UC system at 532 nm yields blue UC luminescence of DPA at ca. 440 nm, accompanied by a delayed luminescence lifetime of 373 ± 5 µs. By determining the sensitizer lifetimes in the absence and in the presence of the annihilator, the triplet-triplet energy transfer efficiency is calculated to be 82%, yielding a theoretical maximum of UC efficiency of 4.3%. Additionally, the UC luminescence displays a clear dependence on excitation-power density P, which transits with increasing P from quadratic dependence to linear. This demonstrates the clear change of the TTA-UC process from a second-order photonic reaction to a pseudo-first order. The threshold value at 329 mW/cm^2 points the start of the TTA-UC saturation, above which the UC efficiency reaches the maximum. This study expands the TTA-UC systems in solid state, which are highly desired for energy upconversion devices, *e.g.* solar cells. Yet this system will be further optimized with the respect to suppression of the oxygen influence while improving the UC efficiency by modifying the sensitizer/annihilator interface.

6 References:

(1) Armaroli, N.; Balzani, V. Solar Electricity and Solar Fuels: Status and Perspectives in the Context of the Energy Transition. *Chem. Eur. J.* **2016**, *22*, 32-57.

(2) Shaner, M. R.; Atwater, H. A.; Lewis, N. S.; McFarland, E. W. A comparative technoeconomic analysis of renewable hydrogen production using solar energy. *Energy Environ. Sci.* **2016**, *9*, 2354-2371.

(3) Zhu, S.; Wang, D. Photocatalysis: Basic Principles, Diverse Forms of Implementations and Emerging Scientific Opportunities. *Adv. Energy Mater.* **2017**, *7*, 1700841.

(4) Larkum, A. Limitations and prospects of natural photosynthesis for bioenergy production. *Curr. Opin. Biotechnol.* **2010**, *21*, 271-276.

(5) Glusac, K. What has light ever done for chemistry? *Nat. Chem.* **2016**, *8*, 734–735.

(6) Saunders, D. S. *Insect Clocks*, 3rd ed.; Elsevier Science: Amsterdam, 2002.

(7) Moortgat, G. K. Important photochemical processes in the atmosphere. *Pure Appl. Chem.* **2001**, *73*, 487–490.

(8) Akasofu, S.-I. Energy coupling between the solar wind and the magnetosphere. *Space Sci. Rev.* **1981**, *28*, 121-190.

(9) McIlwain, C. E. Direct Measurement of Particles Producing Visible Auroras. *J. Geophys. Res.* **1960**, *65*, 2727-2747.

(10) Harvey, E. N. *A History of Luminescence from the Earliest Times Until 1900*; American Philosophical Society: Philadelphia, 1957.

(11) Virk, H. S. History of Luminescence from Ancient to Modern Times. *Defect Diffus. Forum* **2015**, *361*, 1-13.

(12) Thirumalai, J. In *Luminescence - An Outlook on the Phenomena and their Applications*, Thirumalai, J., Ed.; IntechOpen: London, 2016 (DOI: 10.5772/62517).

(13) Karl A. Franz; Wolfgang G. Kehr; Alfred Siggel; Jürgen Wieczoreck; Adam, W. In *Ullmann's Encyclopedia of Industrial Chemistry*; Wiley-VCH: Weinheim, 2000.

(14) Lisensky, G. C.; Patel, M. N.; Reich, M. L. Experiments with Glow-in-the-Dark Toys: Kinetics of Doped ZnS Phosphorescence. *J. Chem. Educ.* **1996**, *73*, 1048.

(15) Mockl, L.; Lamb, D. C.; Brauchle, C. Super-resolved fluorescence microscopy: Nobel Prize in Chemistry 2014 for Eric Betzig, Stefan Hell, and William E. Moerner. *Angew. Chem. Int. Ed.* **2014**, *53*, 13972-13977.

(16) Choquet, D. The 2014 Nobel Prize in Chemistry: a large-scale prize for achievements on the nanoscale. *Neuron* **2014**, *84*, 1116-1119.

(17) Costa, R. D.; Orti, E.; Bolink, H. J.; Monti, F.; Accorsi, G.; Armaroli, N. Luminescent ionic transition-metal complexes for light-emitting electrochemical cells. *Angew. Chem. Int. Ed.* **2012**, *51*, 8178-8211.

(18) Beydoun, D.; Amal, R.; Low, G.; McEvoy, S. Role of Nanoparticles in Photocatalysis. *J. Nanoparticle Res.* **1999**, *1*, 439-458.

(19) Wenger, O. S. Photoactive Complexes with Earth-Abundant Metals. *J. Am. Chem. Soc.* **2018**, *140*, 13522-13533.

(20) Bopp, M. A.; Jia, Y.; Li, L.; Cogdell, R. J.; Hochstrasser, R. M. Fluorescence and photobleaching dynamics of single light-harvesting complexes. *Proc. Natl. Acad. Sci. U.S.A.* **1997**, *94*, 10630–10635.

(21) Croce, R.; van Grondelle, R.; van Amerongen, H.; van Stokkum, I. *Light Harvesting in Photosynthesis*; CRC Press: Boca Raton, 2018.

(22) Zhao, Q.; Huang, C.; Li, F. Phosphorescent heavy-metal complexes for bioimaging. *Chem. Soc. Rev.* **2011**, *40*, 2508-2524.

(23) Wolfbeis, O. S. An overview of nanoparticles commonly used in fluorescent bioimaging. *Chem. Soc. Rev.* **2015**, *44*, 4743-4768.

(24) Resch-Genger, U.; Grabolle, M.; Nitschke, R.; Nann, T. In *Advanced Fluorescence Reporters in Chemistry and Biology II*, Demchenko, A. P., Ed.; Springer: Berlin, Heidelberg, 2010, pp 3-40.

(25) Papkovsky, D. B.; Dmitriev, R. I. Biological detection by optical oxygen sensing. *Chem. Soc. Rev.* **2013**, *42*, 8700-8732.

(26) Graf, C.; Rühl, E. In *Biological Responses to Nanoscale Particles*, P., G.; R., Z., Eds.; Springer, Cham, 2019, pp 213-239.

(27) Zhang, K. Y.; Yu, Q.; Wei, H.; Liu, S.; Zhao, Q.; Huang, W. Long-Lived Emissive Probes for Time-Resolved Photoluminescence Bioimaging and Biosensing. *Chem. Rev.* **2018**, *118*, 1770-1839.

(28) Long, Q.-X.; Liu, B.-Z.; Deng, H.-J.; Wu, G.-C.; Deng, K.; Yao-Kai Chen; Liao, P.; Qiu, J.-F.; Yong Lin; Xue-Fei Cai; De-Qiang Wang; Yuan Hu; Ji-Hua Ren; Ni Tang; Yin-Yin Xu; Li-Hua Yu; Zhan Mo; Fang Gong; Zhang, X.-L.; Tian, W.-G.; Hu, L.; Zhang, X.-X.; Xiang, J.-L.; Du, H.-X.; Liu, H.-W.; Lang, C.-H.; Luo, X.-H.; Wu, S.-B.; Cui, X.-P.; Zhou, Z.; Zhu, M.-M.; Wang, J.; Xue, C.-J.; Li, X.-F.; Li, Z.-J.; Wang, L.; Wang, K.; Niu, C.-C.; Yang, Q.-J.; Tang, X.-J.; Zhang, Y.; Liu, X.-M.; Jin-Jing Li; Zhang, D.-C.; Zhang, F.; Liu, P.; Yuan, J.; Li, Q.; Hu, J.-L.; Chen, J.; Huang, A.-L. Antibody responses to SARS-CoV-2 in patients with COVID-19. *Nat. Med.* **2020**, *26*, 845–848.

(29) Cawte, A. D.; Unrau, P. J.; Rueda, D. S. Live cell imaging of single RNA molecules with fluorogenic Mango II arrays. *Nat. Commun.* **2020**, *11*, 1283.

(30) Schäferling, M.; Resch-Genger, U. In *Reviews in Fluorescence 2016*, Geddes, C. D., Ed.; Springer: Cham, 2016, pp 71-109.

(31) Lakowicz, J. R. *Principles of Fluorescence Spectroscopy*, 3rd ed.; Spinger: New York, 2006.

(32) Liu, J.; Liu, C.; He, W. Fluorophores and Their Applications as Molecular Probes in Living Cells. *Curr. Org. Chem.* **2013**, *17*, 564-579.

(33) Reisch, A.; Klymchenko, A. S. Fluorescent Polymer Nanoparticles Based on Dyes: Seeking Brighter Tools for Bioimaging. *Small* **2016**, *12*, 1968-1992.

(34) Schäferling, M. The art of fluorescence imaging with chemical sensors. *Angew. Chem. Int. Ed.* **2012**, *51*, 3532-3554.

(35) Resch-Genger, U.; Grabolle, M.; Cavaliere-Jaricot, S.; Nitschke, R.; Nann, T. Quantum dots versus organic dyes as fluorescent labels. *Nat. Methods* **2008**, *5*, 763-775.

(36) Xiang, H.; Cheng, J.; Ma, X.; Zhou, X.; Chruma, J. J. Near-infrared phosphorescence: materials and applications. *Chem. Soc. Rev.* **2013**, *42*, 6128-6185.

(37) Napp, J.; Behnke, T.; Fischer, L.; Wurth, C.; Wottawa, M.; Katschinski, D. M.; Alves, F.; Resch-Genger, U.; Schäferling, M. Targeted luminescent near-infrared polymer-nanoprobes for in vivo imaging of tumor hypoxia. *Anal. Chem.* **2011**, *83*, 9039-9046.

(38) Behnke, T.; Mathejczyk, J. E.; Brehm, R.; Wurth, C.; Gomes, F. R.; Dullin, C.; Napp, J.; Alves, F.; Resch-Genger, U. Target-specific nanoparticles containing a broad band emissive NIR dye for the sensitive detection and characterization of tumor development. *Biomaterials* **2013**, *34*, 160-170.

(39) Wang, X. D.; Wolfbeis, O. S.; Meier, R. J. Luminescent probes and sensors for temperature. *Chem. Soc. Rev.* **2013**, *42*, 7834-7869.

(40) Wang, X.-D.; Wolfbeis, O. S. Optical methods for sensing and imaging oxygen: materials, spectroscopies and applications. *Chem. Soc. Rev.* **2014**, *43*, 3666-3761.

(41) Wang, X.-D.; Wolfbeis, O. S. Fiber-optic chemical sensors and biosensors (2008-2012). *Anal. Chem.* **2013**, *85*, 487-508.

(42) Wencel, D.; Abel, T.; McDonagh, C. Optical chemical pH sensors. *Anal. Chem.* **2014**, *86*, 15-29.

(43) Wolfbeis, O. S. Luminescent sensing and imaging of oxygen: fierce competition to the Clark electrode. *Bioessays* **2015**, *37*, 921-928.

(44) Saini, R.; Lee, N. V.; Liu, K. Y.; Poh, C. F. Prospects in the Application of Photodynamic Therapy in Oral Cancer and Premalignant Lesions. *Cancers* **2016**, *8*, 83.

(45) Allison, R. R.; Downie, G. H.; Cuenca, R.; Hu, X.-H.; Childs, C. J.; Sibata, C. H. Photosensitizers in clinical PDT. *Photodiagnosis Photodyn Ther.* **2004**, *1*, 27-42.

(46) Sathish, V.; Ramdass, A.; Velayudham, M.; Lu, K. L.; Thanasekaran, P.; Rajagopal, S. Development of luminescent sensors based on transition metal complexes for the detection of nitroexplosives. *Dalton Trans.* **2017**, *46*, 16738-16769.

(47) Warra, A. A. Transition metal complexes and their application in drugs and cosmetics – A Review. *J. Chem. Pharm. Res.* **2011**, *3*, 951-958.

(48) Nazeeruddin, M. K.; Grätzel, M. In *Photofunctional Transition Metal Complexes*, Yam, V. W. W., Ed.; Springer: Berlin, Heidelberg, 2007, pp 113-175.

(49) Ma, D. L.; He, H. Z.; Leung, K. H.; Chan, D. S.; Leung, C. H. Bioactive luminescent transition-metal complexes for biomedical applications. *Angew. Chem. Int. Ed.* **2013**, *52*, 7666-7682.

(50) Ishida, H.; Tanaka, K.; Tanaka, T. Electrochemical CO_2 reduction catalyzed by ruthenium complexes $[Ru(bpy)_2(CO)_2]^{2+}$ and $[Ru(bpy)_2(CO)Cl]^+$. Effect of pH on the formation of CO and $HCOO^-$. *Organometallics* **1987**, *6*, 181–186.

(51) Mede, T.; Jager, M.; Schubert, U. S. "Chemistry-on-the-complex": functional Ru(II) polypyridyl-type sensitizers as divergent building blocks. *Chem. Soc. Rev.* **2018**, *47*, 7577-7627.

(52) Borisov, S. M.; Zenkl, G.; Klimant, I. Phosphorescent platinum(II) and palladium(II) complexes with azatetrabenzoporphyrins-new red laser diode-compatible indicators for optical oxygen sensing. *ACS Appl. Mater. Interfaces* **2010**, *2*, 366-374.

(53) Hasegawa, Y.; Kitagawa, Y.; Nakanishi, T. Effective photosensitized, electrosensitized, and mechanosensitized luminescence of lanthanide complexes. *NPG Asia Mater.* **2018**, *10*, 52-70.

(54) Wei, C.; Ma, L.; Wei, H.; Liu, Z.; Bian, Z.; Huang, C. Advances in luminescent lanthanide complexes and applications. *Sci. China Technol. Sci.* **2018**, *61*, 1265-1285.

(55) Forster, C.; Heinze, K. Photophysics and photochemistry with Earth-abundant metals - fundamentals and concepts. *Chem. Soc. Rev.* **2020**, *49*, 1057-1070.

(56) Larsen, C. B.; Wenger, O. S. Photoredox Catalysis with Metal Complexes Made from Earth-Abundant Elements. *Chem. Eur. J.* **2018**, *24*, 2039-2058.

(57) Otto, S.; Grabolle, M.; Forster, C.; Kreitner, C.; Resch-Genger, U.; Heinze, K. $[Cr(ddpd)_2]^{3+}$: A Molecular, Water-Soluble, Highly NIR-Emissive Ruby Analogue. *Angew. Chem. Int. Ed.* **2015**, *54*, 11572-11576.

(58) Otto, S.; Scholz, N.; Behnke, T.; Resch-Genger, U.; Heinze, K. Thermo-Chromium: A Contactless Optical Molecular Thermometer. *Chem. Eur. J.* **2017**, *23*, 12131-12135.

(59) Otto, S.; Harris, J. P.; Heinze, K.; Reber, C. Molecular Ruby under Pressure. *Angew. Chem. Int. Ed.* **2018**, *57*, 11069-11073.

(60) Mazzola, L. Commercializing nanotechnology. *Nat. Biotechnol.* **2003**, *21*, 1137-1143.

(61) Paull, R.; Wolfe, J.; Hébert, P.; Sinkula, M. Investing in nanotechnology. *Nat. Biotechnol.* **2003**, *21*, 1144-1147.

(62) Jeevanandam, J.; Barhoum, A.; Chan, Y. S.; Dufresne, A.; Danquah, M. K. Review on nanoparticles and nanostructured materials: history, sources, toxicity and regulations. *Beilstein J. Nanotechnol.* **2018**, *9*, 1050-1074.

(63) Mlinar, V. Engineered nanomaterials for solar energy conversion. *Nanotechnology* **2013**, *24*, 042001.

(64) Sobolev, K.; Flores, I.; Hermosillo, R.; Torres-martínez, L. M. In *Nanotechnology of Concrete: Recent Developments and Future Perspectives*; American Concrete Institute: Denver, USA, 2006.

(65) Kamyshny, A.; Magdassi, S. Conductive nanomaterials for printed electronics. *Small* **2014**, *10*, 3515-3535.

(66) Shafiq, M.; Anjum, S.; Hano, C.; Anjum, I.; Abbasi, B. H. An Overview of the Applications of Nanomaterials and Nanodevices in the Food Industry. *Foods* **2020**, *9*, 148.

(67) Morganti, P. Use and potential of nanotechnology in cosmetic dermatology. *Clin. Cosmet. Investig. Dermatol.* **2010**, *3*, 5-13.

(68) Taton, T. A. Nanostructures as tailored biological probes. *Trends Biotechnol.* **2002**, *20*, 277-279.

(69) Salata, O. Applications of nanoparticles in biology and medicine. *J. Nanobiotechnology* **2004**, *2*, 3.

(70) Parak, W. J.; Gerion, D.; Pellegrino, T.; Zanchet, D.; Micheel, C.; Williams, S. C.; Boudreau, R.; Gros, M. A. L.; Larabell, C. A.; Alivisatos, A. P. Biological applications of colloidal nanocrystals. *Nanotechnology* **2003**, *14*, 15-27.

(71) Rühl, E. In *Encyclopedia of Interacial Chemistry: Surface Science and Electrochemistry*, Wandelt, K., Ed.; Elsevier 2018, pp 795-802.

(72) Mah, C.; Fraites, T. J. J.; Zolotukhin, I.; Song, S. H.; Flotte, T. R.; Dobson, J.; Batich, C.; Byrne, B. J. Improved method of recombinant AAV2 delivery for systemic targeted gene therapy. *Mol. Ther.* **2002**, *6*, 106-112.

(73) Thanou, M. In *Encyclopedia of Biophysics*, Roberts, G. C. K., Ed.; Springer: Berlin, Heidelberg, 2013.

(74) Mirza, Z.; Karim, S. Nanoparticles-based drug delivery and gene therapy for breast cancer: Recent advancements and future challenges. *Semin. Cancer Biol.* **2019**, *in press (doi.org/10.1016/j.semcancer.2019.10.020)*.

(75) Naolou, T.; Rühl, E.; Lendlein, A. Nanocarriers: Architecture, transport, and topical application of drugs for therapeutic use. *Eur. J. Pharm. Biopharm.* **2017**, *116*, 1-3.

(76) Yi, G.; Hong, S. H.; Son, J.; Yoo, J.; Park, C.; Choi, Y.; Koo, H. Recent advances in nanoparticle carriers for photodynamic therapy. *Quant. Imaging Med. Surg.* **2018**, *8*, 433-443.

(77) Lucky, S. S.; Soo, K. C.; Zhang, Y. Nanoparticles in Photodynamic Therapy. *Chem. Rev.* **2015**, *115*, 1990-2042.

(78) Hasan, A.; Morshed, M.; Memic, A.; Hassan, S.; Webster, T. J.; Marei, H. E. Nanoparticles in tissue engineering: applications, challenges and prospects. *Int. J. Nanomedicine* **2018**, *13*, 5637-5655.

(79) Fathi-Achachelouei, M.; Knopf-Marques, H.; Ribeiro da Silva, C. E.; Barthes, J.; Bat, E.; Tezcaner, A.; Vrana, N. E. Use of Nanoparticles in Tissue Engineering and Regenerative Medicine. *Front. Bioeng. Biotechnol.* **2019**, *7*, 113.

(80) Patel, K. D.; Singh, R. K.; Kim, H.-W. Carbon-based nanomaterials as an emerging platform for theranostics. *Mater. Horiz.* **2019**, *6*, 434-469.

(81) Cha, C.; Shin, S. R.; Annabi, N.; Dokmeci, M. R.; Khademhosseini, A. Carbon-based nanomaterials: multifunctional materials for biomedical engineering. *ACS Nano* **2013**, *7*, 2891-2897.

(82) Smith, A. M.; Nie, S. Semiconductor Nanocrystals: Structure, Properties, and Band Gap Engineering. *Acc. Chem. Res.* **2010**, *43*, 190–200.

(83) Moodelly, D.; Kowalik, P.; Bujak, P.; Pron, A.; Reiss, P. Synthesis, photophysical properties and surface chemistry of chalcopyrite-type semiconductor nanocrystals. *J. Mater. Chem. C* **2019**, *7*, 11665-11709.

(84) Crayton, S. H.; Chen, A. K.; Cheng, Z.; Tsourkas, A. In *Comprehensive Biomaterials*, Ducheyne, P., Ed.; Elsevier Science, 2011, pp 305-328.

(85) Wang, M.; Abbineni, G.; Clevenger, A.; Mao, C.; Xu, S. Upconversion nanoparticles: synthesis, surface modification and biological applications. *Nanomedicine* **2011**, *7*, 710-729.

(86) Resch-Genger, U.; Gorris, H. H. Perspectives and challenges of photon-upconversion nanoparticles - Part I: routes to brighter particles and quantitative spectroscopic studies. *Anal. Bioanal. Chem.* **2017**, *409*, 5855-5874.

(87) Wen, S.; Zhou, J.; Zheng, K.; Bednarkiewicz, A.; Liu, X.; Jin, D. Advances in highly doped upconversion nanoparticles. *Nat. Commun.* **2018**, *9*, 2415.

(88) Qian, H.; Li, Z.; Zhang, Y. Multicolor polystyrene nanospheres tagged with up-conversion fluorescent nanocrystals. *Nanotechnology* **2008**, *19*, 225601-225604.

(89) Yan, J. L.; Estevez, M. C.; Smith, J. E.; Wang, K. M.; He, X. X.; Wang, L.; Tan, W. H. Dye-doped nanoparticles for bioanalysis. *Nano Today* **2007**, *2*, 44-50.

(90) Sun, C. Y.; To, W. P.; Wang, X. L.; Chan, K. T.; Su, Z. M.; Che, C. M. Metal-organic framework composites with luminescent gold(iii) complexes. Strongly emissive and long-lived excited states in open air and photo-catalysis. *Chem. Sci.* **2015**, *6*, 7105-7111.

(91) Ma, Y.; Su, H.; Kuang, X.; Li, X.; Zhang, T.; Tang, B. Heterogeneous nano metal-organic framework fluorescence probe for highly selective and sensitive detection of hydrogen sulfide in living cells. *Anal. Chem.* **2014**, *86*, 11459-11463.

(92) Chu, C. S.; Lo, Y. L.; Sung, T. W. Enhanced oxygen sensing properties of Pt(II) complex and dye entrapped core-shell silica nanoparticles embedded in sol-gel matrix. *Talanta* **2010**, *82*, 1044-1051.

(93) Demchenko, A. P. In *Introduction to Fluorescence Sensing* Demchenko, A. P., Ed.; Springer: Dordrecht, 2015.

(94) Khomein, P.; Swaminathan, S.; Young, E. R.; Thayumanavan, S. Fluorescence Enhancement Through Incorporation of Chromophores in Polymeric Nanoparticles. *J. Inorg. Organomet. Polym. Mater.* **2017**, *28*, 407-413.

(95) Shi, J.; Tian, F.; Lyu, J.; Yang, M. Nanoparticle based fluorescence resonance energy transfer (FRET) for biosensing applications. *J. Mater. Chem. B* **2015**, *3*, 6989-7005.

(96) Minoofar, P. N.; Dunn, B. S.; Zink, J. I. Multiply Doped Nanostructured Silicate Sol-Gel Thin Films: Spatial Segregation of Dopants, Energy Transfer, and Distance Measurements. *J. Am. Chem. Soc.* **2005**, *127*, 2656-2665.

(97) Wang, X.; Valiev, R. R.; Ohulchanskyy, T. Y.; Agren, H.; Yang, C.; Chen, G. Dye-sensitized lanthanide-doped upconversion nanoparticles. *Chem. Soc. Rev.* **2017**, *46*, 4150-4167.

(98) Warneck, P. In *Chemistry of the Natural Atmosphere*, Warneck, P., Ed.; Academic Press: San Diego, 1988.

(99) Bunker, P. R.; Jensen, P. *Molecular Symmetry and Spectroscopy*; NRC Research Press: Ottawa, 2006.

(100) Schnermann, M. Organic dyes for deep bioimaging. *Nature* **2017**, *551*, 176–177

(101) Fu, Y.; Finney, N. S. Small-molecule fluorescent probes and their design. *RSC Adv.* **2018**, *8*, 29051-29061.

(102) Sednev, M. V.; Belov, V. N.; Hell, S. W. Fluorescent dyes with large Stokes shifts for super-resolution optical microscopy of biological objects: a review. *Methods Appl. Fluoresc.* **2015**, *3*, 042004.

(103) Lei, Z.; Sun, C.; Pei, P.; Wang, S.; Li, D.; Zhang, X.; Zhang, F. Stable, Wavelength-Tunable Fluorescent Dyes in the NIR-II Region for In Vivo High-Contrast Bioimaging and Multiplexed Biosensing. *Angew. Chem. Int. Ed.* **2019**, *58*, 8166-8171.

(104) Cosco, E. D.; Caram, J. R.; Bruns, O. T.; Franke, D.; Day, R. A.; Farr, E. P.; Bawendi, M. G.; Sletten, E. M. Flavylium Polymethine Fluorophores for Near- and Shortwave Infrared Imaging. *Angew. Chem. Int. Ed.* **2017**, *56*, 13126-13129.

(105) Mukherjee, S.; Thilagar, P. Recent advances in purely organic phosphorescent materials. *Chem. Commun.* **2015**, *51*, 10988-11003.

(106) Xu, S.; Chen, R.; Zheng, C.; Huang, W. Excited State Modulation for Organic Afterglow: Materials and Applications. *Adv. Mater.* **2016**, *28*, 9920-9940.

(107) Hirata, S. Recent Advances in Materials with Room-Temperature Phosphorescence: Photophysics for Triplet Exciton Stabilization. *Adv. Opt. Mater.* **2017**, *5*, 1700116.

(108) Forni, A.; Lucenti, E.; Botta, C.; Cariati, E. Metal free room temperature phosphorescence from molecular self-interactions in the solid state. *J. Mater. Chem. C* **2018**, *6*, 4603-4626.

(109) Kenry; Chen, C.; Liu, B. Enhancing the performance of pure organic room-temperature phosphorescent luminophores. *Nat. Commun.* **2019**, *10*, 2111.

(110) Qin, W.; Li, K.; Feng, G.; Li, M.; Yang, Z.; Liu, B.; Tang, B. Z. Bright and Photostable Organic Fluorescent Dots with Aggregation-Induced Emission Characteristics for Noninvasive Long-Term Cell Imaging. *Adv. Funct. Mater.* **2014**, *24*, 635-643.

(111) Luo, J.; Xie, Z.; Lam, J. W.; Cheng, L.; Chen, H.; Qiu, C.; Kwok, H. S.; Zhan, X.; Liu, Y.; Zhu, D.; Tang, B. Z. Aggregation-induced emission of 1-methyl-1,2,3,4,5-pentaphenylsilole. *Chem. Commun.* **2001**, 1740-1741.

(112) Zheng, Z.; Yu, Z.; Yang, M.; Jin, F.; Zhang, Q.; Zhou, H.; Wu, J.; Tian, Y. Substituent group variations directing the molecular packing, electronic structure, and aggregation-induced emission property of isophorone derivatives. *J. Org. Chem.* **2013**, *78*, 3222-3234.

(113) Huang, J.; Sun, N.; Yang, J.; Tang, R.; Li, Q.; Ma, D.; Li, Z. Blue Aggregation-Induced Emission Luminogens: High External Quantum Efficiencies Up to 3.99% in LED Device, and Restriction of the Conjugation Length through Rational Molecular Design. *Adv. Funct. Mater.* **2014**, *24*, 7645-7654.

(114) Hong, Y.; Lam, J. W.; Tang, B. Z. Aggregation-induced emission: phenomenon, mechanism and applications. *Chem. Commun.* **2009**, 4332-4353.

(115) Tong, H.; Hong, Y.; Dong, Y.; Ren, Y.; Häussler, M.; Lam, J. W. Y.; Wong, K. S.; Tang, B. Z. Color-Tunable, Aggregation-Induced Emission of a Butterfly-Shaped Molecule Comprising a Pyran Skeleton and Two Cholesteryl Wings. *J. Phys. Chem. A* **2007**, *111*, 2000-2007.

(116) Zhao, Z.; He, B.; Tang, B. Z. Aggregation-induced emission of siloles. *Chem. Sci.* **2015**, *6*, 5347-5365.

(117) Nirmalananthan-Budau, N. *Synthesis, Characterization and Surface Group Quantification of Functionalized Polymer Particles for Signal Amplification Strategies*. Dissertation, Freie Universität Berlin, Berlin, 2019.

(118) Amoroso, A. J.; Pope, S. J. Using lanthanide ions in molecular bioimaging. *Chem. Soc. Rev.* **2015**, *44*, 4723-4742.

(119) Nishioka, T.; Fukui, K.; Matsumoto, K. In *Handbook on the Physics and Chemistry of Rare Earths*, Gschneidner Jr., K. A. J.; Büzli, J. C. G.; Pecharsky, V. K., Eds.; Elsevier Science: Amsterdam, 2007, p 171.

(120) Bünzli, J.-C. G. Lanthanide Luminescence for Biomedical Analyses and Imaging. *Chem. Rev.* **2010**, *110*, 2729–2755.

(121) Crosby, G. A.; Whan, R. E.; Alire, R. M. Intramolecular energy transfer in rare earth chelates. Role of the triplet state. *J. Chem. Phys.* **1961**, *34*, 743–748

(122) Leonard, J. P.; Nolan, C. B.; Stomeo, F.; Gunnlaugsson, T. In *Topics in Current Chemistry Photochemistry and Photophysics of Coordination Compounds II*, Balzani, V.; Campagna, S., Eds.; Springer: Berlin Heidelberg, 2007, pp 1-43.

(123) Trinquet, E.; Mathis, G. Fluorescence technologies for the investigation of chemical libraries. *Mol. Biosyst.* **2006**, *2*, 380-387.

(124) Hemmila, I.; Laitala, V. Progress in lanthanides as luminescent probes. *J. Fluoresc.* **2005**, *15*, 529–542.

(125) Bünzli, J. G. Lanthanide luminescent bioprobes (LLBs). *Chem. Lett.* **2009**, *38*, 104-109.

(126) Bünzli, J.-C. G.; Eliseeva, S. V. In *Lanthanide Luminescence: Photophysical, Analytical and Biological Aspects*, Hänninen, P.; Härmä, H., Eds.; Springer: Berlin, Heidelberg, 2010, pp 1-45.

(127) Pham, Y. H.; Trush, V. A.; Carneiro Neto, A. N.; Korabik, M.; Sokolnicki, J.; Weselski, M.; Malta, O. L.; Amirkhanov, V. M.; Gawryszewska, P. Lanthanide complexes with N-phosphorylated carboxamide as UV converters with excellent emission quantum yield and single-ion magnet behavior. *J. Mater. Chem. C* **2020**, *8*, 9993-10009.

(128) Wagenknecht, P. S.; Ford, P. C. Metal centered ligand field excited states: Their roles in the design and performance of transition metal based photochemical molecular devices. *Coord. Chem. Rev.* **2011**, *255*, 591–616.

(129) Marcus, R. A. Chemical and Electrochemical Electron-Transfer Theory. *Annu. Rev. Phys.* **1964**, *15*, 155-196.

(130) Atkins, P. J.; Shriver, D. F. *Inorganic chemistry*, 3rd ed.; Oxford University Press: Oxford 1999.

(131) Tarr, D. A.; Miessler, G. L. *Inorganic chemistry*, 2nd ed.; Prentice Hall: Englewood Cliffs, 1991.

(132) Vogler, A.; Kunkely, H. Photoreactivity of metal-to-ligand charge transfer excited states. *Coord. Chem. Rev.* **1998**, *177*, 81-96.

(133) Dixon, I. M.; Lebon, E.; Sutra, P.; Igau, A. Luminescent ruthenium–polypyridine complexes & phosphorus ligands: anything but a simple story. *Chem. Soc. Rev.* **2009**, *38*, 1621–1634

(134) Bissell, R. A.; de Silva, A. P.; Gunaratne, H. Q. N.; Lynch, P. L. M.; Maguire, G. E. M.; Samankumara Sandanayake, K. R. A. Molecular fluorescent signalling with 'fluor–spacer–receptor' systems: approaches to sensing and switching devices via supramolecular photophysics. *Chem. Soc. Rev.* **1992**, *21*, 187–195.

(135) Li, K.; Ming Tong, G. S.; Wan, Q.; Cheng, G.; Tong, W. Y.; Ang, W. H.; Kwong, W. L.; Che, C. M. Highly phosphorescent platinum(ii) emitters: photophysics, materials and biological applications. *Chem. Sci.* **2016**, *7*, 1653-1673.

(136) Bellows, D.; Aly, S. M.; Gros, C. P.; El Ojaimi, M.; Barbe, J. M.; Guilard, R.; Harvey, P. D. Energy transfers in monomers, dimers, and trimers of zinc(II) and palladium(II) porphyrins bridged by rigid Pt-containing conjugated organometallic spacers. *Inorg. Chem.* **2009**, *48*, 7613-7629.

(137) Miller, M. T.; Gantzel, P. K.; Karpishin, T. B. A Photoluminescent Copper(I) Complex with an Exceptionally High Cu^{II}/Cu^{I} Redox Potential: $[Cu(bfp)_2]^+$ (bfp=2,9-bis(trifluoromethyl)-1,10-phenanthroline). *Angew. Chem. Int. Ed.* **1998**, *37*, 1556-1558.

(138) Cuttell, D. G.; Kuang, S. M.; Fanwick, P. E.; McMillin, D. R.; Walton, R. A. Simple Cu(I) complexes with unprecedented excited-state lifetimes. *J. Am. Chem. Soc.* **2002**, *124*, 6-7.

(139) Yam, V. W.; Wong, K. M. Luminescent metal complexes of d^6, d^8 and d^{10} transition metal centres. *Chem. Commun.* **2011**, *47*, 11579-11592.

(140) Mauro, M.; Aliprandi, A.; Septiadi, D.; Kehr, N. S.; De Cola, L. When self-assembly meets biology: luminescent platinum complexes for imaging applications. *Chem. Soc. Rev.* **2014**, *43*, 4144-4166.

(141) Puntoriero, F.; Nastasi, F.; Galletta, M.; Campagna, S. In *Comprehensive Inorganic Chemistry II* Reedijk, J.; Poeppelmeier, K., Eds.; Elsevier: Amsterdam, 2013, pp 255-337.

(142) Kalyanasundaram, K.; Zakeeruddin, S. M.; Nazeeruddin, M. K. Ligand to metal charge transfer transitions in Ru(III) and Os(III) complexes of substituted 2,2'-bipyridines. *Coord. Chem. Rev.* **1994**, *132*, 259-264

(143) Shin, Y.-g. K.; Brunschwig, B. S.; Creutz, C.; Sutin, N. Electroabsorption Spectroscopy of Charge-Transfer States of Transition-Metal Complexes. 2. Metal-to-Ligand and Ligand-to-Metal Charge-Transfer Excited States of Pentaammineruthenium Complexes1. *J. Phys. Chem.* **1996**, *100*, 8157–8169.

(144) Brunschwig, B. S.; Creutz, C.; Sutin, N. Electroabsorption spectroscopy of charge transfer states of transition metal complexes. *Coord. Chem. Rev.* **1998**, *177*, 61-79.

(145) Furukawa, H.; Ko, N.; Go, Y. B.; Aratani, N.; Choi, S. B.; Choi, E.; Yazaydin, A.; Snurr, R. Q.; O'Keeffe, M.; Kim, J.; Yaghi, O. M. Ultrahigh Porosity in Metal-Organic Frameworks. *Science* **2010**, *239*, 424-428.

(146) Furukawa, H.; Cordova, K. E.; O'Keeffe, M.; Yaghi, O. M. The chemistry and applications of metal-organic frameworks. *Science* **2013**, *341*, 1230444.

(147) Li, H.; Li, L.; Lin, R.-B.; Zhou, W.; Zhang, Z.; Xiang, S.; Chen, B. Porous metal-organic frameworks for gas storage and separation: Status and challenges. *Energy Chem.* **2019**, *1*, 100006.

(148) Ma, S.; Zhou, H. C. Gas storage in porous metal-organic frameworks for clean energy applications. *Chem. Commun.* **2010**, *46*, 44-53.

(149) Feng, D.; Gu, Z. Y.; Li, J. R.; Jiang, H. L.; Wei, Z.; Zhou, H. C. Zirconium-metalloporphyrin PCN-222: mesoporous metal-organic frameworks with ultrahigh stability as biomimetic catalysts. *Angew. Chem. Int. Ed.* **2012**, *51*, 10307-10310.

(150) Park, J.; Xu, M.; Li, F.; Zhou, H. C. 3D Long-Range Triplet Migration in a Water-Stable Metal-Organic Framework for Upconversion-Based Ultralow-Power in Vivo Imaging. *J. Am. Chem. Soc.* **2018**, *140*, 5493-5499.

(151) Liu, W.; Wang, Y. M.; Li, Y. H.; Cai, S. J.; Yin, X. B.; He, X. W.; Zhang, Y. K. Fluorescent Imaging-Guided Chemotherapy-and-Photodynamic Dual Therapy with Nanoscale Porphyrin Metal-Organic Framework. *Small* **2017**, *13*, 1603459.

(152) Knedel, T. O.; Buss, S.; Maisuls, I.; Daniliuc, C. G.; Schlusener, C.; Brandt, P.; Weingart, O.; Vollrath, A.; Janiak, C.; Strassert, C. A. Encapsulation of Phosphorescent Pt(II) Complexes in Zn-Based Metal-Organic Frameworks toward Oxygen-Sensing Porous Materials. *Inorg. Chem.* **2020**, *59*, 7252-7264.

(153) Liu, Y.; Howarth, A. J.; Vermeulen, N. A.; Moon, S.-Y.; Hupp, J. T.; Farha, O. K. Catalytic degradation of chemical warfare agents and their simulants by metal-organic frameworks. *Coord. Chem. Rev.* **2017**, *346*, 101-111.

(154) Zhao, S. N.; Wang, G.; Poelman, D.; Voort, P. V. Luminescent Lanthanide MOFs: A Unique Platform for Chemical Sensing. *Materials (Basel)* **2018**, *11*, 4.

(155) Sun, C. Y.; Wang, X. L.; Zhang, X.; Qin, C.; Li, P.; Su, Z. M.; Zhu, D. X.; Shan, G. G.; Shao, K. Z.; Wu, H.; Li, J. Efficient and tunable white-light emission of metal-organic frameworks by iridium-complex encapsulation. *Nat. Commun.* **2013**, *4*, 2717.

(156) Zhang, W.; Li, B.; Ma, H.; Zhang, L.; Guan, Y.; Zhang, Y.; Zhang, X.; Jing, P.; Yue, S. Combining Ruthenium(II) Complexes with Metal-Organic Frameworks to Realize Effective Two-Photon Absorption for Singlet Oxygen Generation. *ACS Appl. Mater. Interfaces* **2016**, *8*, 21465-21471.

(157) Vert, M.; Doi, Y.; Hellwich, K.-H.; Hess, M.; Hodge, P.; Kubisa, P.; Rinaudo, M.; Schué, F. Terminology for biorelated polymers and applications (IUPAC Recommendations 2012). *Pure Appl. Chem.* **2012**, *84*, 377-410.

(158) Alemán, J. V.; Chadwick, A. V.; He, J.; Hess, M.; Horie, K.; Jones, R. G.; Kratochvíl, P.; Meisel, I.; Mita, I.; Moad, G.; Penczek, S.; Stepto, R. F. T. Definitions of terms relating to the structure and processing of sols, gels, networks, and inorganic-organic hybrid materials (IUPAC Recommendations 2007). *Pure Appl. Chem.* **2007**, *79*, 1801-1829.

(159) Plane, J. M. Cosmic dust in the earth's atmosphere. *Chem. Soc. Rev.* **2012**, *41*, 6507-6518.

(160) Heiligtag, F. J.; Niederberger, M. The fascinating world of nanoparticle research. *Mater. Today* **2013**, *16*, 262-271.

(161) Colomban, P. The Use of Metal Nanoparticles to Produce Yellow, Red and Iridescent Colour, from Bronze Age to Present Times in Lustre Pottery and Glass: Solid State Chemistry, Spectroscopy and Nanostructure. *J. Nano Res-SW* **2009**, *8*, 109-132.

(162) Sciau, P. *The Delivery of Nanoparticles*; IntechOpen: Rijeka, Croatia, 2012 (DOI: 10.5772/2647).

(163) Johnson-McDaniel, D.; Barrett, C. A.; Sharafi, A.; Salguero, T. T. Nanoscience of an ancient pigment. *J. Am. Chem. Soc.* **2013**, *135*, 1677-1679.

(164) Finlay, R. *The Pilgrim Art. Cultures of Porcelain in World History*; University of California Press: Oakland, 2010.

(165) Faraday, M. The Bakerian Lecture—Experimental relations of gold (and other metals) to lightPhil. *Trans. R. Soc.* **1857**, *147*, 145-181.

(166) Thompson, D. Michael Faraday's recognition of ruby gold: the birth of modern nanotechnology. *Gold Bull.* **2007**, *40*, 267-269.

(167) Tang, S. C.; Lo, I. M. Magnetic nanoparticles: essential factors for sustainable environmental applications. *Water Res.* **2013**, *47*, 2613-2632.

(168) Khan, I.; Saeed, K.; Khan, I. Nanoparticles: Properties, applications and toxicities. *Arab. J. Chem.* **2019**, *12*, 908-931.

(169) Doria, G.; Conde, J.; Veigas, B.; Giestas, L.; Almeida, C.; Assuncao, M.; Rosa, J.; Baptista, P. V. Noble metal nanoparticles for biosensing applications. *Sensors* **2012**, *12*, 1657-1687.

(170) KrishnaSailaja, A.; Siddiqua, A. An overall review on polymeric nanoparticles. *Int. Res. J. Pharm. Appl. Sci.* **2017**, *2*, 21-28.

(171) Kobayashi, H.; Watanabe, R.; Choyke, P. L. Improving conventional enhanced permeability and retention (EPR) effects; what is the appropriate target? *Theranostics* **2013**, *4*, 81-89.

(172) Prasad, P. N. *Introduction to Nanomedicine and Nanobioengineering*; Wiley: Weinheim, 2012; Vol. 7.

(173) Perrault, S. D.; Chan, W. C. S. Synthesis and surface modification of highly monodispersed, spherical gold nanoparticles of 50-200 nm. *J. Am. Chem. Soc.* **2010**, *131*, 17042–17043.

(174) Ghassan, A. A.; Mijan, N.-A.; Taufiq-Yap, Y. H. In *Nanorods and Nanocomposites*, Ghamsari, M. S.; Dhara, S., Eds.; IntechOpen: London, 2019 (DOI: 10.5772/intechopen.84550).

(175) Pu, Z.; Cao, M.; Yang, J.; Huang, K.; Hu, C. Controlled synthesis and growth mechanism of hematite nanorhombohedra, nanorods and nanocubes. *Nanotechnology* **2006**, *17*, 799-804.

(176) Dick, K. A. A review of nanowire growth promoted by alloys and non-alloying elements with emphasis on Au-assisted III–V nanowires. *Prog. Cryst. Growth Charact. Mater.* **2008**, *54*, 138-173.

(177) Donaldson, K.; Aitken, R.; Tran, L.; Stone, V.; Duffin, R.; Forrest, G.; Alexander, A. Carbon Nanotubes: A Review of Their Properties in Relation to Pulmonary Toxicology and Workplace Safety. *Toxicol. Sci.* **2006**, *92*, 5-22.

(178) Wu, H. L.; Tsai, H. R.; Hung, Y. T.; Lao, K. U.; Liao, C. W.; Chung, P. J.; Huang, J. S.; Chen, I. C.; Huang, M. H. A comparative study of gold nanocubes, octahedra, and rhombic dodecahedra as highly sensitive SERS substrates. *Inorg. Chem.* **2011**, *50*, 8106-8111.

(179) Velmurugan, M.; Devasenathipathy, R.; Chen, S.-M.; Kohila rani, K.; Wang, S.-F. Facile Synthesis of Graphene/Cobalt Oxide Nanohexagons for the Selective Detection of Dopamine. *Electroanalysis* **2017**, *29*, 923-928.

(180) Sharma, M. In *Applications of Targeted Nano Drugs and Delivery Systems*, Mohapatra, S. S. a. C., Ed.; Elsevier: Amsterdam, 2019, pp 499-550.

(181) Braeken, Y.; Cheruku, S.; Ethirajan, A.; Maes, W. Conjugated Polymer Nanoparticles for Bioimaging. *Materials* **2017**, *10*, 1420.

(182) Sobiech, M.; Luliński, P. In *Nanostructures for the Engineering of Cells, Tissues and Organs*, Grumezescu, A. M., Ed.; Elsevier: Amsterdam, 2018, pp 331-374.

(183) Mallakpour, S.; Behranvand, V. Polymeric nanoparticles: Recent development in synthesis and application. *Express Polym. Lett.* **2016**, *10*, 895-913.

(184) Banik, B. L.; Fattahi, P.; Brown, J. L. Polymeric nanoparticles: the future of nanomedicine. *Wiley Interdiscip. Rev. Nanomed. Nanobiotechnol.* **2016**, *8*, 271-299.

(185) Bolhassani, A.; Javanzad, S.; Saleh, T.; Hashemi, M.; Aghasadeghi, M. R.; Sadat, S. M. Polymeric nanoparticles: potent vectors for vaccine delivery targeting cancer and infectious diseases. *Hum. Vaccin. Immunother.* **2014**, *10*, 321-332.

(186) Palanikumar, L.; Al-Hosani, S.; Kalmouni, M.; Nguyen, V. P.; Ali, L.; Pasricha, R.; Barrera, F. N.; Magzoub, M. pH-responsive high stability polymeric nanoparticles for targeted delivery of anticancer therapeutics. *Commun. Biol.* **2020**, *3*, 95.

(187) Twibanire, J. d. A.; Grindley, T. B. Polyester Dendrimers: Smart Carriers for Drug Delivery. *Polymers* **2014**, *6*, 179-213.

(188) Zhang, Z.; Tsai, P. C.; Ramezanli, T.; Michniak-Kohn, B. Polymeric nanoparticles-based topical delivery systems for the treatment of dermatological diseases. *Wiley Interdiscip. Rev. Nanomed. Nanobiotechnol.* **2013**, *5*, 205-218.

(189) Zhang, Z. J.; Wang, J.; Chen, C. Y. Near-infrared light-mediated nanoplatforms for cancer thermo-chemotherapy and optical imaging. *Adv. Mater.* **2013**, *25*, 3869-3880.

(190) Hasanovic, A.; Zehl, M.; Reznicek, G.; Valenta, C. Chitosan-tripolyphosphate nanoparticles as a possible skin drug delivery system for aciclovir with enhanced stability. *J. Pharm. Pharmacol.* **2009**, *61*, 1609-1616.

(191) Kim, D.; Jeong, Y.; Choi, C.; Roh, S.; Kang, S.; Jang, M.; Nah, J. Retinol-encapsulated low molecular water-soluble chitosan nanoparticles. *Int. J. Pharm.* **2006**, *319*, 130-138.

(192) Bahadar, H.; Maqbool, F.; Niaz, K.; Abdollahi, M. Toxicity of Nanoparticles and an Overview of Current Experimental Models. *Iran Biomed. J.* **2016**, *20*, 1-11.

(193) Vijayan, V.; Reddy, K.; Sakthivel, S.; Swetha, C. Optimization and charaterization of repaglinide biodegradable polymeric nanoparticle loaded transdermal patchs: in vitro and in vivo studies. *Colloids Surf. B* **2013**, *111*, 150-155.

(194) Shah, A. P.; Pietropaoli, A. P.; Frasier, L. M.; Speers, D. M.; Chalupa, D. C.; Delehanty, J. M.; Huang, L. S.; Utell, M. J.; Frampton, M. W. Effect of inhaled carbon ultrafine particles on reactive hyperemia in healthy human subjects. *Environ. Health Perspect.* **2008**, *116*, 375-380.

(195) Tomoda, K.; Terashima, H.; Suzuki, K.; Inagi, T.; Terada, H.; Makino, K. Enhanced transdermal delivery of indomethacin-loaded PLGA nanoparticles by iontophoresis. *Colloids Surf. B* **2011**, *88*, 706-710.

(196) Loos, C.; Syrovets, T.; Musyanovych, A.; Mailander, V.; Landfester, K.; Nienhaus, G. U.; Simmet, T. Functionalized polystyrene nanoparticles as a platform for studying bio-nano interactions. *Beilstein J. Nanotechnol.* **2014**, *5*, 2403-2412.

(197) Wünsch, J. R. *Polystyrene: Synthesis, Production and Applications*; iSmithers Rapra: Shropshire, 2000.

(198) Holzapfel, V.; Musyanovych, A.; Landfester, K.; Lorenz, M. R.; Mailänder, V. Preparation of Fluorescent Carboxyl and Amino Functionalized Polystyrene Particles by Miniemulsion Polymerization as Markers for Cells. *Macromol. Chem. Phys.* **2005**, *206*, 2440-2449.

(199) Im, S. H.; Khalil, G. E.; Callis, J.; Ahn, B. H.; Gouterman, M.; Xia, Y. Synthesis of polystyrene beads loaded with dual luminophors for self-referenced oxygen sensing. *Talanta* **2005**, *67*, 492-497.

(200) Hickey, J. W.; Santos, J. L.; Williford, J. M.; Mao, H. Q. Control of polymeric nanoparticle size to improve therapeutic delivery. *J. Control. Release* **2015**, *219*, 536-547.

(201) Bouwstra, J.; Ponec, M. The skin barrier in healthy and diseased state. *Biochim. Biophys. Acta.* **2006**, *1758*, 2080-2095.

(202) Johnson, M.; Blankschtein, D.; Langer, R. Evaluation of solute permeation through the stratum corneum: lateral bilayer diffusion as the primary transport mechanism. *J. Pharm. Sci.* **1997**, *86*, 1162-1172.

(203) Foroozandeh, P.; Aziz, A. A. Insight into Cellular Uptake and Intracellular Trafficking of Nanoparticles. *Nanoscale Res. Lett.* **2018**, *13*, 339.

(204) Osaki, F.; Kanamori, T.; Sando, S.; Sera, T.; Aoyama, Y. A Quantum Dot Conjugated Sugar Ball and Its Cellular Uptake. On the Size Effects of Endocytosis in the Subviral Region. *J. Am. Chem. Soc.* **2004**, *126*, 6520–6521.

(205) Petros, R.; DeSimone, J. Strategies in the design of nanoparticles for therapeutic applications. *Nat. Rev. Drug Discov.* **2010**, *9*, 615-627.

(206) Behnke, T.; Würth, C.; Laux, E.-M.; Hoffmann, K.; Resch-Genger, U. Simple strategies towards bright polymer particles via one-step staining procedures. *Dyes Pigm.* **2012**, *94*, 247-257.

(207) Yoo, J. W.; Mitragotri, S. Polymer particles that switch shape in response to a stimulus. *Proc. Natl. Acad. Sci. U.S.A.* **2010**, *107*, 11205-11210.

(208) Champion, J. A.; Katare, Y. K.; Mitragotri, S. Making polymeric micro- and nanoparticles of complex shapes. *Proc. Natl. Acad. Sci. U.S.A.* **2007**, *104*, 11901–11904.

(209) Williford, J. M.; Santos, J. L.; Shyam, R.; Mao, H. Q. Shape Control in Engineering of Polymeric Nanoparticles for Therapeutic Delivery. *Biomater. Sci.* **2015**, *3*, 894-907.

(210) Elsabahy, M.; Wooley, K. L. Design of polymeric nanoparticles for biomedical delivery applications. *Chem. Soc. Rev.* **2012**, *41*, 2545-2561.

(211) Geng, Y.; Dalhaimer, P.; Cai, S.; Tsai, R.; Tewari, M.; Minko, T.; Discher, D. E. Shape effects of filaments versus spherical particles in flow and drug delivery. *Nat. Nanotechnol.* **2007**, *2*, 249-255.

(212) Lalloz, A.; Bolzinger, M.-A.; Faivre, J.; Latreille, P.-L.; Garcia Ac, A.; Rakotovao, C.; Rabanel, J.-M.; Hildgen, P.; Banquy, X.; Briançon, S. Effect of surface chemistry of polymeric nanoparticles on cutaneous penetration of cholecalciferol. *Int. J. Pharm.* **2018**, *553*, 120-131.

(213) Amgoth, C.; Phan, C.; Banavoth, M.; Rompivalasa, S.; Tang, G. In *Role of Novel Drug Delivery Vehicles in Nanobiomedicine*, Tyagi, R. K., Ed.; IntechOpen: London, 2020 (DOI: 10.5772/intechopen.84550).

(214) Chen, H. Y.; Hayashi, T.; Koenig, M.; Lai, J. J. Editorial: Polymer Surface Chemistry: Biomolecular Engineering and Biointerfaces. *Front. Chem.* **2019**, *7*, 271.

(215) Delair, T.; Marguet, V.; Pichot, C.; Mandrand, B. Synthesis and characterization of cationic amino functionalized polystyrene latexes. *Colloid. Polym. Sci.* **1994**, *272*, 962–970.

(216) Cox, A. J.; DeWeerd, A. J.; Linden, J. An experiment to measure Mie and Rayleigh total scattering cross sections. *Am. J. Phys.* **2002**, *70*, 620-625.

(217) Lockwood, D. J. In *Encyclopedia of Color Science and Technology*, Luo, M. R., Ed.; Springer: New York, 2016, p 26.

(218) Stratton, J. A. *Electromagnetic Theory*; McGraw-Hill: New York, 1941.

(219) Wagh, A.; Jyoti, F.; Mallik, S.; Qian, S.; Leclerc, E.; Law, B. Polymeric nanoparticles with sequential and multiple FRET cascade mechanisms for multicolor and multiplexed imaging. *Small* **2013**, *9*, 2129-2139.

(220) Wilde, S.; Ma, D.; Koch, T.; Bakker, A.; Gonzalez-Abradelo, D.; Stegemann, L.; Daniliuc, C. G.; Fuchs, H.; Gao, H.; Doltsinis, N. L.; Duan, L.; Strassert, C. A. Toward Tunable Electroluminescent Devices by Correlating Function and Submolecular Structure in 3D Crystals, 2D-Confined Monolayers, and Dimers. *ACS Appl. Mater. Interfaces* **2018**, *10*, 22460-22473.

(221) Zong, L.; Xie, Y.; Wang, C.; Li, J. R.; Li, Q.; Li, Z. From ACQ to AIE: the suppression of the strong pi-pi interaction of naphthalene diimide derivatives through the adjustment of their flexible chains. *Chem. Commun.* **2016**, *52*, 11496-11499.

(222) Mei, J.; Leung, N. L.; Kwok, R. T.; Lam, J. W.; Tang, B. Z. Aggregation-Induced Emission: Together We Shine, United We Soar! *Chem. Rev.* **2015**, *115*, 11718-11940.

(223) Aliprandi, A.; Mauro, M.; De Cola, L. Controlling and imaging biomimetic self-assembly. *Nat. Chem.* **2016**, *8*, 10-15.

(224) Rosiuk, V.; Runser, A.; Klymchenko, A.; Reisch, A. Controlling Size and Fluorescence of Dye-Loaded Polymer Nanoparticles through Polymer Design. *Langmuir* **2019**, *35*, 7009-7017.

(225) Demas, J. N.; Harris, E. W.; McBride, R. P. Energy transfer from luminescent transition metal complexes to oxygen. *J. Am. Chem. Soc.* **1977**, *99*, 3547-3551.

(226) Nirmalananthan, N.; Behnke, T.; Hoffmann, K.; Kage, D.; Gers-Panther, C. F.; Frank, W.; Müller, T. J. J.; Resch-Genger, U. Crystallization and Aggregation-Induced Emission in a Series of Pyrrolidinylvinylquinoxaline Derivatives. *J. Phys. Chem. C* **2018**, *122*, 11119-11127.

(227) Zhu, H. G.; McShane, M. J. Loading of Hydrophobic Materials into Polymer Particles: Implications for Fluorescent Nanosensors and Drug Delivery. *J. Am. Chem. Soc.* **2005**, *127*, 13448–13449.

(228) Errede, L. A.; Hanson, S. C. Polymer swelling. XV. Swelling and deswelling studies of polystyrene–liquid systems in binary solutions. *J. Appl. Polym. Sci.* **1994**, *54*, 619–647.

(229) Beck-Broichsitter, M.; Rytting, E.; Lebhardt, T.; Wang, X.; Kissel, T. Preparation of nanoparticles by solvent displacement for drug delivery: a shift in the "ouzo region" upon drug loading. *Eur. J. Pharm. Sci.* **2010**, *41*, 244-253.

(230) Shamsipur, M.; Barati, A.; Nematifar, Z. Fluorescent pH nanosensors: Design strategies and applications. *J. Photochem. Photobiol. C* **2019**, *39*, 76-141.

(231) Lee, I.; Kim, S.; Kim, S. N.; Jang, Y.; Jang, J. Highly fluorescent amidine/schiff base dual-modified polyacrylonitrile nanoparticles for selective and sensitive detection of copper ions in living cells. *ACS Appl. Mater. Interfaces* **2014**, *6*, 17151-17156.

(232) Wang, X.-D.; Stolwijk, J. A.; Lang, T.; Sperber, M.; Meier, R. J.; Wegener, J.; Wolfbeis, O. S. Ultra-small, highly stable, and sensitive dual nanosensors for imaging intracellular oxygen and pH in cytosol. *J. Am. Chem. Soc.* **2012**, *134*, 17011-17014.

(233) Abd Ellah, N. H.; Abouelmagd, S. A. Surface functionalization of polymeric nanoparticles for tumor drug delivery: approaches and challenges. *Expert Opin. Drug. Deliv.* **2017**, *14*, 201-214.

(234) Ehgartner, J.; Strobl, M.; Bolivar, J. M.; Rabl, D.; Rothbauer, M.; Ertl, P.; Borisov, S. M.; Mayr, T. Simultaneous Determination of Oxygen and pH Inside Microfluidic Devices Using Core-Shell Nanosensors. *Anal. Chem.* **2016**, *88*, 9796-9804.

(235) Allard, E.; Larpent, C. Core-shell type dually fluorescent polymer nanoparticles for ratiometric pH-sensing. *J. Polym. Sci. Pol. Chem.* **2008**, *46*, 6206-6213.

(236) Stöber, W.; Fink, A.; Bohn, E. Controlled Growth of Monodisperse Silica Spheres in the Micron Size Range. *J. Colloid Interface Sci.* **1968**, *26*, 62-69.

(237) Han, Y.; Lu, Z.; Teng, Z.; Liang, J.; Guo, Z.; Wang, D.; Han, M. Y.; Yang, W. Unraveling the Growth Mechanism of Silica Particles in the Stober Method: In Situ Seeded Growth Model. *Langmuir* **2017**, *33*, 5879-5890.

(238) Wang, X.-D.; Shen, Z.-X.; Sang, T.; Cheng, X.-B.; Li, M.-F.; Chen, L.-Y.; Wang, Z.-S. Preparation of spherical silica particles by Stober process with high concentration of tetra-ethyl-orthosilicate. *J. Colloid Interface Sci.* **2010**, *341*, 23-29.

(239) Boissière, C.; van der Lee, A.; Mansouri, A. E.; Larbot, A.; Prouzet, E. A double step synthesis of mesoporous micrometric spherical MSU-X silica particles. *Chem. Commun.* **1999**, *20*, 2047–2048.

(240) Van Blaaderen, A.; Van Geest, J.; Vrij, A. Monodisperse colloidal silica spheres from tetraalkoxysilanes: Particle formation and growth mechanism. *J. Colloid Interface Sci.* **1992**, *154*, 481-501.

(241) Masse, S.; Laurent, G.; Chuburu, F.; Cadiou, C.; Déchamps, I.; Coradin, T. Modification of the Stöber Process by a Polyazamacrocycle Leading to Unusual Core–Shell Silica Nanoparticles. *Langmuir* **2008**, *24*, 4026–4031.

(242) Masse, S.; Laurent, G.; Coradin, T. Influence of cyclic polyamines on silica formation during the Stober process. *Phys. Chem. Chem. Phys.* **2009**, *11*, 10204-10210.

(243) Sperling, R. A.; Parak, W. J. Surface modification, functionalization and bioconjugation of colloidal inorganic nanoparticles. *Philos. Trans. A Math. Phys. Eng. Sci.* **2010**, *368*, 1333-1383.

(244) Yang, Z.; Cong, H.; Cao, W. Narrowly dispersed micrometer-sized composite spheres based on diazonium-polystyrene. *J. Polym. Sci. Pol. Chem.* **2004**, *42*, 4284-4288.

(245) Hong, J.; Han, H.; Hong, C. K.; Shim, S. E. A direct preparation of silica shell on polystyrene microspheres prepared by dispersion polymerization with polyvinylpyrrolidone. *J. Polym. Sci. Pol. Chem.* **2008**, *46*, 2884-2890.

(246) Lu, X.; Xin, Z. Preparation and characterization of micron-sized polystyrene/polysiloxane core/shell particles. *Colloid Polym. Sci.* **2006**, *284*, 1062-1066.

(247) Ding, X.; Jiang, Y.; Yu, K.; Hari, B.; Tao, N.; Zhao, J.; Wang, Z. Silicon dioxide as coating on polystyrene nanoparticles in situ emulsion polymerization. *Mater. Lett.* **2004**, *58*, 1722-1725.

(248) Wang, L.; Zhao, W.; Tan, W. Bioconjugated silica nanoparticles: Development and applications. *Nano Res.* **2008**, *1*, 99-115.

(249) Luo, F.; Yin, J.; Gao, F.; Wang, L. A non-enzyme hydrogen peroxide sensor based on core/shell silica nanoparticles using synchronous fluorescence spectroscopy. *Microchim. Acta* **2008**, *165*, 23-28.

(250) Jennette, K. W.; Gill, J. T.; Sadownick, J. A.; Lippard, S. J. Metallointercalation reagents. Synthesis, characterization, and structural properties of thiolato(2,2',2''-terpyridine)platinum(II) complexes. *J. Am. Chem. Soc.* **1976**, *98*, 6159-6168.

(251) Ding, J.; Pan, D.; Tung, C.-H.; Wu, L.-Z. Synthesis and Photophysical Studies of Calix[4]arene-based Binuclear Platinum(II) Complexes: Probing Metal-Metal and Ligand-Ligand Interactions. *Inorg. Chem.* **2008**, *47*, 5099-5106.

(252) Sun, C. Y.; To, W. P.; Hung, F. F.; Wang, X. L.; Su, Z. M.; Che, C. M. Metal-organic framework composites with luminescent pincer platinum(ii) complexes: [3]MMLCT emission and photoinduced dehydrogenation catalysis. *Chem. Sci.* **2018**, *9*, 2357-2364.

(253) Proetto, M. T.; Sanning, J.; Peterlechner, M.; Thunemann, M.; Stegemann, L.; Sadegh, S.; Devor, A.; Gianneschi, N. C.; Strassert, C. A. Phosphorescent Pt(ii) complexes spatially arrayed in micellar polymeric nanoparticles providing dual readout for multimodal imaging. *Chem. Commun.* **2019**, *55*, 501-504.

(254) Chen, W.-C.; Chou, P.-T.; Cheng, Y.-C. Low Internal Reorganization Energy of the Metal–Metal-to-Ligand Charge Transfer Emission in Dimeric Pt(II) Complexes. *J. Phys. Chem. C* **2019**, *123*, 10225-10236.

(255) Wan, Q.; To, W. P.; Yang, C.; Che, C. M. The Metal-Metal-to-Ligand Charge Transfer Excited State and Supramolecular Polymerization of Luminescent Pincer Pd(II) -Isocyanide Complexes. *Angew. Chem. Int. Ed.* **2018**, *57*, 3089-3093.

(256) Zou, C.; Lin, J.; Suo, S.; Xie, M.; Chang, X.; Lu, W. Palladium(ii) N-heterocyclic allenylidene complexes with extended intercationic PdPd interactions and MMLCT phosphorescence. *Chem. Commun.* **2018**, *54*, 5319-5322.

(257) Dexter, D. L. A Theory of Sensitized Luminescence in Solids. *J. Chem. Phys.* **1953**, *21*, 836-850.

(258) McNaught, A. D.; Wilkinson, A. *Compendium of Chemical Terminology (IUPAC Gold Book)*, 2nd ed.; Blackwell Scientific Publications: Oxford, 1997.

(259) Skourtis, S. S.; Liu, C.; Antoniou, P.; Virshup, A. M.; Beratan, D. N. Dexter energy transfer pathways. *Proc. Natl. Acad. Sci. U.S.A.* **2016**, *113*, 8115-8120.

(260) Helms, V. In *Principles of Computational Cell Biology: From Protein Complexes to Cellular Networks*; Wiley-VCH: Weinheim, 2008, p 202.

(261) Sekar, R. B.; Periasamy, A. Fluorescence resonance energy transfer (FRET) microscopy imaging of live cell protein localizations. *J. Cell. Biol.* **2003**, *160*, 629-633.

(262) Murphy, C. B.; Zhang, Y.; Troxler, T.; Ferry, V.; Martin, J. J.; Jones, W. E. Probing Förster and Dexter Energy-Transfer Mechanisms in Fluorescent Conjugated Polymer Chemosensors. *J. Phys. Chem. B* **2004**, *108*, 1537–1543.

(263) Ho, J.; Kish, E.; Mendez-Hernandez, D. D.; WongCarter, K.; Pillai, S.; Kodis, G.; Niklas, J.; Poluektov, O. G.; Gust, D.; Moore, T. A.; Moore, A. L.; Batista, V. S.; Robert, B. Triplet-triplet energy

transfer in artificial and natural photosynthetic antennas. *Proc. Natl. Acad. Sci. U.S.A.* **2017**, *114*, E5513-E5521.

(264) Reineke, S.; Lindner, F.; Schwartz, G.; Seidler, N.; Walzer, K.; Lussem, B.; Leo, K. White organic light-emitting diodes with fluorescent tube efficiency. *Nature* **2009**, *459*, 234-238.

(265) Sun, Q.-C.; Ding, Y. C.; Sagar, D. M.; Nagpal, P. Photon upconversion towards applications in energy conversion and bioimaging. *Prog. Surf. Sci.* **2017**, *92*, 281-316.

(266) Gray, V.; Wikimedia Commons: (https://commons.wikimedia.org/wiki/File:Stokes_and_Anti-Stokes_emission.jpg), https://creativecommons.org/licenses/by-sa/4.0/legalcode, 2015.

(267) Auzel, F. Upconversion and Anti-Stokes Processes with f and d Ions in Solids. *Chem. Rev.* **2004**, *104*, 139–173.

(268) Reddy, K. L.; Balaji, R.; Kumar, A.; Krishnan, V. Lanthanide Doped Near Infrared Active Upconversion Nanophosphors: Fundamental Concepts, Synthesis Strategies, and Technological Applications. *Small* **2018**, *14*, 1801304.

(269) Li, D.; Agren, H.; Chen, G. Near infrared harvesting dye-sensitized solar cells enabled by rare-earth upconversion materials. *Dalton Trans.* **2018**, *47*, 8526-8537.

(270) Joubert, M.-F. Photon avalanche upconversion in rare earth laser materials. *Opt. Mater.* **1999**, *11*, 181-203.

(271) Parker, C. A.; Hatchard, C. G. Delayed Fluorescence from Solutions of Anthracene and Phenanthrene. *Proc. R. Soc. Lond. A* **1962**, *269*, 574–584.

(272) Parker, C. A.; Hatchard, C. G. Sensitized Anti-Stokes Delayed Fluorescence. *Proc. Chem. Soc.* **1962**, 386-387.

(273) Zhou, J.; Liu, Q.; Feng, W.; Sun, Y.; Li, F. Upconversion luminescent materials: advances and applications. *Chem. Rev.* **2015**, *115*, 395-465.

(274) Singh-Rachford, T. N.; Castellano, F. N. Photon upconversion based on sensitized triplet–triplet annihilation. *Coord. Chem. Rev.* **2010**, *254*, 2560-2573.

(275) Gray, V.; Moth-Poulsen, K.; Albinsson, B.; Abrahamsson, M. Towards efficient solid-state triplet–triplet annihilation based photon upconversion: Supramolecular, macromolecular and self-assembled systems. *Coord. Chem. Rev.* **2018**, *362*, 54-71.

(276) Cheng, Y. Y.; Khoury, T.; Clady, R. G. C. R.; Tayebjee, M. J. Y.; Ekins-Daukes, N. J.; Crossleya, M. J.; Schmidt, T. W. On the efficiency limit of triplet–triplet annihilation for photochemical upconversion. *Phys. Chem. Chem. Phys.* **2010**, *12*, 66-71.

(277) Kouno, H.; Sasaki, Y.; Yanai, N.; Kimizuka, N. Supramolecular Crowding Can Avoid Oxygen Quenching of Photon Upconversion in Water. *Chem. Eur. J.* **2019**, *25*, 6124-6130.

(278) Kamada, K.; Sakagami, Y.; Mizokuro, T.; Fujiwara, Y.; Kobayashi, K.; Narushima, K.; Hirata, S.; Vacha, M. Efficient triplet–triplet annihilation upconversion in binary crystalline solids fabricated via solution casting and operated in air. *Mater. Horiz.* **2017**, *4*, 83-87.

(279) Mahato, P.; Monguzzi, A.; Yanai, N.; Yamada, T.; Kimizuka, N. Fast and long-range triplet exciton diffusion in metal-organic frameworks for photon upconversion at ultralow excitation power. *Nat. Mater.* **2015**, *14*, 924-930.

(280) Cui, X.; Zhao, J.; Mohmood, Z.; Zhang, C. Accessing the Long-Lived Triplet Excited States in Transition-Metal Complexes: Molecular Design Rationales and Applications. *Chem. Rev.* **2016**, *16*, 173-188.

(281) Ahuja, D.; Parande, D. Optical sensors and their applications. *J. Sci. Res. Rev.* **2012**, *1*, 60 - 68.

(282) Miki, H.; Matsubara, F.; Nakashima, S.; Ochi, S.; Nakagawa, K.; Matsuguchi, M.; Sadaoka, Y. A fractional exhaled nitric oxide sensor based on optical absorption of cobalt tetraphenylporphyrin derivatives. *Sens. Actuators B Chem.* **2016**, *231*, 458-468.

(283) Tan, L. L.; Ahmad, M.; Lee, Y. H. A novel optical ammonia sensor based on reflectance measurements for highly polluted and coloured water. *Sens. Actuators B Chem.* **2012**, *171-172*, 994-1000.

(284) Rivero, P. J.; Urrutia, A.; Goicoechea, J.; Matías, I. R.; Arregui, F. J. A Lossy Mode Resonance optical sensor using silver nanoparticles-loaded films for monitoring human breathing. *Sens. Actuators B Chem.* **2013**, *187*, 40-44.

(285) Lobnik, A.; Turel, M.; Urek, Š. K. In *Advances in Chemical Sensors*, Wang, W., Ed.; IntechOpen: London, 2012 (DOI: 10.5772/31534).

(286) De Silva, A. P.; Gunaratne, H. Q. N.; Gunnlaugsson, T.; Huxley, A. J. M.; McCoy, C. P.; Rademacher, J. T.; Rice, T. E. Signaling Recognition Events with Fluorescent Sensors and Switches. *Chem. Rev.* **1997**, *97*, 1515-1566.

(287) Rurack, K.; Resch-Genger, U. Rigidization, preorientation and electronic decoupling—the 'magic triangle' for the design of highly efficient fluorescent sensors and switches. *Chem. Soc. Rev.* **2002**, *31*, 116-127.

(288) Valeur, B.; Leray, I. In *New Trends in Fluorescence Spectroscopy.* , Valeur, B.; Brochon, J., Eds.; Springer: Berlin Heidelberg, 2001.

(289) Choi, Y.; Kotthoff, L.; Olejko, L.; Resch-Genger, U.; Bald, I. DNA Origami-Based Forster Resonance Energy-Transfer Nanoarrays and Their Application as Ratiometric Sensors. *ACS Appl. Mater. Interfaces* **2018**, *10*, 23295-23302.

(290) Oh, W.; Jeong, Y.; Kim, S.; Jang, J. Fluorescent Polymer Nanoparticle for Selective Sensing of Intracellular Hydrogen Peroxide. *ACS Nano* **2012**, *6*, 8516-8524.

(291) Stern, O.; Volmer, M. Über die Abklingzeit der Fluoreszenz. *Z. Phys.* **1919**, *20*, 183–188.

(292) Gehlen, M. H. The centenary of the Stern-Volmer equation of fluorescence quenching: From the single line plot to the SV quenching map. *J. Photochem. Photobiol. C* **2020**, *42*, 100338.

(293) Boaz, H.; Rollefson, G. K. The quenching of fluorescence. Deviations from the Stern-Volmer Law. *J. Am. Chem. Soc.* **1950**, *72*, 3435–3443.

(294) Noyes, R. M. The competition of unimolecular and bimolecular processeswith special applications to the quenching of fluorescence in solution. *J. Am.Chem. Soc.* **1957**, *79*, 551-555.

(295) Weller, A. Eine verallgemeinerte Theorie Diffusion bestimmter Reacktionen und ihre Anwendugn auf die Fluoreszenzöschung. *Z. Phys. Chem.* **1957**, *13*, 335-352.

(296) Keizer, J. Nonlinear fluorescence quenching and the origin of the positivecurvature in Stern-Volmer plots. *J. Am. Chem. Soc.* **1983**, *105*, 1494–1498.

(297) Skoog, D. A.; West, D. M.; Holler, F. J. *Fundamentals of analytical chemistry*, 5th ed.; Saunders: Philadelphia, 1988.

(298) Clark, L. C. Electrochemical device for chemical analysis. *US Patent 2 913 386,* **1959**.

(299) Freeman, T. M.; Seitz, W. R. Oxygen probe based on tetrakis(alkylamino)ethylene chemiluminescence. *Anal. Chem.* **1981**, *53*, 98-102.

(300) Hendricks, H. D. Method of detecting oxygen in a gas. *US Patent 3 709 663,* **1973**.

(301) Amao, Y. Probes and Polymers for Optical Sensing of Oxygen. *Microchim. Acta* **2003**, *143*, 1-12.

(302) Tusa, J. K.; He, H. Critical care analyzer with fluorescent optical chemosensors for blood analytes. *J. Mater. Chem.* **2005**, *15*, 2640–2647.

(303) Millikan, G. A. The oximeter, an instrument for measuring continuously the oxygen saturation of arterial blood in man. *Rev. Sci. Instrum.* **1942**, *13*, 434-444.

(304) Schreml, S.; Meier, R. J.; Wolfbeis, O. S.; Maisch, T.; Szeimies, R. M.; Landthaler, M.; Regensburger, J.; Santarelli, F.; Klimant, I.; Babilas, P. 2D luminescence imaging of physiological wound oxygenation. *Exp. Dermatol.* **2011**, *20*, 550-554.

(305) Babilas, P.; Lamby, P.; Prantl, L.; Schreml, S.; Jung, E. M.; Liebsch, G.; Wolfbeis, O. S.; Landthaler, M.; Szeimies, R.-M.; Abels, C. Transcutaneous pO$_2$ imaging during tourniquet-induced forearm ischemia using planar optical oxygen sensors. *Skin Res. Technol.* **2008**, *14*, 304-311.

(306) Zhang, G.; Palmer, G. M.; Dewhirst, M. W.; Fraser, C. L. A dual-emissive-materials design concept enables tumour hypoxia imaging. *Nat. Mater.* **2009**, *8*, 747-751.

(307) Voraberger, H. S.; Kreimaier, H.; Biebernik, K.; Kern, W. Novel oxygen optrode withstanding autoclavation: technical solutions and performance. *Sens. Actuators B Chem.* **2001**, *74*, 179-185.

(308) Park, E. J.; Reid, K. R.; Tang, W.; Kennedy, R. T.; Kopelman, R. Ratiometric fiber optic sensors for the detection of inter- and intra-cellular dissolved oxygen. *J. Mater. Chem.* **2005**, *15*, 2913-2919.

(309) Quaranta, M.; Borisov, S. M.; Klimant, I. Indicators for optical oxygen sensors. *Bioanal. Rev.* **2012**, *4*, 115-157.

(310) Otto, S.; Nauth, A. M.; Ermilov, E.; Scholz, N.; Friedrich, A.; Resch-Genger, U.; Lochbrunner, S.; Opatz, T.; Heinze, K. Photo-Chromium: Sensitizer for Visible-Light-Induced Oxidative C-H Bond Functionalization. *ChemPhotoChem* **2017**, *1*, 344-349.

(311) DeRosa, M. C.; Crutchley, R. J. Photosensitized singlet oxygen and its applications. *Coord. Chem. Rev.* **2002**, *233-234,* , 351-371.

(312) Ast, C.; Schmalzlin, E.; Lohmannsroben, H. G.; van Dongen, J. T. Optical oxygen micro- and nanosensors for plant applications. *Sensors* **2012**, *12*, 7015-7032.

(313) Carraway, E. R.; Demas, J. N.; DeGraff, B. A. Luminescence quenching mechanism for microheterogeneous systems. *Anal. Chem.* **1991**, *63*, 332–336.

(314) Zhou, C.; Zhao, W. X.; You, F. T.; Geng, Z. X.; Peng, H. S. Highly Stable and Luminescent Oxygen Nanosensor Based on Ruthenium-Containing Metallopolymer for Real-Time Imaging of Intracellular Oxygenation. *ACS Sens.* **2019**, *4*, 984-991.

(315) Hirsch, A. *The chemistry of the fullerenes*; Wiley-VCH: Weinheim, 1994.

(316) Kochmann, S.; Baleizao, C.; Berberan-Santos, M. N.; Wolfbeis, O. S. Sensing and imaging of oxygen with parts per billion limits of detection and based on the quenching of the delayed fluorescence of $^{(13)}C_{70}$ fullerene in polymer hosts. *Anal. Chem.* **2013**, *85*, 1300-1304.

(317) Moßhammer, M.; Strobl, M.; Kühl, M.; Klimant, I.; Borisov, S. M.; Koren, K. Design and Application of an Optical Sensor for Simultaneous Imaging of pH and Dissolved O_2 with Low Cross-Talk. *ACS Sens.* **2016**, *1*, 681-687.

(318) Otto, S.; Dorn, M.; Förster, C.; Bauer, M.; Seitz, M.; Heinze, K. Understanding and exploiting long-lived near-infrared emission of a molecular ruby. *Coord. Chem. Rev.* **2018**, *359*, 102-111.

(319) Lin, Q.; Lu, T. T.; Zhu, X.; Wei, T. B.; Li, H.; Zhang, Y. M. Rationally introduce multi-competitive binding interactions in supramolecular gels: a simple and efficient approach to develop multi-analyte sensor array. *Chem. Sci.* **2016**, *7*, 5341-5346.

(320) Kolanowski, J. L.; Liu, F.; New, E. J. Fluorescent probes for the simultaneous detection of multiple analytes in biology. *Chem. Soc. Rev.* **2018**, *47*, 195-208.

(321) Sinhababu, A. K.; Thakker, D. R. Prodrugs of anticancer agents. *Adv. Drug Deliv. Rev.* **1996**, *19*, 241–273.

(322) Visvader, J. E. Cells of origin in cancer. *Nature* **2011**, *469*, 314-322.

(323) Grüning, N.-M.; Ralser, M. Sacrifice for survival. *Nature* **2011**, *480*, 190-191.

(324) Stich, M. I.; Fischer, L. H.; Wolfbeis, O. S. Multiple fluorescent chemical sensing and imaging. *Chem. Soc. Rev.* **2010**, *39*, 3102-3114.

(325) Zach, P. W.; Freunberger, S. A.; Klimant, I.; Borisov, S. M. Electron-Deficient Near-Infrared Pt(II) and Pd(II) Benzoporphyrins with Dual Phosphorescence and Unusually Efficient Thermally Activated Delayed Fluorescence: First Demonstration of Simultaneous Oxygen and Temperature Sensing with a Single Emitter. *ACS Appl. Mater. Interfaces* **2017**, *9*, 38008-38023.

(326) Stich, M. I. J.; Schäferling, M.; Wolfbeis, O. S. Multicolor Fluorescent and Permeation-Selective Microbeads Enable Simultaneous Sensing of pH, Oxygen, and Temperature. *Adv. Mater.* **2009**, *21*, 2216-2220.

(327) Hollas, J. M. *Modern Spectroscopy*, 4th ed.; John Wiley & Sons: Chichester, 2003.

(328) Sobarwiki. Schematic of UV- visible spectrophotometer. *Wikimedia Commons https://commons.wikimedia.org/wiki/File:Schematic_of_UV-_visible_spectrophotometer.png* **2013**.

(329) Robinson, J. W.; Frame, E. M. S.; Frame II, G. M. *Undergraduate Instrumental Analysis*, 6th ed.; CRC Press: Boca Raton, 2004.

(330) Lewis, M. *Advanced Chemistry Through Diagrams*, 2nd ed.; Oxford University Press: Oxford 2001.

(331) Antosiewicz, J. M.; Shugar, D. UV-Vis spectroscopy of tyrosine side-groups in studies of protein structure. Part 1: basic principles and properties of tyrosine chromophore. *Biophys. Rev.* **2016**, *8*, 151-161.

(332) Raja, P. M. V.; Barron, A. R. In *Physical Methods in Chemistry and Nano Science*; OpenStax CNX http://cnx.org/contents/ba27839d-5042-4a40-afcf-c0e6e39fb454@25.2: Davis, California, 2019.

(333) Brouwer, A. M. Standards for photoluminescence quantum yield measurements in solution (IUPAC Technical Report). *Pure Appl. Chem.* **2011**, *83*, 2213–2228.

(334) Resch-Genger, U.; DeRose, P. C. Characterization of photoluminescence measuring systems (IUPAC Technical Report). *Pure Appl. Chem.* **2012**, *84*, 1815-1835.

(335) Wurth, C.; Geissler, D.; Behnke, T.; Kaiser, M.; Resch-Genger, U. Critical review of the determination of photoluminescence quantum yields of luminescent reporters. *Anal. Bioanal. Chem.* **2015**, *407*, 59-78.

(336) Suzuki, K.; Kobayashi, A.; Kaneko, S.; Takehira, K.; Yoshihara, T.; Ishida, H.; Shiina, Y.; Oishi, S.; Tobita, S. Reevaluation of absolute luminescence quantum yields of standard solutions using a spectrometer with an integrating sphere and a back-thinned CCD detector. *Phys. Chem. Chem. Phys.* **2009**, *11*, 9850-9860.

(337) Crosby, G. A.; Demas, J. N. Measurement of photoluminescence quantum yields. Review. *J. Phys. Chem.* **1971**, *75*, 991-1024.

(338) Porres, L.; Holland, A.; Palsson, L. O.; Monkman, A. P.; Kemp, C.; Beeby, A. Absolute measurements of photoluminescence quantum yields of solutions using an integrating sphere. *J. Fluoresc.* **2006**, *16*, 267-272.

(339) Würth, C.; Pauli, J.; Lochmann, C.; Spieles, M.; Resch-Genger, U. Integrating Sphere Setup for the Traceable Measurement of Absolute Photoluminescence Quantum Yields in the Near Infrared. *Anal. Chem.* **2012**, *84*, 1345-1352.

(340) Carr, K. F. Integrating Sphere Theory and Applications Part II: Integrating Sphere Applications. *Surf. Coat. Int.* **1997**, *10*, 485-490.

(341) Saylan, S.; Howells, C. T.; Dahlem, M. S. Integrating sphere based reflectance measurements for small-area semiconductor samples. *Rev. Sci. Instrum.* **2018**, *89*, 053101.

(342) Würth, C.; Fischer, S.; Grauel, B.; Alivisatos, A. P.; Resch-Genger, U. Quantum Yields, Surface Quenching, and Passivation Efficiency for Ultrasmall Core/Shell Upconverting Nanoparticles. *J. Am. Chem. Soc.* **2018**, *140*, 4922-4928.

(343) Yanai, N.; Suzuki, K.; Ogawa, T.; Sasaki, Y.; Harada, N.; Kimizuka, N. Absolute Method to Certify Quantum Yields of Photon Upconversion via Triplet-Triplet Annihilation. *J. Phys. Chem. A* **2019**, *123*, 10197-10203.

(344) Sauer, M.; Hofkens, J.; Enderlein, J. In *Handbook of fluorescence spectroscopy and imaging: From single molecules to ensembles*; Wiley-VCH: Weinheim, 2011, pp 1-30.

(345) Berezin, M. Y.; Achilefu, S. Fluorescence Lifetime Measurements and Biological Imaging. *Chem. Rev.* **2010**, *110*, 2641-2684.

(346) Sillen, A.; Engelborghs, Y. The Correct Use of "Average" Fluorescence Parameters. *Photochem. Photobiol.* **1998**, *67*, 475-486.

(347) Fišerová, E.; Kubala, M. Mean fluorescence lifetime and its error. *J. Lumin.* **2012**, *132*, 2059-2064.

(348) Sytsma, J.; Vroom, J. M.; De Grauw, C. J.; Gerritsen, H. C. Time-gated fluorescence lifetime imaging and microvolume spectroscopy using two-photon excitation. *J. Microsc.* **1998**, *191*, 39-51.

(349) Cominelli, A.; Acconcia, G.; Peronio, P.; Rech, I.; Ghioni, M. Readout Architectures for High Efficiency in Time-Correlated Single Photon Counting Experiments-Analysis and Review. *IEEE Photonics J.* **2017**, *9*, 1-15.

(350) Tyndall, D.; Rae, B. R.; Li, D. D.-U.; Arlt, J.; Johnston, A.; Richardson, J. A.; Henderson, R. K. A High-Throughput Time-Resolved Mini-Silicon Photomultiplier with Embedded Fluorescence Lifetime Estimation in 0.13 μm CMOS. *IEEE Trans. Biomed. Circuits Syst.* **2012**, *6*, 562–570.

(351) Wei, L.; Yan, W.; Ho, D. Recent Advances in Fluorescence Lifetime Analytical Microsystems: Contact Optics and CMOS Time-Resolved Electronics. *Sensors* **2017**, *17*, 2800.

(352) Chen, Y.; Periasamy, A. Characterization of two-photon excitation fluorescence lifetime imaging microscopy for protein localization. *Microsc. Res. Tech.* **2004**, *63*, 72-80.

(353) Bastiaens, P. I. H.; Squire, A. Fluorescencelifetime imagingmicroscopy: spatialresolution ofbiochemicalprocesses inthe cell. *Trends Cell Biol.* **1999**, *9*, 48-52.

(354) Xie, Y.; Arno, M. C.; Husband, J. T.; Torrent-Sucarrat, M.; O'Reilly, R. K. Manipulating the fluorescence lifetime at the sub-cellular scale via photo-switchable barcoding. *Nat. Commun.* **2020**, *11*, 2460.

(355) Suhling, K.; Hirvonen, L.; Levitt, J.; Chung, P.-H.; Tregidgo, C.; Marois, A. L.; Rusakov, D.; Zheng, K.; Ameer-Beg, S.; Poland, S.; Coelho, S.; Henderson, R.; Krstajic, N. Fluorescence lifetime imaging (FLIM): Basic concepts and some recent developments. *Medical Photonics* **2015**, *27*, 3-40.

(356) Berne, B. J.; Pecora, R. *Dynamic Light Scattering: With Applications to Chemistry, Biology, and Physics*; Courier Dover Publications: New York, 2000.

(357) Stetefeld, J.; McKenna, S. A.; Patel, T. R. Dynamic light scattering: a practical guide and applications in biomedical sciences. *Biophys. Rev.* **2016**, *8*, 409-427.

(358) 3P Instruments: Particle size measurement using multiangle dynamic light scattering, 2020.

(359) Particle Size Analysis – Dynamic Light Scattering (DLS), International Organization for Standardization (ISO): **ISO 22412**, 2017.

(360) Velu, S. K. P.; Yan, M.; Tseng, K.-P.; Wong, K.-T.; Bassani, D. M.; Terech, P. Spontaneous Formation of Artificial Vesicles in Organic Media through Hydrogen-Bonding Interactions. *Macromolecules* **2013**, *46*, 1591-1598.

(361) Jena, S. S.; Joshi, H. M.; Sabareesh, K. P. V.; Tata, B. V. R.; Rao, T. S. Dynamics of Deinococcus radiodurans under Controlled Growth Conditions. *Biophys. J.* **2006**, *91*, 2699–2707.

(362) Sabareesh, K. P. V.; Jena, S. S.; Tata, B. V. R. Dynamic Light Scattering Studies on Photo Polymerized and Chemically Cross-linked Polyacrylamide Hydrogels. *AIP Conf. Proc.* **2006**, *832*, 307-310.

(363) Filatov, M. A.; Baluschev, S.; Landfester, K. Protection of densely populated excited triplet state ensembles against deactivation by molecular oxygen. *Chem Soc Rev* **2016**, *45*, 4668-4689.

(364) Malvern Instruments, ZETASIZER NANO Series: PERFORMANCE, SIMPLICITY, VERSATILITY. *Https://www.Malvernpanalytical.Com/en/products/product-range/zetasizer-range/zetasizer-nano-range/zetasizer-nano-zs*.

(365) Aligent Technologies, Cary 100/300/4000/5000/6000i/7000 Spectrophotometers. *User´s Guide*, *https://www.agilent.com/cs/library/usermanuals/public/1972_7000.pdf*.

(366) Resch-Genger, U.; Bremser, W.; Pfeifer, D.; Spieles, M.; Hoffmann, A.; DeRose, P. C.; Zwinkels, J. C.; Gauthier, F.; Ebert, B.; Taubert, R. D.; Monte, C.; Voigt, J.; Hollandt, J.; Macdonald, R. State-of-the art comparability of corrected emission spectra. 1. Spectral correction with physical transfer standards and spectral fluorescence standards by expert laboratories. *Anal. Chem.* **2012**, *84*, 3889-3898.

(367) Resch-Genger, U.; Hoffmann, K.; Würth, C.; Behnke, T.; Hoffmann, A.; Pfeifer, D.; Engel, A. In *Sensors, and Command, Control, Communications, and Intelligence (C3I) Technologies for Homeland Security and Homeland Defense IX*, Carapezza, E. M., Ed.; SPIE Proceedings, 2010, p doi: 10.1117/1112.853133.

(368) Edinburgh Instruments, FLSP920 Series User Guide, Rev. 4. **2012**, *https://is.muni.cz/el/1431/podzim2016/C8785/um/59740449/59945287/FLSP920_Series_User_Guide_rev4.pdf*

(369) Edinburgh Instruments, FLS 980 Photoluminescence Spectrometer. *https://www.edinst.com/wp-content/uploads/2015/04/FLS980-Spectrometer.pdf*.

(370) Wurth, C.; Gonzalez, M. G.; Niessner, R.; Panne, U.; Haisch, C.; Genger, U. R. Determination of the absolute fluorescence quantum yield of rhodamine 6G with optical and photoacoustic methods-- providing the basis for fluorescence quantum yield standards. *Talanta* **2012**, *90*, 30-37.

(371) Lo, K. K.-W.; Li, S. P.-Y. Utilization of the photophysical and photochemical properties of phosphorescent transition metal complexes in the development of photofunctional cellular sensors, imaging reagents, and cytotoxic agents. *RSC Advances* **2014**, *4*.

(372) Hauser, A.; Reber, C. In *Structure and Bonding*; Springer: Berlin, 2016, p 291.

(373) Serpone, N.; Hoffman, M. Z. Chromium(III)-polypyridyls: A case study. *J. Chem. Educ.* **1983**, *60*, 853–860.

(374) Bernardi, F.; Olivucci, M.; Robb, M. A. Potential Energy Surface Crossings in Organic Photochemistry *Chem. Soc. Rev.* **1996**, *25*, 321-328.

(375) Iwamura, M.; Takeuchi, S.; Tahara, T. Ultrafast excited-state dynamics of copper(I) complexes. *Acc. Chem. Res.* **2015**, *48*, 782-791.

(376) Perkovic, M. W.; Heeg, M. J.; Endicott, J. F. Stereochemical perturbations of the relaxation behavior of (2E)chromium(III). Ground-state x-ray crystal structure, photophysics, and molecular mechanics simulations of the quasi-cage complex [4,4',4''-ethylidynetris(3-azabutan-1-amine)]chromium tribromide. *Inorg. Chem.* **1991**, *30*, 3140–3147.

(377) Kreitner, C.; Heinze, K. Excited state decay of cyclometalated polypyridine ruthenium complexes: insight from theory and experiment. *Dalton Trans.* **2016**, *45*, 13631-13647.

(378) Brown, K. N.; Geue, R. J.; Moran, G.; Ralph, S. F.; Riesen, H.; Sargeson, A. M. A long-lived ^{2}E state for a Cr(III)N$_6$ amine chromophore at 298 K: [Cr(fac-Me$_5$-D$_{3h}$tricosaneN$_6$)]Cl$_3$. *Chem. Commun.* **1998**, 2291–2292.

(379) Wang, C.; Otto, S.; Dorn, M.; Kreidt, E.; Lebon, J.; Srsan, L.; Di Martino-Fumo, P.; Gerhards, M.; Resch-Genger, U.; Seitz, M.; Heinze, K. Deuterated Molecular Ruby with Record Luminescence Quantum Yield. *Angew. Chem. Int. Ed.* **2018**, *57*, 1112-1116.

(380) Forster, L. S. Thermal relaxation in excited electronic states of d^3 and d^6 metal complexes. *Coord. Chem. Rev.* **2002**, *227*, 59– 92.

(381) Supkowski, R. M.; Horrocks, J., W. D. . On the determination of the number of water molecules, q, coordinated to europium(III) ions in solution from luminescence decay lifetimes. *Inorg. Chim. Acta* **2002**, *340*, 44.

(382) Hu, J. Y.; Ning, Y.; Meng, Y. S.; Zhang, J.; Wu, Z. Y.; Gao, S.; Zhang, J. L. Highly near-IR emissive ytterbium(iii) complexes with unprecedented quantum yields. *Chem Sci* **2017**, *8*, 2702-2709.

(383) Wurth, C.; Kaiser, M.; Wilhelm, S.; Grauel, B.; Hirsch, T.; Resch-Genger, U. Excitation power dependent population pathways and absolute quantum yields of upconversion nanoparticles in different solvents. *Nanoscale* **2017**, *9*, 4283-4294.

(384) Serpone, N.; Jamieson, M. A.; Siriam, R.; Hoffman, M. Z. Photophysics and photochemistry of polypyridyl complexes of chromium(III). *Inorg. Chem.* **1981**, *20*, 3983–3988.

(385) Turro, N. J.; Ramamurthy, V.; Scaiano, J. C. *Modern Molecular Photochemistry of Organic Molecules*; University Science Books: Sausalito, CA, USA, 2010.

(386) Wadhawan, J.; Welford, P.; McPeak, H.; Hahn, C.; Compton, R. The simultaneous voltammetric determination and detection of oxygen and carbon dioxide. A study of the kinetics of the reaction between superoxide and carbon dioxide in non-aqueous media using membrane-free gold disc microelectrodes. *Sens. Actuat. B* **2003**, *88*, 40–52.

(387) Kane-Maguire, N. A. P.; Kerr, R. C.; Walters, J. R. Environmental effects on the phosphorescence lifetime of cationic Cr(III) complexes. *Inorg. Chim. Acta* **1979**, *33*, 163–L165

(388) Ermolaev, V. L.; Sveshnikova, E. B. The application of luminescence-kinetic methods in the study of the formation of lanthanide ion complexes in solution. *Russ. Chem. Rev.* **1994**, *63*, 905-922.

(389) Doffek, C.; Wahsner, J.; Kreidt, E.; Seitz, M. Breakdown of the energy gap law in molecular lanthanoid luminescence: the smallest energy gap is not universally relevant for nonradiative deactivation. *Inorg. Chem.* **2014**, *53*, 3263-3265.

(390) Doffek, C.; Seitz, M. The Radiative Lifetime in Near-IR-Luminescent Ytterbium Cryptates: The Key to Extremely High Quantum Yields. *Angew. Chem. Int. Ed.* **2015**, *54*, 9719-9721.

(391) Doffek, C.; Alzakhem, N.; Bischof, C.; Wahsner, J.; Guden-Silber, T.; Lugger, J.; Platas-Iglesias, C.; Seitz, M. Understanding the quenching effects of aromatic C-H- and C-D-oscillators in near-IR lanthanoid luminescence. *J. Am. Chem. Soc.* **2012**, *134*, 16413-16423.

(392) Swofford, R. L.; Long, M. E.; Burberry, M. S.; Albrecht, A. C. ''Free'' O–H overtone absorption of methanols in the visible region by thermal lensing spectroscopy *J. Chem. Phys.* **1977**, *66*, 664–668.

(393) Förster, C.; Dorn, M.; Reuter, T.; Otto, S.; Davarci, G.; Reich, T.; Carrella, L. M.; Rentschler, E.; Heinze, K. Ddpd as expanded terpyridine: dramatic effects of symmetry and electronic properties in first row transition metal complexes. *Inorganics* **2018**, *6*, 1-37.

(394) Basu, U.; Otto, S.; Heinze, K.; Gasser, G. Biological Evaluation of the NIR-Emissive Ruby Analogue [Cr(ddpd)2][BF4]3 as a Photodynamic Therapy Photosensitizer. *Eur. J. Inorg. Chem.* **2018**, in press.

(395) Zhu, Y.; Ma, Y.; Zhu, J. The counter anion effect of ion-type phosphorescent dye tris(4,7-diphenyl-1,10-phenanthroline)ruthenium(II) complexes as dopant for light-emitting diodes. *J. Lumin.* **2013**, *137*, 198-203.

(396) Eom, G. H.; Kim, J. H.; Jo, Y. D.; Kim, E. Y.; Bae, J. M.; Kim, C.; Kim, S.-J.; Kim, Y. Anion effects on construction of cadmium(II) compounds with a chelating ligand bis(2-pyridylmethyl)amine: Their photoluminescence and catalytic activities. *Inorg. Chim. Acta* **2012**, *387*, 106-116.

(397) Pan, M.; Lan, M.-H.; Wang, X.-T.; Yan, C.; Liu, Y.; Su, C.-Y. Near infrared photoluminescence of ytterbium(III) complexes from tripodal ligands with different coordination conformations. *Inorg. Chim. Acta* **2010**, *363*, 3757-3764.

(398) Soulie, M.; Carayon, C.; Saffon, N.; Blanc, S.; Fery-Forgues, S. A comparative study of nine berberine salts in the solid state: optimization of the photoluminescence and self-association properties through the choice of the anion. *Phys. Chem. Chem. Phys.* **2016**, *18*, 29999-30008.

(399) Ma, D.; Duan, L.; Wei, Y.; He, L.; Wang, L.; Qiu, Y. Increased phosphorescent quantum yields of cationic iridium(III) complexes by wisely controlling the counter anions. *Chem. Commun.* **2014**, *50*, 530-532.

(400) Wang, C.; Otto, S.; Dorn, M.; Heinze, K.; Resch-Genger, U. Luminescent TOP Nanosensors for Simultaneously Measuring Temperature, Oxygen, and pH at a Single Excitation Wavelength. *Anal. Chem.* **2019**, *91*, 2337-2344.

(401) Breivogel, A.; Forster, C.; Heinze, K. A heteroleptic bis(tridentate)ruthenium(II) polypyridine complex with improved photophysical properties and integrated functionalizability. *Inorg. Chem.* **2010**, *49*, 7052-7056.

(402) Cussler, E. L. *Diffusion – Mass Transfer in Fluid Systems*; Cambridge University Press: Cambridge/New York, 1997.

(403) Ye, S.; Song, E. H.; Zhang, Q. Y. Transition Metal-Involved Photon Upconversion. *Adv. Sci. (Weinh)* **2016**, *3*, 1600302.

(404) Gamelin, D. R.; Güdel, H. U. Design of Luminescent Inorganic Materials: New Photophysical Processes Studied by Optical Spectroscopy. *Acc. Chem. Res.* **2000**, *33*, 235.

(405) Zhou, B.; Shi, B.; Jin, D.; Liu, X. Controlling upconversion nanocrystals for emerging applications. *Nat. Nanotechnol.* **2015**, *10*, 924.

(406) Wang, F.; Liu, X. Recent advances in the chemistry of lanthanide-doped upconversion nanocrystals. *Chem. Soc. Rev.* **2009**, *38*, 976-989.

(407) Golesorkhi, B.; Nozary, H.; Fürstenberg, A.; Piguet, C. Erbium complexes as pioneers for implementing linear light-upconversion in molecules. *Mater. Horiz.* **2020**, *7*, 1279-1296.

(408) Nonat, A. M.; Charbonniere, L. J. Upconversion of light with molecular and supramolecular lanthanide complexes. *Coord. Chem. Rev.* **2020**, *409*, 213192.

(409) Kiseleva, N.; Nazari, P.; Dee, C.; Busko, D.; Richards, B. S.; Seitz, M.; Howard, I. A.; Turshatov, A. Lanthanide Sensitizers for Large Anti-Stokes Shift Near-Infrared-to-Visible Triplet-Triplet Annihilation Photon Upconversion. *J. Phys. Chem. Lett.* **2020**, *11*, 2477-2481.

(410) Golesorkhi, B.; Furstenberg, A.; Nozary, H.; Piguet, C. Deciphering and quantifying linear light upconversion in molecular erbium complexes. *Chem. Sci.* **2019**, *10*, 6876-6885.

(411) Nonat, A.; Bahamyirou, S.; Lecointre, A.; Przybilla, F.; Mely, Y.; Platas-Iglesias, C.; Camerel, F.; Jeannin, O.; Charbonniere, L. J. Molecular Upconversion in Water in Heteropolynuclear Supramolecular Tb/Yb Assemblies. *J. Am. Chem. Soc.* **2019**, *141*, 1568-1576.

(412) Souri, N.; Tian, P.; Platas-Iglesias, C.; Wong, K. L.; Nonat, A.; Charbonniere, L. J. Upconverted Photosensitization of Tb Visible Emission by NIR Yb Excitation in Discrete Supramolecular Heteropolynuclear Complexes. *J. Am. Chem. Soc.* **2017**, *139*, 1456-1459.

(413) Aboshyan-Sorgho, L.; Besnard, C.; Pattison, P.; Kittilstved, K. R.; Aebischer, A.; Bunzli, J. C.; Hauser, A.; Piguet, C. Near-infrared-->visible light upconversion in a molecular trinuclear d-f-d complex. *Angew. Chem. Int. Ed.* **2011**, *50*, 4108-4112.

(414) Zare, D.; Suffren, Y.; Nozary, H.; Hauser, A.; Piguet, C. Controlling Lanthanide Exchange in Triple-Stranded Helicates: A Way to Optimize Molecular Light-Upconversion. *Angew. Chem. Int. Ed.* **2017**, *56*, 14612-14617.

(415) Heer, S.; Petermann, K.; Güdel, H. U. Upconversion excitation of Cr^{3+} emission in $YAlO_3$ codoped with Cr^{3+} and Yb^{3+}. *J. Lumin.* **2003**, *102-103*, 144-150.

(416) Heer, S.; Wermuth, M.; Krämer, K.; Güdel, H. U. Upconversion excitation of Cr^{3+} ^2E emission in $Y_3Ga_5O_{12}$ codoped with Cr^{3+} and Yb^{3+}. *Chem. Phys. Lett.* **2001**, *334*, 293.

(417) Kalmbach, J.; Wang, C.; You, Y.; Forster, C.; Schubert, H.; Heinze, K.; Resch-Genger, U.; Seitz, M. Near-IR to Near-IR Upconversion Luminescence in Molecular Chromium Ytterbium Salts. *Angew. Chem. Int. Ed.* **2020**, *59*, 18804-18808.

(418) de Sa´, G. F.; Malta, O. L.; de Mello Donega, C.; Simas, A. M.; Longo, R. L.; Santa-Cruz, P. A.; da Silva, J., E. F. . Spectroscopic properties and design of highly luminescent lanthanide coordination complexes. *Coord. Chem. Rev.* **2000**, *196*, 165.

(419) Imbert, D.; Cantuel, M.; Bünzli, J.-C. G.; Bernardinelli, G.; Piguet, C. Extending Lifetimes of Lanthanide-Based Near-Infrared Emitters (Nd, Yb) in the Millisecond Range through Cr(III) Sensitization in Discrete Bimetallic Edifices *J. Am. Chem. Soc.* **2003**, *125*, 15698.

(420) Aboshyan-Sorgho, L.; Nozary, H.; Aebischer, A.; Bunzli, J. C.; Morgantini, P. Y.; Kittilstved, K. R.; Hauser, A.; Eliseeva, S. V.; Petoud, S.; Piguet, C. Optimizing millisecond time scale near-infrared emission in polynuclear chrome(III)-lanthanide(III) complexes. *J. Am. Chem. Soc.* **2012**, *134*, 12675-12684.

(421) Torelli, S.; Imbert, D.; Cantuel, M.; Bernardinelli, G.; Delahaye, S.; Hauser, A.; Bunzli, J. C.; Piguet, C. Tuning the decay time of lanthanide-based near infrared luminescence from micro- to milliseconds through d-->f energy transfer in discrete heterobimetallic complexes. *Chem. Eur. J.* **2005**, *11*, 3228-3242.

(422) Kaiser, M.; Wurth, C.; Kraft, M.; Hyppanen, I.; Soukka, T.; Resch-Genger, U. Power-dependent upconversion quantum yield of NaYF4:Yb(3+),Er(3+) nano- and micrometer-sized particles - measurements and simulations. *Nanoscale* **2017**, *9*, 10051-10058.

(423) Charbonniere, L. J. Bringing upconversion down to the molecular scale. *Dalton Trans.* **2018**, *47*, 8566-8570.

(424) Borisov, S. M.; Wolfbeis, O. S. Optical Biosensors. *Chem. Rev.* **2008**, *108*, 423-461.

(425) Radunz, S.; Rune Tschiche, H.; Moldenhauer, D.; Resch-Genger, U. Broad range ON/OFF pH sensors based on p K a tunable fluorescent BODIPYs. *Sens. Actuators B Chem.* **2017**, *251*, 490-494.

(426) Wang, R.; Yu, C.; Yu, F.; Chen, L.; Yu, C. Molecular fluorescent probes for monitoring pH changes in living cells. *Trends Anal. Chem.* **2010**, *29*, 1004-1013.

(427) Han, J.; Burgess, K. Fluorescent Indicators for Intracellular pH. *Chem. Rev.* **2010**, *110*, 2709-2728.

(428) Stich, M. I. J.; Nagl, S.; Wolfbeis, O. S.; Henne, U.; Schäferling, M. A Dual Luminescent Sensor Material for Simultaneous Imaging of Pressure and Temperature on Surfaces. *Adv. Funct. Mater.* **2008**, *18*, 1399-1406.

(429) Chauhan, V. M.; Hopper, R. H.; Ali, S. Z.; King, E. M.; Udrea, F.; Oxley, C. H.; Aylott, J. W. Thermo-optical characterization of fluorescent rhodamine B based temperature-sensitive nanosensors using a CMOS MEMS micro-hotplate. *Sens. Actuators B Chem.* **2014**, *192*, 126-133.

(430) Fischer, L. H.; Stich, M. I. J.; Wolfbeis, O. S.; Tian, N.; Holder, E.; Schäferling, M. Red- and green-emitting iridium(III) complexes for a dual barometric and temperature-sensitive paint. *Chemistry* **2009**, *15*, 10857-10863.

(431) Hagen, T.; Taylor, C. T.; Lam, F.; Moncada, S. Redistribution of Intracellular Oxygen in Hypoxia by Nitric Oxide: Effect on HIF1α. *Science* **2003**, *302*, 1975.

(432) Borchert, N. B.; Ponomarev, G. V.; Kerry, J. P.; Papkovsky, D. B. O_2/pH Multisensor Based on One Phosphorescent Dye. *Anal. Chem.* **2011**, *83*, 18-22.

(433) Lu, H. G.; Jin, Y. G.; Tian, Y. Q.; Zhang, W. W.; Holl, M. R.; Meldrum, D. R. New ratiometric optical oxygen and pH dual sensors with three emission colors for measuring photosynthetic activity in Cyanobacteria. *J. Mater. Chem.* **2011**, *48*, 19293-192301.

(434) Bradley, M.; Alexander, L.; Duncan, K.; Chennaoui, M.; Jones, A. C.; Sa´nchez-Martı´n, R. M. pH sensing in living cells using fluorescent microspheres. *Bioorg. Med. Chem. Lett.* **2008**, *18*, 313-317.

(435) Quevedo, P. D.; Behnke, T.; Resch-Genger, U. Streptavidin conjugation and quantification-a method evaluation for nanoparticles. *Anal. Bioanal. Chem.* **2016**, *408*, 4133-4149.

(436) Vezzu, D. A.; Deaton, J. C.; Jones, J. S.; Bartolotti, L.; Harris, C. F.; Marchetti, A. P.; Kondakova, M.; Pike, R. D.; Huo, S. Highly luminescent tetradentate bis-cyclometalated platinum complexes: design, synthesis, structure, photophysics, and electroluminescence application. *Inorg. Chem.* **2010**, *49*, 5107-5119.

(437) Delcanale, P.; Galstyan, A.; Daniliuc, C. G.; Grecco, H. E.; Abbruzzetti, S.; Faust, A.; Viappiani, C.; Strassert, C. A. Oxygen-Insensitive Aggregates of Pt(II) Complexes as Phosphorescent Labels of Proteins with Luminescence Lifetime-Based Readouts. *ACS Appl. Mater. Interfaces* **2018**, *10*, 24361-24369.

(438) Mydlak, M.; Mauro, M.; Polo, F.; Felicetti, M.; Leonhardt, J.; Diener, G.; De Cola, L.; Strassert, C. A. Controlling Aggregation in Highly Emissive Pt(II) Complexes Bearing Tridentate Dianionic N $\wedge$ N $\wedge$ N Ligands. Synthesis, Photophysics, and Electroluminescence. *Chem. Mater.* **2011**, *23*, 3659-3667.

(439) Kuwabara, J.; Ogawa, Y.; Taketoshi, A.; Kanbara, T. Enhancement of the Photoluminescence of a Thioamide-based Pincer Palladium Complex in the Crystalline State. *J. Organomet. Chem.* **2011**, *696*, 1289–1293.

(440) Ghedini, M.; Pugliese, T.; La Deda, M.; Godbert, N.; Aiello, I.; Amati, M.; Belviso, S.; Lelj, F.; Accorsi, G.; Barigelletti, F. Spectroscopy and electrochemical properties of a homologous series of acetylacetonato and hexafluoroacetylacetonato cyclopalladated and cycloplatinated complexes. *Dalton Trans.* **2008**, 4303-4318.

(441) Förster, T.; Kasper, K. Ein Konzentrationsumschlag der Fluoreszenz. *Z Phys Chem (N F)* **1954**, *1*, 275-277.

(442) Chaaban, M.; Zhou, C.; Lin, H.; Chyi, B.; Ma, B. Platinum(ii) binuclear complexes: molecular structures, photophysical properties, and applications. *J. Mater. Chem. C* **2019**, *7*, 5910-5924.

(443) Chen, Y.-Z.; Pan, D.; Chen, B.; Wang, G.-X.; Tung, C.-H.; Wu, L.-Z. Synthesis, Characterization, and Selective Sr^{2+} Sensing Study of Copper(I)-Bridged Calix[4]arene-Based Binuclear Alkynylplatinum(II) Complexes. *Eur. J. Inorg. Chem.* **2017**, *2017*, 5108-5113.

(444) Huang, L.; Kakadiaris, E.; Vaneckova, T.; Huang, K.; Vaculovicova, M.; Han, G. Designing next generation of photon upconversion: Recent advances in organic triplet-triplet annihilation upconversion nanoparticles. *Biomaterials* **2019**, *201*, 77–86.

(445) Duan, P.; Yanai, N.; Kimizuka, N. Photon upconverting liquids: matrix-free molecular upconversion systems functioning in air. *J. Am. Chem. Soc.* **2013**, *135*, 19056-19059.

(446) Kwon, O. S.; Song, H. S.; Conde, J.; Kim, H. I.; Artzi, N.; Kim, J. H. Dual-Color Emissive Upconversion Nanocapsules for Differential Cancer Bioimaging In Vivo. *ACS Nano* **2016**, *10*, 1512-1521.

(447) Liu, Q.; Yang, T.; Feng, W.; Li, F. Blue-emissive upconversion nanoparticles for low-power-excited bioimaging in vivo. *J. Am. Chem. Soc.* **2012**, *134*, 5390-5397.

(448) Askes, S. H.; Pomp, W.; Hopkins, S. L.; Kros, A.; Wu, S.; Schmidt, T.; Bonnet, S. Imaging Upconverting Polymersomes in Cancer Cells: Biocompatible Antioxidants Brighten Triplet-Triplet Annihilation Upconversion. *Small* **2016**, *12*, 5579-5590.

(449) Son, H. J.; Jin, S.; Patwardhan, S.; Wezenberg, S. J.; Jeong, N. C.; So, M.; Wilmer, C. E.; Sarjeant, A. A.; Schatz, G. C.; Snurr, R. Q.; Farha, O. K.; Wiederrecht, G. P.; Hupp, J. T. Light-harvesting and ultrafast energy migration in porphyrin-based metal-organic frameworks. *J. Am. Chem. Soc.* **2013**, *135*, 862-869.

(450) Rowea, J. M.; Zhu, J.; Soderstrom, E. M.; Xu, W.; Yakovenkob, A.; Morris, A. J. Sensitized photon upconversion in anthracene-based zirconium metal-organic frameworks *Chem. Commun.* **2018**, *54*, 7798-7801.

(451) Oldenburg, M.; Turshatov, A.; Busko, D.; Wollgarten, S.; Adams, M.; Baroni, N.; Welle, A.; Redel, E.; Woll, C.; Richards, B. S.; Howard, I. A. Photon Upconversion at Crystalline Organic-Organic Heterojunctions. *Adv. Mater.* **2016**, *28*, 8477-8482.

(452) Gharaati, S.; Wang, C.; Forster, C.; Weigert, F.; Resch-Genger, U.; Heinze, K. Triplet-Triplet Annihilation Upconversion in a MOF with Acceptor-Filled Channels. *Chemistry* **2020**, *26*, 1003-1007.

(453) Borisov, S. M. In *Quenched-phosphorescence Detection of Molecular Oxygen: Applications in Life Sciences*, Papkovsky, D. B.; Dmitriev, R. I., Eds.; Royal Socienty of Chemistry: Cambridge, 2018, pp 1-18.

(454) Baluschev, S.; Katta, K.; Avlasevich, Y.; Landfester, K. Annihilation upconversion in nanoconfinement: solving the oxygen quenching problem. *Mater. Horiz.* **2016**, *3*, 478-486.

(455) Baluschev, S.; Yakutkin, V.; Wegner, G.; Minch, B.; Miteva, T.; Nelles, G.; Yasuda, A. Two pathways for photon upconversion in model organic compound systems. *J. Appl. Phys.* **2007**, *101*, 023101.

List of Abbreviations

ACQ	Aggregation caused quenching
AIE	Aggregation-induced emission
CSU	Cooperative sensitization upconversion
DLS	Dynamic light scattering
ESA	Excited-state absorption
ETU	Energy transfer upconversion
FLIM	Fluorescence lifetime imaging
FRET	Förster resonance energy transfer
HOMO	Highest occupied molecular orbital
ISC	Intersystem crossing
LMCT	Ligand-to-metal charge transfer
LC	ligand-centered
LUMO	Lowest unoccupied molecular orbital
MC	Metal-centered
MMLCT	Metal-Metal to ligand charge transfer
MOFs	Metal-organic frameworks
MLCT	Metal-to-ligand charge transfer
MO	Molecular orbitals
NIR	Near infrared
NPs	Nanoparticles
NMs	Nanomaterials
PDT	Photodynamic therapy
PL	Photoluminescence
PLQY	Photoluminescence quantum yield
PMT	Photomultiplier tube
PA	Photon avalanche
PLIM	Phosphorescence lifetime imaging microscopy
PLGA	Poly(d,l-lactic-co-glycolic acid)
PNPs	Polymeric nanoparticles
PMMA	Poly(methyl methacrylate)

PS	Polystyrene
PSNPs	Polystyrene nanoparticles
QDs	Quantum dots
ROS	Reactive oxygen species
SBU	Secondary building unit
SWIR	Short-wave infrared
SV	Stern-Volmer
TCSPC	Time-correlated single photon counting
TMCs	Transition metal complexes
TTA-UC	Triplet-triplet annihilation upconversion
TTET	Triplet-triplet energy transfer
UV	Ultraviolet
UC	Upconversion
UCL	Upconversion Luminescence
UCNPs	Upconversion nanoparticles

Publication and Patent

1. Ligand-controlled aggregation and nanoconfinement-boosted phosphorescence from Pt(II) and Pd(II) complexes: Towards color tunable reporters and self-referenced oxygen sensors

   Iván Maisuls[†], **Cui Wang[†]**, Matias E. Gutierrez Suburu, Sebastian Wilde, Constantin-Gabriel Daniliuc, Dana Brünink, Nikos L. Doltsinis, Stefan Ostendorp, Gerhard Wilde, Jutta Kösters, Ute Resch-Genger and Cristian A. Strassert
   Chemical Science (submitted on 06. Nov. 2020)
   (†: equal contribution)
   - **This publication is relevant to the dissertation.**

2. Near-IR to Near-IR Upconversion Luminescence in Molecular Chromium Ytterbium Salts

   Jens Kalmbach,[#] **Cui Wang,[#]** Yi You, Christoph Förster, Hartmut Schubert, Katja Heinze, Ute Resch-Genger and Michael Seitz
   Angew. Chem. Int. Ed. **2020**, 59, 18804-18808; *Angew. Chem.* **2020**, 132, 18966 – 18970.
   (#: equal contribution)
   - **This publication is relevant to the dissertation.**

3. Green-Light Activation of Push–Pull Ruthenium(II) Complexes

   J. Moll, **C. Wang**, A. Päpcke, C. Förster, U. Resch-Genger, S. Lochbrunner and K. Heinze.
   Chem. Eur. J. **2020**, *26*, 6820-6832

4. Triplet-Triplet Annihilation Upconversion in a Crystalline MOF with Acceptor-filled Pores

   S. Gharaati‡, **C. Wang‡**, C. Förster, U. Resch-Genger and K. Heinze
   Chem. Eur. J. **2020**, *26,*1003 –1007
   (‡: equal contribution)
   - **This publication is relevant to the dissertation.**

5. Luminescence and Light-driven Energy and Electron Transfer from an Exceptionally Long-lived Excited State of a Non-innocent Chromium(III) Complex

   S. Treiling, **C. Wang**, C. Förster, F. Reichenauer, J. Kalmbach, P. Boden, J. P. Harris, L. Carrella, E. Rentschler, U. Resch-Genger, C. Reber, M. Seitz, M. Gerhards, K. Heinze.
   Angew.Chem. Int. Ed. **2019**, 58,18075 –18085*; Angew. Chem.* **2019**, 131, 18243 – 18253

6. A π-conjugated, covalent phosphinine framework

   J. Huang, J. Tarábek, R. Kulkarni, **C. Wang**, M. Dračínský, G. J. Smales, Y. Tian, S. Ren, B. R. Pauw, U. Resch-Genger, M. J. Bojdys.
   Chem. Eur. J. **2019**, *25*, 12342–12348

7. Luminescent TOP Nanosensors for Simultaneously Measuring Temperature, Oxygen, and pH at a Single Excitation Wavelength

   C. Wang, S. Otto, M. Dorn, K. Heinze, U. Resch-Genger;
   Anal. Chem. **2019**, 91(3), 2337–2344
   - **This publication is relevant to the dissertation.**

8. A strongly luminescent chromium(III) complex acid

   S. Otto, C. Förster, **C. Wang**, U. Resch-Genger, K. Heinze;
   Chem. Eur. J. **2018**, 24(48), 12555-12563

9. Deuterated Molecular Ruby with Record Luminescence Quantum Yield

   C. Wang, S. Otto, M. Dorn, E. Kreidt, J. Lebon, L. Sršan, P. Di Martino-Fumo, M. Gerhards, U. Resch-Genger*, M. Seitz*, K. Heinze*
   Angew. Chem. Int. Ed. **2018**, *57*, 1112 –1116. *Angew. Chem.* **2018**, *130*, 1125–1130.
   - **This publication is relevant to the dissertation.**

10. Three-in-One Crystal: The Coordination Diversity of Zinc Polypyridine Complexes

    S. Otto, J. Moll, C. Förster, D. Geißler, **C. Wang**, U. Resch-Genger*, K. Heinze*
    Eur. J. Inorg. Chem. **2017**, 5033-5040

Patent

Verwendung von d8-Metallkomplexverbindungen mit Liganden-kontrollierten Aggregations- und Lumineszenzeigenschaften

Inventors: Dr. Ute Resch-Genger, **Cui Wang**, Prof. Cristian Alejandro Strassert, Matias Ezequiel Gutierrez Suburu, Dr. Ivan Maisuls.

Deutsche Patent- und Markenamt, submitted on 15. April 2020

Curriculum Vitae

The CV is not included in the online version.

The CV is not included in the online version.

Acknowledgements

Finally, I want to thank my families and friends who always stand behind me. 谢谢你们这几年来对我无条件的支持，让我能追求自己喜欢的东西。你们将是我继续前进的动力，感谢!